Assessing the influence of lifter profiles on the velocity profile and the charge toe and shoulder using data from the PEPT system

By

Hartmut Brodner

Center for Mineral Research (CMR)

Declaration of plagiarism

I acknowledge that plagiarism is wrong. Plagiarism is to use another's work and to pretend that it is one's own.

Each significant contribution to, and quotation in, this report from the work, or works, of other people has been attributed, and has been cited and referenced.

This report is my own work.

I have not allowed, and will not allow, anyone to copy my work with the intention of passing it off as his or her own work.

Hartmut Brodner…… Date: 1 April 2013

Acknowledgements

I would like acknowledge the University of Cape Town (UCT), the National Research Fund (NRF), the Technology and Human Resources Programme (THRIP) and the South African Minerals to Metals Research Institute (SAMMRI) for funding my experiments and experimental equipment and consumables. Without the financial support my thesis work would have not been possible. I would like to extend my appreciation to Professor Reddy for allowing me to use the facilities of the Centre for Research in Computational and Applied Mechanics (CERECAM). I would like to extend my gratitude to IThemba Labs for allowing me to use their facilities to conduct my particle tracking experiments.

Throughout my thesis I received some good advice and I received help from fellow academics. I would like to firstly thank all my supervisors. Dr.Mainza for the support, advice and countless hours he put into assisting me with corrections to my thesis. Dr.Govender for the patience extended to me while I was developing my ideas and theories and for the good advice. Finally I would like to thank Prof.Powell for the thought provoking ideas and questions. Mr.Morrison, my fellow academic, was influential in assisting me with the logic behind some of the intricate Matlab codes and with coding data anomalies. I would like to extend my gratefulness to Mr. Van Heerden (Michael) and Mr.Cong (Liu) for assisting me so diligently throughout my experiments and being prepared to go the extra mile with me so that I could complete my experiments in the set time.

Dedication

I would like to dedicate the completion of my thesis to my family and to god. I want to thank my mother for always supporting me through the highs and lows of my thesis. I appreciate the effort she went through to make my life as simple as possible. My mother is a strong advocate for education at any level and statements such as 'I want you to finish your studies no matter what it takes. I will sell everything I have to make sure you boys have a good education' just proved the point. She has done more for me than I could ever ask for and ever wanted. My mother has inspired me and has given me the energy to successfully complete my thesis and to achieve what I set out to do. I love you mom.

No family is complete without siblings. I want to thank my brothers for always being there for me throughout my thesis, especially when the going was tough and I had lost some motivation. They have always managed to help when I get knocked down by different challenges. Without you guys the journey of the thesis would have been much tougher and less fun. I just hope I can one day assist in your life goals as you guys did/are doing for me. I love you guys.

I would like to say a special thanks to god for helping me through my thesis. For answering all my prayers and giving me the guidance and wisdom I needed to complete my thesis. I will forever be grateful.

Synopsis

The research focus of this thesis is lifter height effect on different charge characteristics. The charge characteristics identified were shoulder and toe angle, charge size and toe height. An attempt was made to develop a model for the velocity profile incorporating lifter height. Therefore the objectives of the study are to:

- Determine the effect of lifter height on the velocity profile using the particle tracking data.
- Determine the effect the lifter height on the charge shoulder and toe.
- Develop a velocity profile model including lifter height using granular flow theory and to compare the model to experimental data.

The motivation for the study is that lifters are one of the most important design variables in a mill. Without lifters the mill's energy efficiency would decrease. In Meaders & MacPherson, (1964) the effect of lifters on energy was quantified to be between 20% and 30%. The lifters control the height and angle of departure from the charge at the mill shell and therefore control the impact area and magnitude. The area and magnitude of the charge impact will affect the grind of the mill and energy utilization in the mill.

The thesis was also aimed at generating data that can be used to model the velocity profile that can be incorporated in power models. Most of the power models do not account for the effect of lifters.

The experiments involved collecting data from three dimensional particle tracking of selected particles in the charge. using the PEPT system. The PEPT experiments were conducted at IThemba Labs in Cape Town South Africa using a 300 mm x 285 mm experimental mill. The charge used for the experiments were glass beads with an approximate specific gravity (SG) of 2.7. The PEPT system operates by tracking the x, y and z coordinates with respect to time of an irradiated particle (tracer). The experiments were run under different conditions to evaluate the effect of the lifter height. The experiments were operated by varying mill speed (55%, 70% and 85%), mill fill (20%, 30% and 40%) and lifter heights (1.5 mm, 3 mm, 6 mm and 10 mm).

The lifter height has the most significant effect at a mill filling of 20%, where higher velocity magnitudes were observed with increase in lifter height. At 30% and 40% mill filling the lifter height does not have a significant effect.

The lifter height does not seem have an influence on the toe region, but the results show that the shoulder angle increased with lifter height. This could be due to the charge particles taking a longer time to discontinue contact with higher lifters and hence are carried to a higher position within the mill resulting in a larger shoulder angle. The lifter height did not seem to have an effect on the charge size.

The toe height is affected by lifter height although not well pronounced for the 30% and 40% mill filling. The toe height increased with lifter height and this trend was more defined for low filling degrees.

A model for the prediction of the velocity profile for the mill operated with different lifter profiles was developed. However, the model appeared to capture the description well in some regions. It was found that the model matched the experiments in certain regions, but gave incorrect predictions in others. Further work is required to make the model generally applicable.

Contents

List of Figures

List of Tables

Nomenclature

Variables	Units	Description
F	N	Applied force
F_x	N	Applied force in the x-direction
v	m/s	velocity
v_x	m/s	Velocity in the x-direction
ρ	kg/m^3	density
n	dimensionless	Unit vector (indicates direction of vector)
τ_{yx}	N	Shear stress in the x-direction perpendicular to the y-axis
σ_{xx}	N	Normal stress in the x-direction
g	m/s^2	Gravitational acceleration
g_x	m/s^2	X-component of the gravitational acceleration
P	Pa	Applied pressure
t	s	time
C.V.	m^3	Control volume
C.S.	m^2	Control surface
μ	Pa*s	Fluid viscosity
x	dimensionless	x-component
y	dimensionless	y-component
z	dimensionless	z-component
v_{mill}	m/s	Tangential velocity of the mill
L_2	m	Distance from center of circulation to the mill shell
F_f	N	Frictional force
F_N	N	Normal force of particle
F_g	N	Gravitational force
F_{N2}	N	Normal force of particles above particle of interest
m	kg	Mass of particle
μ_k	dimensionless	Friction coefficient
D	m	Particle diameter
F^e	N	Applied force in region 1
N_{yy}	N	Normal force of a particle in region 1
P_{atm}	Pa	Atmospheric pressure
A	dimensionless	Indefinite integral constant
V_x	m/s	Velocity of particles within region 1
V_c	m/s	Velocity of the cascading particles
L_1	m	Distance from the center of circulation to the charge free surface
μ_e	dimensionless	Friction coefficient

Glossary

Critical mill speed: The critical mill speed is the rotational speed of the mill when material in the mill is centrifuging

Mill speed: The mill speed indicates the speed the mill is rotating and it is usually reported as a fraction of the critical mill speed

Mill fill: The mill fill is the percentage filling of the mill

Charge: The charge describes the process material in the mill, which usually is ore and water

Grinding media: The grinding media is the material in the mill to assist in ore breakage and grinding, usually it consists of steel balls or rods

Cataracting: Cataracting describes the material in the mill that is in flight

Cascading: Cascading describes the material rolling and sliding down the main body (bulk charge) of the material in the mill

Centrifuging: Centrifuging describes the material that is moving with the mill and at the same speed

En-masse region: The en-masse region is the main body of the material in the mill, also known as the bulk charge.

Liner: The liner is a layer of steel that is usually put in the mill to protect the mill shell from wear and impact

Lifter: The lifter is a unit that is attached to the liner of the mill and prompts high impact in the mill

Slumping: Slumping describes the sliding and downward movement of the material in the mill while it is suppose to be moving up against the mill

1 Introduction

1.1 Purpose

The focus of this study is to assess the effect of lifter height on the velocity profile, attempt to include the lifter height in the development of a velocity profile model and quantify the charge's toe and shoulder under different operating conditions using different lifter heights.

1.2 Mining in the World

The mining industry has existed for hundreds of years and it is one the most important industries in the world. It can be seen in the same light as the agriculture industry in terms of importance. This becomes quite obvious when one looks around to see how much metal and other minerals are used for the production of everyday objects and technologies. It has been estimated by the Minerals Information Institute of Colorado (2002) that every American uses 3.6 million pounds of minerals in their lifetime.

The production rates of the mining industry are quite staggering and serve as an additional indicator of its importance. The world principle mineral commodities production stood at a staggering 11.7 billion metric tons for 2003 (Othmer, 2007), which excludes the petroleum industry. The petroleum industry produced an additional 3.6 billion metric tons of principle mineral commodities for the production of hydrocarbons.

1.2.1 Different types of Mining

The mining industry is the front runner of many technologies and sciences. This can be attributed to the variability of the mining industry. The variability has driven different types of mining, such as open pit mining, underground mining and alluvial and solution mining.

1.3 Mining in South Africa

The South African mining industry has been around since the late 1880's, when the Witwatersrand Gold Rush occurred, and has played a very important role in the history of the country. Even nowadays mining is an important factor in South Africa, as mining directly sustains 458 600 jobs and indirectly sustains 555 000 jobs (Chambers of Mines of South Africa

(2006)). Mining in South Africa is world renowned for their primary mineral exports (platinum group metals, gold and coal) and their secondary mineral derivatives (chemicals, alloys and aluminium) exports.

1.3.1 Economics

The South African mining industry contributes a substantial portion to the GDP. The direct contribution of the mining industry to the South African GDP is 7%, which is R120 billion (Chambers of Mines of South Africa (2006)). The total contribution of the mining industry to the GDP of South Africa is about 15% to 20% (Chambers of Mines of South Africa (2006)), as it contributes to other upstream and downstream industries such as the insurance and banking.

1.3.2 Energy usage

Despite the South African mining industry's contribution to the economy and social development, it is a significant raw materials consumer. The industry consumes 15.3% of Eskom's local electricity sales. Even with the large energy consumption, the mining industry contributes a large portion of energy. In the report by Chambers of Mines of South Africa (2006) it is stated that without the mining industry 70% of the primary energy supply would be lost. This however is not a surprise, as 93% of South Africa's electricity is produced from coal.

1.4 Subdivision of the Mineral processing

The mining industry is responsible for the production of many basic and precious metals. In spite of the variability of the products the general process of extraction and processing of the raw material is similar for specific types of mining. In this case a combination of underground and open pit mining is considered. In order to give a general overview of the mineral recovery process a basic flow diagram is presented in Figure 1. Mining and transporting the ore to the processing plant are the first two steps in mineral processing, as can be seen in Figure 1. The next step in the process is comminution and classification, which is shown in Figure 2. The comminution step is there to reduce the size of the ore, so that the valuable minerals can be exposed for separation and extraction to take place. The classification step scalps out the particles that are too large for further processing and recycles these back to the comminution

step. The separation of the valuable ore and the waste ore is facilitated in the separation step. The type of separation, chemical or physical, is dependent on the type of ore.

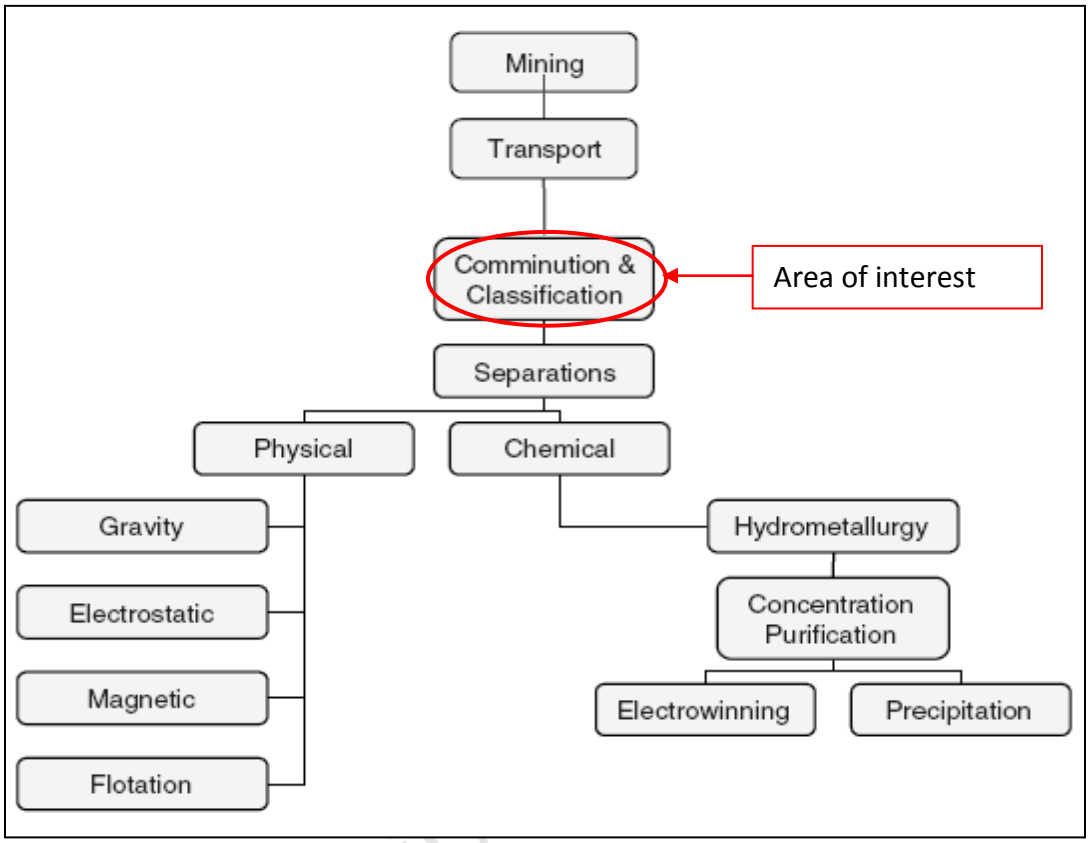

Figure 1: General Mineral Processing Flow Diagram (Othmer, 2007)

In some cases both types of separation are used. Once the separation process is complete, the material containing base and precious metals reports to either the pyrometallurgical or hydrometallurgical processes where the final product is extracted. The process of particular interest in this thesis is the comminution step highlighted in Figure 1.

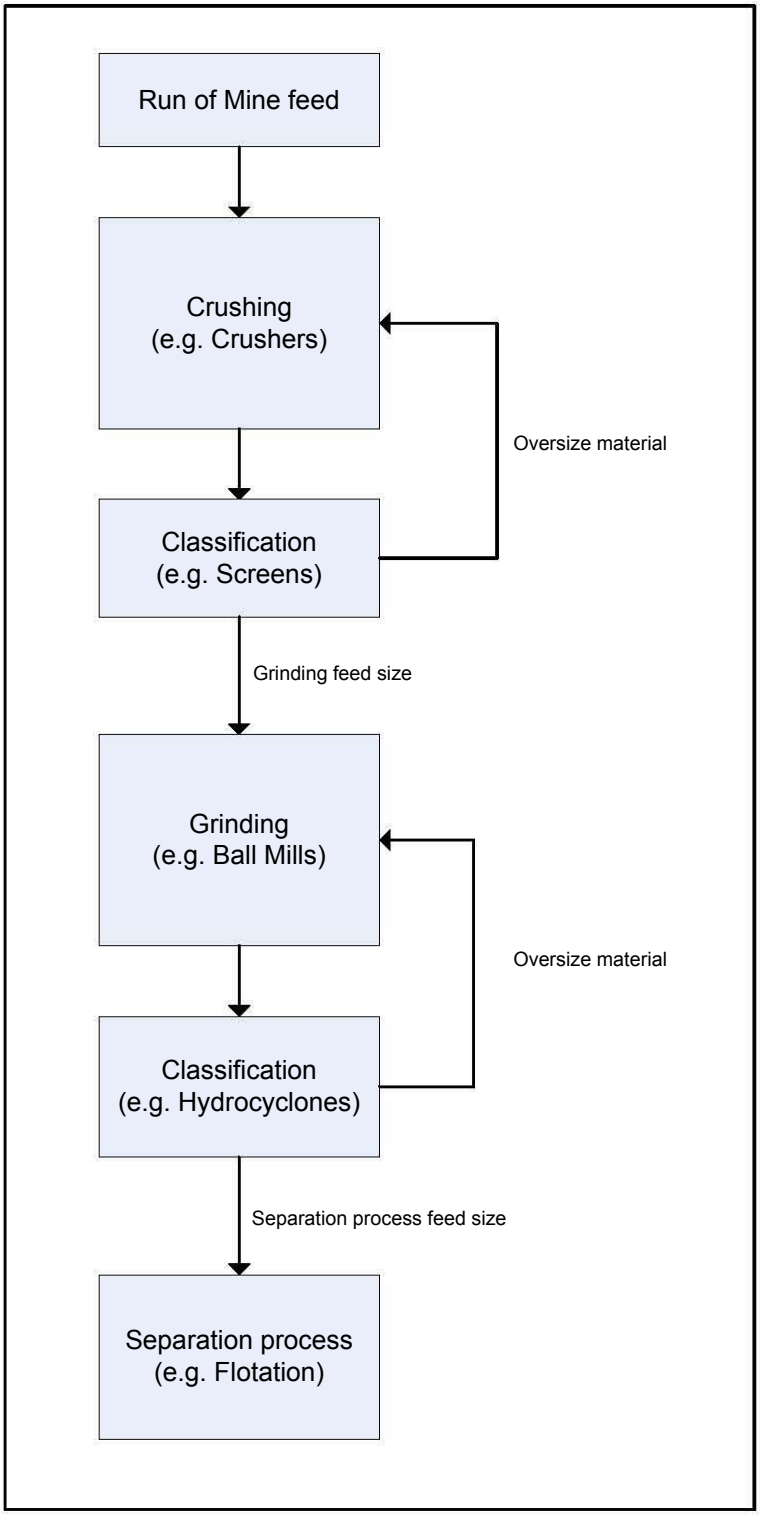

Figure 2: Basic flow sheet of the comminution, classification and separation process

1.5 Comminution

1.5.1 Crushing

Comminution is the first stage of the ore concentration process and it is concerned with size reduction. Comminution can be split up into the crushing and grinding processes. According to Napier-Munn et al (2005) main role of the crushers is to maximize size reduction, which aids as feed preparation for grinding. The crushing machines used in industry are Jaw Crushers, Gyratory Crushers, Cone Crushers and Rolls and Impact Crushers.

1.5.2 Grinding

Once the rock size has been reduced, the crushed material is sent to the grinding process. The size of the crushed material is further reduced to liberate the desired material and to allow for effective separation, as described in Napier-Munn et al (2005). According to Othmer (2007) the size depends on the mineralogy of the ore, economic climate and the process that is being implemented. Grinding in this case occurs by abrasion and impact in mills using different grinding media. Different mills use different grinding media. The ball, rod and autogenous mills use steel balls, steel rods and large pieces of ore as grinding media, respectively. The semi-autogenous (SAG) and pebble mills use ore/ steel balls and competent pebbles (can be pebbles from the same ore), respectively. Ceramic pebbles are also used in some cases. The high pressure grinding rolls uses rolls that are kept close to each other by springs to grind the material. Grinding can occur in wet or dry conditions. Wet grinding is the most common form of grinding. Wet grinding is the process of grinding the ore in a mixture of ore charge and water, which is called slurry. The research will be focusing on a dry environment.

1.5.2.1 Tumbling mills

The most commonly used piece of equipment for any type of grinding is the tumbling mill. The tumbling mill is rotating drum that achieves grinding through the tumbling charge. The charge comprises of grinding media and the ore to be ground. The grinding media that are used for the tumbling mill is either large rocks, large rocks and steel balls, steel balls or steel rods only. The balls and rods are made up of either forged or rolled high carbon or alloy steel or cast alloy steel or ceramic beads. The grinding media generally occupies 15% to 45% of the volume of the

tumbling mill, although Napier-Munn et al (2005) claims an average mill fill volume of between 35% to 45% mill fill. The tumbling mill is lined with abrasion-resistant material to minimize the wear on the mill shell, which is known as a liner. According to Othmer (2007) the liners are made of cast or rolled steel and rubber and are replaced regularly. Lifters are installed inside of the tumbling mill to maximize high impact charge behaviour and reduce slip between the charge and mill shell. Additionally lifters are used to minimize mill shell impacts, as explained in Othmer (2007). The lifter has an effect on charge characteristics that influence power draw, which in this research is investigated using the Positron Emission Particle Tracking (PEPT) (Parker et al (1997)) technique. The investigation is the first of its kind, where the PEPT system, as described in Parker et al (1997), is used to analyze the lifter effect. Further information on lifters and their function is provided in the literature review.

1.5.2.2 Energy and cost

Comminution is the most energy intensive section of the mineral extraction process. The energy estimated for the comminution section is between 30%-50% (Othmer, 2007) of the total energy of the mineral recovery process.

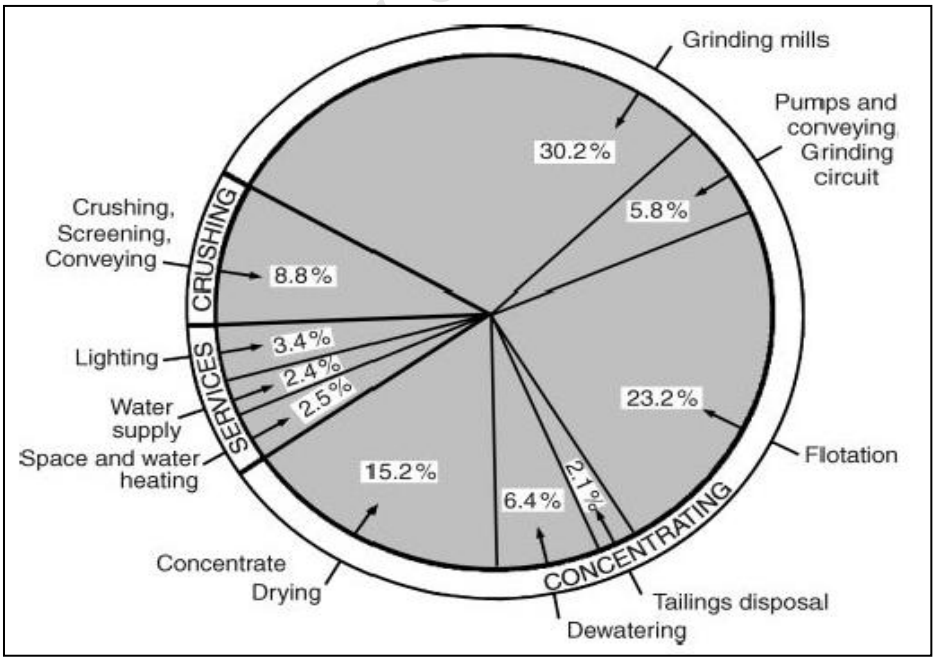

Figure 3: Energy distribution graph (Fuerstenau and Han (2003))

In Figure 3, taken from Fuerstenau and Han (2003), the typical energy distribution for a mineral processing plant is shown. The grinding mill consumes the most energy at 30% of the total energy. Additionally the milling process is energy inefficient with only 1% of the energy input used for rock breakage (Fuerstenau & Abouzeid (2002)). The factors that affect energy consumption in a mill are mill speed, mass inside the mill, discharge type (overflow or grate discharge) and lifter configuration. The operating costs of the comminution process are estimated to be between 50% and 60% (Othmer, 2007) of the total operating costs of the entire plant. The factors affecting the operating costs in a mill are energy consumption (mill speed and **lifter configuration)** and **liner and lifter replacing (cost of liner and lifter and down time)**.

Energy consumption and operating cost are two important aspects of a mineral processing plant. There is a continuous desire to optimize both aspects and maximize profits on the mineral processing plant. Lifters can play a role in achieving these goals.

1.5.3 Energy Models

The approach that has been taken by researchers to tackle the energy consumption challenge has been largely influenced by industry. The belief in industry is that the higher the power draw is of a tumbling mill the better the mill will perform, as more energy is used for the breakage process. Although this assumption is correct in some cases it does not take into account factors that influence the breakage rate of the rock in the mill at different design and operating conditions. One of the most important factors omitted is the influence of the lifter configuration and solids concentration in the mill, which alter the effective energy consumption up to 20 - 30% (Meaders & MacPherson, (1964)).

The approach to energy optimization so far has been to create energy models of the milling systems. The earliest energy models in literature are empirically developed and are bias towards the parent data sets. It is evident that the earlier models did not take all the aspects of the mill into account. This resulted in variations in the pre predictive performances.

In the 1990's a more robust power model was developed by Morrell (1993). The Morrell power model was a mixture of fundamental understanding with empirical adjustments to certain aspects of the power equation to ensure that the factors he did not incorporate where taken

into account. The concept of a velocity profile was introduced as part of the development of his power model. Although the lifter configuration is important to mill performance and is known to influence the charge trajectory, it was left out of the power models developed thus far.

2 Literature Review

2.1 Introduction

The thesis will address the development of the velocity profile for use in power models. Among the deficiencies highlighted is that the effect of lifters is not included. Another focus area is the effect of lifters on charge characteristics such as toe and shoulder angle. The lifter's literature review is presented in section 2.6 and the velocity profile's literature review is presented in sections 2.2 to 2.5.

The power model literature review's focus is on the power model development, because there is limited literature on velocity profiles. No set of research has been dedicated towards the analysis or development of the velocity profile. The velocity profile was introduced through the development of the Morrell power model. Therefore the velocity profile's development is tracked through the power model development. Three milestone power models are reviewed in detail. The reviewed power models are Davis, Bond and Morrell. The reviews will highlight the differences and similarities of the power models. Each power model has a chapter dedicated to the particular model. The variables for the different equations in each chapter are available at the end of each section. After each section critical thoughts and opinions of the author are given. In particular, the thoughts and opinions related to the lifter profiles omission from the power model development. After the power model development a review on the use of the velocity profile with 'comments' is represented. The last chapter reviews lifter configurations, where lifters are introduced, defined and their effect on power draw is presented.

2.2 Davis Power Model

Davis was one of the first researchers in the mining industry to develop a power model for tumbling mills. Davis in 1919 believed that the mill's power draw could be estimated by quantifying the energy lost by the cataracting charge in the toe region of the mill. Therefore energy lost by the particles in the charge could be determined by the kinetic energy of the particles in free flight. In order to calculate the magnitude of the kinetic energy Davis needed to

determine the points at which a particle would depart the charge shoulder and the impact area of the particle in the toe region.

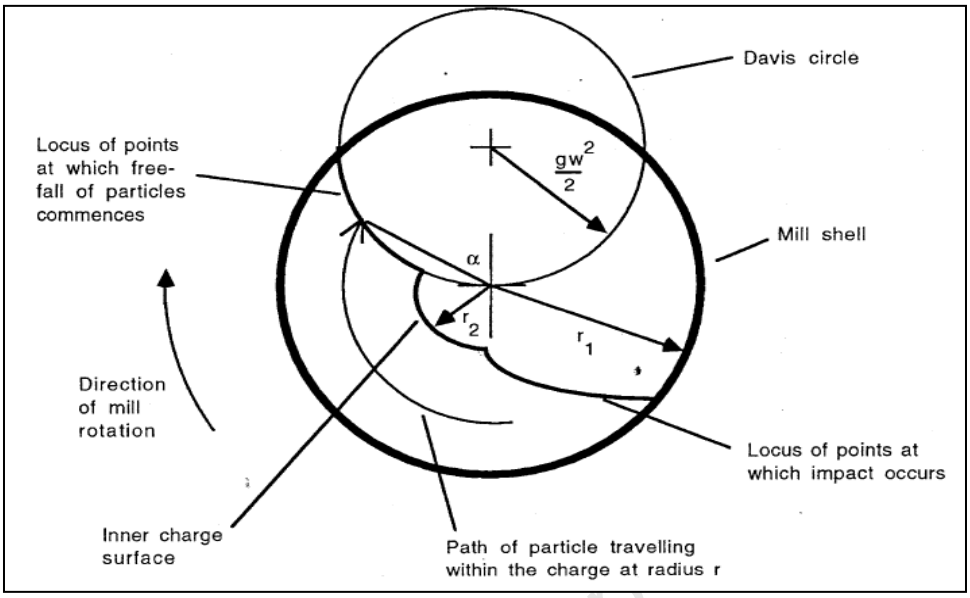

Figure 4: Particle's movement (Morrell (1993))

According to Davis (1919) the departure points from the charge shoulder is determined with the help of a circle with a radius of $gw^2/2$ (Figure 4).The circle's centre is in line with the centre of rotation of the mill. The variables for all the equations are represented and explained in Table 1.

The calculated points of impact of the particles in the mill are defined by equation 1 and 2:

$$x = 4r \sin \alpha \cos^2 \alpha \quad (1)$$

$$y = -4r \sin^2 \alpha \cos \alpha \quad (2)$$

A unique characteristic to this power model was the estimated particle path in the mill. Davis (1919) assumed that during free flight the particle would have a parabolic path, but would have a set circular path while moving through the charge. Davis (1919) stated further that the particle would be released from its set circular path and move in free flight once the centrifugal and gravitational forces balance. The point of impact chosen for the development of the power model was the mill shell, as this presented a situation where a maximum energy transfer would

occur. Therefore the kinetic energy for a particle colliding with the mill shell is described by equation 3 and 4:

$$e = w(8Fr^2 - 16F^3r^4 + 8F^5r^6) \quad (3)$$

$$F = 1.226n^2 \quad (4)$$

The equation of F relates the mill speed to the kinetic energy of the cataracting particle.

In Davis (1919) it is explained that the power model is developed using the 'most efficient speed'. Before the 'most efficient speed' could be determined an expression for the mill volume not in flight needed to be determined. A relationship between the mill radius (r_1) and the inner charge radius (r_2) needed to also be established, which can be seen in equation 5. Variable 'K' in equation 5 is the volume of the charge not in flight. In equation 6 the volume of the charge not in flight (K) is related to the charge volume when the mill is stationary (P).

$$r_2 = Kr_1 \quad (5)$$

$$K = -0.024 + 0.39\sqrt{7 - 10\boldsymbol{P}} \quad (6)$$

The 'most efficient speed' was determined by the equation 7:

$$N = \frac{48.948}{{r_1}^{0.5}(1+K^2)^{0.25}} \quad (7)$$

The power model was developed under the basis of the 'most efficient speed'. Davis (1919) therefore claimed that the power model was only valid under those conditions. The final form of the Davis power model is given in equation 8.

$$P = W \cdot r_1^{3/2} \cdot \left[0.004467 \cdot \frac{(1-K^3)}{(1+K^2)^{1/8}} - 0.0037 \cdot \frac{(1-K^5)}{(1+K^2)^{3/8}} + 0.0008 \cdot \frac{(1-K^7)}{(1+K^2)^{5/8}}\right] \text{(hp)} \quad (8)$$

Once the power model was developed Davis validated and tested it against experimental data from a 3 inch diameter mill. Unfortunately it was not validated using a larger experimental mill or industrial data (Davis (1919)).

Table 1: Variables for the Davis power model

Variables	Units	Description
g	m/s^2	Gravitational acceleration
e	hp	Kinetic energy
w	lbm	Weight of particle
n	rev/s	Mill speed
r	ft	Radius of circular path
r_1	ft	Mill radius
W	lbm	Weight of charge
N	rev/s	Most efficient speed
P	ft^3	Mill volume in stationary mill
P	hp	Power
K	dimensionless	fraction of the mill volume that is not in flight
x	m	x-component of the impact point
y	m	y-component of the impact point

2.2.1 Comments on Davis power model

Assumptions

Taking a fundamental approach to the power model is difficult and is heavily dependent in the manner the power is described and understood. Even though it is always critical to state the assumptions made Davis (1919) did not mention why frictional force and inter-particle interaction were neglected. Although it is difficult to add these in a model if one is not using software or if one approaches the physical nature of the system differently the reasons for the omission should be stated, to demonstrate how the system was understood. The frictional force and inter-particle interaction could make a difference to the charge shoulder departure loci and this would affect the point at which the particle strikes the mill wall or charge.

Mill speed

The development of the 'most efficient speed' has not been sufficiently explained. No frame of reference has been given for the efficiency of the speed, as it does not explain if the efficiency has to do with the power consumption or impact areas.

Lifter configuration

Lifter configuration is not considered in the development of the Davis Model and there is no discussion on its contribution to power draw. The lifter configuration has a significant influence on the departure point of the charge, which forms an integral part of the development of the Davis model.

2.3 Bond Power Model

2.3.1 Bond Power Model (1961)

After Davis, many researchers focused on modeling power draw for comminution devices (Hogg and Fuerstenau (1972), Arbeiter and Harris (1982), Liddell (1986) and Moys (1990). However, most of these were equipment specific which made their usage in the industry limited. In 1961 Bond developed a power model that was more flexible and was deemed to be more accurate than all the other power models prior to this model. The Bond Power Model has been used ever since as the standard power model and it has been explained, presented and broken down in many textbooks over the years (e.g. Napier-Munn et al (2005)).

The power model in Bond (1961) was developed empirically. The database that was used to develop the power model was not published. The Bond power model is given by equation 9.

$$P = 2.8 \cdot D^{0.4} \cdot \left(3.2 - 3 \cdot V_p\right) \cdot C_S \cdot \left(1 - \frac{0.1}{2^{(9-10 \cdot C_S)}}\right) \text{(kWb)} \quad (9)$$

The power model describes the power that is put into the mill per ton of grinding balls. The variables in the initial and revised version of the Bond Power Model are given in Table 2. The power model as described in Bond (1961) is applicable to grate and overflow ball mills with a grinding ball diameter greater than D/80. Adjustments needed to be made to the power model

when operating under different grinding conditions. Therefore factors were introduced for wet and dry grinding for grate discharge mills. A factor of 1.08 was used for a dry grinding grate discharge operation and the factor for wet grinding in a grate discharge mill was determined by equation 10:

$$Grate\ discharge\ factor = 1 + \left(\frac{0.4 - V_{pd}}{2.5}\right) \quad (10)$$

Through the grate discharge factor the effect of mill fill volume of slurry is explicitly recognized. It can be seen that as fractional interior mill volume below the discharge level (V_{pd}) increases the power of the mill decreases. Once V_{pd} reached unity the mill is operating as an over flow mill and the grate discharge factor decreases to 0.76. The V_{pd} would only be able to reach unity if the grates were intentionally or naturally blocked. An additional observation made is the point at which the wet grinding factor is lower than the dry grinding factor. The point at which the wet grinding factor is lower than the dry grinding factor is at V_{pd} equal to 0.2. Therefore at V_{pd} lower than 0.2 the wet grinding consumes more power than dry grinding.

In Bond (1961) an additional factor is introduced, namely the 'slump correction' factor. The 'slump correction' factor is described by equation 11:

$$S_s = \left(\frac{12D}{10B} - 8\right)^{1/3} \quad (11)$$

The 'slump correction' factor came about when 'excessive downward slippage' occurred in large mills (greater than 8 feet) when small grinding balls (< D/80) were added as makeup. The 'excessive downward slippage' resulted in a decrease in power. Adjustments needed to be added to the power model to account for this phenomenon in the form of the 'slump correction' factor. In conjunction with the previous observation it was found in Bond (1961) that grinding balls would slip down with respect to the next outer layer, because of the grinding ball arrangement. Bond (1961) therefore claimed that grinding occurred in this portion of the mill. The 'slump correction' factor is added to the power model in equation X by multiplying it to the expression.

Table 2: Variables for the Bond power model

Variables	Units	Description
P	kWb	Power (kilowatts per ton grinding ball)
D	ft	Internal mill diameter
B	in	Diameter of make-up ball
C_s	dimensionless	Fraction of critical speed
V_p	ft^3	Total interior mill volume occupied by grinding charge
V_{pd}	dimensionless	Fraction of interior mill volume below discharge level
S_s	dimensionless	Slump correction
D	m	Internal mill diameter
L	m	Internal mill length
ϕ	Dimensionless	Fraction of critical speed
J	Dimensionless	Volume fraction of ball charge
ρ	ton/m^3	Bulk density of steel balls

2.3.2 Revised Bond Power Model (1962)

Bond published a revised model in 1962 given in equation 12.

$$P = 3.1 \cdot D^{0.3} \cdot \left(3.2 - 3 \cdot V_p\right) \cdot C_S \cdot \left(1 - \frac{0.1}{2^{(9-10 \cdot C_S)}}\right) \text{(kWb)} \quad (12)$$

A comparison of the original and revised Bond models shows that the scaling value was changed from 2.8 to 3.1 and the exponential value of D was changed from 0.4 to 0.3. There is no explanation given for the changes in these revisions. Since as the Bond power model is emperical, it can be assumed that the database was extended to include conditions that were not in the original data used. Similar changes were done on the 'slump correction'. The 'slump correction' in its revised form only has the diameter of the make-up balls as a variable. The revised 'slump correction' factor is given in equation 13.

$$S_s = \frac{1.8 - B}{2} \quad (13)$$

The revised Bond model after incorporating the 'slump correction' is given by equation 14.

$$P = 12.262 \cdot D^{2.3} \cdot L \cdot \rho \cdot \phi \cdot J \cdot (1 - 0.937 \cdot J) \cdot \left(1 - \frac{0.1}{2^{(9-10 \cdot \phi)}}\right) \text{(kW)} \quad (14)$$

It should be noted that the mass of the grinding balls has been moved to the right hand side in the revised equation, which explains the change in the units from kWb to kW. The grinding ball mass has been defined by the steel ball bulk density, diameter of the mill (hence the exponent of D changed from 0.3 to 2.3), internal mill length and volume fraction of ball charge.

2.3.3 Bond Model comments

Database

The Bond Power Model is an empirical model that is based on industrial data. The industrial data used in the model development was not published. It would have been helpful to see the range of operating conditions covered in the data used to develop the model to determine the range of applicability. It would have also assisted in determining if there was any bias in the data used. No validation of the power model was published; but Bond (1961) claimed that the power model had been validated by the data.

Bias

The inherent problem with empirically developed model is to be applicable for conditions other than those from which the model was built. Therefore an empirical model can be one dimensional and this can be seen by the fact that there was a revision of the work in Bond (1961). The constants and 'slump correction' factor from Bond (1961) changed and were published again in Bond (1962).

Types of grinding

An observation was made on the difference between the wet and dry grinding techniques. According to Bond (1961) the grate discharge factor shows the relationship between slurry level and power. The relationship states that under a V_{pd} of 0.2 wet grinding consumes more power than dry grinding. This does contradict a well accepted fact that wet grinding consumes less

energy than dry grinding. This inconsistency does not affect the use of the power model in most industrial applications, because most mills are operated at V_{pd} values above 20%.

Lifter configuration

The lifter configuration is not considered in Bond Power Model. The lifter configuration would make a difference to the slumping in the mill. With lifters the charge is keyed in and has more traction. Including lifters into the slumping factor would give a more representative description of the charge behavior in a tumbling mill.

2.4 Morrell Power Model

A few other power models were developed after the revised Bond power model such as the power models from Hogg and Fuerstenau (1972), Arbeiter and Harris (1982), Liddell (1986) and Moys (1990), but the predictions from these were poor in comparison to Bond. The poor predictions were a result of equipment specific models. The Morrell Power Model published in paper in 1993, however, gave significantly better predictions for a wide range of industrial mills. (Morrell (1993)). The Morrell Power Model is a fundamental Power Model with empirical adjustments for certain unaccounted for losses.

Among the three distinct theories that could have been used to develop the power model Morrell chose the energy balance approach. The other options were a frictional force and torque approach. The energy balance theory is the most appropriate for developing the fundamental power model. The other approaches 'over simplify' the system.

The energy balance used for the Morrell Power Model was a measure of the rate of energy that was generated within the charge of the mill. Therefore the energy balance consisted of a kinectic and potential energy balance. There are two important aspects that need to be determined, namely particle velocity in the charge (velocity profile) and charge shape. The velocity profile of the charge is required for the kinetic energy. The charge shape is used to extract the area over which the energy balance is integrated to determine the total power draw of the system. The charge shape aspect did not just include an estimation of the charge shape, but also determining characteristic relationships for the charge's boundaries such as the toe

and shoulder region. The velocity profile and the charge shape were extracted from laboratory experiments conducted by Morrell (1993).

The experiments were conducted using a 300mm x 150mm (diameter x length) mill with a glass front plate, so that the charge behaviour could be observed. The mill was mounted on two rollers. A speed controller and motor were used to vary the mill speed between 73% and 112% for the experiments. Three different lifters were used during the experiments, namely a beveled, double wave and a noranda lifter which are illustrated in Figure 5.

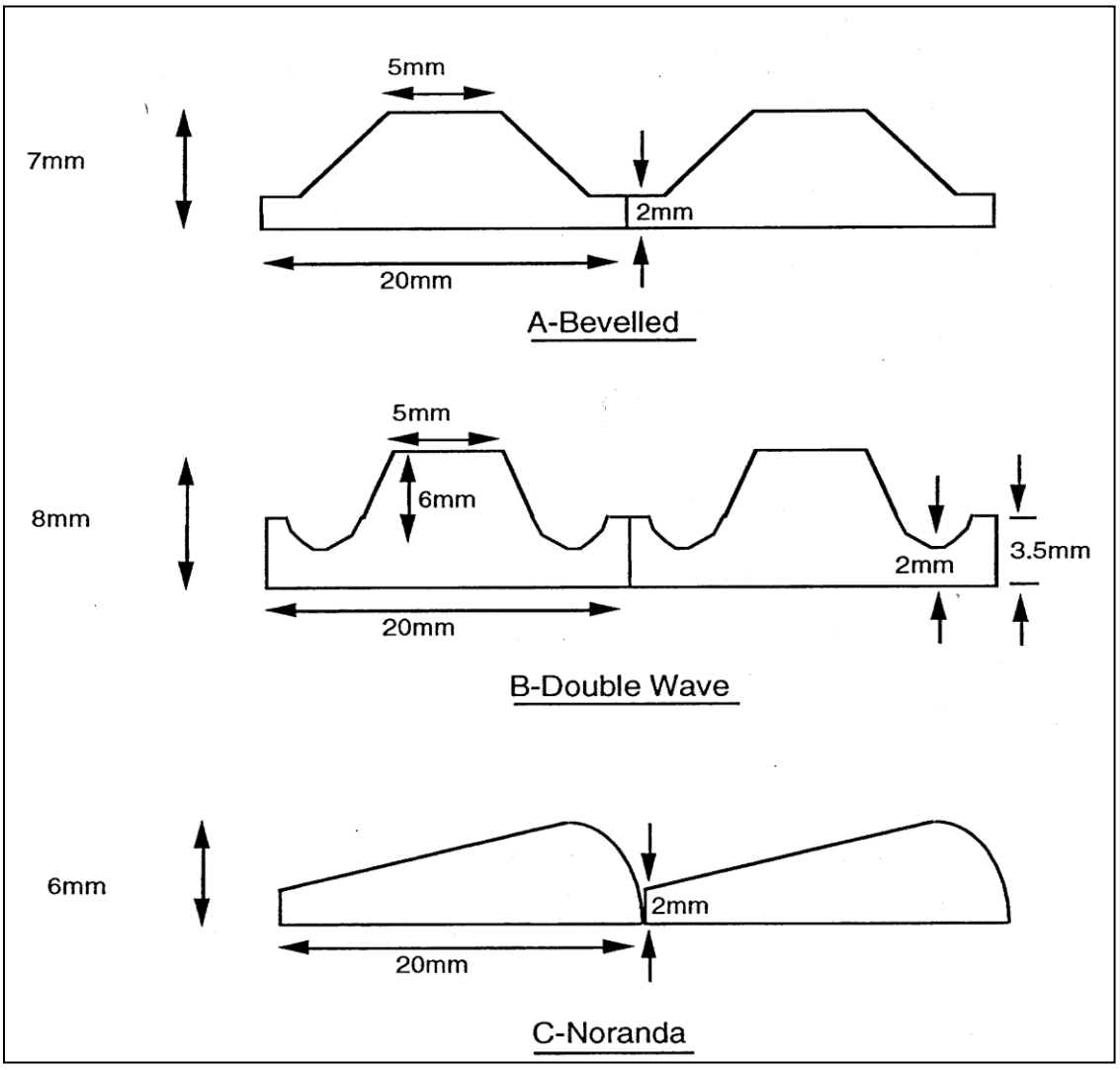

Figure 5: Illustrations of the different types of lifters used for the Morrell experiments (Morrell 1993)

The mill fill was varied between 15% and 45% mill volume. The charge that was used for the experiment was nickel sulphide ore (uniform colour), which was taken from a scaled version of an equilibrium charge from a 6' x 2' autogenous pilot mill. Before the charge was used it was rounded by tumbling it for a set period. Once the charge was prepared a few rocks were painted with bright colours. The bright colours allowed the rocks to be traced in the charge by taking still photos. Still photos were taken of the charge through the glass front plate by using a camera with a slow shutter speed. The slow shutter speed allowed the brightly coloured rocks to appear as streaks on the photos. These were used to determine the velocity profile of the charge. The results of the experiment are represented in Figure 6.

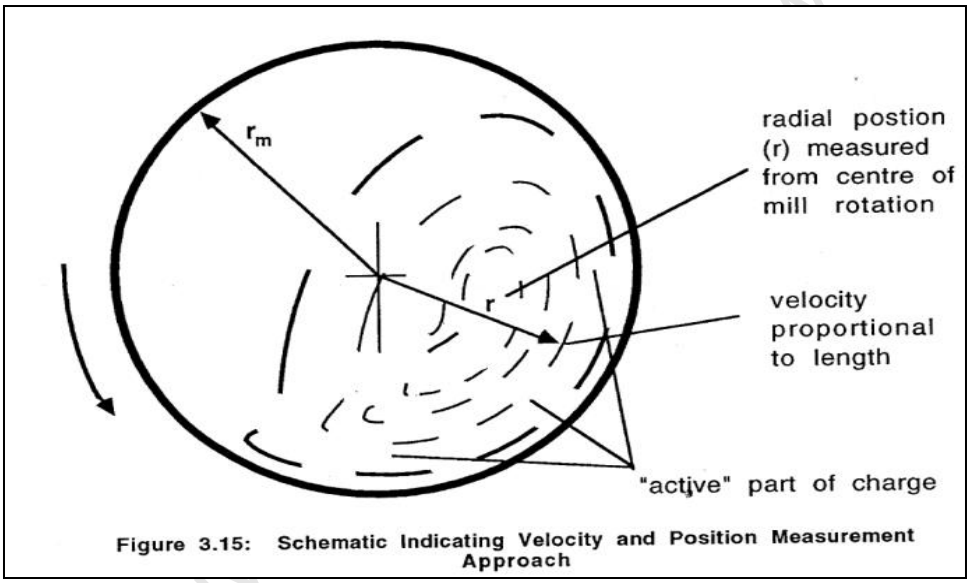

Figure 3.15: Schematic Indicating Velocity and Position Measurement Approach

Figure 6: Morrell Power Model velocity profile (Morrell (1993))

From the photos taken the shape of the charge was estimated to be an extended C-shape, as can be seen in Figure 7. The velocities, as can be seen in Figure 6, vary along the radius of the mill, which was correlated into a relationship. The underlining trend in the velocity profile was then taken and a new velocity relationship was developed using the mill speed.

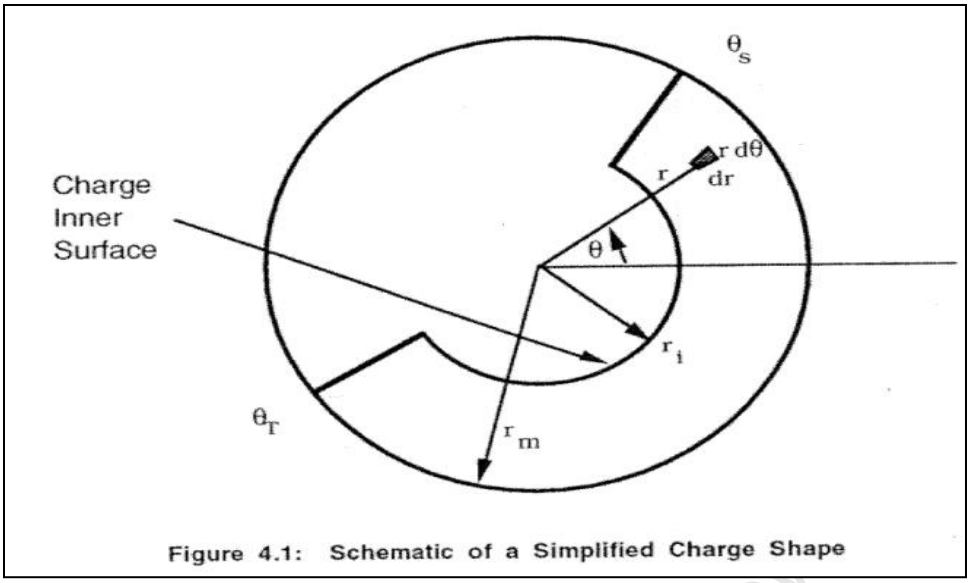

Figure 7: Morrell Power Model charge shape (Morrell (1993))

Using the velocity profile description derived from the experiments Morrell's power term is integrated across the charge shape that was observed. The charge shape chosen represents the 'solid' region in the charge, also known as the en-masse region, and does not take the cascading or cataracting regions in the charge into account. This was intentional, because most of the grinding takes place in the solid region and hence the energy is described in this region. The resultant Morrell Power Model is described by the potential and kinetic energy equations in equations 15 and 16 respectively. Equation 17 represents the load fraction term.

$$P_{kinetic} = L \cdot p_c \cdot \left[\frac{N_m \cdot r_m \cdot \pi}{(r_m - z \cdot r_i)}\right]^3 \cdot [(r_m - z \cdot r_i)^4 - r_i^4 \cdot (z-1)^4] \quad (15)$$

$$P_{Potential} = \frac{\pi \cdot g \cdot L \cdot p_c \cdot N_m \cdot r_m}{3 \cdot (r_m - z \cdot r_i)} \cdot [2 \cdot r_m^3 - 3 \cdot z \cdot r_m^2 \cdot r_i + r_i^3 \cdot (3 \cdot z - 2)] \cdot (\sin\theta_s - \sin\theta_T) \quad (16)$$

$$z = (1 - J_t)^{0.4532} \quad (17)$$

Equations 15 and 16 describe the power generated in the cylindrical section of the mill. Separate derivations were made for the additional power generation at the ends of the mill, which are described in greater detail in Morrell (1993).

The Morrell Power Model then validated and compared to other power models such as the Bond and Davis Power Model. Extensive industrial data was used to validate the Morrell Power

Model. The comparisons in Morrell (1993) showed that the Morrell Power Model is significantly superior to the other power models. Due to this superiority the Morrell Power Model is widely used in industry.

The final Morrell model is a semi-empirical model, which has been adjusted using the extensive database that was made available to Morrell by the Julius Kruttschnitt Mineral Research Centre (JKMRC), JK-Tech (commercial unit of the JKMRC) and companies sponsoring the JKMRC. In addition to the power generated within the charge a no-load power needed to be determined and adjustments needed to be made for the mechanical energy loses. The total energy consumption (Gross power draw) is described by equation 18:

$$P_{Gross} = P_{No\text{-}Load} + k\, P_{Net} \quad (18)$$

The gross power draw of a mill is therefore dependent on the no-load power of the mill and a correlated constant (k). The no-load power was correlated and calibrated to form equation 19:

$$\text{No-Load Power} = 2.62(D^{2.5} L\phi)^{0.804} \quad (19)$$

Table 3: Variables for the Morrell power model

Variables	Units	Description
G	m/s^2	Gravitational acceleration
$P_{Kinetic}$	kW	Kinetic Energy
$P_{Potential}$	kW	Potential Energy
L	m	Inside liner length (cylindrical section)
p_c	t/m^3	Total charge density
N_m	rev/s	Mill rotational speed
r_m	m	Mill radius
r_i	m	Radial position of the charge inner surface
Θ_S	rad	Shoulder angle
Θ_T	rad	Toe angle
J_t	fraction	Mill filling
r_{exp}	m	Radius of the experimental mill
V_{mill}	m/s	Mill velocity

Φ	fraction	Fraction of critical speed
L	m	Inside liner length (cylindrical section)
D	m	Mill inner diameter (cylindrical section)

2.4.1 Morrell Model comments

Despite the resounding success of the Morrell Power Model there are aspects that can be included such as the charge profile, velocity profile and lifter configurations that were not considered.

Charge Profile

The charge shape given in Figure 7 does not represent the action of a tumbling mill. The typical charge shape is given in Figure 6.The charge shape in a typical tumbling mill is made up of the cascading and cataracting regions. The only region that has been taken into account in Morrell's work is the 'solid' uniform lower section of the charge. Throughout the description of the charge shape the other constituents were not mentioned and explained. Through further investigation an explanation for the charge shape is offered in Napier-Munn et al (2005). The cataracting material has no effect on the mill shell. The kidney zone material is stationary and has a small mass and would have an effect amounting to less than 5% of the mill power. These sections were presumably left out to simplify the shape so that integration across the charge would be easier. In an attempt to overcome the charge shape estimate Morrell over estimates the lower charge region. The evidence of this is the C-shaped charge in the Morrell interpretation that covers more than half of the circumference of the entire mill shell.

Constant

The empirical nature of the power model came in the form of the gross power equation that included the 'no load' power and a variable 'k'. The no load power is developed using industrial data and has the same form as the Bond equations. The K-variable is supposed to account for the mechanical losses due to friction and heat at the bearings. At the time the K-variable added

approximately 26% to the power calculated by the original basic power model. This number will change depending on the region of the particular mine, because of the potential data bias.

Charge velocity profile

The method that was used to determine the velocity profile was very innovative and uncomplicated. In the Morrell thesis there is no mention of repeat experiments, hence the repeatability and consistency of the results has not been made clear. It was never indicated if enough time was given to reach steady state in terms of the particle segregation, which could affect the profile's trend. The preciseness of the profile is not important, but rather the trend. The trend is used to develop a velocity profile based on the mill's rotational speed. Particle segregation has a significant effect on the location of different size and density particles. These effects could be strong enough to alter the trend of the velocity profile as described in Morrell (1993). The experiment was run with a real charge and does mimic reality, which is a great advantage.

Lifter Characteristics

Lifters affect power draw significantly and this was highlighted by Cleary (2001), Powell and Nurick (1996) and Djordjevic (2003). A correct lifter configuration in industry can increase output by 20% to 30%. It can also increase energy efficiency per ton of output, as was observed in Meaders & MacPherson (1964), Parker et al (1997), Hlungwani et al (2003) and Djordjevic (2003). Parker et al (1997) shows charge profile results of a mill operated without lifters and no cataracting motion of the charge was observed at high speeds. Hlungwani et al (2003) and Djordjevic (2003) observed that at high mill speeds a mill with lifters will have a large portion of the charge cataracting. This shows that lifters change the charge kinematics. The experimental and simulation results in Hlungwani et al (2003) show that cataracting occurs at 70% of the critical mill speed. Therefore the desired charge profile is created by operating at lower mill speeds and as a result uses less energy.

Additionally the lifters affect the charge shape and in particular the toe and shoulder of the charge in the mill. The gradient of the charge has a distinct affect on the velocity profile, as the

material is more significantly affected by gravity and changes its acceleration. The lifter characteristics have however not been included in the Morrell Power Model despite their well documented effects.

The Morrell Power Model works because of the 'k' constant and the no load power that is part of the gross power definition. Both these aspects are empirical factors, which cause a bias towards the database used to determine these factors. The inaccuracies in the Morrell Power Model are caused by the aforementioned bias and the exclusion of the lifters in its development.

2.5 Velocity Profile

After the development of the velocity profile in Morrell (1993) for use in the power model Govender et al (2011) used it to analyze the shear rates within a tumbling mill.

In Govender et al (2011) experiments to extract the shear rate profile in the tumbling mill were done using a recirculating slurry. The slurry was pumped through the mill and allowed to pass through the 5 mm glass bead charge. The flow characteristics of the system were tracked using an irradiated 5 mm glass bead.

The particles are tracked using the positron emission particle tracking (PEPT) technique. A review of the PEPT system is given in section 3.2.3. The PEPT system and standard PEPT algorithms are used to extract time-averaged tangential velocities of the particles in the experimental mill. To obtain the shear rate profiles. In their work the tangential velocities were extracted along a line that goes through the center of circulation (CoC) (Powell and Nurick (1996)), as shown in Figure 8.

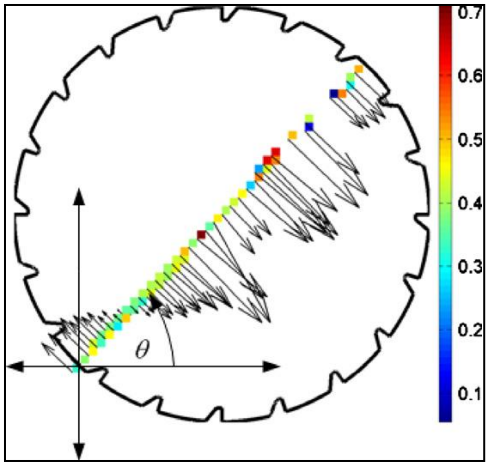

Figure 8: Velocity profile along a diametrical line passing through the mean COC (Govender et al (2011))

The magnitude of the velocity vectors in Figure 8 were plotted as profiles shown in Figure 9. In order to determine the shear rates a velocity profile model is needed. An equation is fitted to the experimental data and is then used to determine the shear rate of the system. The fitted line to the experimental data has the following equation:

$$V(r,\theta) = a_1 \sin(b_1 r + c_1) + a_2 \sin(b_2 r + c_2)$$

The equation needs six parameters to be fitted. The fitted velocity profile in this work was the second attempt in literature to use the velocity profile. Using the velocity profile the shear rates were successfully determined.

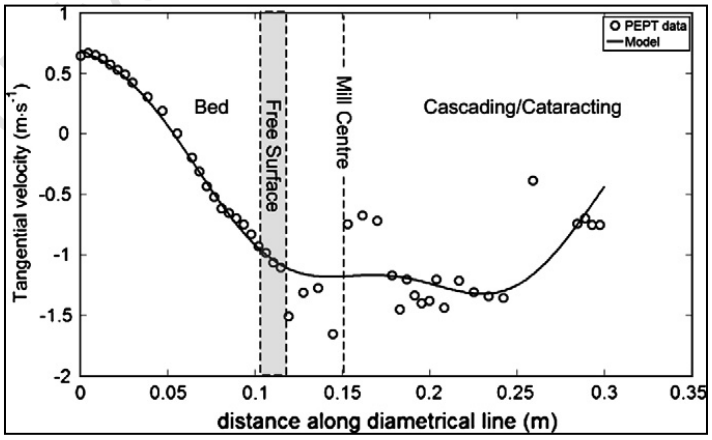

Figure 9 Variation of tangential velocity with radial distance along the diametrical (Govender et al (2011))

Research conducted by Perez-Alonso and Delgadillo (2012) measured the velocity profile within a tumbling mill by using digital image analysis. The primary purpose of the study was to validate a 2D DEM simulation of different lifter face angles in a tumbling mill with an internal mill diameter of 0.383 m and a length of 0.0255 m. The charge consisted of uniform sized 1 inch steel balls. The velocity profile measurements revealed a gradual decrease in particle velocity from the mill shell towards the centre of circulation, which is the same that was observed in Govender et al (2011).

2.5.1 Velocity profile comments

The system used to extract shear rates from particle trajectories is closer to a realistic charge behavior. The charge used in the experimental work in Govender et al (2011) is made up of conditioned bluestone and water and the system allows slurry to flow through. This is in contrast to previous experiments in Kallon et al (2011) and Bbosa et al (2011), where glass beads are used as charge in a dry environment The one significant challenge the velocity profile and hence the shear rate model have is applicability due to the large amount of variable inputs that are needed for the model. The velocity model, and hence the shear rate model, is a fitted equation with six variables. Therefore for each new condition or change in the mill environment a new set of variables will have to be fitted. Fitting the model to data does not allow detailed understanding of the model nor does it highlight the different effects of the operating variables, because the fitted variables do not have any physical or operational meaning. In order to allow for greater flexibility and understanding a fundamental development of the velocity profile might be more useful than simply fitting an equation to data.

2.6 Lifter configuration

In the previous sections it has been mentioned that the lifter configuration has a significant effect on the power draw of mill. This section shows the importance of the velocity profile in the development of the power model and how the lifter affects the power draw.

2.6.1 Lifter's purpose

A lifter is installed inside the mill. The primary function of the lifters is to promote high impact motion for the charge. The charge gets lifted and is released at the highest point possible.

Lifters also prevent the charge in the mill of slipping while the mill is in operation. The primary function of the mill liner is to protect the mill shell from impacts. The lifter is able to protect the mill liner from severe wear, as it can prevent direct impact between the charge and the mill liner by controlling the charge motion. The lifters are usually made of certain steels, but will vary depending on the material being processed, the required roughness and durability.

2.6.2 Power draw

Apart from influencing charge motion, lifters also have an effect on energy utilization. There are two ways of approaching the effect of lifter configuration on power draw. The direct method is through experiments and simulations involving different lifter profiles. The indirect method is quantifying the effect it has on the charge motion and how the resultant charge motion affects the power draw.

In work done by Cleary (2001) the power draw of a mill was analyzed in relation to lifter height and mill speed using a DEM model. It was found that at low speeds and the highest lifters the maximum power was drawn. Djordjevic (2003) using a DEM simulation found that using larger lifters in the mill allowed the mill to use less energy than if smaller lifters were used. Further research was conducted by Djordjevic et al (2004) on the effects of lifter design, mill speed and mill filling in an AG mill using 3D DEM simulations. It was found that lower lifter heights resulted in higher power draws when compared to higher lifter heights. The same was observed in Cleary (2001) and Hlungwani et al (2003). A similar result was observed in the research conducted by Mishra and Rajamani (1993), where different lifter configurations were tested and the mill's power was measured. One of the conditions compared two rectangular lifters with different lifter heights. A 0.5% increase in power draw was observed while operating with the small lifter height when compared to the higher lifter. Moys (1993) attempted to develop a power model which takes design and control variables into account and compare it to data from an experimental mill filled with grinding media. One of the design variables is the lifter. It was found that some of the model parameters did not relate to the lifter parameters; therefore the lifter was not successfully incorporated into the power model. However, the power model did correlate well with the experimental data. From these studies one can conclude that energy

consumption in a tumbling mill can be optimized with the correct liner design (Powell and Nurick (1996)).

2.6.3 Charge Motion

The lifters inside a tumbling mill are able to influence the energy consumption and fine production in a mill by manipulating the charge motion. A significant amount of research has been conducted on this topic. A summary of some high impact research is presented in this section.

In Powell (1991) a theoretical analysis on the trajectory of an isolated ball/rod in a tumbling mill was developed. The model developed from the analysis is meant to simulate the movement of the outer most rod/ball. The model compared well to an experiment using an experimental mill with a glass end to track the mill charge. The research found that lifters have a significant effect on the trajectory of the ball/rod charge. However, this was not the first attempt at understanding the motion of grinding charge within a mill. In Vermeulen (1985) the movement of a rod on a lifter was investigated. The movement was categorized as rolling and sliding. The movement of the outer most rod was mathematically modeled and then validated against experimental data. Similar work was conducted by Mishra and Rajamani (1993) where the charge motion was investigated using DEM simulations. It was found that the lifter configuration (height and face angle) has a significant effect on the outer most particles within a mill and can affect the shoulder height and hence the impact height.

The research into theoretical trajectories was implemented before being published in Powell (1990). The theoretical grinding media trajectories were used to alter the liner life of the Kloof and Deelkraal Gold Mines in South Africa. The investigation pointed out that the increasing the lifter height increased the trajectory height of the grinding media until a critical lifter height where the trajectory height is the same. This point is reached once the lifter height is greater than the radius of the grinding media.

Powell and Nurick (1996) observed that liner profiles could be adjusted so that cataracting media impacts the toe of the charge and hence optimizing the impact. Another example is seen in Govender et al (2001), where it has been shown that lifter face angle can be used to optimize

the impact area of the cataracting charge. The lifters are able to influence where the charge lands and generally how the charge behaves. The charge behavior and shape have a significant impact on the type of grinding (high impact or abrasion) that occurs in the mill. The type of grinding influences the power draw of the mill and, more importantly, how the power is used in the mill. This can be the difference between efficient and inefficient power usage. Research focusing on milling rates, fines production and hence energy efficiency was conducted by Powell and Vermeulen (1993) and Makokha and Moys (2006). Powell and Vermeulen (1993) investigated the influence of lifter on fines production. The experiments were conducting using a 1.8 m batch mill using a mineralogical consistent ore from a waste stockpile. The experimental results showed a variation of 40% in fines production and energy efficiency while using different lifters. It was therefore argued that the milling rate and energy efficiency can be maximized by choosing the correct lifters. Makokha and Moys (2006) investigated the effects of lifter design on capacity optimization in a ball mill. Three lifter configurations were tested, namely a 45^{o} and 60^{o} face angle bevel lifter and a worn bevel lifter modified with a cone lifter. It was found that liner profiles have a significant effect on the fines production and the milling rate. In this case the cone lifter was found to be the best lifter in terms of fines production and milling rates.

All the investigations into the effect of lifters on charge motion, fine production and milling rates were combined into an implementation program. The report by Powell et al (2005) details the effect of the implementation of theoretical liner performance predictions on different operations around the world. Most of the operations (Candelaria, Los Pelambres and Collahuasi) reported an increase in throughput of between 11% and 15%.

2.7 Direction

The lifter profiles are an important aspect of the tumbling mill's operation and design. The lifters can have a significant effect on energy efficiency, as mentioned before. Therefore the current research is focused on the effect of lifters on the velocity profile and toe and shoulder position.

2.8 Experimental techniques

From the power model literature considered earlier it was shown that particle tracking experiments is crucial in developing a power model. It allows the charge to be correctly characterized and it also allows physical data of the tracked particle to be recorded. The next section of this literature review is devoted to the different particle tracking techniques that have been applied in comminution research.

These include the two dimensional (2D) and three dimensional (3D) experimental methods. For each technique the experimental setup, history of use and drawbacks of each experimental method are discussed.

2.9 2D Particle Tracking

2.9.1 Experimental setup

The experimental setups for the 2D experiments are very similar with a few subtle differences with regard to the diameter of the mills, charge material and number of lifters installed into the mill. The way the experiments are performed is different due to the unique objectives of the studies.

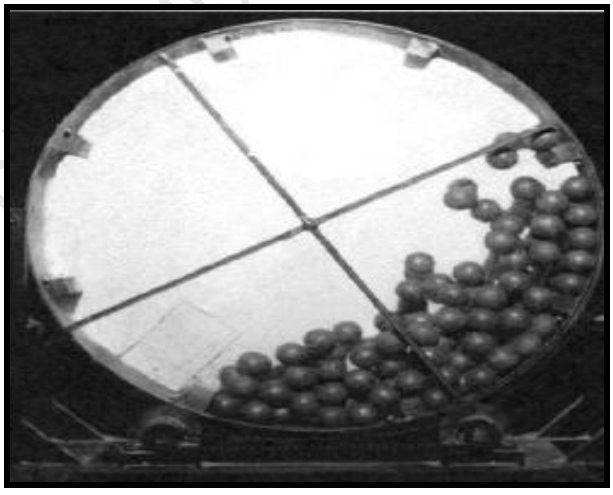

Figure 10: 2D Experimental Method (Venugopal and Rajamani, 2001)

The general setup, as can be seen in Figure 10, by Venugopal and Rajamani (2001), for the 2D experiments consists of a mill with a glass or PVC plate end, where the charge can be observed.

The diameter of the mill is different for different experiments, but the length of the mill is usually marginally larger than the diameter of the balls/beads used as the charge. In Hlungwani et al (2003), Venugopal and Rajamani (2001) and Cleary and Hoyer (2000) it is shown that the charge is usually made of plastic or glass or steel beads/balls and the tracked particles are marked. Observations are made by recording the charge motion with a high speed camera. The variables are mill speed, percentage volumetric filling and lifter configuration (height, face angle and spacing).

2.9.2 History of use

The 2D experimental setup was first used in 1940 (Powell, 1993) and it is still being used today, because it is easily reproducible and it is an accepted particle tracking method. In literature the 2D method has been used by Hlungwani et al (2003), Cleary and Hoyer (2000) and Venugopal and Rajamani (2001) amongst others. The 2D experiments have been used to prove and observe different aspects of the mill's performance. For example Venugopal and Rajamani (2001) used the 2D method to validate DEM data with a specific interest in charge motion and power draw. Hlungwani et al (2003) instead used the 2D experiment to validate the DEM model, specifically looking at effects of lifter profiles and mill speed. Cleary and Hoyer (2000) on the other hand used the 2D experiment to compare the charge motion and power draw with that predicted by a DEM model.

2.9.3 Drawbacks

The drawbacks for the 2D system have been highlighted by Govender et al (2001). Govender et al (2001) argued that 2D experimental setups are subject to 'end window effects', which influences the particle trajectory, and are not able to track particles deep within the mill. This implies that any further studies into the particle tracking and charge behavior should be completed using a 3D experimental setup, so that the entire mill is taken into consideration and not just a section of it as the case is in 2D experiments.

2.9.4 Method reasoning

The 2D experimental method has been widely used in the research area of particles tracking. There have been numerous sets of literature that have made use of the 2D experimental

method, such as Hlungwani et al (2003), Cleary and Hoyer (2000) and Venugopal and Rajamani (2001). Despite the popularity of the 2D experimental method it will not be used in this research, because the particle cannot be tracked along the axial direction of the mill.

2.9.5 2D particle tracking comments

Most of the literature represents results indicating that the 2D model experiments are in 'good agreement' with the DEM models. Although most authors indicated that there was 'good agreement' between the 2D experiments and DEM models no experimental data for the validity of the 2D experiments was represented. In the absence of good 3D experimental methods 2D methods were used as an approximation.

In the drawbacks section it is mentioned that the 'end window effects' disadvantage the observations made from the 2D experimental data. The effect of the end window on the observed trends is not clear, because most of the analysis for the 2D experimental results and models are qualitative. Therefore any minor changes to the position of the charge will not make a great difference to the results and the observations made. If there is a great difference as a result of the 'end window effect', then it is understandable that there would be some inaccuracies. However it is never mentioned by Govender et al (2001) to what degree the charge position changes of the recorded material.

2.10 3D particle tracking

2.10.1 X-rays

2.10.1.1 Experimental setup

The experimental setup for the X-ray method is standardized. Powell and Nurick (1996) and Govender et al (2001) used the Biplanar Angioscope configuration, where two angioscopes are situated at 90^{o} to each other as shown in Figure 11 (Govender et al, 2001) and Figure 12 (Govender (2008))

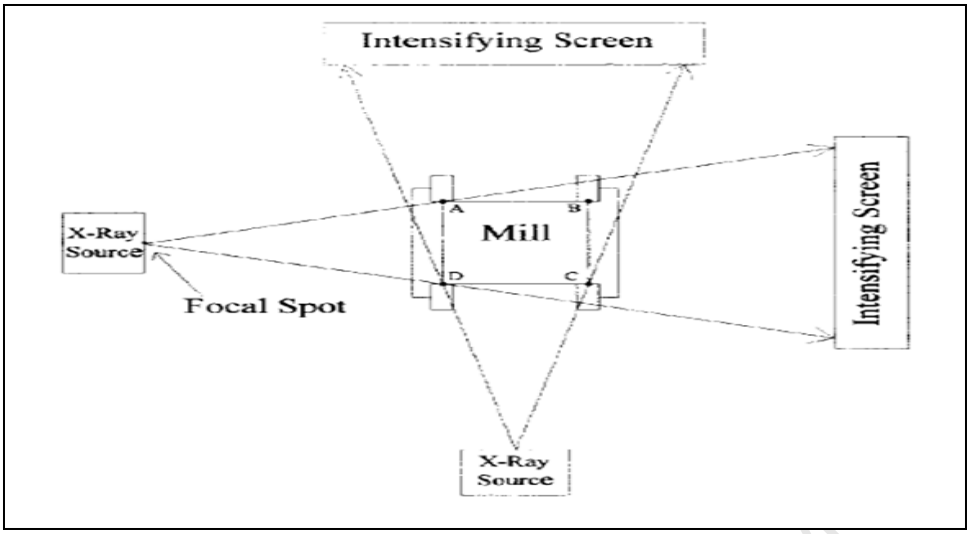

Figure 11: X-ray experimental setup of Angioscopes (Govender et al, 2001)

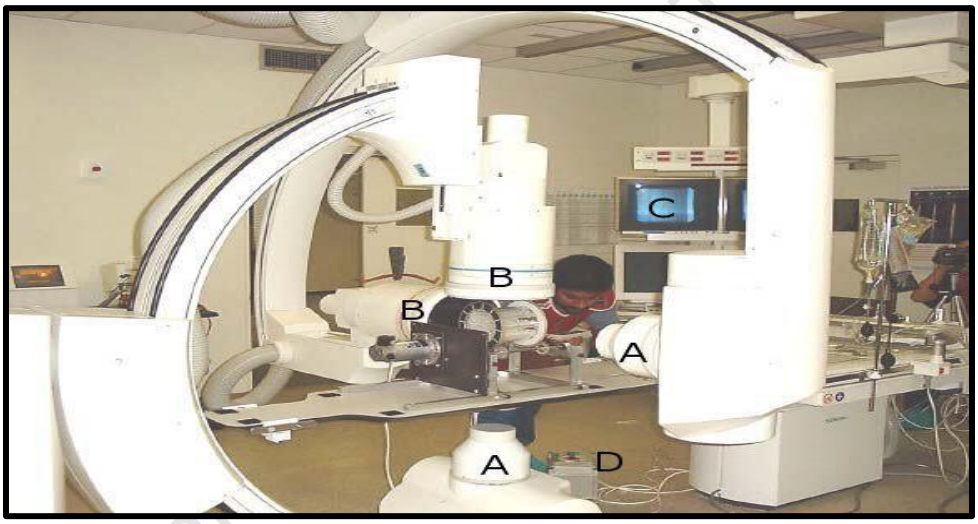

Figure 12: X-ray cameras (Govender (2008))

The mills used were made of Perspex, as it is transparent to X-rays. The charge particles of the experiments were made up of material with different transparencies, so that they could be tracked by their different shades. In Govender et al (2001) the bulk of the charge was made up of 6.1 mm plastic beads. The tracking particles consisted of steel ball bearings, a plastic bead containing a lead rod, silver painted plastic bead and a plastic bead with an opaque red pigmentation. The X-rays passing through the mill and its contents were captured by a scintillating screen. The images on the screen were recorded by a TV camera.

2.10.1.2 How does it work?

Two angioscopes are placed 90^{o} degrees to each other, as can be seen in Figure 11. The angioscope emits high energy x-rays. These X-rays are emitted in short pulses and the images produced from passing through the experimental setup stimulate a scintillating screen. From the scintillating screen the x and y coordinates of the tracked particles are presented and recorded by a high speed 50 frames per second TV camera. The x and y data are put through image processing and a transformation process. The processing technique was developed by Govender et al (2001) and is based on the Canny edge detection scheme (Canny (1996)). Using the technique developed by Govender et al (2001) 3D coordinates were produced to allow for 3D particle tracking.

2.10.1.3 History of use

The X-ray method is one of the first 3D tracking methods used. The X-ray method was first introduced by Powell, M.S. (1993) and later used by Govender et al (2001) and Govender (2006). After this only a few sets of literature have used the X-ray method to conduct experiments. The reasons for this could be the difficulty of acquiring or using an angioscope. Powell (1993) focused on the study of the charge motion in a rotary mill, while Govender et al (2001) focused on developing a rigorous method of verifying the DEM predictions.

2.10.1.4 Drawbacks

The experimental setup for the X-ray method needs to be very well planned and precise. The angioscope it not readily available and can only be used for short periods of time (Powell, 1993). Due to the time constraints there is no opportunity for many repeats of runs, which does not allow data to be examined to be with statistical rigor. It is further mentioned in Powell (1993) that slurry cannot be introduced into the system, because the x-rays do not attenuate in water. The particles being tracked need to be of a certain density, so that they can be tracked by the X-ray method.

2.10.1.5 Method reasoning

The X-ray method has proven itself to be a viable and accurate experimental method with dry and well setup systems. Despite these positives the X-ray method will not be used for the

current research due to the X-ray method's operational time constraints, the low x-ray imagining resolution and experimental constraints on tracking material. Future extensions of the current research might include slurries and material with different density media which cannot be tracked using the X-ray method.

2.10.1.6X- ray experiments comments

The novel idea by Powell (1993) to design the X-ray experiment provided a methodology of obtaining 3D particle tracking data which could validate DEM models in detail. Powell and Nurick (1996) however stated that improvements to the experimental method could positively impact results. Govender et al (2001) and Powell and Nurick (1996) state that the data collected with the X-ray method is not accurate enough to be evaluated quantitatively, which is the ultimate goal for 3D tracking.

2.10.2 Gamma camera

2.10.2.1Experimental setup

The experiment for the gamma camera method is not standardized, as it has not been used extensively in literature. Powell and Nurick (1996) used the gamma camera method to observe the size and mass radial segregation interactions.

The literature has indicated that it is possible to track a particle using the gamma camera (Powell and Nurick (1996)). A Perspex mill is used with the charge consisting of different size glass beads. The tracked ball is made radioactive and is then filmed by the gamma camera.

2.10.2.2How does it work?

A particle is made radioactive by filling it with 13.6 mcurie cobalt 60 radioactive fluid and it is then tracked by the gamma camera. The gamma camera detects the radiation from the tracked particle and records the motion.

2.10.2.3History of use

The gamma camera was never used solely to track a particle in a mill. It was used by Powell and Nurick (1996) and Powell (1993) as an addition method to determine the degree of radial segregation.

2.10.2.4 Drawbacks

In Powell and Nurick (1996) and Powell (1993) the gamma camera method resulted in blurry and inaccurate data. Hence it was difficult to extract information for quantitative analysis. Instead the data was evaluated qualitatively and the trends that were observed.

2.10.2.5 Method reasoning

The gamma camera technology has not been chosen as the experimental method due to the problems encountered by Powell (1993), which included blurriness and inaccuracies of the results.

2.10.3 PEPT

2.10.3.1 Experimental setup

The general experimental setup for the Positron Emission Particle Tracking (PEPT) system is standardized. The PEPT experimental setup is inflexible and the different experimental setup variations will depend on the shape and size of the PEPT camera. The experimental method has been adapted from Parker et al (1997). Even though the experimental objectives in Parker et al (1997) are different from those in this research, the experimental method for 3D particle tracking is applicable to this research.

The drum is placed between the PEPT cameras and is positioned with its axis horizontal. The driving force for the drum is created through an electric motor. The PEPT system consists of two PEPT detectors, which are separated by 300 mm or 400 mm. The drum is placed in parallel to the PEPT cameras, as shown in Figure 13. Figure 13 has been adapted from Parker et al (1997). The charge is made up of glass spheres with one of the glass beads irradiated, so that it can be tracked. The particle is then tracked by the PEPT camera as the particle emits β^+-rays. The drum did not have lifters inside. This is the experimental setup as presented in Parker et al (1997).

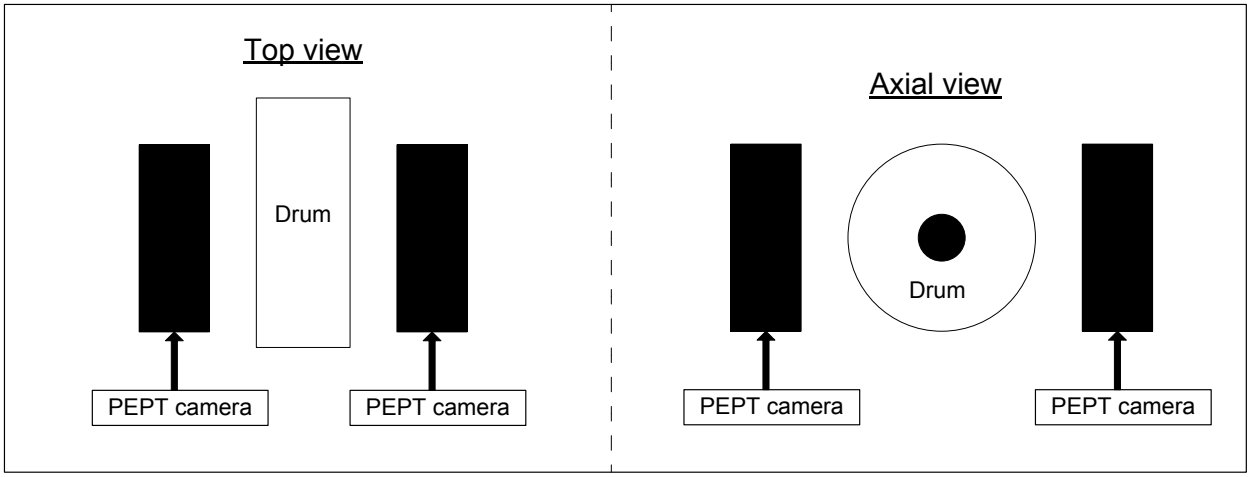

Figure 13: Topographical and axial view of the PEPT experimental setup (adapted from Parker et al (1997))

2.10.3.2 How does it work?

The Positron Emission Particle Tracking (PEPT) system uses radiation detectors to track a single particle in the charge. The tracked particle needs to be irradiated first before it can be detected by the PEPT camera. There are two methods of irradiating the particle. The first, as indicated by Parker and Fan (2008), being direct activation, where a particle (bead) is irradiated by bombarding it with the 33MeV ^{3}He beam from a cyclotron. In Parker et al (1997) it is stated that the glass beads irradiated contain a radionuclide ^{18}F or if copper beads are used then the beads will contain ^{61}Cu. It is also mentioned that in order to use the direct activation method the particle needs to be greater than 1mm, otherwise particle handling will become problematic. The second method, as stated in Parker and Fan (2008) and Parker et al (1997), for irradiation is ion exchange. This is generally used for particles (beads) that are less than 1mm. The nuclide (^{18}F) is produced in solution, where ^{18}F that is absorbed is from radioactive water by using a strong F based resin, and it is then transferred to the particle by ion-exchange (Parker and Fan, 2008).

Once the particle (tracer) is irradiated it is tracked by the PEPT camera. The PEPT camera detects the γ-rays and records the x,y and z position of the particle with time. In Parker et al (2002) it is stated that the tracer is located by triangulation of a number of detected annihilations from the tracer. The method of how the tracer is tracked is presented in Parker (1997), where the details of the algorithm that filters out the corrupt data are given. As a result

of the rigorous location calculations, a high accuracy is achieved. Even though the accuracy is high it tends to fluctuate and according to Parker et al (2002) the location precision decreases with an increase in tracer speed. It was observed that at a particle speed of 1m/s the particle was located within 5mm at 250 times per second from the actual location and at a speed of 0.1 m/s it was located within 2mm at 25 times per second of the actual location.

2.10.3.3 History of use

The Positron Emission Particle Tracking (PEPT) system is not a recent development, but the recent applications of the PEPT system are quite novel. The first Positron camera was built for the University of Birmingham in 1984 at the Rutherford Appelton Laboratory (Parker et al, 2002). The aim of building the camera, as stated in Parker et al (2002), was to allow the study of engineering systems with the use of positron emission tomography. The PEPT system has been used for granular systems, which include mixing, conveying, fluidization, agglomeration and more recently the study of viscous fluids for the food industry (Parker et al, 2002). In addition to these, flows in comminution and flotation devices have also been studied in Govender et al (2011), Kallon et al (2011), Bbosa et al (2011) and Cilliers (2010).

Govender et al (2011) used the PEPT system to analyze shear rates in an experimental tumbling mill using a recirculating slurry. Kallon et al (2011) used the PEPT system to model the circulation rate of a mill charge. Bbosa et al (2011) used the PEPT system to estimate the power draw in a tumbling mill. The PEPT system has been used successfully to track particles in tumbling mill devices.

2.10.3.4 Drawbacks

The PEPT system has restriction on the particle size that can be tracked. The particle cannot be smaller than 250 um, because of restrictions on the handling of such small particles (Parker et al, 2002). Another limitation is that the PEPT system is restricted to logging 3000 events per second as explained in Parker et al (1997). In order for statistically relevant data in a tumbling mill to be produced the experiments need to run for a minimum of one hour. Therefore fluctuations in the experiments will not be noted, as the data will be averaged over the hour.

The accessibility of the PEPT system would be dependent on the availability of the Birmingham or the Cape Town facility.

The aforementioned drawbacks will not have any bearing on the proposed experiments for this research. The experiments will be run at steady state with minimal fluctuations in the operating conditions. The particle size restriction is no hindrance, as the particles that are going to be used for the experiments will be larger than 1mm. The access to the Cape Town PEPT facility has been granted.

2.10.3.5 Method reasoning

Even though the literature of particle tracking using this method is sparse, the technique has provided valuable data for systems where it has been used. The accuracy compared to the other methods is much improved. The PEPT technology will allow for quantitative analysis of charge motion, which is one of the reasons why this technology is so attractive. The PEPT system allows material flexibility and is able to operate under slurry conditions. Therefore the PEPT experimental system will be used as a 3D particle tracking technique.

2.10.3.6 PEPT experiments comments

The PEPT technology is a tool that has widened the scope of research and possibilities of further investigating fluid flow phenomena. Parker et al (1997) introduced and pioneered the PEPT technology to a point where it could be used for real engineering systems. The evidence of his contribution can be seen in the research that has been conducted so far using the PEPT system, such as Govender et al (2011), Kallon et al (2011), Bbosa et al (2011) and Cilliers (2010). As the PEPT techniques are refined and the data becomes more accurate more in depth investigations into fluid flow and characteristics will be made possible.

3 Problem statement

3.1 Problem statement

Increasing energy cost and decreasing energy security has placed a significant emphasis on energy consumption and efficiency for the mineral processing industry. In most of the mineral processing plants billions of dollars have been spent to develop the current flow sheets and install equipment. Instead of looking at new technologies, the focus is on improving current technologies and optimizing their performance. Energy optimization to date has been implemented with the help of power models that predict the mills performance with changes to operating conditions, such as the Morrell Power Model (Morrell (1993)). The Morrell Power Model uses concepts such as velocity profile and charge shape, but completely ignores the effects of liner design. Liner design could alter velocity profiles and charge characteristics significantly, which may result in different mill performances. The velocity profile of the charge and charge's toe and shoulder position are central to understanding the operation of a tumbling mill in terms of energy utilization. Therefore the research in this project is dedicated to investigate the effect of lifter height on the velocity profile and the toe and shoulder of the charge. An attempt will be made to model the velocity profile and incorporating the lifter height into the model. The velocity profile and the charge's toe and shoulder are studied using the Positron Emissions Particle Tracking (PEPT) system which is a 3D particle tracking system.

3.2 Scope of the study

The scope of this research is determining the effects of lifter height on the velocity profiles, the lifter height's effect on the charge's toe and shoulder at different operating condition and attempting to model the velocity profile while incorporating the lifter height effect using granular flow theory and compare it to the PEPT data. Lifter face angle and lifter spacing are not considered in this work. The experiments will be performed using the Positron Emission Particle Tracking (PEPT) scanner to track the motion of particles and extract charge kinematic information. The experiments will be run with mono-size particles (glass beads) with varying lifter heights. The operating conditions of the experiment will be varied according to industrial operating conditions.

3.3 Aim

The aim of the research is to determine the effect the lifter height has on the velocity profile, attempt to model the velocity profile while incorporating the lifter height and compare it to the PEPT data and quantify the charge's toe and shoulder under different operating conditions using different lifter heights.

3.4 Proposed work

3.4.1 Objectives of study

- Evaluate the effect of lifter height on velocity profiles
- Evaluate the effect of lifter height on the charge toe and shoulder
- Develop a velocity profile model using granular flow theory
- Validate the velocity profile model using PEPT experimental data

3.4.2 Hypothesis

Lifter height has a significant effect on the velocity profile and the toe and shoulder region, because lifter height affects the shape of the charge and the amount of slip the charge undergoes.

3.4.3 Key Questions

1. Can the PEPT data be used to extract the charge shoulder and toe, equilibrium and charge free surface and charge velocity profile?
2. Can a velocity profile be modeled from granular flow theory?
3. Does the modeled velocity profile compare well with the PEPT experimental data?
4. How does the velocity profile change with lifter height?
5. What effect does lifter height have on the toe and shoulder region?

4 Experimental Method: Particle Tracking Experiments

In the literature review it has been shown that particle tracking experiments are the most attractive experiments to obtain charge characterization information (including velocity profile). The particle tracking experiments are meant to provide data that will validate the shape of the velocity profile and allow analysis on velocity profiles at different lifters. The Positron Emission Particle Tracking (PEPT) will be used, because the PEPT system can accurately track the velocity of a particle in an experimental mill.

4.1 Equipment

There are two PEPT cameras available, one is located at the University of Birmingham in Birmingham in the United Kingdom and the other is the PEPT Cape Town at IThemba labs in Cape Town in South Africa. The PEPT camera that is used for these experiments is the PEPT camera in the PEPT Cape Town facility. A photograph of the PEPT is shown in Figure 14.

Figure 14: Cape Town PEPT facility (www.pept.uct.ac.za)

The equipment used for the experiments are as follows: PEPT camera (ring shaped) (Figure 15), Electric Motor (Figure 14), Speed controller (Figure 17), Mill shell (Figure 16), Tachometer (Figure 19), Lifters (Figure 20 and Figure 21) and the complete experimental mill assembly (Figure 22).

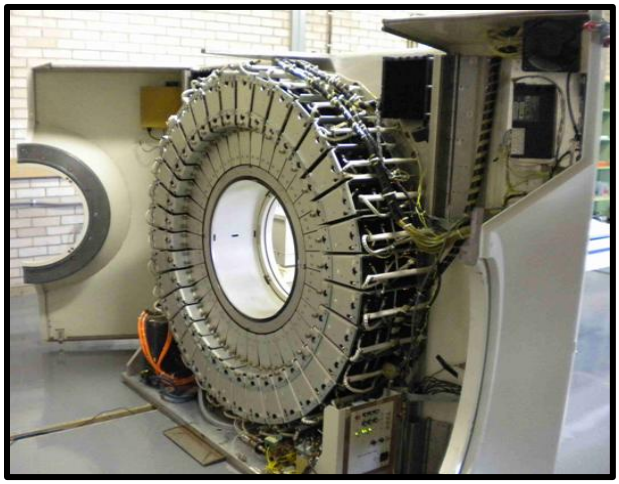

Figure 15: PEPT camera (www.pept.uct.ac.za)

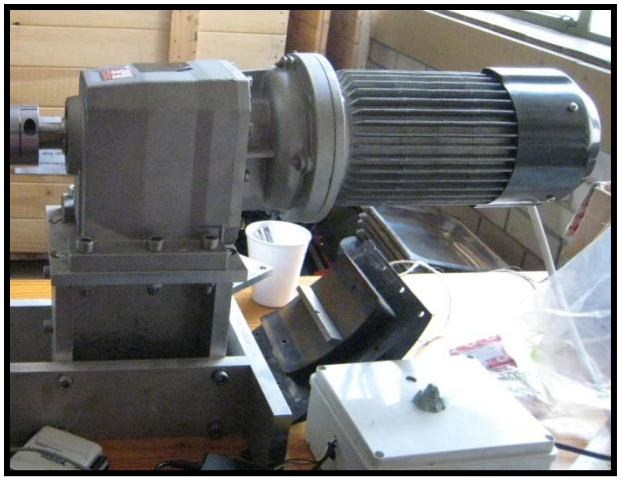

Figure 16: Electric Motor

Figure 17: Speed controller

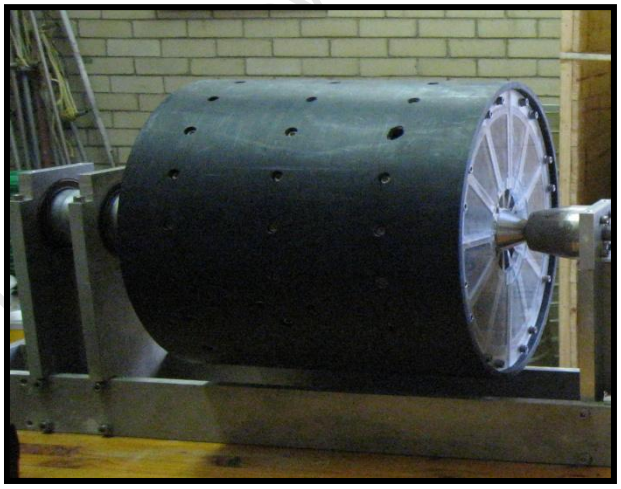

Figure 18: Steel base

Figure 19: Tachometer

Figure 20: Lifters

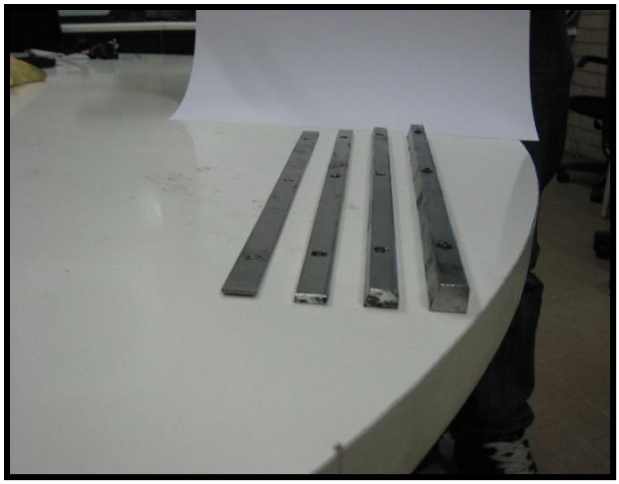

Figure 21: Lifters

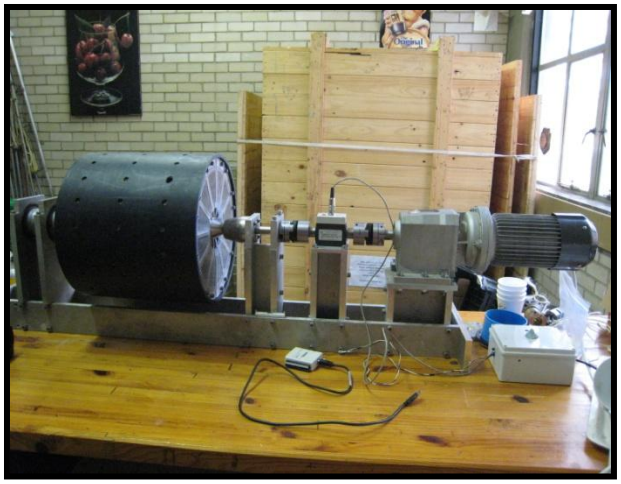

Figure 22: Experimental tumbling mill

The experimental setup for this research is similar to Parker et al (1997), Bbosa et al (2011) and Kallon et al (2011). The difference lies in the PEPT camera used for the data collection and the variety of lifters. The camera that is used for this experimental setup has a ring shape and that does represent length restrictions for the mill. The PEPT camera has dimensions of 820mm x 234mm (diameter x length) and the viewing dimensions are 450mmx230mm, which means the mill needs to be equal or smaller than the PEPT camera's field of view. Therefore the maximum theoretical mill would be a bit smaller than the dimensions of the PEPT camera. The mill that is used for the current experiments has dimensions of 300mm x 285.5mm (diameter x length). The limited field of view restricts data recording to a certain portion of the mill. There will be approximately 55.5mm of mill length that will not be able to be used for data recording.

The PEPT camera used for the data collection is a Siemens camera, which was initially used for head scans, and it is based in IThemba Labs in Cape Town. The camera is able to record 4.5×10^6 events per second, which is significantly more accurate than the Birmingham PEPT camera described in Parker et al (1997). The data that is collected by the PEPT camera is sent to a PC (Sun PC from the 1990's), where the gamma ray data is recorded and stored. This setup allows for a particle to be tracked.

Figure 23: Front view of the experimental setup

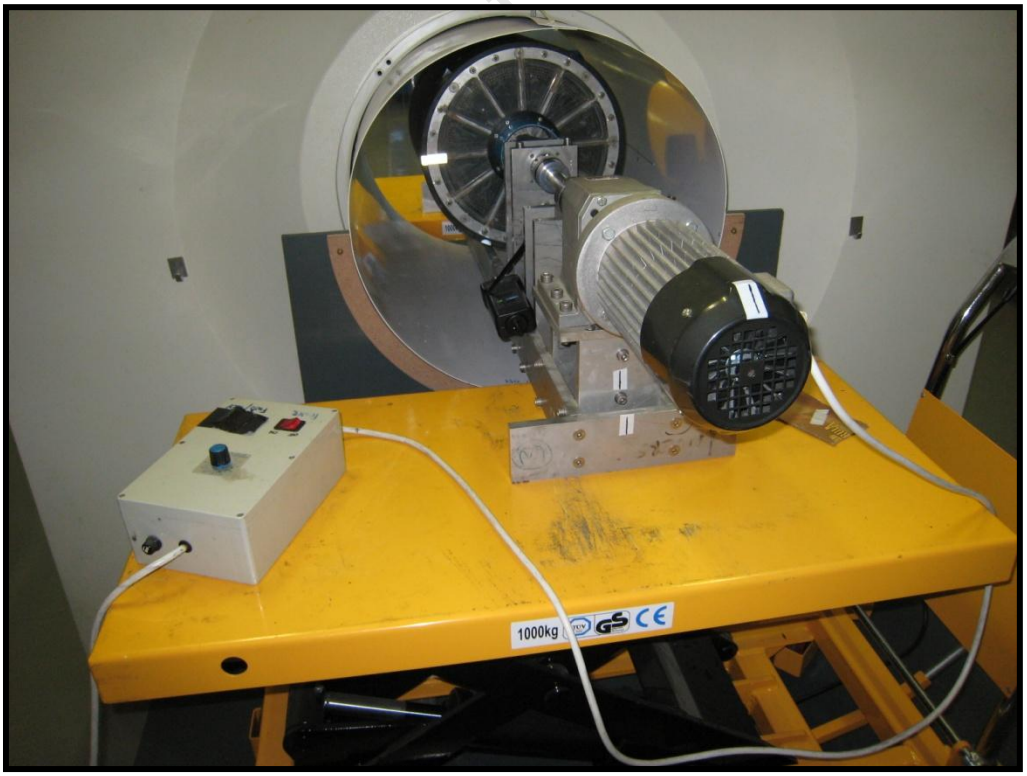

Figure 24: View of the back of the experimental setup

The experimental mill (300mm x 285.5mm) is placed in the PEPT camera, as can be seen in Figure 23 and Figure 24. The electric motor and the mill are both supported by a steel base, as can be seen in Figure 18. The steel base, with the mill and the electric motor attached to it, is lifted with a trolley, so that the experimental mill configuration can be place inside the PEPT camera. The electric motor and the mill are connected to each other by a steel shaft which acts as the drive train. The electric motor specified to operate the mill at variable speeds between 25% and 180% of the critical speed.

The mill speed is set by a controller for the electric motor. A tachometer is used to confirm the mill speed. The tachometer (Figure 19) uses light reflection to count the number of revolutions and represents the speed in rpm. In order to ensure the reflection of the light is transmitted to the tachometer, a piece of white tape is attached on the side of the mill.

4.2 Experimental setup

4.2.1 Experimental charge

The charge used for the particle tracking experiments was made up of glass beads with a specific gravity of 2.5, which was also used in Bbosa et al (2011) and Kallon et al (2011). The glass beads have a mono-size distribution, which means all the glass beads have diameters that are close to 5mm. The glass bead diameter of 5mm was chosen after taking into account the lifter configurations that were under study, which will be explained in the section below. The mass of glass beads needed for the experiments is dependent on the mill fill and the void fraction. The void fraction is 0.4 and it is the average void fraction of a spherical particle.

4.2.2 Variables

The three major variables that are varied throughout these experiments:

- Mill speed
- Mill fill
- Lifter configuration

These variables were altered within feasible operating ranges which will be explained in the sections that follow.

4.2.3 Mill speed

The mill speeds used for the experiment are 55%, 70% and 85% of the critical speed. The critical speed is the speed at which point material in the mill starts to cataract. The mill speeds cover a slow, intermediate and fast mill speeds. The intermediate mill speed represents the mill speed at which industrial mills operate. The slow and fast mill speeds have been chosen, because if the velocity profile holds for extreme mill speeds then it will most likely be true for most of the values in between the two extremes. The critical mill speed is not considered for the extreme mill speeds, because only operationally desirable mill speeds have been chosen. Cataracting material is an inefficient use of energy and it does not promote breakage. The velocity profile should be applicable to all mill speeds. Otherwise there is no difference between empirically or mechanically developed velocity profile. The fundamental approach should allow for greater flexibility and a wider range of application.

4.2.4 Mill filling

The mill fill values chosen are 20%, 30% and 40% of the volume of the mill. The mill fill values are meant to mimic three different scenarios in industry. The variation in mill fill simulates a ball mill with low, average and high ball filling.

Table 4: Mass of glass beads for different mill fillings

Mill Filling	Total Mass of glass beads 5 mm (g)
20%	6054
30%	9081
40%	12108

The masses of 5mm glass beads that are need when using a void fraction of 0.4 can be seen in Table 4. Table 4 shows that approximately 1514g of 5mm glass beads needs to be added to the initial mill fill in order to achieve the next highest mill fill (30% mill fill). The same is required to achieve 40% mill fill.

4.2.5 Lifter configuration

The particular aspect of the lifter configuration that was varied in this research is the lifter height. Four different lifter configurations were used for the experiments. The lifter face angle and lifter spacing were kept constant. The face angle of the lifter will be held at 90^{o}. The lifter heights that were chosen for the experiments are 10mm, 6mm, 3mm and 1.5mm as can be seen in Figure 25.

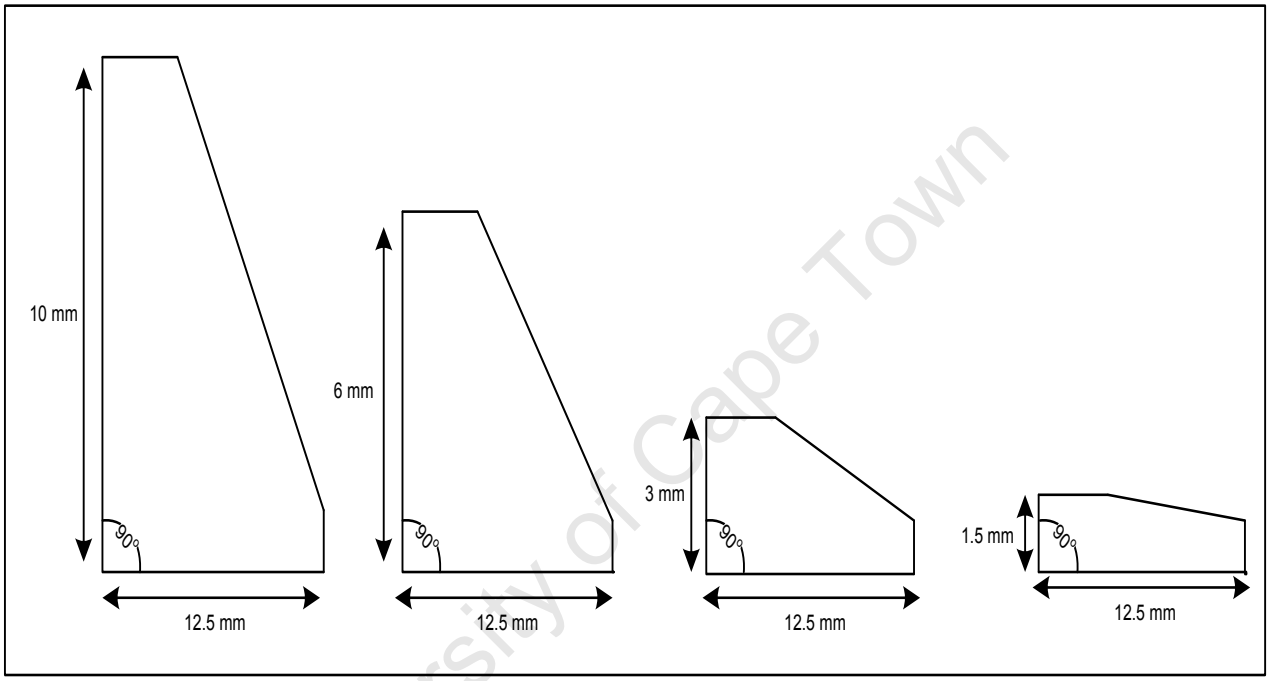

Figure 25: Illustrations of the lifters used for the PEPT experiments

The lifter heights represent the different stages that a lifter goes through in its life time. The 10mm, 6mm, 3mm and 1.5mm lifter heights may be used to simulate a new, intermediate, worn and extremely worn lifter respectively.

The maximum lifter height was calculated using industrial data from a 6m diameter mill scaled down to a 300mm diameter mill. The industrial data gave two extremes, namely an extremely worn lifter and then a new lifter. Using the industrial data ratios between the mill diameter and lifter height were determined. These values can be seen in Table 5, where the new and extremely worn lifters have a ratio (D/H_{Lifter}) of 24 and 150, respectively.

Table 5: Industrial and experimental lifter height data

Data	Lifter type	Mill Diameter (mm)	Lifter Height (mm)	Ratio (mm/mm)
Industrial	New	6000	250	24
Industrial	Worn	6000	40	150
Experimental	New	300	12.5	24
Experimental	Worn	300	2	150

Using these ratios the theoretical lifter heights were determined, which is represented in Table 5. The theoretical lifter height for a new and extremely worn lifter for the experimental mill is 12.5mm and 2mm, respectively. With these values it was possible to choose the glass bead size that was required to allow the lifter heights to mimic new and extremely worn lifters. The conditions of the new and extremely worn lifters were as follows. The new lifter needed to be approximately twice the size of the glass bead and the extremely worn lifter needed to be less than half the size of the glass bead. The glass bead that was therefore chosen was the 5mm diameter size. The lifter heights were therefore scaled so that the constraints of the different phases of the lifter were upheld with respect to the glass bead size. Therefore the new lifter was taken to be 10mm with the extremely worn lifter being 1.5mm, which is much less than half the size of the glass bead. Seeing as the lifters are significant to the velocity profile it was decided to add two more variations to the lifter height. One intermediate and worn lifter, where the intermediate lifter is slightly larger than the bead and the worn lifter is slightly larger than half of the bead. The intermediate lifter and worn lifter have heights of 6mm and 3mm, respectively.

4.3 Mill environment

The same mill was used for all experiments. The only changes made involved the lifter configuration, mill filling and mill speed. The mill was operated under atmospheric pressure and room temperature. There could have been a temperature change in the mill resulting from the cascading (friction) and cataracting (high impact) charge in the mill. Temperature changes would not affect the performance of the tumbling mill or change the characteristics of the charge.

4.4 Experimental plan

The experiments were performed with two variables kept constant while a third was varied. Once the entire range of an experiment was complete another variable was chosen while keeping all other factors. Therefore the total number of experiments that were performed for this thesis is 36 which are based on the factorial design method. The breakdown of the total experiments can be seen in Table 6. The experiments ran for 7 working days between 24 May 2011 and 3 June 2011. The experimental matrix that shows the combination of variables that were considered in this study, are given in Table 7. In Table 7 the mill speed and mill fill have been characterized as low, medium and high. The mill speed of 55%, 70% and 85% represents the low, medium and high mill speed, respectively. The same description is used for the mill fill, where 20%, 30% and 40% mill fill represent the low, medium and high mill fill, respectively.

Table 6: Breakdown of experiments

Variable	Variation
Lifter types	4
Mill Speed Experiments	3
Mill Filling Experiments	3
Types of balls (5mm)	1
Total Experiments	**36**

Table 7: Experimental matrix

	Mill fill		
Mill speed	*Low*	*Medium*	*High*
Low	New	New	New
	Intermediate	Intermediate	Intermediate
	Worn	Worn	Worn
	Extremely Worn	Extremely Worn	Extremely Worn
Medium	New	New	New
	Intermediate	Intermediate	Intermediate
	Worn	Worn	Worn
	Extremely Worn	Extremely Worn	Extremely Worn
High	New	New	New
	Intermediate	Intermediate	Intermediate
	Worn	Worn	Worn
	Extremely Worn	Extremely Worn	Extremely Worn

4.4.1 Run time and duration of experiments

Each experimental run operates for approximately 45 minutes, so that reliable and statistical data can be recorded from the PEPT system. The PEPT data needs to be triangulated (preprocessed) and smaller data sets are easier to preprocess. Therefore the 45 minute data recording session is split up into three smaller sessions. Each session is reduced to 15 minutes. There is no need for experimental repeats, as the data that is collected is run for a long enough time as to allow steady state to be reached. The processed data is averaged across the experimental run time. Therefore any repeat experiments that are run at a steady state for the same length of time will have the similar results.

4.5 Experimental procedures

4.5.1 Activation

The PEPT system requires a radioactive medium that it can track. In this work a 5mm glass bead was made radioactive (activation) and tracked in the experimental mill. There are two main methods for activation, namely direct and indirect. Direct activation is a process where the desired object is directly bombarded by a beam from the cyclotron and through that is made radioactive. For indirect activation there are two methods available and those are ion-exchange and surface modification. In this case the ion-exchange method is used. The glass bead activation as well as the resin activation is discussed in greater detail in sections 5.5.2 and 5.5.3.

4.5.2 Glass bead activation

Glass bead activation is a relatively simple process when compared to that of the activation of the resin. A hole needs to be carefully drilled into the 5mm glass bead. The hole needs to be deep enough to comfortably place the radioactive resin inside of the 5mm glass bead. If the hole is over drilled, then the glass bead will be fatigued and there is a high possibility that the glass bead shatters and contaminates the experimental mill. Contamination would mean that the experiments need to be stopped immediately and continued only after the charge and mill no longer have traces of radiation. The hole in the 5mm glass bead is drilled using a diamond drill bit and a coolant. Once the hole is drilled the radioactive resin is placed inside the glass bead and is sealed with super glue (cyanoacrolate).

4.5.3 Resin activation

The centre piece of the experiments is the radioactive resin. Without the resin the experiments would not be possible. The resin activation process is a delicate and time consuming process. The activation of the particle was done by PEPT Cape Town personnel Michael van Heerden and Cong Liu. The following process description is a very basic explanation of the activation process as described by Van Heerden (2011).

A cylinder with 70 µm sinters on each end is filled with modified tin dioxide, which is used as an inorganic resin, is then equilibrated and a solution of ^{68}Ge is passed through it. The^{68} Ge is dissolved in hydrochloric acid (HCl). The Germanium is adsorbed on the tin dioxide column. The ^{68}Ge decays to ^{68}Ga. ^{68}Ge decays via electron capture to ^{68}Ga. It takes approximately four hours for 90% of the ^{68}Ga to "grow in". The 'grow in time' is the duration over which the ^{68}Ga growth reaches a maximum. Depending on the desired activity the ^{68}Ga is eluted with 5-10 ml of dilute HCl. The ^{68}Ga solution is then dried. ^{68}Ga is then dissolved into another HCl solution, but this time the HCl concentration is much weaker than the previous HCl solution. HCl is used for this process because Ga^{68} dissolves more readily in HCl than H_2O, which would have been used as a more ideal alternative. A cationic exchange resin is then added to the Ga^{68} and HCl solution and the mixture is shaken for between 30 and 60 minutes depending on the desired activity. Once the shaking period has lapsed the resin is removed from the solution and is then placed into the glass bead. The glass bead is then sealed with super glue.

4.5.4 Determining the glass beads masses

The mass of the glass beads is determined by multiplying the glass bead density (2500kg/m^3) with the volume the glass beads occupy, as can be seen in the equation below. Where M_{GB} (kg) is the mass of the glass beads, ρ_{GB} (kg/m^3) is the density of the glass beads and the volume occupied by the glass beads is represented by V_{GB} (m^3).

$$M_{GB} = \rho_{GB} V_{GB}$$

The volume that the glass beads occupy is determined as follows. Firstly the total volume of the mill is determined by the equation below.

$$V_{mill\ total} = \pi r_{mill}{}^2 L_{mill}$$

The mill volume is determined by multiplying the inner surface area of the mill (πr_{mill}^2) to the inner length of the mill (L_{mill}). Once the total volume of the mill has been determined the fractional volume of the mill can be determined. Therefore the actual mill volume (V_{mill}) is calculated by multiplying the mill fill fraction (F_{mill}) by the total mill volume. This can be seen in the following equation:

$$V_{mill} = V_{mill\ total} F_{mill}$$

The volume occupied by the glass beads is determined by the actual volume of the mill (V_{mill}) and a void fraction (e).

$$V_{GB} = V_{mill} (1 - e)$$

The void fraction is a variable that needs to be determined and is governed by the shape of the material that is being used. The glass beads are spherical therefore the void fraction used for these calculations is 0.4. The void fraction gives an indication of the volume fraction that will be filled by the gas phase. Therefore the volume fraction that is occupied by the glass beads is 1-e.

4.5.5 Weighing glass beads for the mill fill

The weighing of the glass beads is a straightforward procedure, but it does have to be done carefully to avoid any loses. An electronic scale is used to weigh the glass beads. A small bucket is placed on the scale and the 'Tare' function of the scale is used. The 'Tare' function zeros the scale with the small bucket on top of it. Once the scale is zeroed the glass beads are carefully poured into the bucket. A funnel is used to pour the glass beads into the small bucket. The accuracy of the weighing is within 0.01g of the actual weights. Once the glass beads have been weighed they are transferred into the mill.

4.5.6 Glass bead removal

The radioactive glass bead needs to be removed from the experimental mill once the count rates are too low or when another set of mill fill conditions need to be tested. Count rate is a measurement made by the PEPT camera to indicate the magnitude of activity of the radiated particle. High activity is identified with high count rates and low activity with low count rates. The activated glass bead removal is a simple process, but it needs to be done carefully to

minimize glass bead losses. The first step in the process is to move the steel base and the mill out of the camera by shifting it onto one of the trolleys. Once the steel base and mill are secured onto the trolley the hatch of the mill is removed. A steel tray is placed under the mill and against the steel base. The mill is then tilted to allow the glass beads to flow out of the mill and into the steel tray. The glass beads will build up on one side of the steel tray, so they will need to be moved and spread to other sections of the tray to avoid over flowing and to minimize losses. The glass beads will stop flowing at a certain point and either a hand or another object has to be used to assist the glass bead flow. This needs to continue until the mill is empty. Now all the glass beads are out of the mill, but the radioactive glass bead is still present. The radioactive bead needs to be removed so that there is no disturbance in the data recording for the next set of conditions. The radioactive bead is found by using a Geiger counter. The Geiger counter scans across the bed of glass beads and where it is highest is the location of the radiated bead. Then the glass beads around this area are removed and transferred into another tray. This process is repeated until there are a few glass beads left in the area with the highest radioactivity. The glass bead is then visually identified, as it looks significantly different with its embedded resin to the other glass beads. Once the radioactive glass bead is removed the rest of the glass beads can be used again for the other experiments.

4.5.7 Location marker

Every time the mill is moved for a lifter change or a change in mill fill the mill needs to be realigned. Despite using two separate lasers to realign and position the mill in the PEPT camera, as can be seen in Figure 26 and Figure 27, there will always be a margin of error. If the mill is off-center, then the PEPT data will also be off-center to the coordinate axis. The location markers' positional data can be used to realign the data to the center of the coordinate system. The locations marker used is a Na^{22} point source (permanent source), which has a half life of 2.6 years. The location marker is placed in three different places (front, middle and end) of the mill, so that the vertical and horizontal alignment can be recorded. The front and end location markers are placed at the edge of the field of view. Each location is recorded for 30 seconds by the PEPT system. It gives an outline of the mill for three different positions. The location marker data is used to fix key positions in the coordinate system chosen.

Figure 26: Laser realignment on the side of the mill

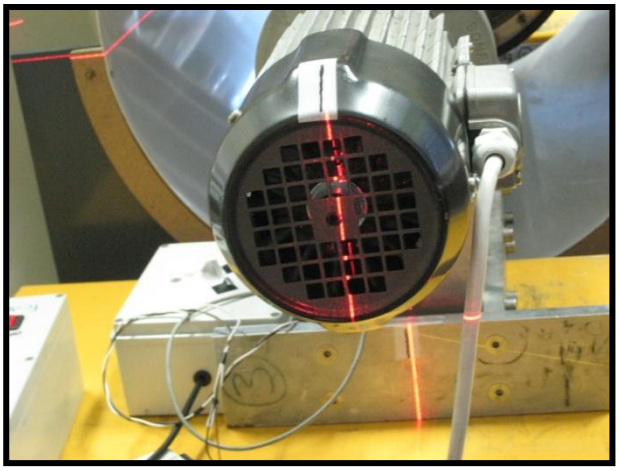

Figure 27: Laser realignment at the back of the mill setup

4.6 Changing mill conditions

4.6.1 Lifter change

The experiments require removal of the lifters in the mill. The first step in this process is to take the mill out of the PEPT camera and secure the steel base and the mill on a trolley. The glass beads are removed from the mill and this is done according to the glass bead removal procedure discussed in section 5.5.6. Once all glass beads the mill is taken off the steel base and the drive train is disconnected. The mill is opened at one end by removing the front cover of the mill. The lifters are removed by unscrewing them from the mill shell. The old lifters are then replaced by new lifters.

It is important to note that the screw length needs to be smaller than the length of the mill shell thickness and lifter height combined. Otherwise the screw will be protruding from the lifter and it will cause an unwanted disturbance to the flow of the material in the mill. Another consideration when working with small lifters (1.5 mm) is that attaching them to the mill shell is a delicate process. 1.5 mm lifters only have one turn of thread and if the thread fatigues then there is one less point of contact for lifter to the mill shell.

Once the lifters are in place the front cover is re-attached to the mill. The mill is then attached to the steel base and the drive train is reconnected to the mill and the motor. It is important that the drive train is correctly connected to the mill and the motor. The consequences of not

doing so could results in considerable damage to the mill, motor, drive train and could be harmful to anyone close to the experimental mill. With the drive train in place the desired amount of glass beads is added to the mill. The glass beads are poured into the mill via a funnel through the hatch that was open during the glass bead removal process. The hatch is closed and the steel base and mill are placed inside of the PEPT camera. The mill is then aligned inside the PEPT camera to ensure experimental consistency. Two lasers are used to assist in the alignment of the experimental mill. One laser is placed behind the mill and allows the motor end of the experimental rig to be in place. The second laser is an inbuilt laser of the PEPT camera, which ensures the correct depth of the experimental mill inside the camera. The aim is to have a consistent field of view for all the experiments. As soon as the alignment has been completed the location markers are used to virtually assess the mill's alignment. This is done according to the location marker process. After the location markers the radioactive glass bead (tracer) is added to the charge. The tracer is added through the front opening of the mill, which is blocked by a specially cut foam during runs. Once the tracer is added and the front hole is closed with the foam the mill is started and set to the desired mill speed. A tachometer is used to make sure the desired mill speed is reached and is not varying during the test. The tachometer is attached to the side of the steel base. The tachometer uses reflection to measure the mill speed. It counts the amount of reflections per time interval and converts this to a revolution per minute (rpm) reading. A white tape is attached to the mill to assist with the reflections and it is placed so that the tachometer can take the readings without human intervention. The data recording commences once the mill is operating at the required mill speed.

4.6.2 Without lifter change

Mill preparation without any lifter change is a very similar process to the preparation of the mill with lifter change. The difference is that no lifters need to be changed. This means the mill does not need to be taken off the steel base and disassembled. The mill needs to be secured onto the trolley and the glass bead removal procedure needs to be followed. Once the tracer is found and removed from the glass beads, the weighing procedure is followed. After that the mill is filled with the required amount of glass beads and prepared for use, which includes the

closing of the hatch, alignment and location markers. Just as is the case with the lifter change procedure, the mill is started and brought up to the desired operating speed. A special case does however exist where the tracer is left over night in the mill. The activity of the tracer becomes so low that it does not need to be removed from the mill. As a result only the additional glass beads need to be added to the mill in the case of a mill fill change. If only the mill speed needs to be changed, then the tracer only needs to be added to the system. There are two ways that the mill can be filled. The first method is to move the mill, open the hatch and fill in the additional beads. The second method is filling the mill from the front hole. The first method is used, because it is more accurate and minimizes the loss of glass beads.

4.7 Experimental Instructions

The detailed experimental instructions can be found in section 16.13 in the appendix. Following the experimental instructions will allow for the experiments to be replicated.

5 Charge Data

Experimental tracking data using the Positron Emission Particle Tracking (PEPT) is used to build up an understanding of the charge of the mill. The PEPT data that is presented in this chapter does not represent research specific data. The data is shown to highlight certain characteristics of the charge and assist in the development of the basic surfaces required for the charge analysis.

5.1 Positron Emission Particle Tracking (PEPT)

The PEPT method is a 3D particle tracking method that uses a powerful camera to track nuclear irradiated particles. For further information on the camera and its performance, please refer back to the literature review. The way the PEPT system works and operates has been discussed on the literature review, but the data processing has not been mentioned yet.

The PEPT method is used to analyze the velocity function, because PEPT measures the average velocity of a particle in experimental tumbling mill accurately. An example of this can be seen in Figure 28. In addition to the velocity readings the PEPT method is able to represent the probability distribution of the particles in the experimental mill, which can be seen in Figure 30.

The PEPT data used in this project are based on tracking glass beads in an experimental tumbling mill. This is not a reflection of the limitations of the PEPT system, but rather a result of the simplified experimental setup. The PEPT system is able to track particles in real systems, where the charge is made of slurry. In Govender et al (2010) irradiated glass beads were tracked while in a slurry, which was made of approximately 1 mm bluestone particles. The difference between the experiments is the clarity and accuracy of the experiments. The β^+ gamma-rays of the irradiated particle in the glass bead experiments have to travel through less material and less dense material. Therefore the data has a greater accuracy.

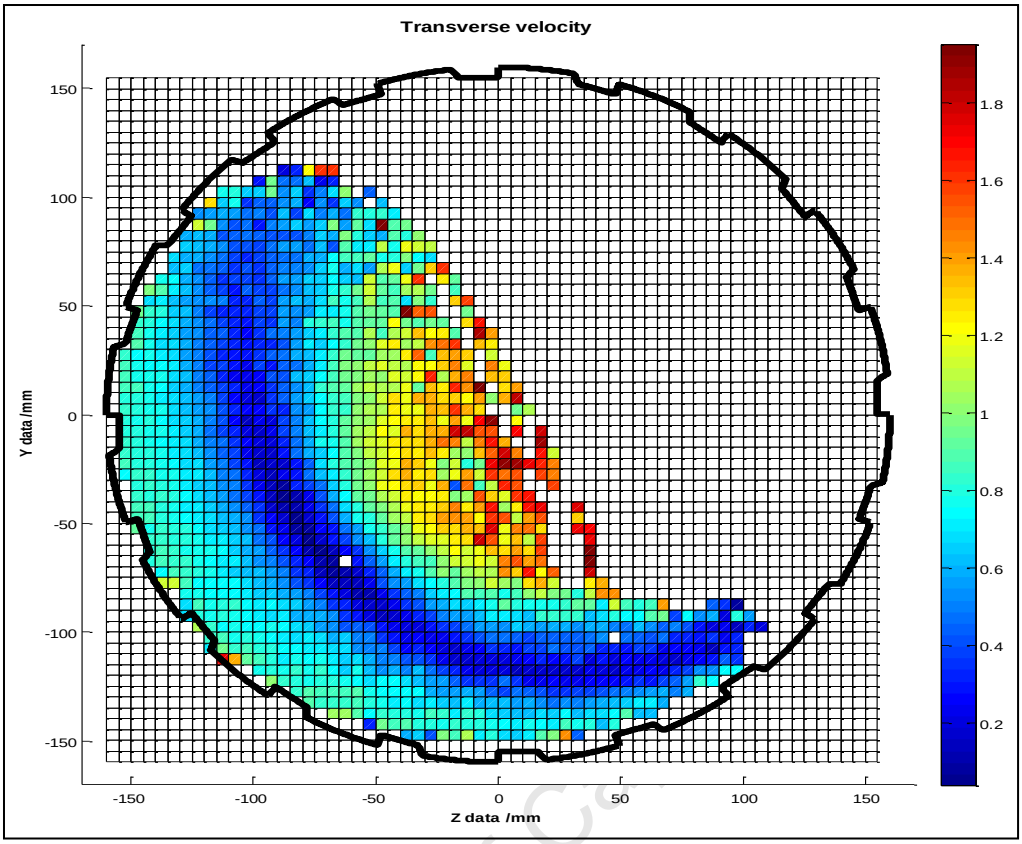

Figure 28: Transverse velocity

5.2 Different flow regions

The PEPT data can be presented in different ways. Figure 28 and Figure 29 are examples of the same variable being presented in two different ways. Both methods will assist in describing the characteristics of the charge. From Figure 29 it is clear to see that there are two different flow regions in the charge. These flow regions are separated by turning points, which are the moments the particles change the velocity direction and therefore direction of flow. Changing the direction of the velocity means that there is a point at which the particle has a zero velocity. Therefore every different layer of particles will have a different point at which it is zero, which creates a line of zero velocities. However this is not isolated to the slice of data that we are exposed to and it is true for the entire charge. Therefore the zero velocity line actual is a zero velocity surface. The zero velocity surface is called the equilibrium surface (Powell and Nurick (1996)) and it presented by the solid (red) line in Figure 29. It can clearly be seen in Figure 28 that the equilibrium surface from Figure 29 follows a similar form to the dark blue region in

Figure 28, this confirms the observation. The definition of the equilibrium surface was first presented in Powell and Nurick (1996), where it was visually determined from experimental x-ray data. In Mc Bride et al (2004) a DEM model was validated using the comparison between the equilibrium surface of the DEM and experimental x-ray data. The flow regions below (region 2) and above (region 1) the equilibrium surface are significantly different. The flow pattern in region 2 is steady and consistent in terms of its velocity magnitudes when compared to that of region 1, which can also be seen in Figure 28. The velocities vary between about 0 m/s to 0.8 m/s. The same cannot be said for the flow pattern of region 1, as it is more volatile and has a larger range of velocity values. The velocities of the particles in region 1 increase outwards to the centre of the mill. The velocities in region 1 vary between 0 m/s to above 1.8 m/s. The increase in velocity is because of the cataracting region of the charge. The cataracting region of the charge can be identified by the larger velocities, which means the cascading region of the charge can therefore also be identified. The cascading region of the charge is the layer of charge between the cataracting charge and the equilibrium surface. Region 1 has two different flow patterns, but this will be properly defined further on.

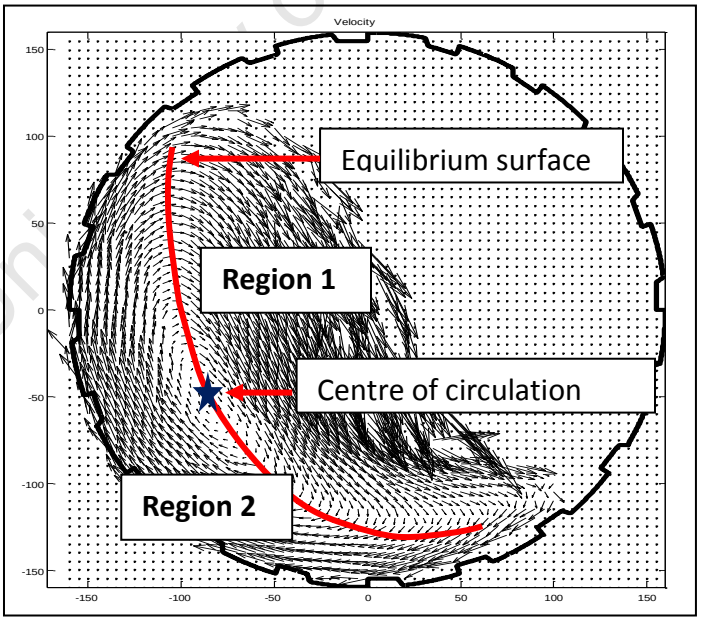

Figure 29: Velocity plot indicating the COC and equilibrium surface

5.3 Charge characteristics

The characteristics of the charge are the physical features of the charge in the experimental mill. The charge characteristics that can be identified by the PEPT data are the center of circulation (COC), equilibrium surface and the charge free surface. The equilibrium surface has already been defined and explained. It is represented by the red line in Figure 29.

The COC (Powell and Nurick (1996)) is a unique point in the charge and can be found on the equilibrium surface. According to Powell and Nurick (1996) the COC is the point around which the entire charge in the mill circulates. It is the point at which there is an absolute zero velocity in all directions, which is different to the equilibrium surface. The equilibrium surface is direction specific. This means that there is a different equilibrium surface for each direction (x,y and z). The equilibrium surface that is used for this flow description is specific to the x-direction. The COC is the point at which all these equilibrium surfaces intersect each other. The blue star in Figure 29 represents the COC of the data set.

Region 1 has two flow patterns, namely the cascading charge and the cataracting charge. The surface separating both regions is called the charge free surface. Using the velocity and particle probability distribution data it is possible to identify the charge free surface. The charge free surface in Figure 28 can be identified as the surface below the cataracting material (yellow and red region). The cataracting material can also be clearly identified by the dark blue region in Figure 30. The probability distribution of the particles is determined by using the time spent in a specific bin (Small Square in grid); therefore the higher the velocity the less time spent in the bin and the lower the distribution. The cataracting region can therefore be clearly separated from the main charge body. The charge free surface is represented by the white line in Figure 30. The white line follows a similar trend line that tracks the charge material in Figure 28.

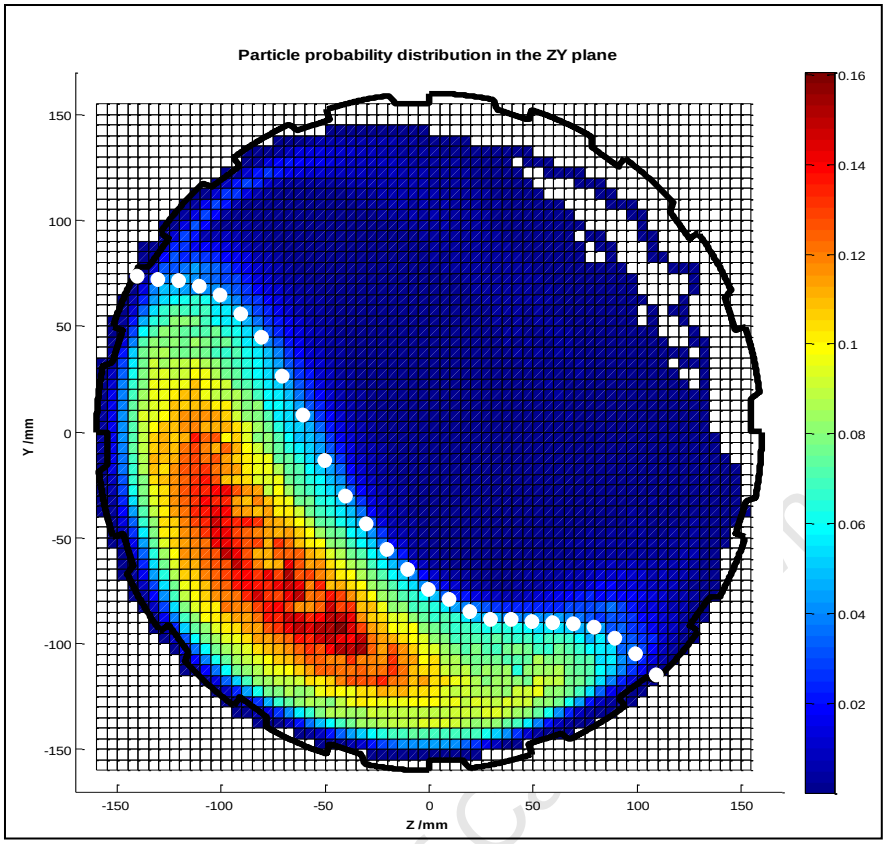

Figure 30: Particle probability distribution

All the charge features will be tracked and defined numerically in order to be accurate. The descriptions so far are meant to explain the concept of each characteristic, as they will be used in the granular flow theory development.

5.4 Particle flow types

The particles movement can be divided up into three types. The first type is a force driven flow, where the particles are driven up the side of the mill to a certain turning point by the forces exerted on them by the mill and lifters. This type of flow is observed in region 2 and can be seen in Figure 28 and Figure 29. The second type of flow is a free flowing gravity driven flow. This type of flow can be seen in region 1 in Figure 28 and Figure 29 between the equilibrium surface and the in-flight material. The last type of flow occurring in the mill is the material that is in flight, which is in region 1. The in-flight material is called the cataracting charge and can be seen as the material with the high velocities (yellow and orange colours) in Figure 28 and Figure 29.

5.5 Area of interest

The area of interest is the main body of the charge in the experimental mill. The main body of the charge will for now exclude the cataracting material. Therefore the material in flight will be ignored for this part of the development of the granular flow theory. The cataracting material is left out, because it cannot be adequately explained by the fluid mechanics used so far. An additional consideration is that the cataracting region does not contribute to the power draw of the system. The main body of the charge is separated by the charge free surface, which is the boundary between the cascading and cataracting material. The charge free surface is represented by the blue dots in Figure 31. The charge free surface shown in Figure 31 is an accurate representation of the charge free surface and it is extracted by using Figure 30. In this case the charge free surface is used to illustrate the boundary of the main charge body.

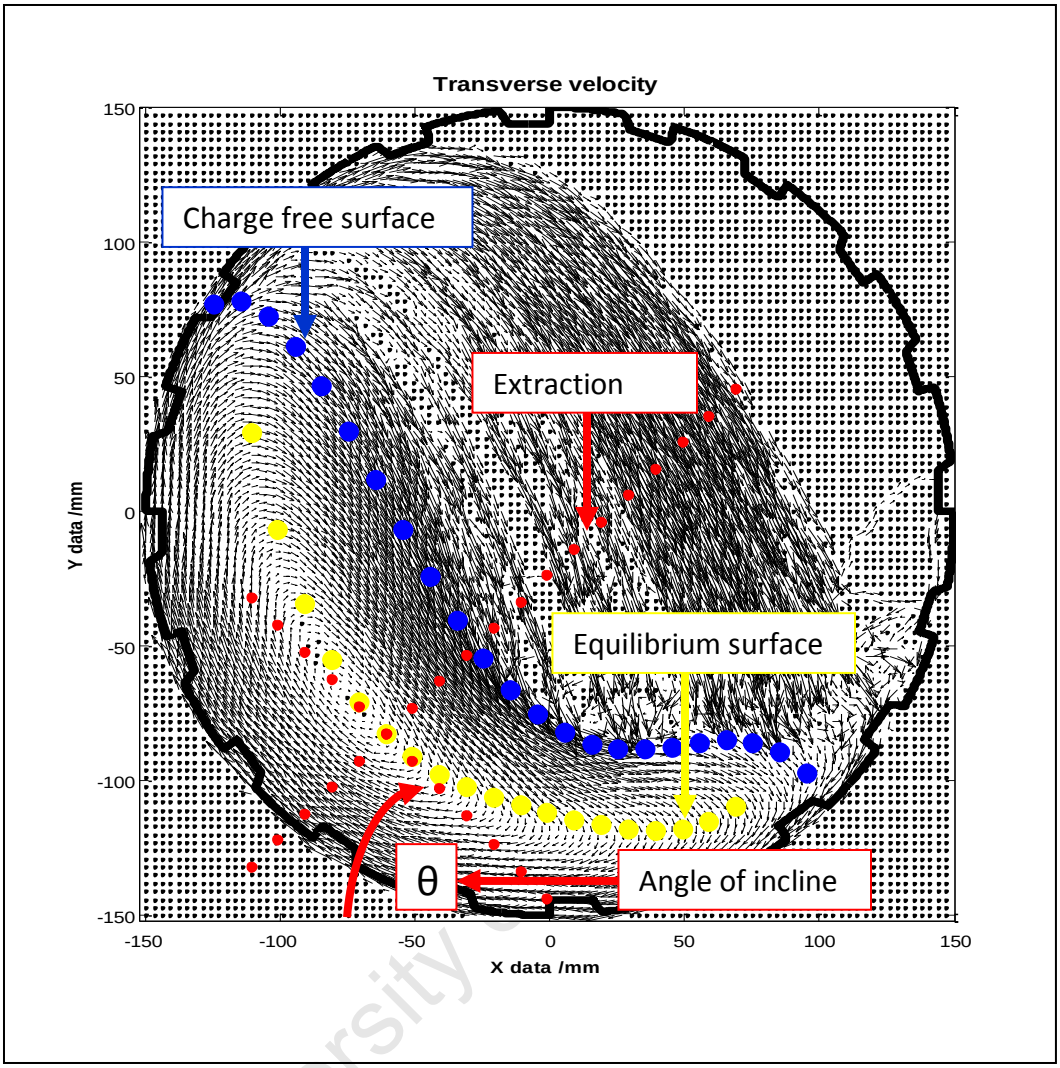

Figure 31: Velocity plot indicating the area of interest

The equilibrium surface is represented by the yellow line in Figure 31. The charge free surface and equilibrium surface are important to the development of the granular flow theory, as these charge characteristics represent the boundary layers of the fluid flow. The other important boundary is the mill shell. With correctly defined boundary layers the desired fluid flow region can be extracted and simplified. The flow region of interest is represented by a line that is perpendicular to and passes through the equilibrium surface, which in this case is represented by the red line in Figure 31. The red line is called the extraction line, because it is the line along which the experimental data will be extracted. The extraction line is perpendicular to the equilibrium surface, so that the tangential velocities of the fluid are parallel with the boundary

layer and so that any changes in slope of the equilibrium surface can be tracked and easily incorporated into the granular flow model. The angle by which the equilibrium surface changes, is represented by θ in Figure 31 and it is measured from the line perpendicular to the extraction line. This configuration will allow for the flow region in any part of the charge to be determined.

6 Data preprocessing

Data preprocessing is required after the data has been recorded by PEPT computer system. The data from the PEPT system needs to be cleaned to remove the β rays that are recorded from the activated particle which are present. Without 'cleaning' the particle cannot be located or tracked accurately because of too many spurious lines. The preprocessing 'cleans' the data so that only the β rays that are related to the particle tracking are recorded. The technique used for the preprocessing is called triangulation. In addition to this the data files from the PEPT computers is not compatible with Matlab, because the data is recorded in binary code. After Triangulation the data is converted to ascii, which allows post-processing of the data using Matlab.

6.1 Triangulation

The triangulation technique used was initially developed at Birmingham University to preprocess data from their PEPT camera at the position imagining center at the University of Birmingham (Parker et al (1993)). The technique was adapted and then coded a program called 'CTrack.exe' at the University of Cape Town. Further details on triangulation technique are found in Morrison et al (2010), Giovannoni (2009) and Parker et al (1993).

6.2 Triangulation variables

There are three variables that need to be defined in order for the data to be processed by the CTrack program. The variables are:

- Number of events per slice (Events)
- Percentage of the data that is used for the preprocessing (Fopt)
- Error allowed for the particles position

Fopt was estimated by the suggested Fopt value in Parker et al (1993), which is between 0.2 and 0.33. These were helpful starting points, but most of the Fopt values tended to be between 0.1 and 0.3. No mention is made in the literature with regards to the error and events per slice associated with Fopt. The reason being there is no distinct relationship or trend between any of the variables. The data set for one condition is split into three smaller data sets and different pre-processing variables for each smaller data set could be used. The entire set of preprocessing variables for all the experiments can be found in section 16.3 in the appendix.

6.3 Evaluating PEPT data

There are many methods to check if the PEPT data, which has been put through the triangulation routine, is of acceptable quality. The methods range from plotting a certain portion of the data and checking the sinusoidal shape of the data to assess the error of the average location of the particle. Visual inspection is also recommended. The data is evaluated by firstly running the data through the triangulation routine (CTrack.exe) and then a batch version of 'CTrack.exe' called 'winpept.exe' employed. The batch version of 'CTrack.exe' allowed multiple conditions to be run. In order to retain data that is reliable and to reduce the data preprocessing matrix the error is set to 5 mm. With the error held constant the events per slice and Fopt values need to vary until the acceptable data quality is produced. Acceptable data is characterized by no spurious β rays and should have few outliers if any. Bad quality has a high number of spurious lines and many outliers as shown Figure 32. It can be seen that the data had many spurious lines and outliers. In Figure 33 and Figure 34 the same set of data is preprocessed under different conditions and only a few spurious β rays can be seen. This illustrates the sensitivity of the Fopt value which was changed from 5 to 10 and 15 in Figure 32, Figure 33 and Figure 34, respectively. The effect of changing the events variable is shown in Figure 35 and Figure 36. It was observed that the location of the spurious lines can change even when the difference is of only 2 units in the choice of the events variable. The data in Figure 36 corresponding to the events variable of 123 had more spurious lines close to the body of the charge, whereas the data in Figure 35 processes with the events variable of 125 has more spurious lines in the cataracting area of the charge. The choice of these two vraibles was critical in this work and a lot of effort was applied to choose the optimum values. An example of an

acceptable data set after processing is given in Figure 37. It can be noted that there are no spurious β rays within the mill and two outliers.

6.4 Dealing with inferior PEPT data

Despite the best efforts the bulk of the PEPT data does not reduce to the quality of data seen in Figure 37. In most cases, the best data sets would be similar to the quality seen in Figure 33 to Figure 36. Approximately 8000 conditions were tested in total for 36 experimental runs each with three sets of data for the pre-processing and each data set was checked and scrutinized. The spurious lines do not represent a problem in this processing step and it does not take away from the visual analysis that can be made on the data. The effects of the spurious lines manifest themselves in the next processing step where the data is cleaned, binned and averaged. The spurious lines represent a big jump between two points, which is unrealistic. This jump affects the velocity calculations. A Matlab code was developed at UCT to deal with the spurious lines from the PEPT experiments. This code provides an elegant solution in dealing with the spurious lines from the PEPT data. Therefore if the data needs all the other criteria but has a few spurious lines the code is applied prior to post-processing that data to remove the majority of the spurious lines. Further information regarding the code can be found in section 7.3.

6.5 Data preprocessing method

A total of 108 data sets needed to be preprocessed. The criteria used to determine if the data was high enough quality for further processing were primarily the amount and severity of spurious β rays. To remove the spurious β rays random values of events and Fopt were used and results evaluated. Then the number of events per slice was increased by 50 to 100 units at a time and the Fopt by 5% until the spurious lines were minimized or eliminated. Fopt and events were varied and analyzed to see if they followed any particular trend, but none were observed. A list of the conditions used for every data set is given in the appendix section 16.3.

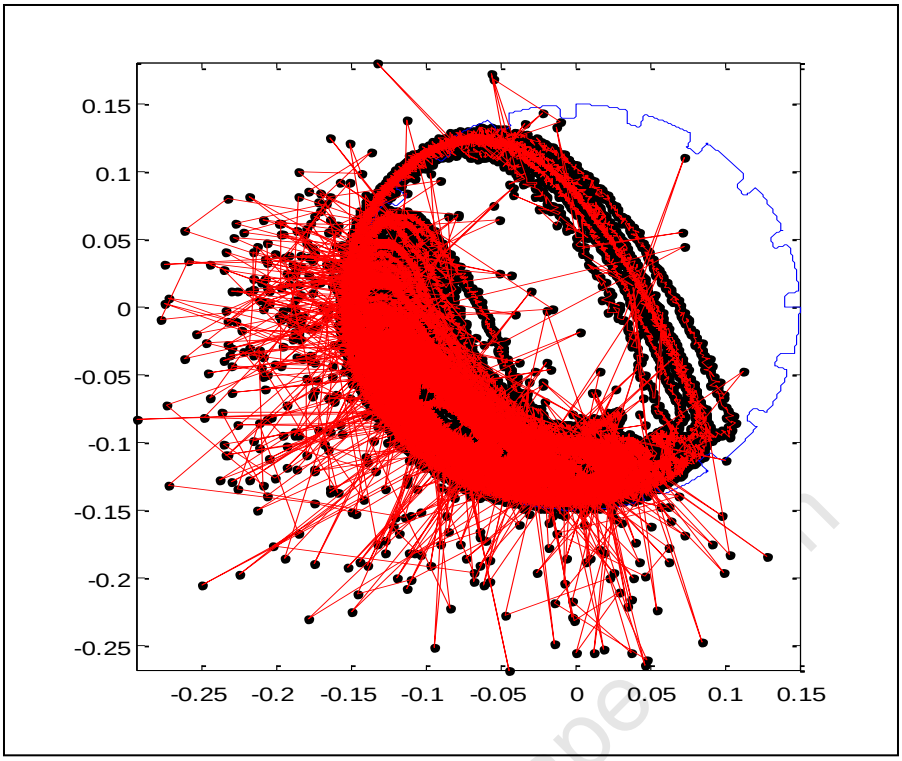

Figure 32: PEPT data with spurious lines whose locations do not match the particle being tracked from experiment 11 sessions 2 (Events: 100, Fopt: 5)

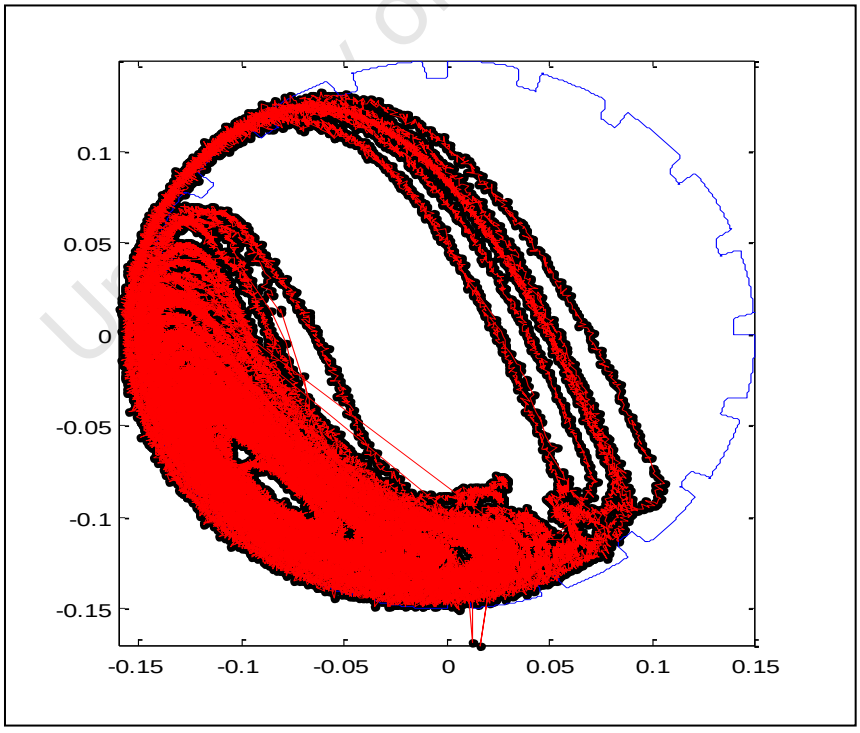

Figure 33: PEPT data that represents the tracked particle from experiment 11 sessions 2 reasonably well but has some locations that are not related to the particle position (Events: 100, Fopt: 10)

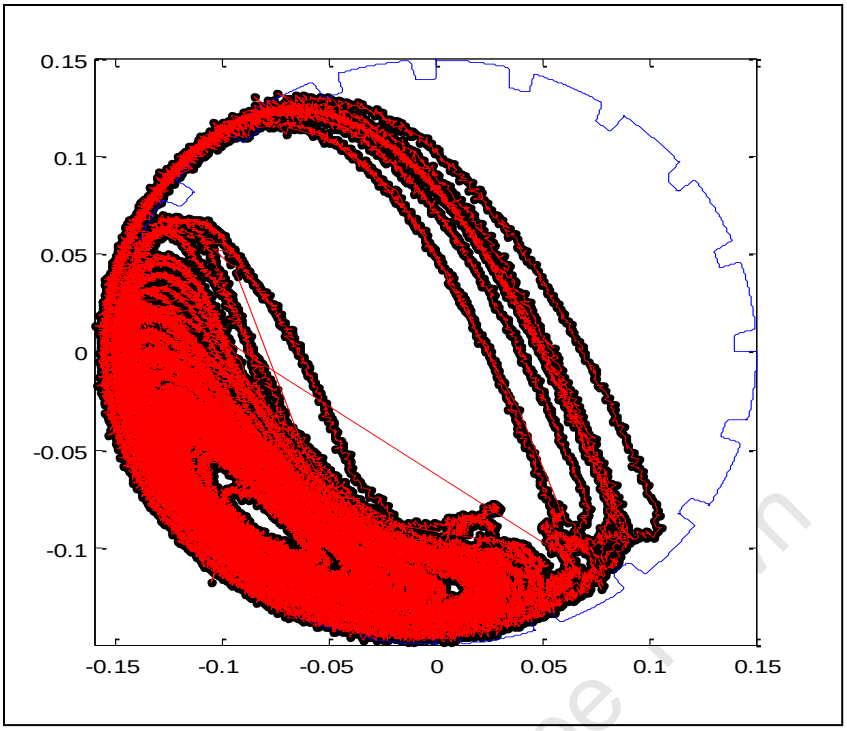

Figure 34: PEPT data that represents the tracked particle from experiment 11 sessions 2 reasonably well but has two locations that are not related to the particles position (Events: 100, Fopt: 15)

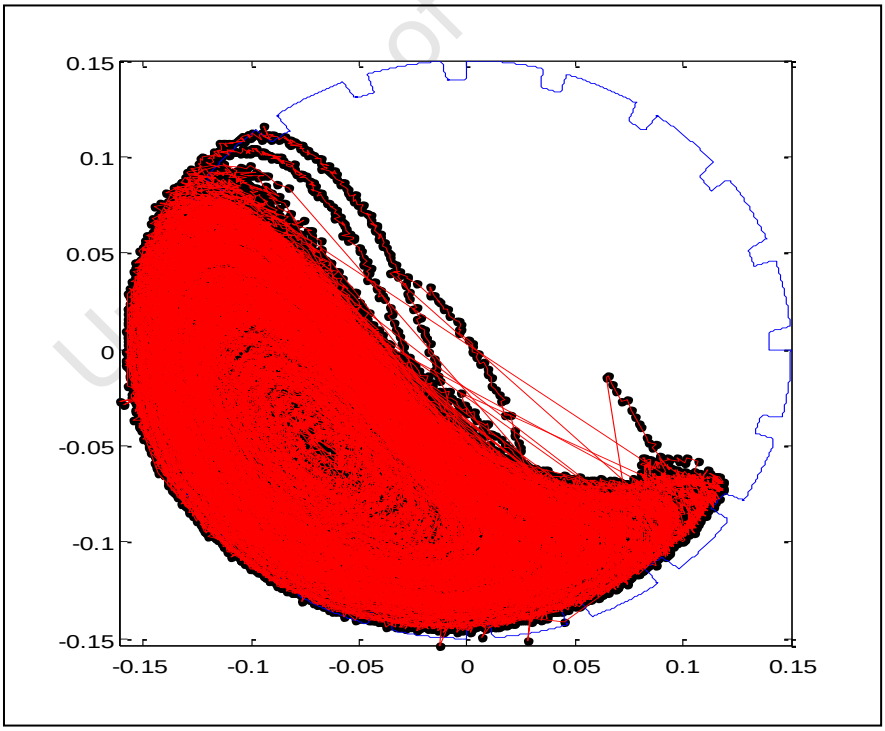

Figure 35: PEPT data with spurious lines whose location do not match the tracked particle from experiment 41 sessions 1 (Events: 125, Fopt: 15)

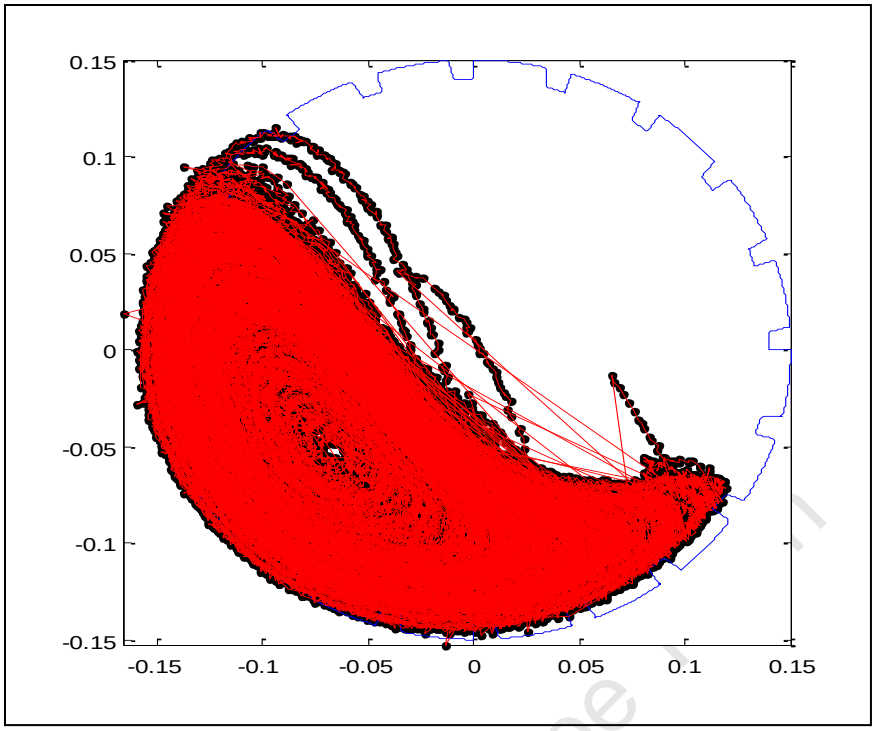

Figure 36: PEPT data with spurious lines whose location do not match the tracked particle from experiment 41 sessions 1 (Events: 123, Fopt: 15)

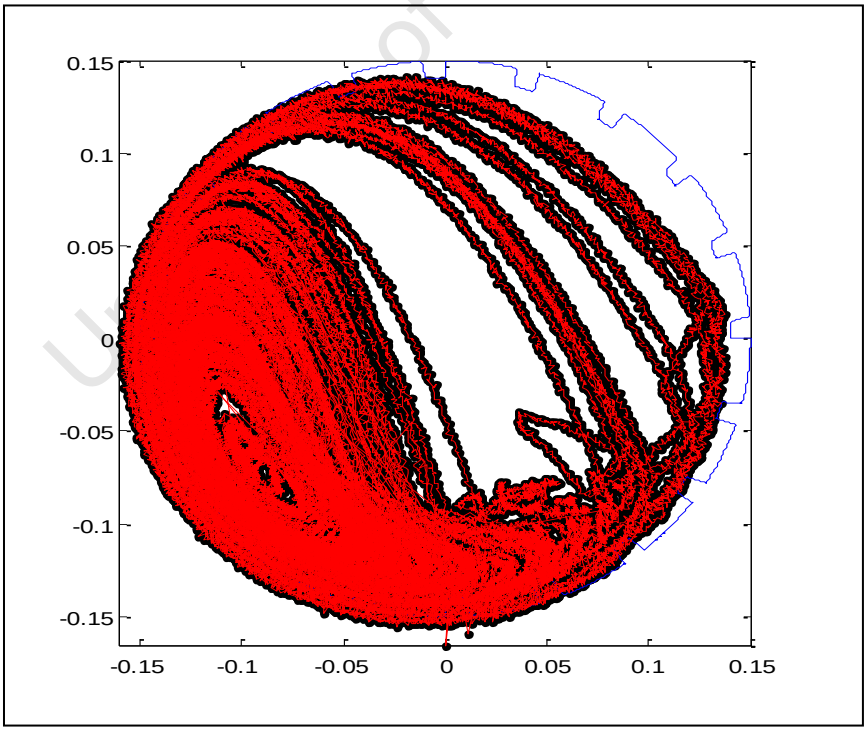

Figure 37: PEPT data without any spurious lines which matches the movement and location of the tracked particle in experiment 4b sessions 2b (Events: 150, Fopt: 10)

7 Data processing

After the triangulation the raw PEPT data is a combination of x,y and z coordinates at certain times. The data in this form has limited use. The raw data can be used to infer charge motions and the approximate charge profiles and this is done through visual inspection. By processing the data further the time averaged velocity and probability distribution can be extracted from the raw data by using an in-house PEPT data Matlab code which was designed to extract all the essential analyses. This chapter discusses some of the steps involved in processing PEPT data using the UCT in-house Matlab code.

7.1 Reference frame

The raw PEPT data is first adjusted so that it fits into the virtual mill that is drawn in Matlab, as shown in Figure 38.

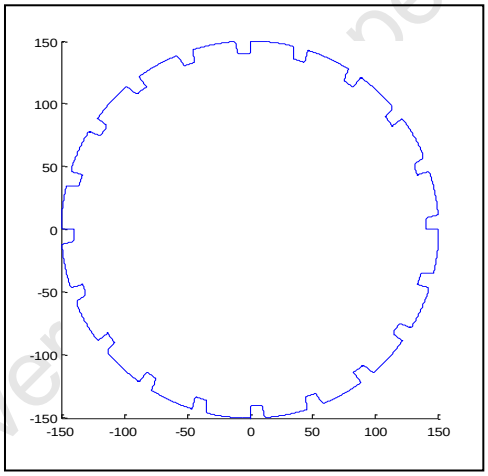

Figure 38: Virtual mill shell

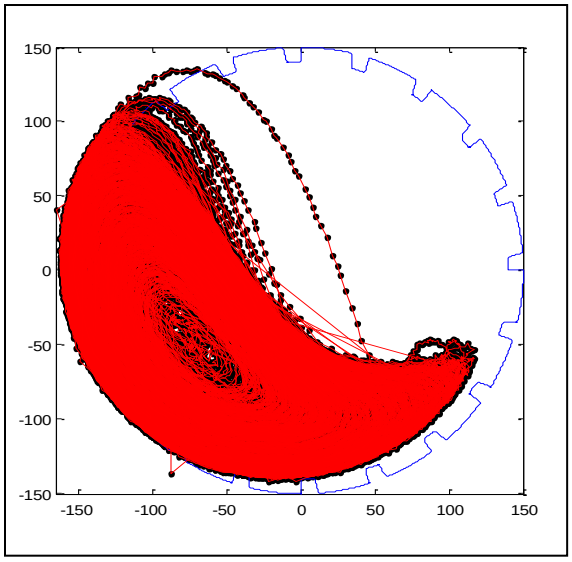

Figure 39: Raw PEPT data off center

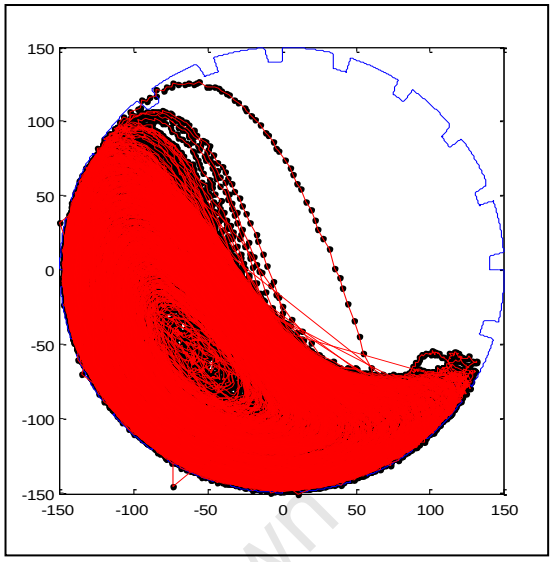

Figure 40: Raw PEPT data adjusted

This adjustment allows all the data to have the same reference frame. The data can easily be compared from the same reference frame. In this part of the code the data is adjusted by a simple vector ([x y z]) that shifts the data in any direction. For example the data in Figure 39 can be shifted to the results shown in Figure 40. The appropriate adjustment values are reported in the appendix section 16.4.

7.2 Cleaning outliers

Occasions arise when spurious data points outside of the virtual mill shell are observed in the data set, which can be seen in Figure 39 and Figure 40. Hence the outliers need to be removed from the data set. This is removed by simply converting the data from the Cartesian coordinates to polar coordinates. This will convert the data to a set or radius' and angles. Then by setting a radius limitation, which is the size of the mill, the data that lies outside of the mill is identified, its position in the data set is found and is then taken out.

7.3 Data separation and interpolation

Once the data is cleaned and adjusted to a reference frame interpolation techniques are applied to regions with gaps to provide continuity in the motion of the charge. The interpolation is a piecewise cubic Hermite interpolation which is a third degree spline function. The interpolation predicts the possible path of the particle between two points. The

interpolation time step that has been used is 1 millisecond. Before the interpolation can be completed a data separation step needs to be concluded. In the event of spurious lines, which are created by the inefficiencies of the triangulation and particle movement, a large step and distance is created between two data points without any data in between it. An example of this can be seen in Figure 37, where spurious lines can be seen near the toe region of the charge. Interpolation along these spurious lines will create unrealistic data in the velocity calculation step.

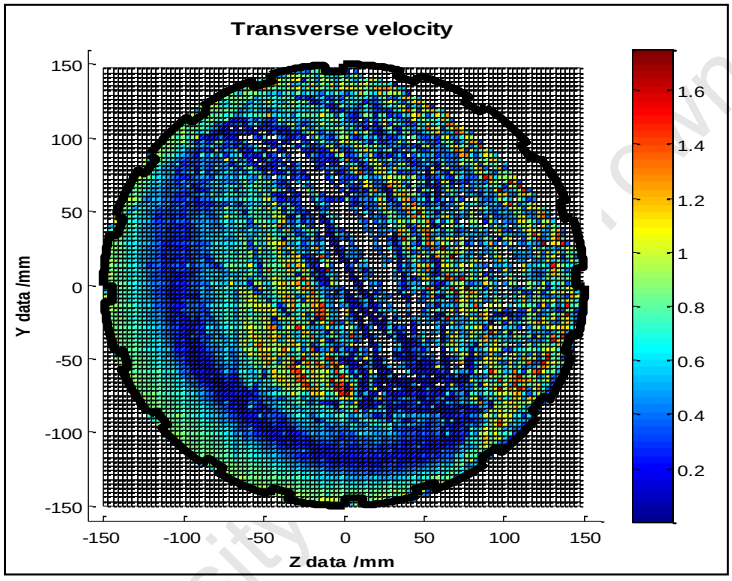

Figure 41: Transverse velocity profile with spurious lines which create dark lines (blue) in the cataracting area where only light lines (red or orange) should be

The interpolation will fill in a lot of data between the two data points and a small time step will create paths of very low velocities which is a misrepresentation of what is going on in the mill. Additionally it will represent an incorrect particle path. This can be seen in Figure 41, where the dark blue lines (very low velocities) are found in the cataracting region where only red and orange lines (high velocities) should be found, therefore spurious lines are present.

The large distances between the particles are primarily created by the small viewing area of the PEPT camera. The mill's length is 285.5mm and the viewing area of the mill is 230mm. The particle therefore is able to move out of sight for a few seconds and then enter the viewing area again. The particle enters the viewing area at a different location from departure one. The

difference in location creates the large distances between the particles and hence the spurious lines that are shown in Figure 41.

Unfortunately these spurious lines cannot be completely removed, but they can be minimized through a routine that has been developed. The routine has been developed by Morrison (2011) especially for the data from the Cape Town PEPT lab, which is very different to any data that has come out of the Birmingham PEPT facility. The logic behind the routine is to create smaller data sets which will be interpolated and put through the binning algorithm. The routine determines the average distance between any two particles in the mill. This does include the massive leaps caused by the spurious lines, but the variation caused by the large values is dampened out by the sheer volume of data that is being processed. A tolerance is set for the allowed distance between two data points and the limit is determined as two standard deviations from the average value. When the distance between two data points exceeds this distance the data is cut and stored as a smaller data set. The next data set starts at the data point which created the offset. This routine therefore does not take any data points, but cuts the data set into smaller data sets to meet the requirements of the binning routine. The binning routine counts the amount of times a particle enters a particular bin and does not need a completed path. The result of the data separation routine can be seen in Figure 44.

7.4 Determining time average velocity and acceleration

The time averaged velocity of the data is determined by taking the derivative of the data set. A time derivative using an nth order LaGrange polynomial is used to determine the velocity from the x, y and z data. The same routine is used to determine the time average acceleration of the particle from the derivative of the velocity data. The time averaged data set and not instantaneous data is used.

7.5 Binning

The binning routine subdivides the mill into smaller areas using a grid. The grid can be any size and in this case the grid size is 100 x 100. The diameter of the mill is 300 mm; therefore the grid's size is 300 mm x 300 mm, because the grid is square. Dividing the grid into 100 smaller grids would make a bin 3mm x 3mm. The binning routine uses this grid to count the number of

times the particle passes through one bin. Using this method the probability distribution of the particle is determined. The total number of counts is stored and is used to determine the relative amount of counts that occur in the different bins. All these probabilities will add up to 100%; hence the values are very small and within the range of 0.02% or less. An example of this can be seen in Figure 42. A particle moves from position 1 to 4 in an area. A 2 x 2 grid is chosen and the data is divided into 4 bins.

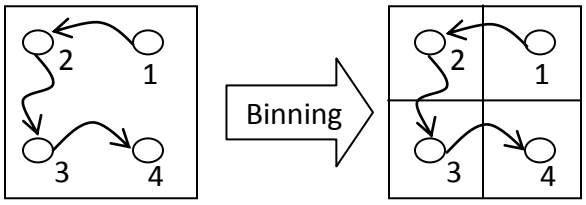

Figure 42: Binning data

The particle has been in each bin once. With a total of four counts and one in each bin, this means that the probability distribution of each bin is ¼ and is equivalent to 25%.

The probability distribution of the tracked particle can be determined by using its residence time in each cell (bin) that it passes through. The time that is spent in a particular cell regardless of direction and then normalizing it over the entire time of the experiment will allow the particle probability distribution to be determined. The counting method is seen as the less accurate binning method, but it is dependent on the data set that is used. If the data set is small, then using the residence time method would yield a more accurate description of the probability distribution. But in the case of a large data set, which is the case here, the accuracy difference between both methods is insignificant. The deciding factor was the reduction in computation. Using the residence time is more computationally expensive and therefore the counting method is used to determine the probability distribution.

A similar routine is used for the velocity data, where the velocity magnitudes are subdivided. In this case the velocities are averaged over a bin. All the velocities are taken into account for a certain bin and the average velocity is taken in the bin.

An alternative for the velocity calculation is using the residence time concept. The distance and time spent in each bin is known. The time is derived through the residence time method. The distance between two particle positions is determined. Then by using change in distance divided by time the velocity of the particle is determined. The velocities are recorded for each cell and are averaged with respect to the number of readings that were detected.

7.6 Data plotting

The time averaged probability distribution and velocity can be seen in Figure 43 and Figure 44 respectively. The data is plotted on an x and y-axis with the magnitude of the distribution and velocity plotted as colour plots on the same set of axis. The plots represent transverse view of the mill data and not axial. Presenting the data in this fashion allows analysis of different areas of the mill. Figure 43 can clearly show areas of high and low occupancy. The areas of low occupancy have the color blue. The colours ranging from green to red represent those areas of high occupancy. It has to be noted that the probability distribution values are not fractions, but are percentage values. The highest probability distribution value in Figure 43 is 0.08%. The same colour scheme is applicable to the velocity plots. The blue colours represent the low velocities and the green to red colours show areas of high velocity. The velocity values are represented in m/s. Therefore the highest velocity value in Figure 44 is 1.8 m/s.

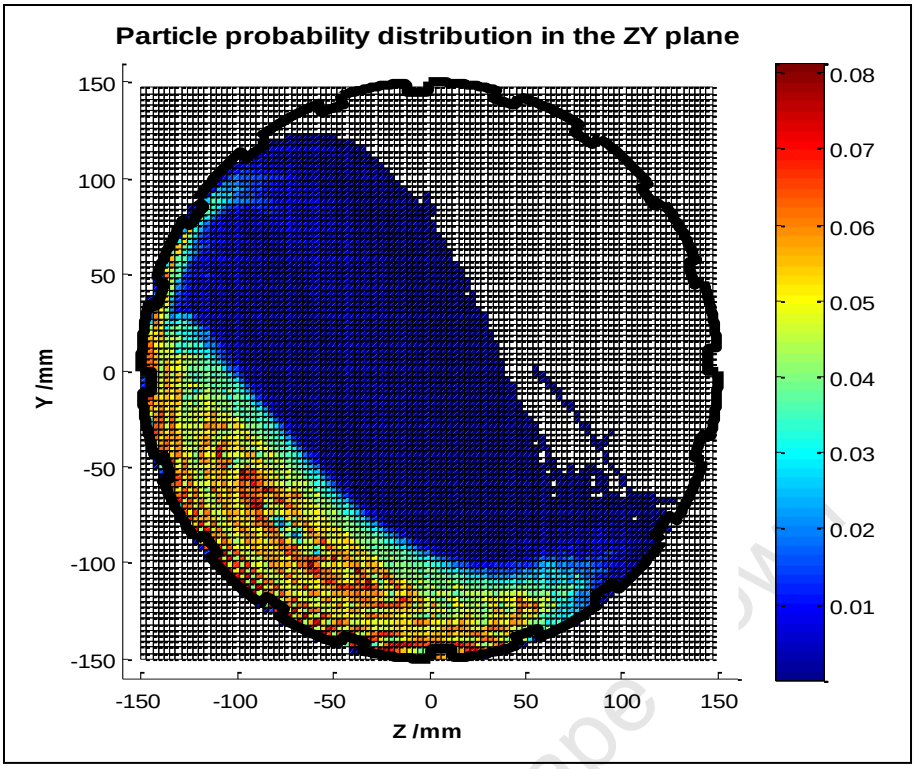

Figure 43: Time average probability distribution data at 55% mill speed, 30% mill fill and 3mm lifter

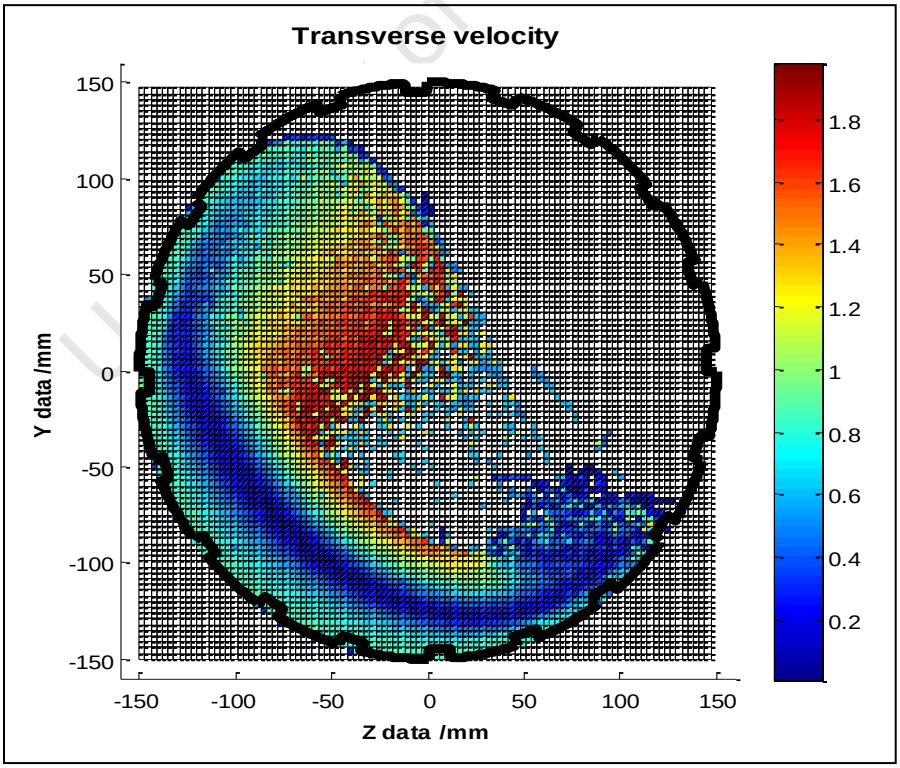

Figure 44: Time average velocity data at 85% mill speed, 30% mill fill and 3mm lifter

8 Surface extraction

8.1 Data Extraction

Extracting the velocity profile requires the equilibrium surface and the charge free surface to be defined, because these surfaces form part of its boundary conditions. In addition the procedure of extracting the velocity profile is validated with experimental data collected under different mill operating conditions using the two boundary conditions. Therefore defining and extracting the equilibrium and charge free surfaces is essential.

A manual data collection method was used to extract the equilibrium and charge free surfaces. The manual data collection method involves extracting the x and y coordinates of the equilibrium and charge free surfaces by using the 'Ginput' function in Matlab and then smoothing the data by fitting a polynomial to the data. The manual method is reliable and repeatable and hence it was used for the data extraction.

8.1.1 Charge free surface

The charge free surface separates the cascading region from the free flight region. The particle probability distribution data, such as one shown in Figure 45, is required to determine the charge free surface. The particle probability distribution shows the difference between the bulk charge and the material that is in flight. The darkly shaded (dark blue) regions indicate particles that are in free flight and the rest of the particles are part of the bulk charge. A tolerance function can be applied in order to make the bulk charge stand out. Figure 46 shows the effect of the tolerance function on the data.

Once the particle probability distribution data set with or without the tolerance function is plotted the surface tracking process can commence. The detailed surface tracking instructions can be found in section 16.14 in the appendix.

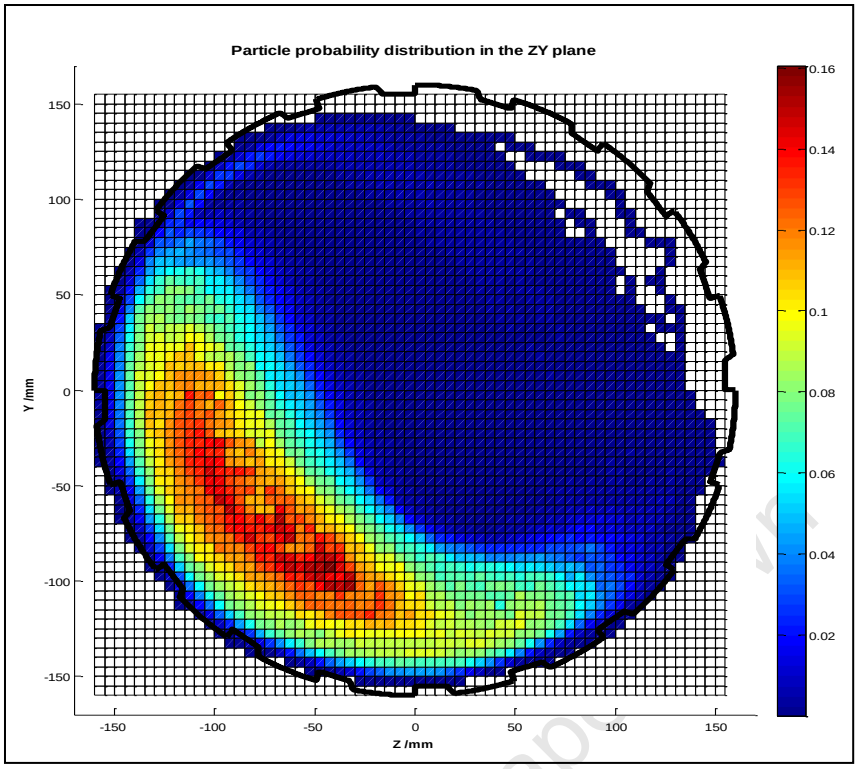

Figure 45: Particle probability distribution data at 55% mill speed, 40% mill fill and 6mm lifter without tolerance function

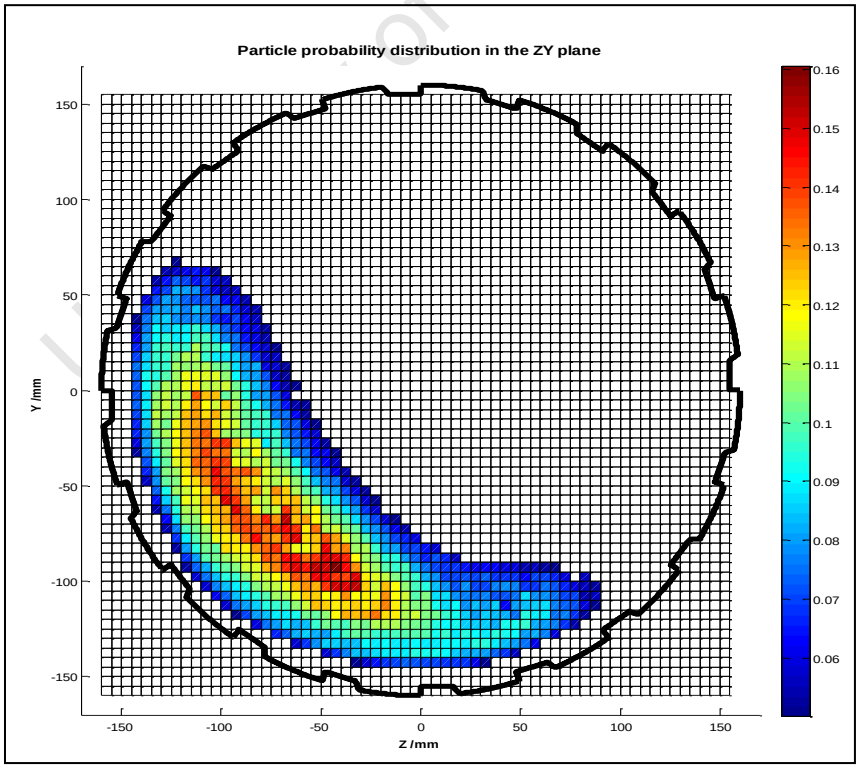

Figure 46: Particle probability distribution data at 55% mill speed, 40% mill fill and 6mm lifter with tolerance function

In order to improve repeatability of the data and to extract a surface, the data is smoothed using a spline routine in MatLab. The smoothness and accuracy of the processed data is dependent on the x-value increments that are chosen for the spline function. If the difference between the x-values is large (50 units), then only a few data points will result from the spline routine, as shown by the dots following the charge free surface (white dots) in Figure 47. The white data points represent the charge free surface. The charge free surface cannot be defined by a few data points, because there are still too many unknowns between the plotted values.

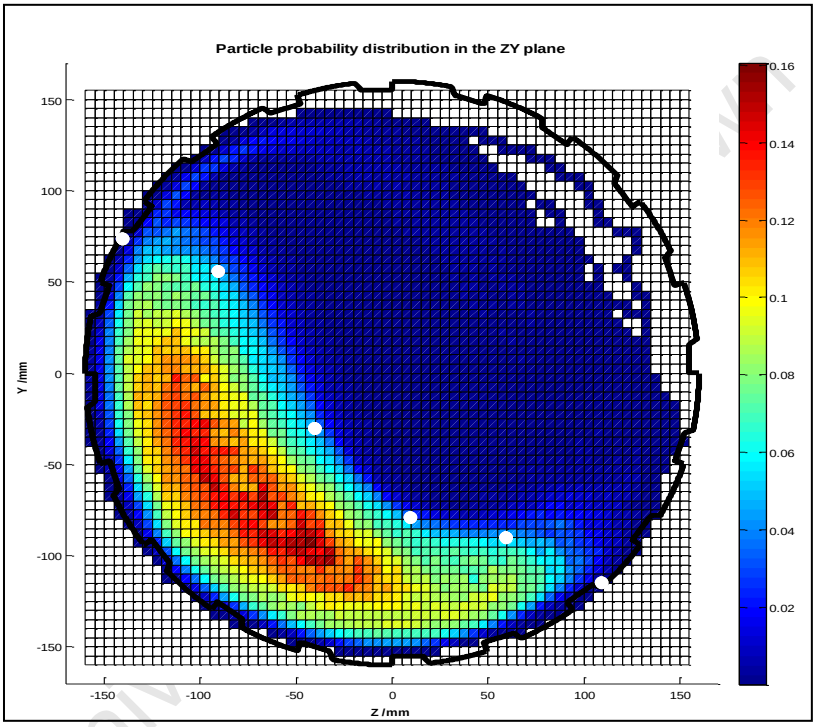

Figure 47: Charge free surface spline fit with 50 unit increments

Increasing the x-value increments will increase the amount of data available for the charge free surface, but increasing the increments too much will result in an uneven surface as shown in Figure 48. Figure 48 shows the charge free surface with a spline fit with an increment value of 1 unit. It is desired to have to have enough data to represent the charge free surface while keeping the surface smooth. By trial and error it was determined that an increment value of 10 units results in a smooth and representative plot of the charge free surface, as can be seen in Figure 49. Figure 49 represents the charge free surface with a spline fit with an increment value of 10 units.

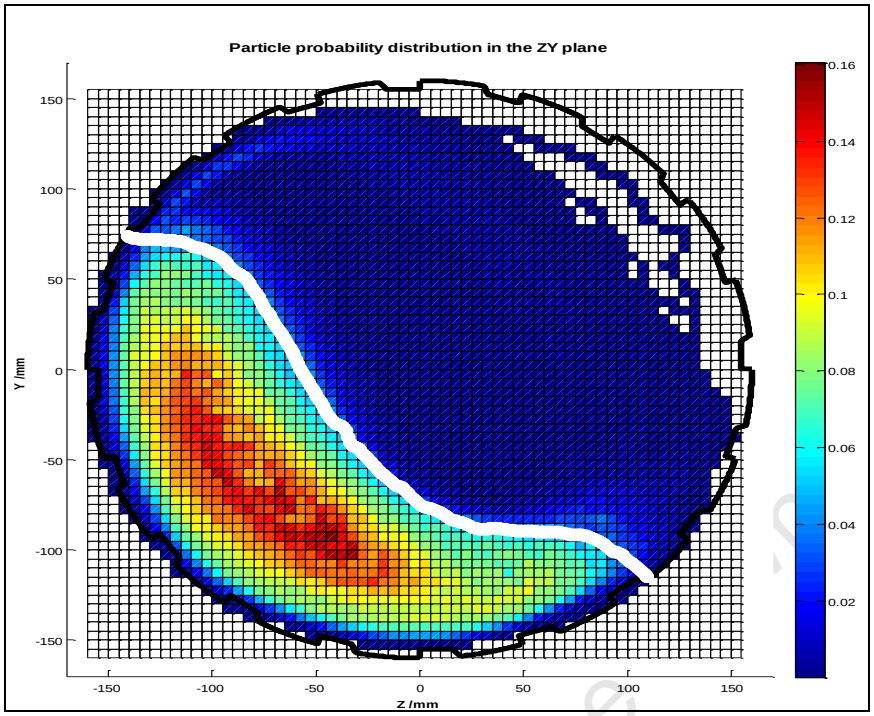

Figure 48: Charge free surface at 55% mill speed, 40% mill fill and 6mm lifter spline fit with 1 unit increments

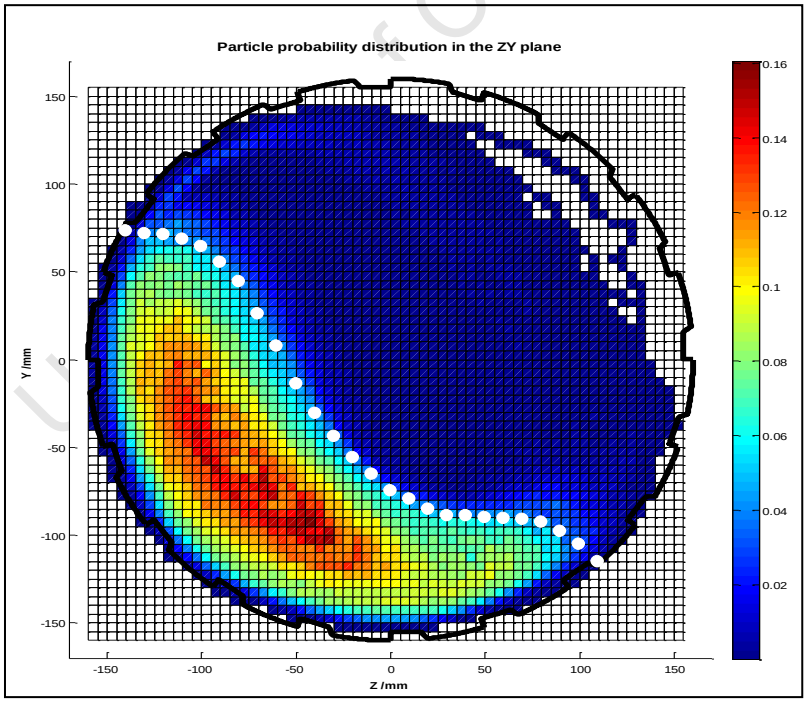

Figure 49: Charge free surface at 55% mill speed, 40% mill fill and 6mm lifter spline fit with optimal increments (10 units)

8.1.2 Equilibrium surface

The equilibrium surface of the charge is the surface along which the particle velocities are zero. It is the turning point for the particles, where they transition from a region where particles are being lifted along the mill shell to a region where particles are cascading towards the charge toe area and vice versa. The transverse velocity magnitude plot, shown in Figure 50, is needed to determine the equilibrium surface. The dark shaded (dark blue) areas indicate the location of the equilibrium's surface. However, the data extracted from Figure 50 should be supplemented by the velocity vectors and magnitude shown in Figure 51.

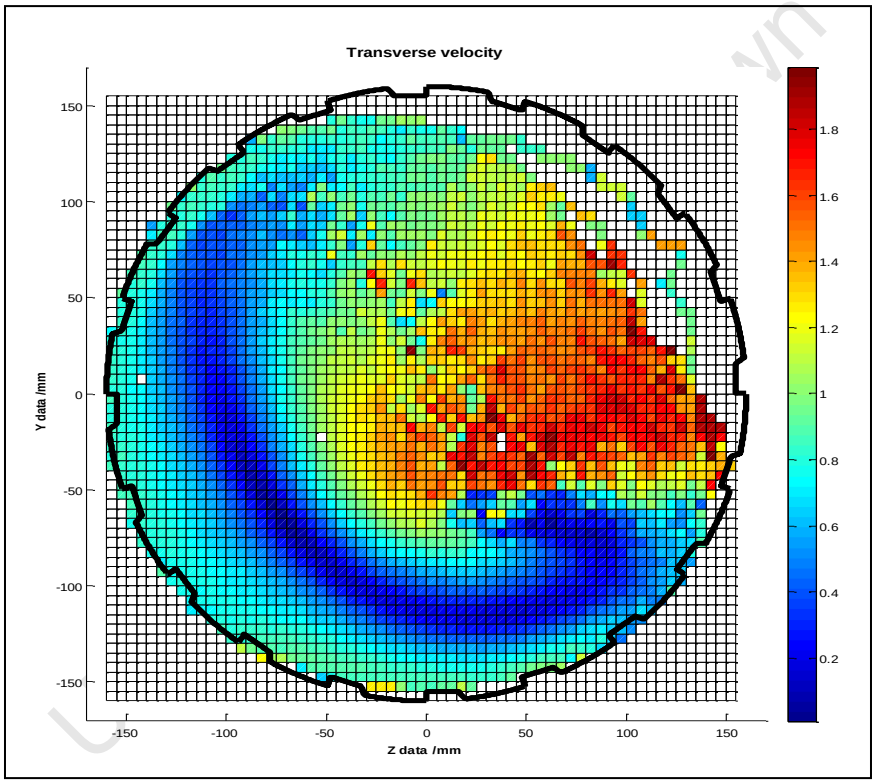

Figure 50: Velocity magnitude plot

The data in Figure 51 is generated by using a function in Matlab called 'quiver', which takes in the y and z velocity components and then plots the velocity vectors. It is easier to locate turning points by combining data presented in the velocity vector form (Figure 51) and magnitude plot (Figure 50) which are then used simultaneously to trace the equilibrium surface. The plot showing a combination of the two is presented in Figure 52.

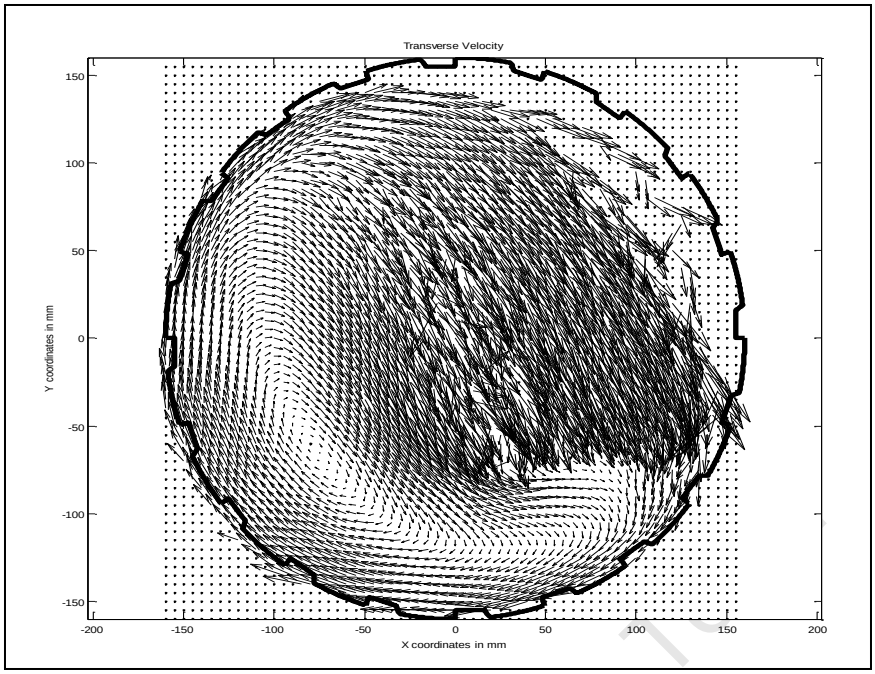

Figure 51: Velocity plot showing direction and magnitude

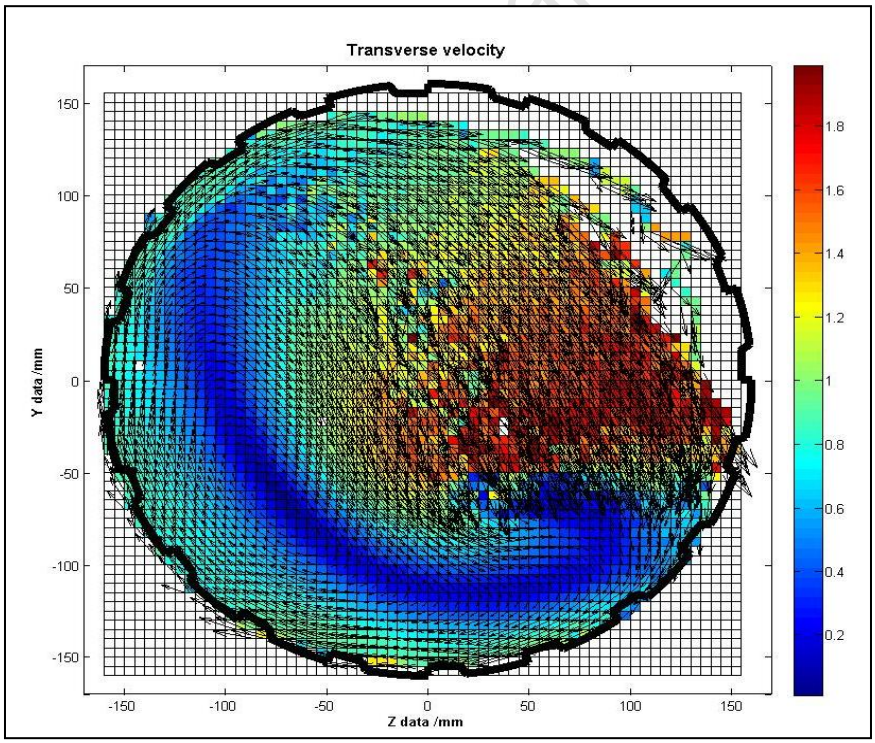

Figure 52: Combining velocity magnitude and direction plot

The procedure used to extract the equilibrium surface is the same as that employed in the location of the charge free surface.

A spline routine is then used to enable consistency in the extraction of the surface, similar to the equilibrium surface. Using an increment value of 10 units, an example of the resultant equilibrium surface (yellow dots) is shown in Figure 53. It should be noted that if the x-value increment is too high or too low, the equilibrium surface generated will not be smooth. The boundaries of the equilibrium surface are guided by the charge free surface. Alternatively the equilibrium surface would follow the dark blue regions. However, this will lead to an unrealistic equilibrium surface in the toe region.

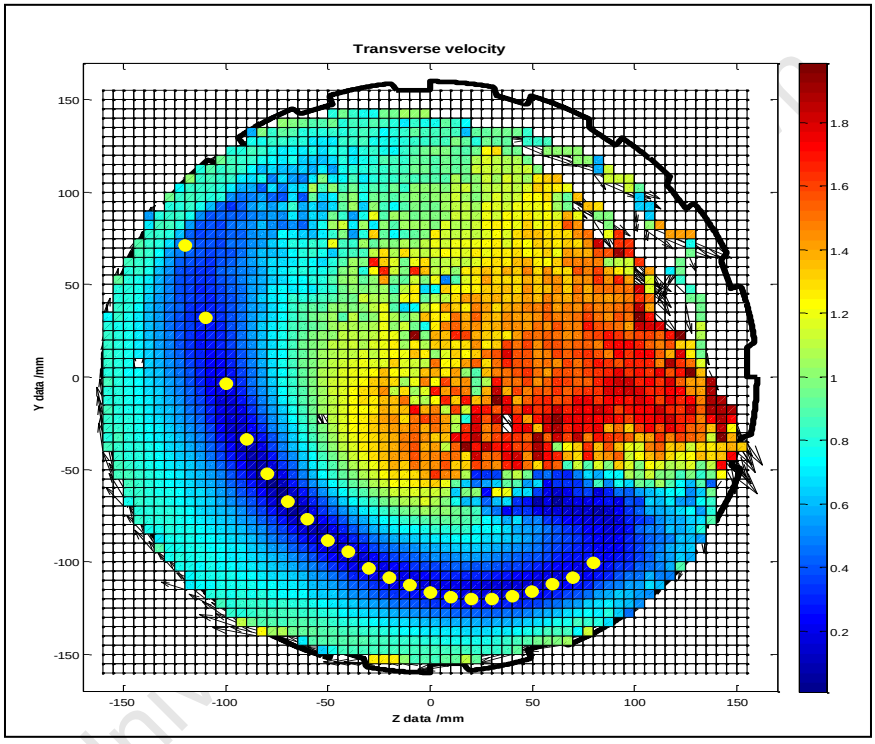

Figure 53: Equilibrium surface spline fit with optimal increments (10 units)

9 Data extraction procedure

The equilibrium and the charge free surfaces are essential in extracting the experimental data and surface characteristics important to the fundamental velocity profiles. Figure 54 shows the classification of the features deemed important.

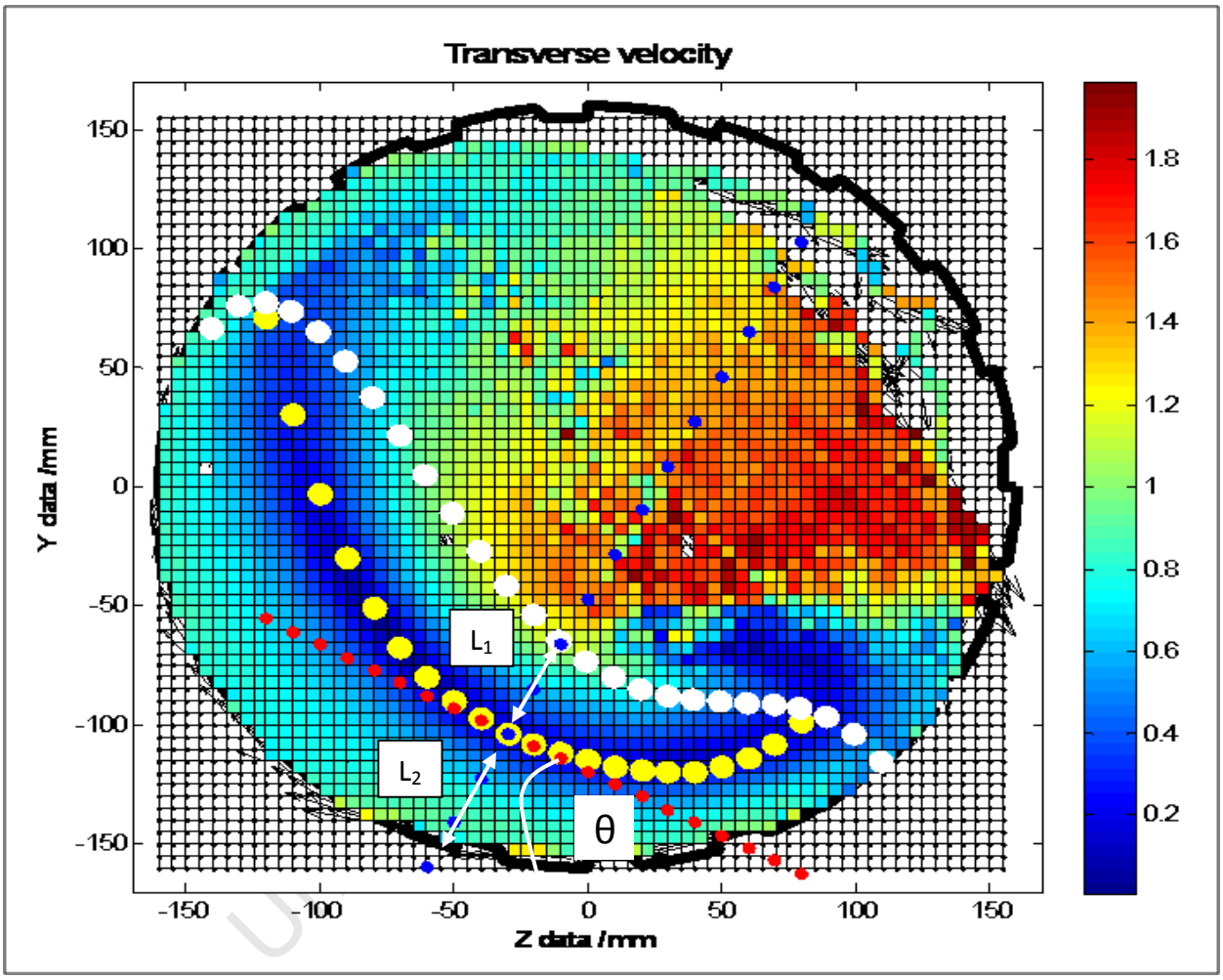

Figure 54: Velocity profile indicating the area of interest

The surface characteristics refer to the angle (θ) which describes the inclination of the surface perpendicular to the equilibrium surface and the distance between the equilibrium surface and the inner mill diameter. The angle theta is dependent on position of the extraction line along the equilibrium surface. It does incorporate the lifter height and is described as the length of region 2 (L_2). Included in the surface characteristics is the distance from the charge free surface to the equilibrium surface, which is the length of region 1 (L_1). The angle (θ) is common for both

surfaces, because the reference frames moves along the equilibrium surface. The angle theta, length of region 1 and region 2 are illustrated in Figure 54.

9.1 Data fitting

Extracting the necessary data from the experimental results requires the equilibrium and charge free surface to be empirically described by a fitted equation. L_1, L_2 and θ require the surfaces to be mathematically described as equations so that critical intersection points and gradients can be determined.

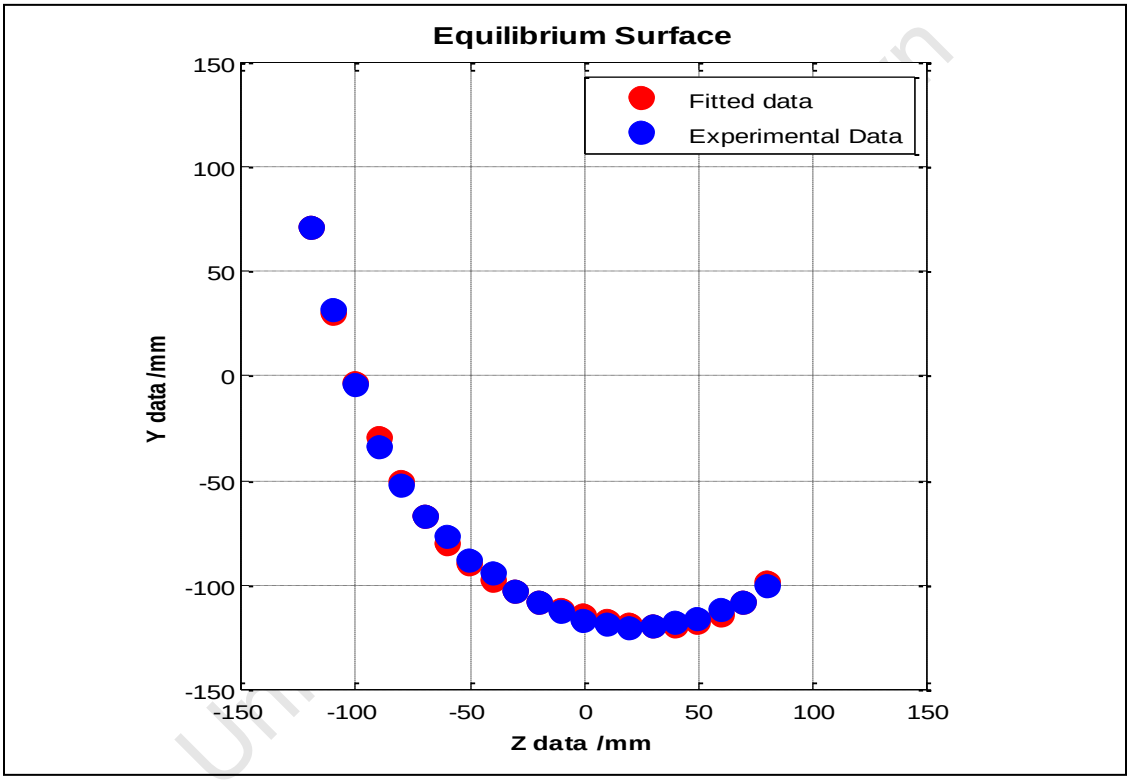

Figure 55: Experimental and fitted data for equilibrium surface

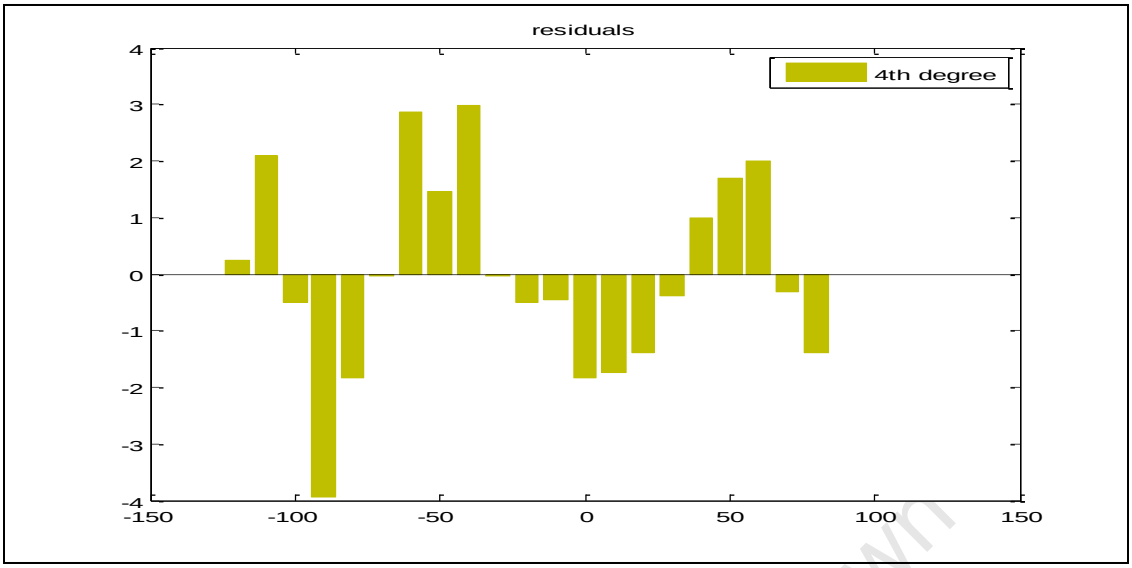

Figure 56: Residual of equilibrium surface plot comparison

The equilibrium and charge free surface are fitted to a 4th degree polynomial. The 4th degree polynomial describes the experimental data well as indicated in Figure 55. The difference between the 4th degree polynomial and other higher degree polynomials is minimal, therefore the 4th degree polynomial was chosen. The light (red) and dark (blue) dots in Figure 55 represent experimental data and the data fitted using a 4th order polynomial. There is no significant difference between the experimental and fitted data. Figure 56 shows the residual plots. The goodness of the fit of the polynomial to the data can be seen in Figure 56. The fit is reasonably good, because the differences between the data sets are equally spread across the zero line.

The same fitting process was applied on the charge free surface. Figure 57 shows the experimental and fitted data represented by the dark (blue) and light (red) dots, respectively. The difference between the fitted and experimental data is negligible, but there are areas with small inconsistencies like the data between -150mm and -100mm x-axis.

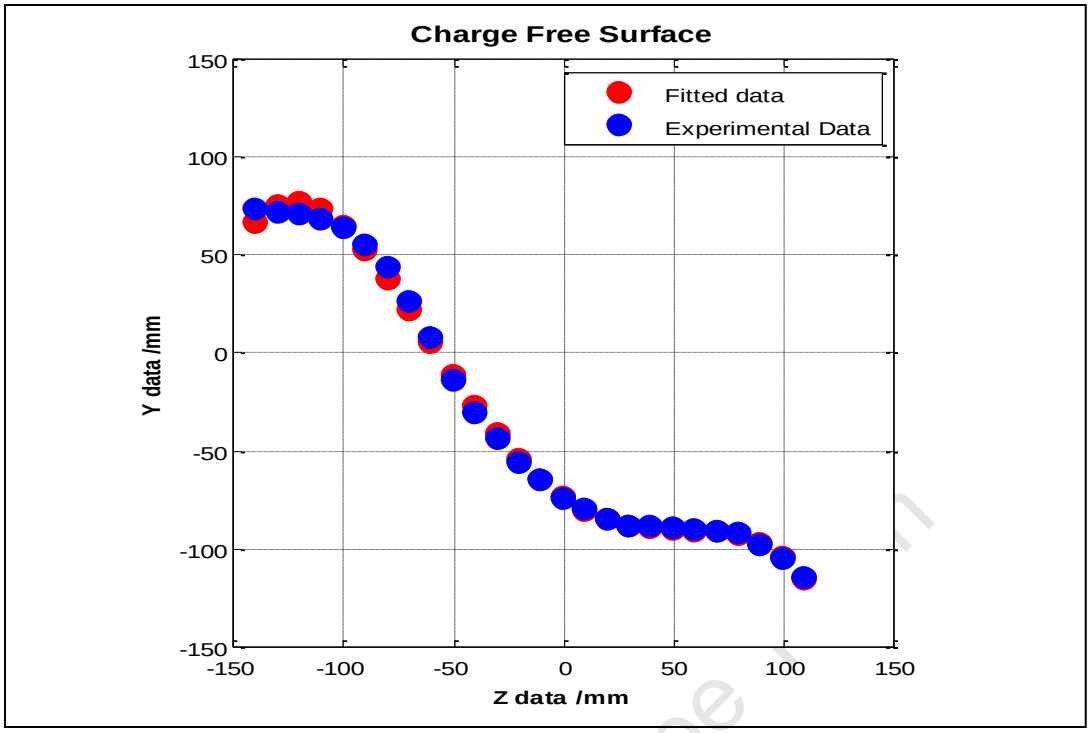

Figure 57: Experimental and fitted data for charge free surface

The residual plot for the charge free surface in Figure 58 show large differences between the fitted and experimental data initially but this reduces significantly for the data for the chaotic regions of the mill. The fit is good, because the differences between the data sets are equally distributed across the zero line. There if no bias towards one side.

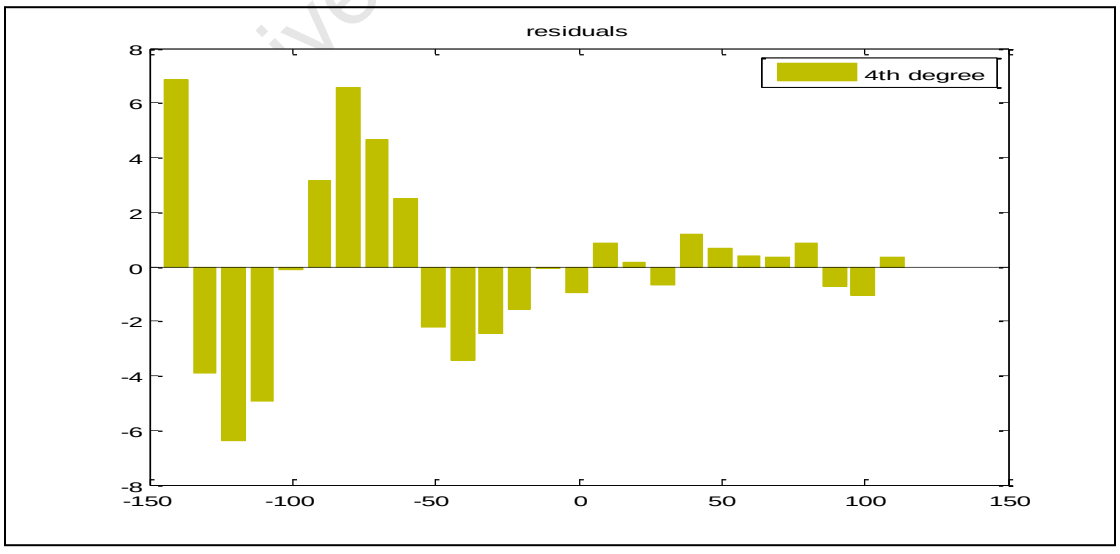

Figure 58: Residual of charge free surface plot comparison

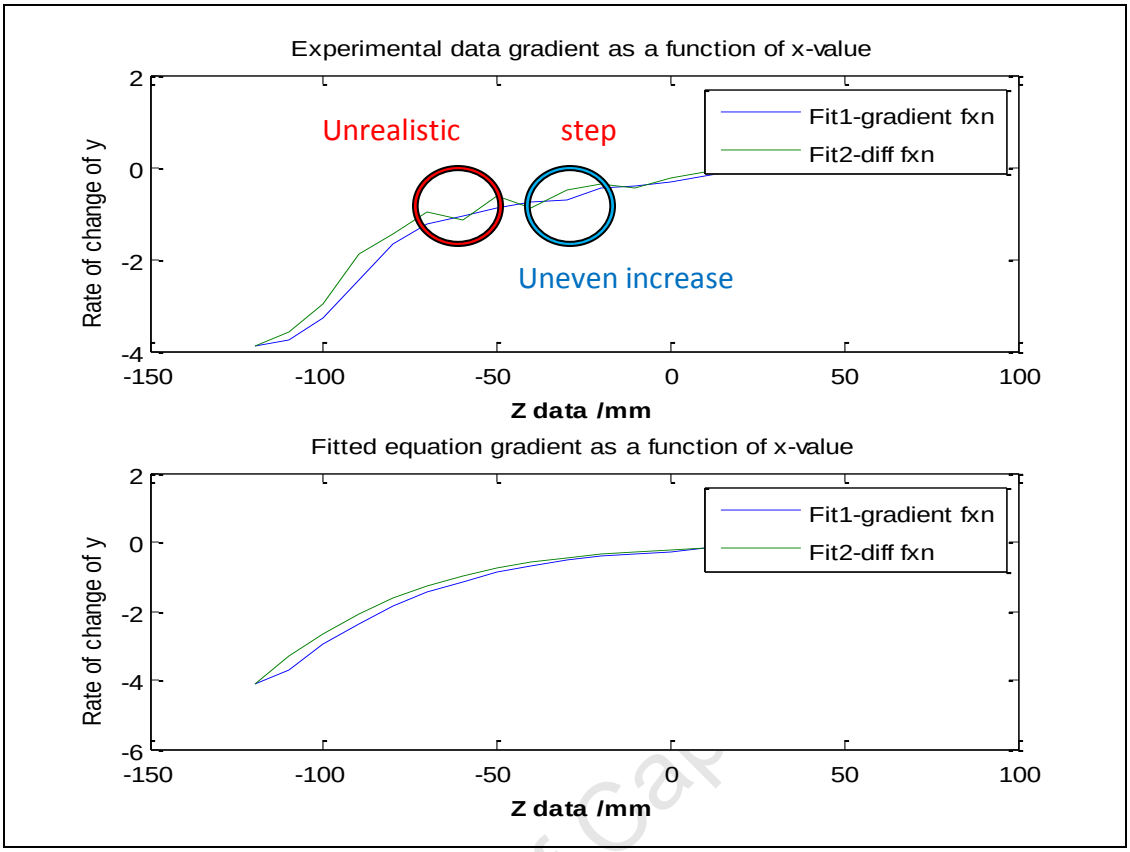

Figure 59: Gradient as a function of mill diameter

In addition to determining the intersection points by defining the surfaces as equations, the gradient of each surface at any point can be obtained. The gradient of the fitted polynomial is smoother than that of the experimental data, as shown in Figure 59. The gradient of the fitted and experimental data was determined using two different functions. The 'diff' function takes the difference in y and z data and then divides them to produce a gradient. The 'diff' function is a simplified way of getting the gradient. The other method is using the gradient function. The 'gradient' function allows for a smoother set of data and it does not include unrealistic step changes in gradient, as indicated in Figure 59.

9.2 Characteristic Data

The procedure used to describe and extract data from the equilibrium and charge free surface is similar. Therefore the equilibrium surface will be used to describe the data extraction process. The variables of interest are which are discussed in the sections that follow are angle of incline (θ) and length of region 2 (L_2).

In order to determine the angle of incline and the length of region 2 the tangent and perpendicular lines to the equilibrium surface and inner mill diameter need to be found.

The different lines of orientation that are needed to determine the desired charge characteristics are the tangent line to the equilibrium surface, tangent line to the mill shell and the perpendicular line to the tangent to the equilibrium surface

9.2.1 Angle of incline (θ)

The angle of incline is a variable that is required in extracting the velocity model. It can be used to determine the magnitude of each force acting on a particle. The angle of incline measures the angle that a line tangential to the equilibrium surface would have with the horizontal tangent to the mill shell. In Figure 60 the equilibrium surface is represented by the yellow data points (yellow dots). The red data set (red dots) is the tangent to the equilibrium surface. The horizontal tangent to the mill shell is represented by the z-data axis. The incline angle is illustrated as θ in Figure 60.

The gradient of the equilibrium surface tangent was determined by using the 'gradient' function in Matlab. The 'gradient' function allowed all the gradients along the equilibrium surface to be determined. A point on the equilibrium surface is chosen by choosing an x-value and then calculating the y-value with the fitted surface equation. With a set point and a gradient the tangent's straight line equation could be determined. The straight line equation was not needed to calculate the angle of incline (θ), but it was done so that the line could be illustrated (Figure 60). In order to calculate θ only the gradient (m_{tan}) of the tangent line is needed. The following relationship was used to:

$\tan\theta = \Delta y/\Delta x$ but $\mathrm{m}_{\tan} = \Delta y/\Delta x$

$\therefore \tan\theta = m_{tan}$

$\therefore \theta = \tan^{-1}(m_{tan})$

The resultant angle had a negative value, because θ is usually measured from right to left and not left to right. Therefore the angle needed to be adjusted when appropriate. Beyond

approximately 50 mm on the Z-axis the angle adjustment changes, because of the line's orientation. An example of such a situation can be seen in Figure 61, where the chosen point of the equilibrium surface is at approximately 50 mm.

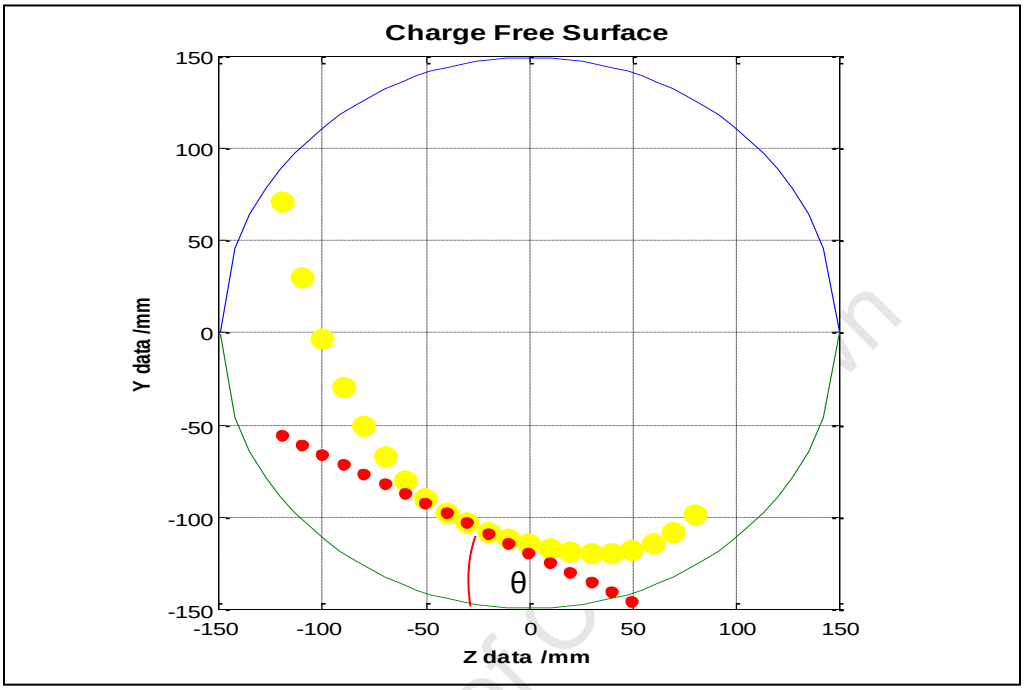

Figure 60: Equilibrium surface and tangent line at 70% mill speed, 30% mill fill and 6mm lifter

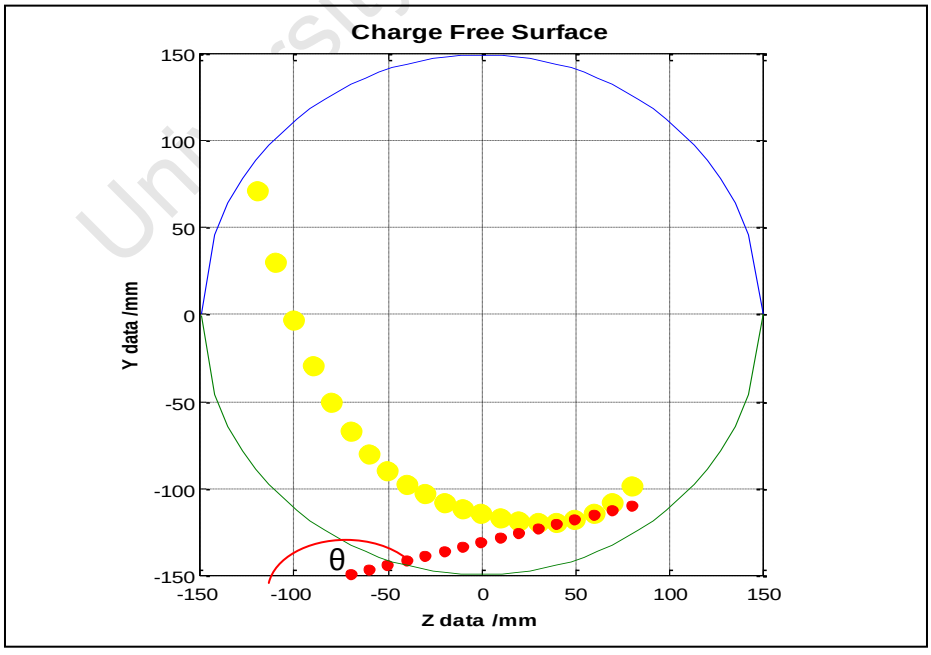

Figure 61: Equilibrium surface and tangent line at 70% mill speed, 30% mill fill and 6mm lifter

9.2.2 Length of region 2

The length of region 2 (L_2) is vital to the fundamental velocity profile, because it determines the length over which the velocity profile is integrated. The length of region 2 is the distance between the equilibrium surface and the inner mill diameter. The length of region 2 (L_2) is depicted in Figure 62. It can also be seen that L_2 is dependent on the development of the perpendicular line to the equilibrium surface tangent.

The perpendicular line is dependent on the tangent to the equilibriums surface. The relationship that binds both surfaces is their gradients and can be expressed as follows:

$$m_{tan}\ m_{\perp} = -1$$

$$\therefore m_{\perp} = {}^{-1}/_{m_{tan}}$$

With the gradient and point chosen for the equilibrium tangent line an equation for the perpendicular line can be developed. The resultant perpendicular line can be seen in Figure 62. Then using the characteristic equation of the inner mill diameter and the perpendicular line the intersection point between the line and mill shell can be determined. The lifter height is incorporated into the inner mill diameter equation, because the lifter height will decrease the inner diameter measured from the tip of the lifters to the centre of the mill.

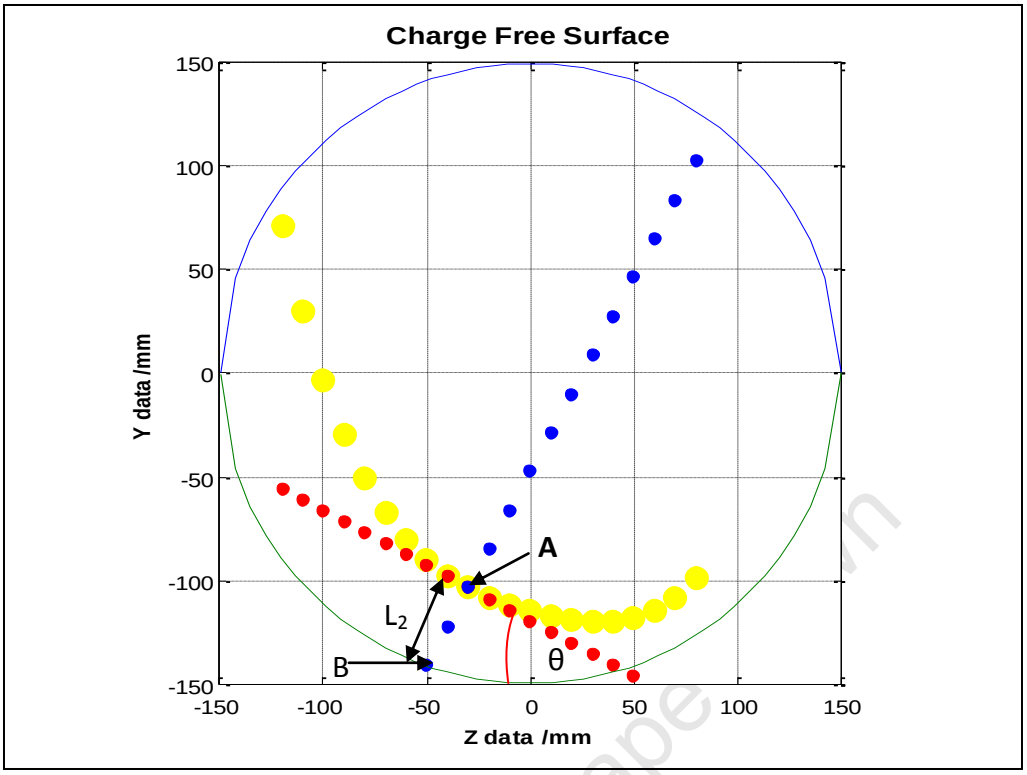

Figure 62: Equilibrium surface, tangent and perpendicular line at 70% mill speed, 30% mill fill and 6mm lifter

In Figure 62 point A represents the intersection point of the tangent and perpendicular line to the equilibrium surface. Point B shows the intersection point of the perpendicular line with the inner mill diameter (green and blue circle). The length of region 2 (L_2) is determined from point A and B. The following equation is used to determine L_2:

$$L_2 = \sqrt{(x_A - x_B)^2 + (y_A - y_B)^2}$$

The algorithm used to determine the characteristic data of the charge is used for the experimental data extraction method. The method used above for the characteristic data gives the desired reference frame for the experimental data extraction. Therefore this algorithm will be used to define the coordinate system of the data extraction, which will be discussed in the next section.

10 Data Analysis

The fundamental velocity profile model for the mill charge needs to be validated with experimental data. The comparison between the experimental and model data can highlight any areas of agreement and/or disagreement. The experimental data in this work was obtained using the Positron Emission Particle Tracking (PEPT) system. The PEPT system is able to provide data for particle probability distribution and velocity of the particle being tracked, as discussed earlier. The data shown in Figure 54, Figure 64 and Figure 65 are examples of the collected data for this research. The data is only for illustrative purposes and not for analysis.

10.1 Required data

The required data for the validation of the fundamental velocity profile model is based on the region between the shell and equilibrium surface (en masse region). The area of interest has been discussed under the theory section and is given by the blue line in Figure 63.

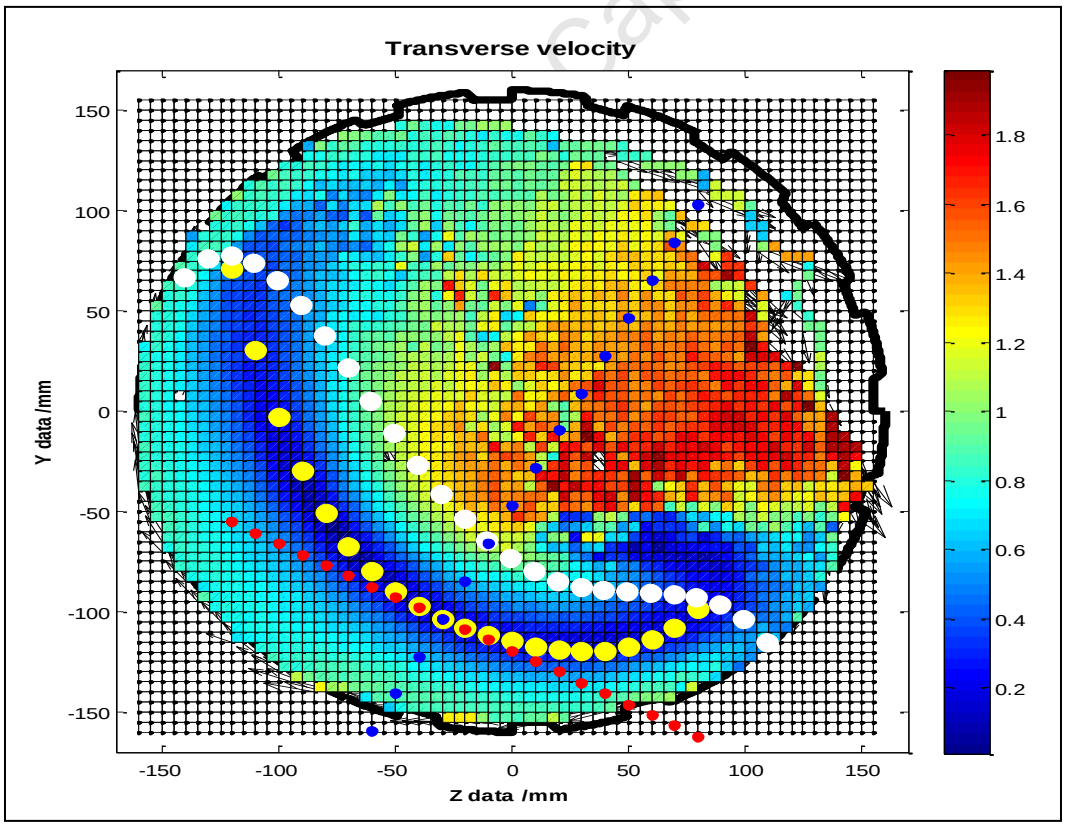

Figure 63: Velocity profile indicating the area of interest (illustrative)

The blue line is perpendicular to the equilibrium surface, which is the yellow line in Figure 63. The blue line, from which the required data needs to be extracted, is oriented in such a manner so that the fluid flow is perpendicular to the y-axis of the coordinate system. The proposed coordinate system can be illustrated by the blue and red line in Figure 63. The red line in Figure 63 is the tangent to the equilibrium surface. Nevertheless the blue line is the extraction line that will be referred to in the rest of this section.

10.2 Data handling

The experimental data that is available for analysis has been prepared by a Matlab code that converts location and time data to velocity data (Morrison (2011)). The velocity data is then put through another series of Matlab codes that produce all the information (particle probability distribution and transverse velocity data) that is needed for an analysis, which was first used and developed by the Department of Physics at the University of Cape Town (UCT). The processed data ranges from the x-component velocities to tangential velocities of the particles, so that different plots can be produced to highlight different areas of interest. The tangential velocity of the particle is of particular interest in the comparison between the fundamental and experimental results.

10.3 Velocity profile data extraction

The required data for the validation of the fundamental velocity profile model is extracted from the blue line in Figure 63. The data extraction line (blue line) moves along the equilibrium surface so that pertinent data can be extracted from most of the charge. The data extraction line is always perpendicular to the equilibrium surface and hence its tangent line (red line). The results of the data extraction along a line similar to the blue line can be seen in Figure 64. The format of the data in Figure 64 was suggested by Govender et al (2010). The data extracted in Govender et al (2010) was used to develop an expression for shear rate. The extraction line takes data from flow region 1 and 2. The evidence of this is the fluid flow direction changing across the equilibrium surface. Even though flow region 2 remains the area of interest.

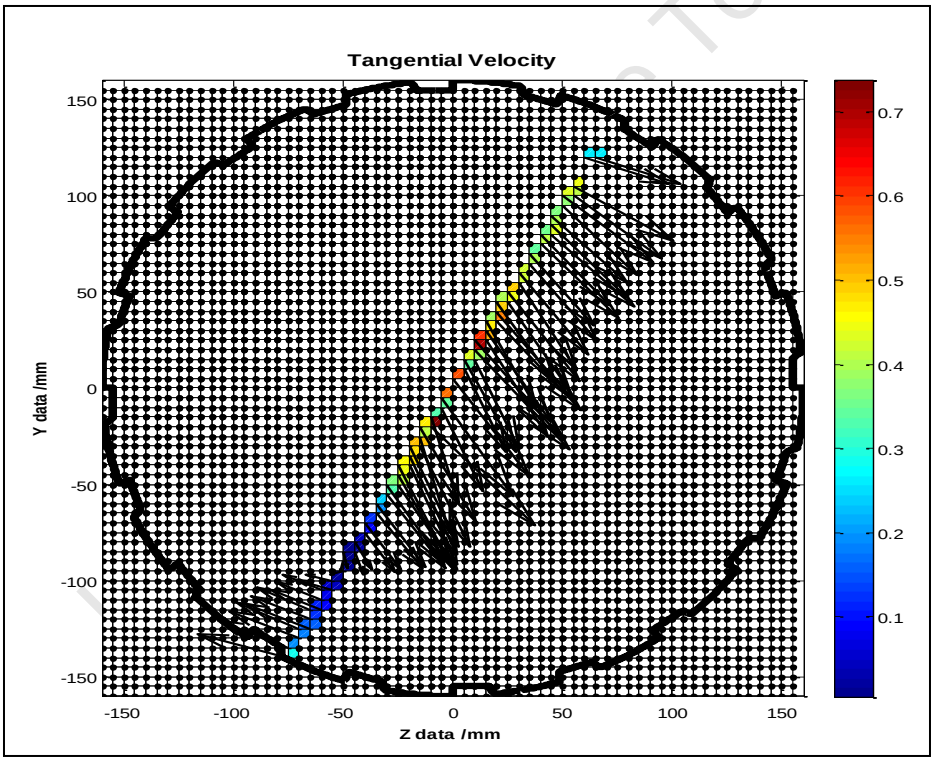

Figure 64: Data extraction for velocity profile (illustrative)

10.4 Data formatting for data comparisons

The data extracted from the blue line and shown in Figure 64 can be further represented as a velocity plot as a function of the distance from the mill shell, as can be seen below. A similar plot was used for the velocity data as discussed by Govender et al (2010), where this approach was used to determine the shear rate of the system.

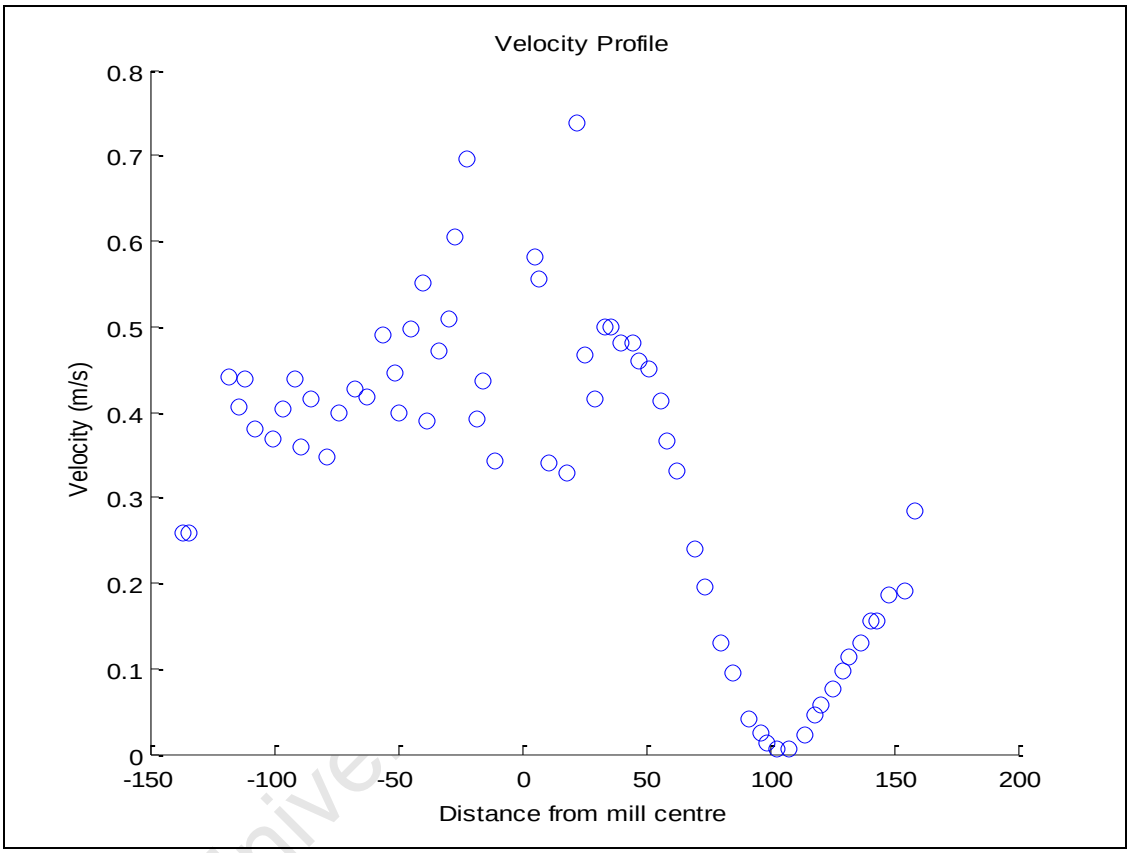

Figure 65: Velocity profile along data extraction line (illustrative)

The experimental data is converted in the format seen in Figure 65, because the model's output will be similar to this format. For the direct comparison between the model and experimental data sets, the model data is plotted on the same axis as the experimental data.

11 Velocity profile model

The velocity profile model has been developed by using the general Navier-Stokes equation. The reduced general Navier-Stokes equation is described as the following equation:

$$\rho \frac{\mathrm{D}\mathbf{v}}{\mathrm{D}t} = \rho \boldsymbol{g} - \boldsymbol{\nabla} P + \mu \boldsymbol{\nabla}^2 \mathbf{v}$$

For a detailed derivation and explanation of the Navier-Stokes equation please refer to section 16.2 in the appendix. The following assumptions were used to develop the velocity profile:

1. Laminar flow
2. Incompressible flow (constant density)
3. Constant viscosity
4. Newtonian fluid

Implementing the assumptions reduced the general Navier-Stokes equation to a velocity profile:

$$v_x = \left(\rho g \sin\theta + \frac{dP}{dx} + F_f(y)\right) \frac{(y^2 - L_2 y)}{2\mu} + \frac{v_{mill}\, y}{\mathrm{L}_2}$$

The detailed velocity profile development can be found in section 16.1 in the appendix. The velocity profile will be compared to the PEPT experimental data.

12 Results

12.1 Introduction

This chapter presents the outcomes of the experimental work performed to assess the influence of lifters on the performance of the tumbling mill using PEPT. The first analysis performed was the comparison of the velocity profile obtained from the model developed from granular flow theory to that obtained from experimental data. The second set of results focus on the influence of lifter on the velocity profile that was produced by the PEPT data. The third set of results shows the influence of the lifters on toe and shoulder behaviour at different operating conditions.

12.2 Effect of lifter height on the velocity profile

The data used to evaluate the effect of lifter height on the velocity profile analysis was the experimental data collected from the PEPT experiments. A detailed breakdown of the PEPT experiments is shown in Table 8. To ensure there was consistency in the evaluation the data was extracted from approximately the same areas. In order to adhere to these constraints the areas in the different zones, from which the data was extracted was held constant. The three different zones used of the data extraction are illustrated in Figure 66. The analysis was performed to evaluate the influence of lifter height at different % volumetric filling and mill speeds. The purpose of the analysis is to observe and identify any possible relationship between lifter height and velocity profile. Therefore the velocity profiles at different lifter heights are plotted on the same axis. The velocity profile data is shown in plots where the different lifter heights are represented by different symbols. The 10 mm, 6 mm, 3 mm and 1.5 mm lifter heights are represented by a cross (X), square (□), diamond (◊) and a dashed line (- - -), respectively.

Table 8: Detailed breakdown of PEPT experiments including time stamps

Experiment no.	Mill speed	Mill fill	Lifter height	Day	Time start	Time end	Duration
1	85%	20%	10 mm	1	10:52	11:37	00:45
2	70%	20%	10 mm	1	11:46	12:32	00:46
3	55%	20%	10 mm	1	12:36	13:23	00:47
4	85%	30%	10 mm	2	09:41	10:29	00:48
5	70%	30%	10 mm	2	10:32	11:28	00:56
6	55%	30%	10 mm	2	11:31	12:24	00:53
7	85%	40%	10 mm	2	17:44	18:31	00:47
8	70%	40%	10 mm	2	18:34	19:21	00:47
9	55%	40%	10 mm	2	19:23	20:11	00:48
10	85%	20%	6 mm	3	09:50	10:39	00:49
11	70%	20%	6 mm	3	10:41	11:31	00:50
12	55%	20%	6 mm	3	12:01	12:44	00:43
13	85%	30%	6 mm	3	13:46	14:33	00:47
14	70%	30%	6 mm	3	14:34	15:33	00:59
15	55%	30%	6 mm	3	15:36	16:24	00:48
16	85%	40%	6 mm	3	17:00	17:48	00:48
17	70%	40%	6 mm	3	17:50	18:39	00:49
18	55%	40%	6 mm	3	18:42	19:37	00:55
19	85%	20%	3 mm	6	10:48	11:35	00:47
20	70%	20%	3 mm	6	11:39	12:27	00:48
21	55%	20%	3 mm	6	12:29	13:20	00:51
22	85%	30%	3 mm	6	14:25	15:14	00:49
23	70%	30%	3 mm	6	15:18	16:05	00:47
24	55%	30%	3 mm	6	16:08	16:56	00:48
25	85%	40%	3 mm	6	17:29	18:21	00:52
26	70%	40%	3 mm	7	10:21	11:26	01:05
27	55%	40%	3 mm	7	11:32	12:21	00:49
28	85%	20%	1.5 mm	6	18:23	19:16	00:53
29	70%	20%	1.5 mm	6	19:18	20:06	00:48
30	55%	20%	1.5 mm	7	12:24	13:12	00:48
31	85%	30%	1.5 mm	7	13:16	14:05	00:49
32	70%	30%	1.5 mm	7	14:05	14:55	00:50
33	55%	30%	1.5 mm	7	15:00	15:46	00:46
34	85%	40%	1.5 mm	4	10:10	11:04	00:54
35	70%	40%	1.5 mm	4	11:10	12:00	00:50
36	55%	40%	1.5 mm	4	12:20	13:10	00:50

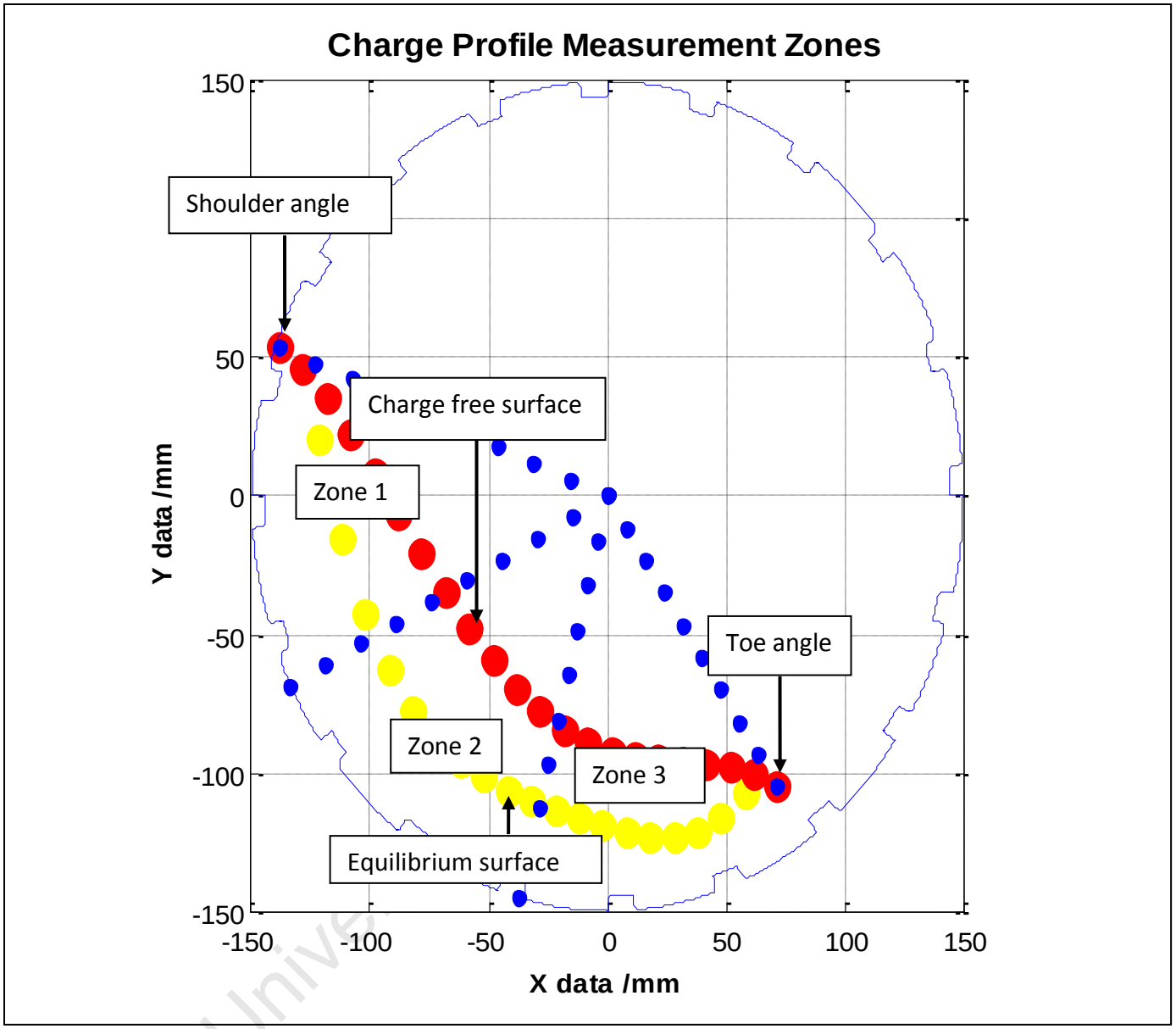

Figure 66: Different zones of the mill charge

12.2.1 Mill volumetric filling at 20%

To get an overview of the entire charge area analyzed the velocity profiles from the different zones are presented in the same graph as shown in Figure 67. This section shows all the data at a mill volumetric filling of 20% at different mill speeds and lifter heights.

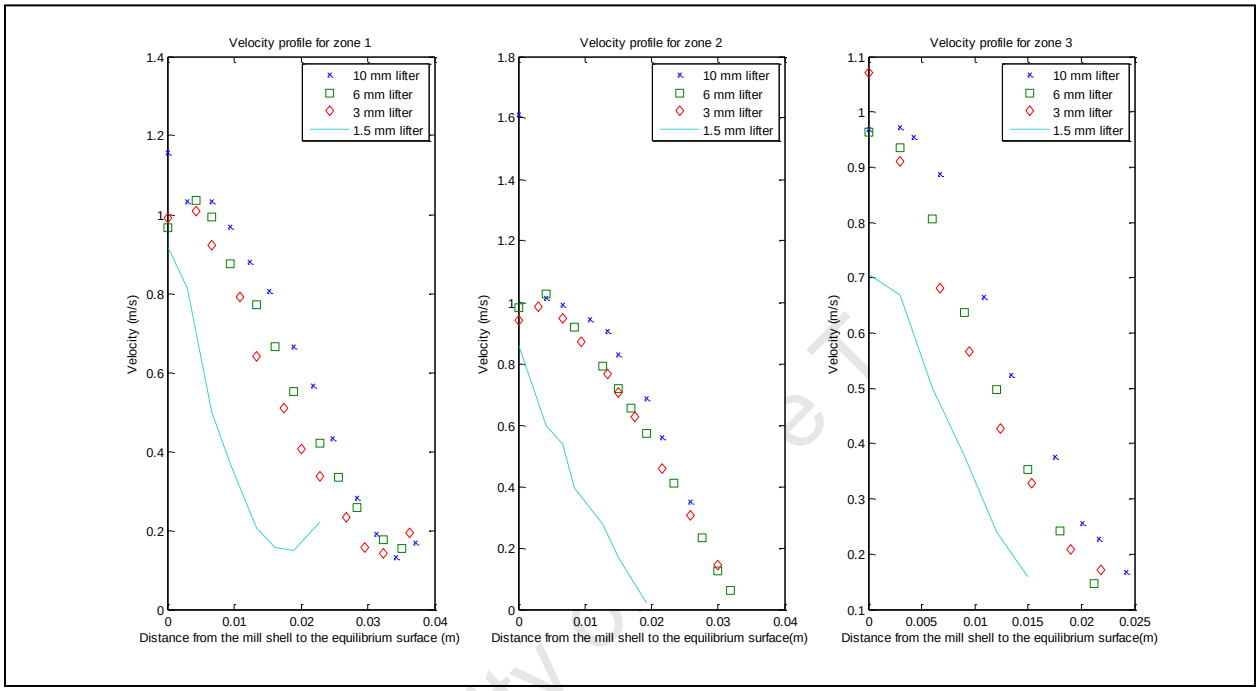

Figure 67: Velocity profile analysis for 20% mill fill and 85% mill speed with varying lifter heights

It was observed from Figure 67, that the 10 mm lifter height produced velocities with higher magnitudes when compared to the other lifter heights for the mill that was operating at 20% volumetric filling and 85% critical speed. The local velocities decreased with a decrease in lifter height. A consistent decrease was observed between the lifter height of 10 mm to 6 mm and between 6 mm and 3 mm but a significant shift was seen between the 3 mm and 1.5 mm lifter.

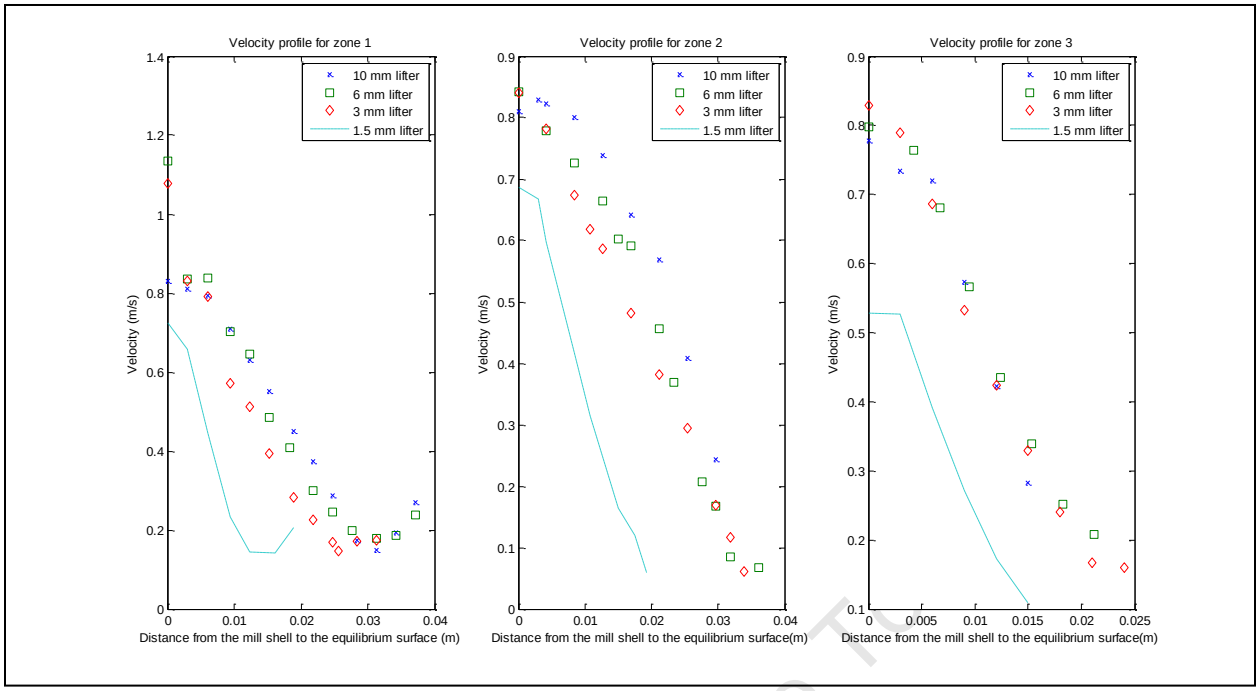

Figure 68: Velocity profile analysis for 20% mill fill and 70% mill speed with varying lifter heights

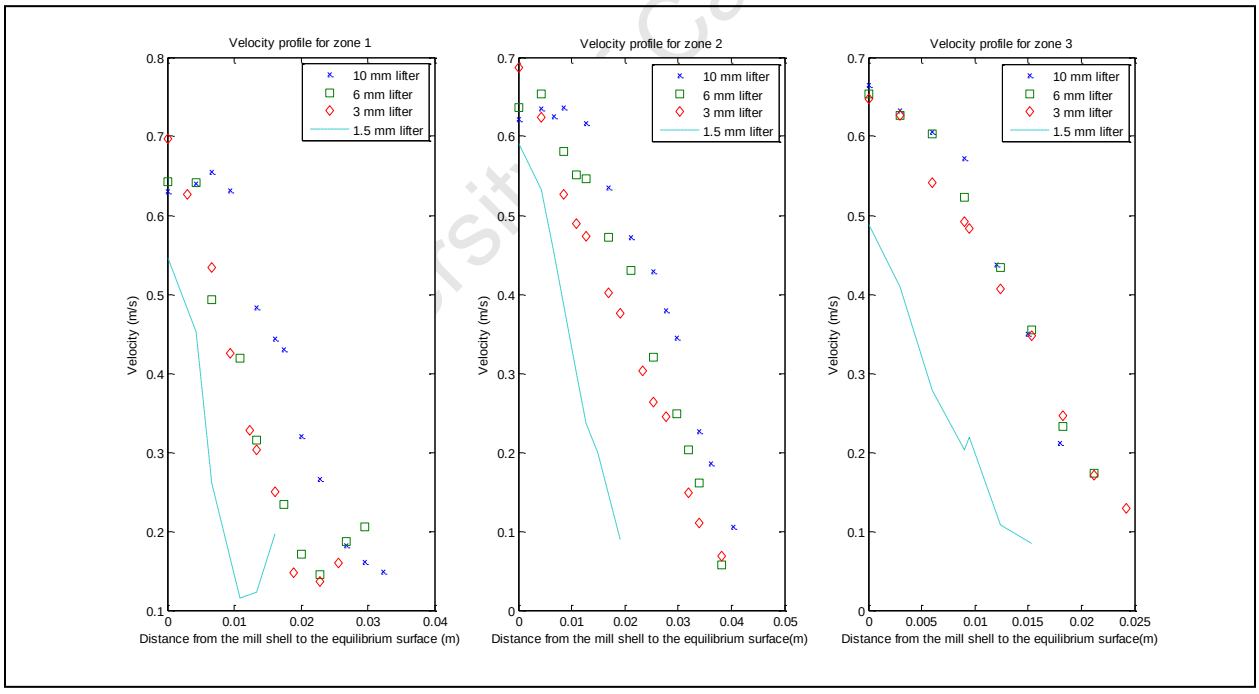

Figure 69: Velocity profile analysis for 20% mill fill and 55% mill speed with varying lifter heights

The velocity profile data at 70% mill speed in zone 2 and zone 1 (left and middle plots) have the same trends as the data at 85% mill speed as shown in Figure 68. The exception is the 10 mm

lifter behaviour in zone 1, where the 10 mm lifter height data has approximately the same velocities as the 6 mm lifter. Zone 3 does not have the same trend as zone 1 and zone 2, because the 10 mm, 6 mm and 3 mm lifters have approximately the same velocities along the en masse region. The lowest velocity in all the zones belongs to the 1.5 mm lifter, which is the same observation made at 85% mill speed.

Operating the mill at 55% mill speed produces velocity profile trends as can be seen in Figure 69. The velocity profile trends in zone 2 (middle plot) are the same as those at 85% mill speed. The data for zone 1 (left plot) are similar, except the velocities for the 6 mm and 3 mm lifters are approximately the same. The velocity profiles in zone 3 (right plot) show that the velocity for 10 mm, 6 mm and 3 mm lifters are the same. The most obvious trend between the different zones is the lowest velocity belonging to the 1.5 mm lifter.

Additionally the gradient of the velocity profiles of the different lifter heights for a particular zone are the same for speeds of 55%, 70% and 85% critical at a mill volumetric filling of 20%.

12.2.2 Mill volumetric filling at 30%

The results in this section show the data extracted from the mill operating at 30% mill volumetric filling and at different mill speeds and lifter heights.

The data in Figure 70 shows velocity profiles at 85% mill speed and 30% mill filling. The trends in Figure 70 are similar to those found in Figure 67 (85% mill speed and 20% mill fill). The distinctions are the velocity profiles are closer together and hence the difference between the 3 mm and 1.5 mm lifter is not as significant. There is some uniformity in the velocity profile trends from one lifter height to the next. However, this does not appear to be the case in zone 3. Zone 3 shows that the 1.5 mm and 3 mm lifter height velocity profiles are fairly close and so are the velocity profiles for the 6 mm and 10 mm lifter heights.

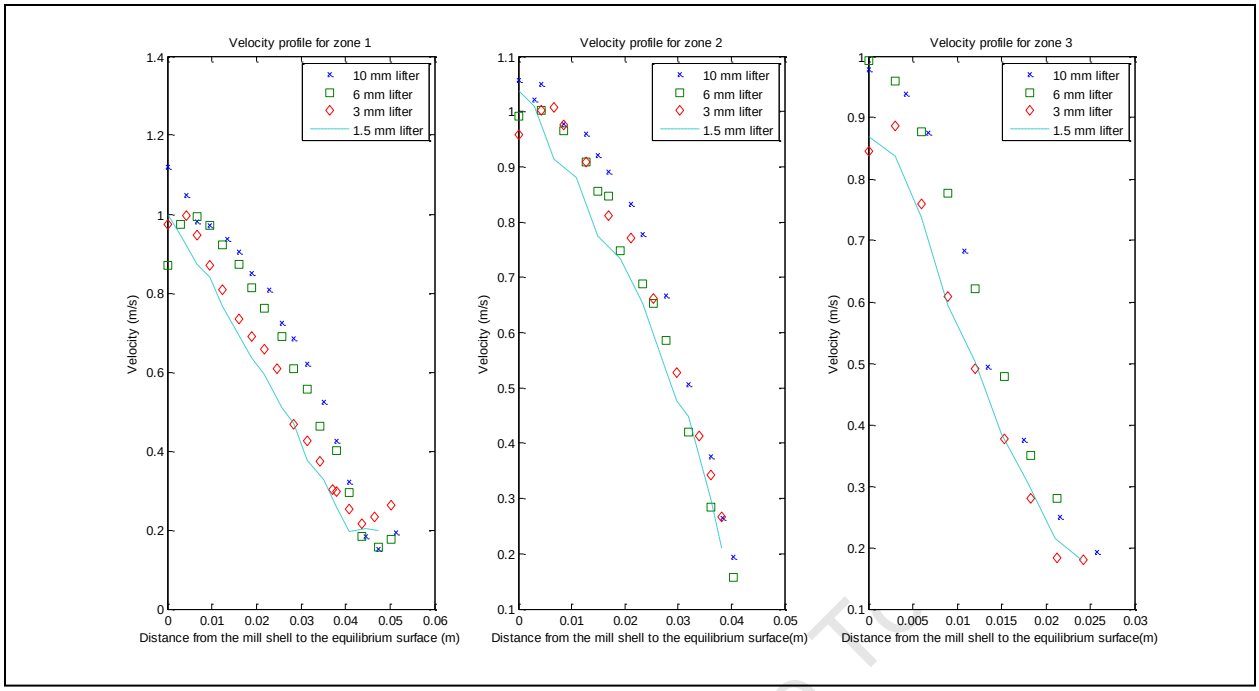

Figure 70: Velocity profile analysis for 30% mill fill and 85% mill speed with varying lifter heights

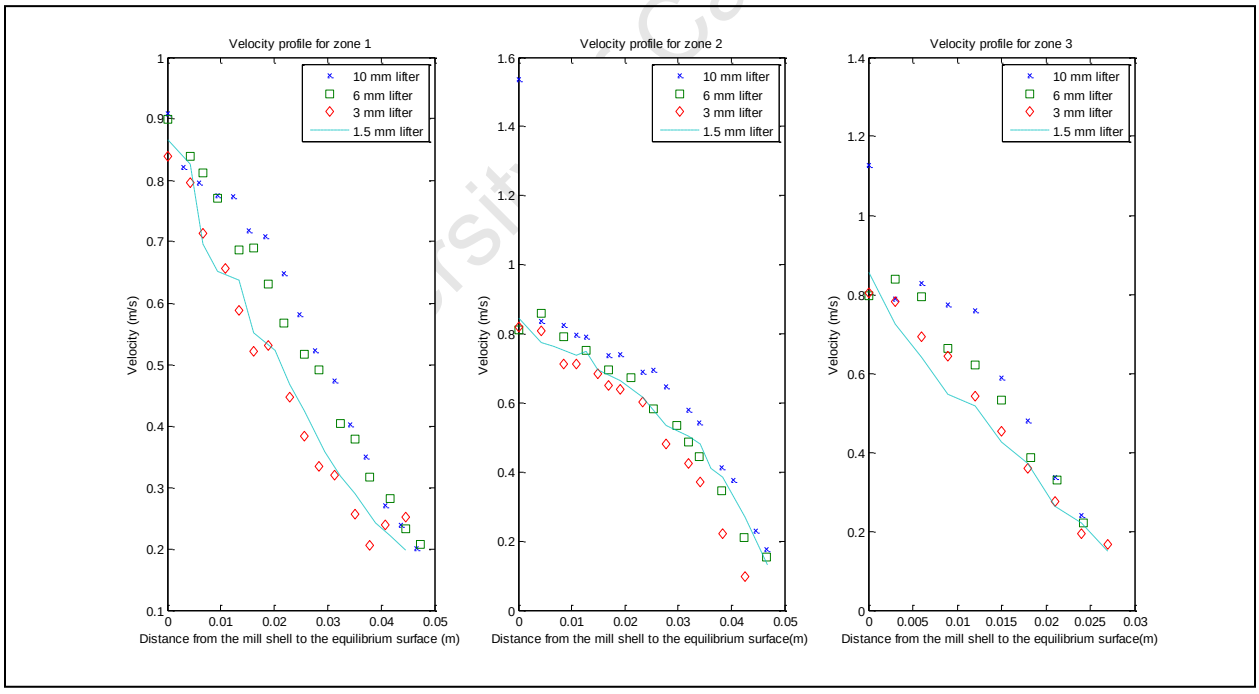

Figure 71: Velocity profile analysis for 30% mill fill and 70% mill speed with varying lifter heights

The velocity profiles at 70% mill speed are shown in Figure 71. The trends for 70% mill speed are the same as 85% mill speed. The velocity profile for the 1.5 mm and 3 mm lifter are close in

zone 1. Zone 2 is different to zone 1, because the velocity profiles for 1.5 mm, 3 mm and 6 mm lifters are fairly close to each.

The velocity profiles at 55% of the critical mill speed, as can be seen in Figure 72, do not have the same trends at 85% and 70% mill speed. The velocity profiles for 1.5 mm, 3 mm, 6 mm and 10 mm lifters are very close to each other (approximately the same) in zone 1, zone 2 and zone 3. The velocity profile at the 10 mm lifter in zone 1 is slightly more than the rest of the lifters.

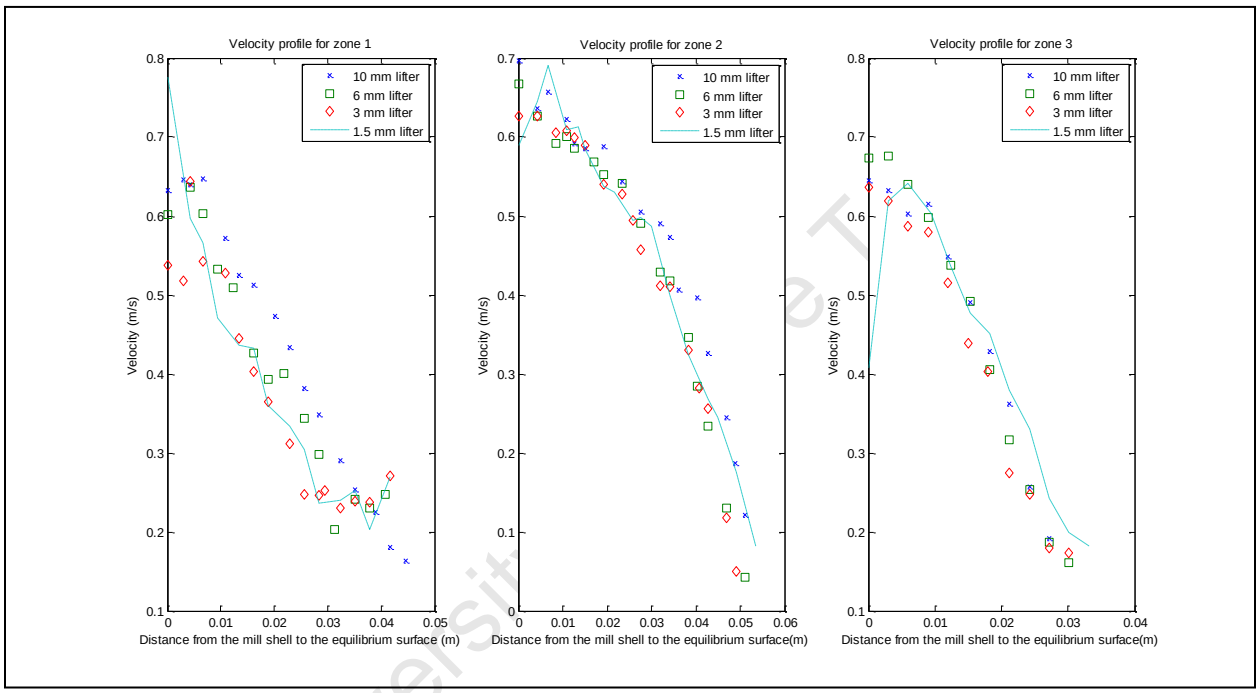

Figure 72: Velocity profile analysis for 30% mill fill and 55% mill speed with varying lifter heights

Additionally the gradient of the velocity profiles of the different lifter heights for a particular zone are the same for speeds of 55%, 70% and 85% critical at a mill volumetric filling of 30%.

12.2.3 Mill volumetric filling at 40%

The results in this section have been extracted from a mill operating at 40% mill volumetric filling and different mill speeds and lifter heights.

In Figure 73 for an experimental mill operating at 40% mill fill and 85% mill speed the trends are very different when compared to the previous trends. The velocity profiles for the different lifter heights appear to be fairly similar in zone 1 and zone 2 but significant differences were

noted in zone 3. For zone 3 the velocity profile for the shorter lifter is consistently lower than the next lifter. The same trend was observed when comparing 3 mm and 6 mm lifters and 6 mm and 10 mm lifters. Similar zone 1 and zone 2 trends were observed for the mill fill of 40% and speed of 55% critical. (see Figure 75)

The velocity profile data for the speed of 70% critical does not have the same trends as those found at 85% and 55% of critical mill speed. The data in Figure 74 shows that the 10 mm, 3 mm and 1.5 mm lifter in zone 1 and zone 2 are similar with the lowest velocities belonging to the 6 mm lifter. Zone 3 the data for the 3 mm and 1.5 mm lifter are very close. The 6 mm lifter data is the lowest at the mill shell and then increases closer to the equilibrium surface.

Additionally the gradient of the velocity profiles of the different lifter heights for a particular zone are the same for speeds of 55%, 70% and 85% critical at a mill volumetric filling of 40%.

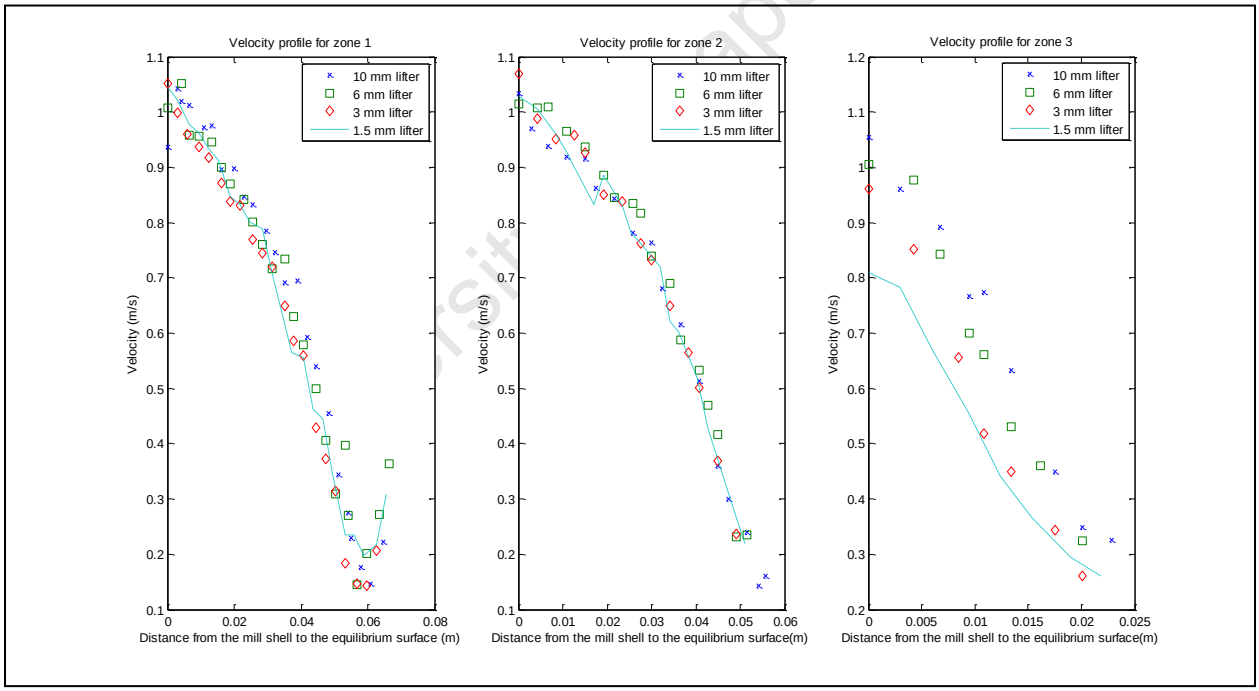

Figure 73: Velocity profile analysis for 40% mill fill and 85% mill speed with varying lifter heights

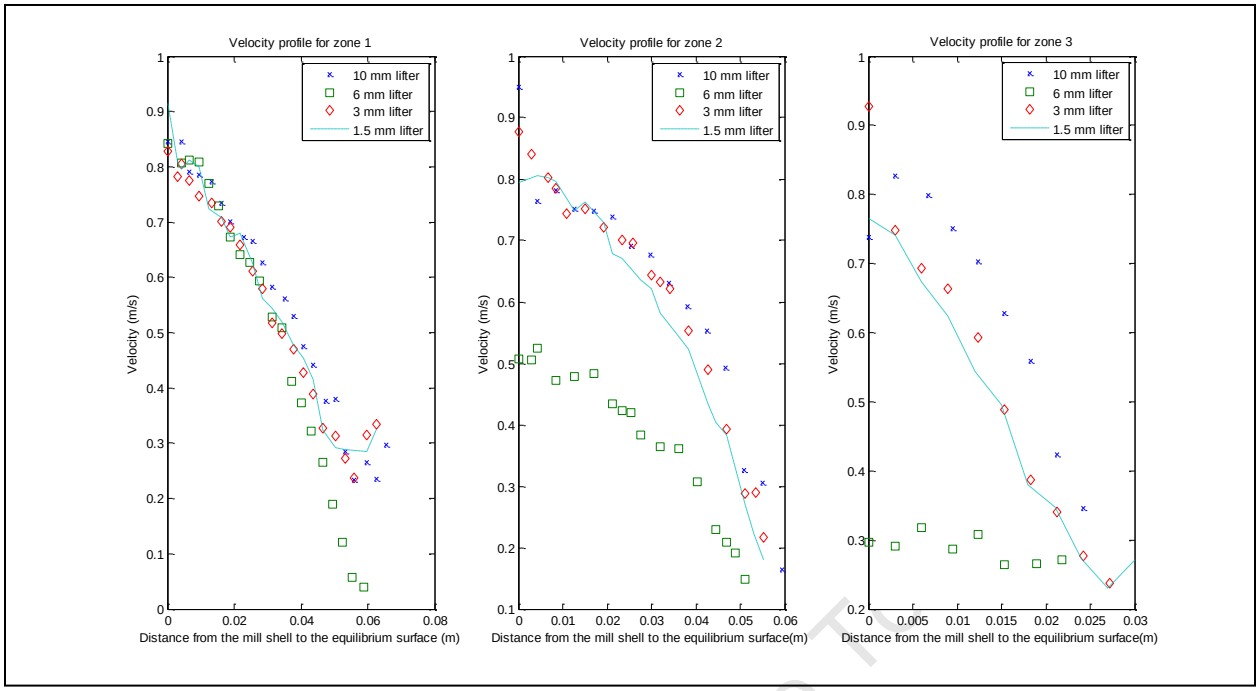

Figure 74: Velocity profile analysis for 40% mill fill and 70% mill speed with varying lifter heights

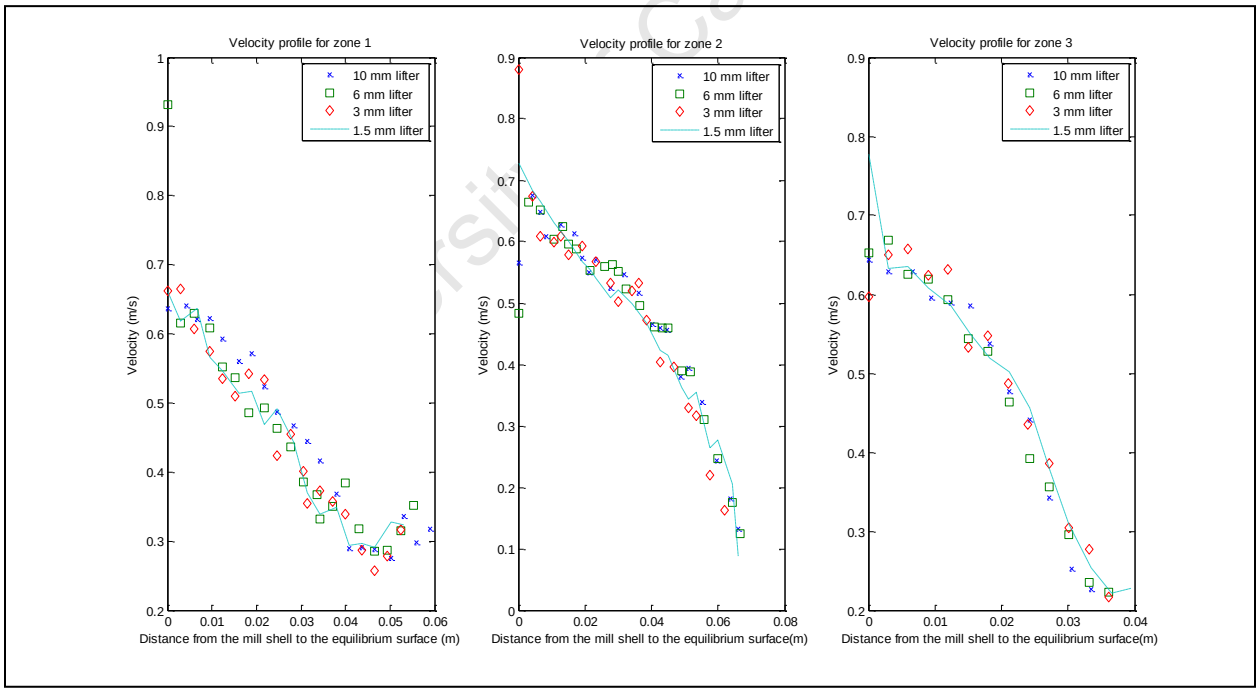

Figure 75: Velocity profile analysis for 40% mill fill and 55% mill speed with varying lifter heights

12.3 Toe and shoulder analysis

The toe and shoulder profile (charge profile) analysis in this work is focused on three different aspects. For each aspect the effects of varying the lifter height on the charge profile for the range of mill operating conditions is assessed. The first aspect is focused on the relative positions of the toe and shoulder. The second aspect is the analysis of the charge dilation which is also referred to as the charge size. The last is the change in the height of the toe region under different conditions.

12.3.1 Toe and shoulder movement

The toe and shoulder movement is based on the behavior of the charge in the cross section of the mill. The probability distribution data was used for the analysis.

12.3.1.1 Toe and shoulder movement with standard plots

The position of the toe and shoulder can be located from the particle probability distribution plot, as shown in Figure 76 and Figure 77. The relative change in the position of these important charge descriptions can be evaluated by assessing the probability distribution plots for different lifter heights at specific operating conditions.

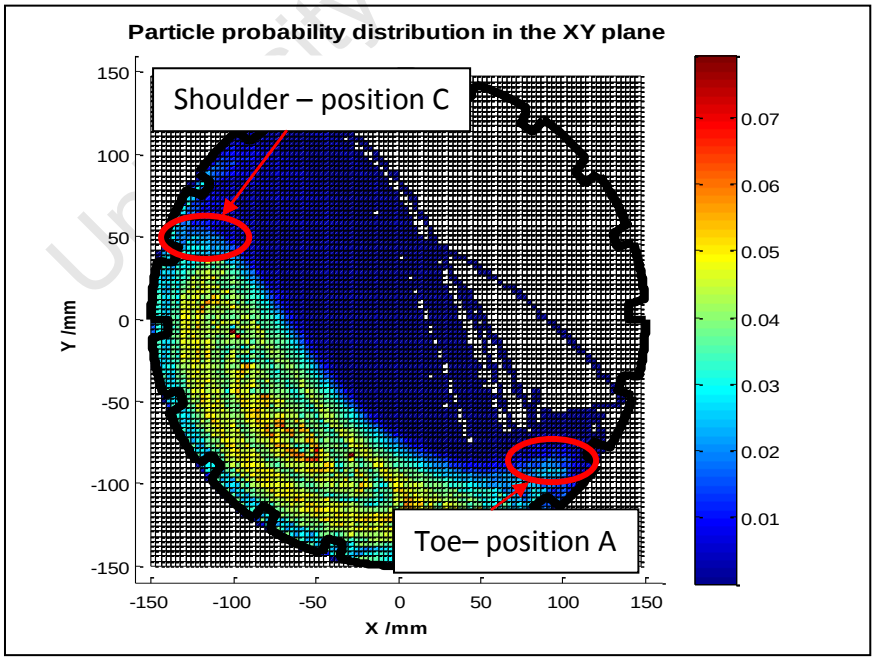

Figure 76: Probability Distribution at 30% mill fill, 55% mill speed and 10 mm lifter height

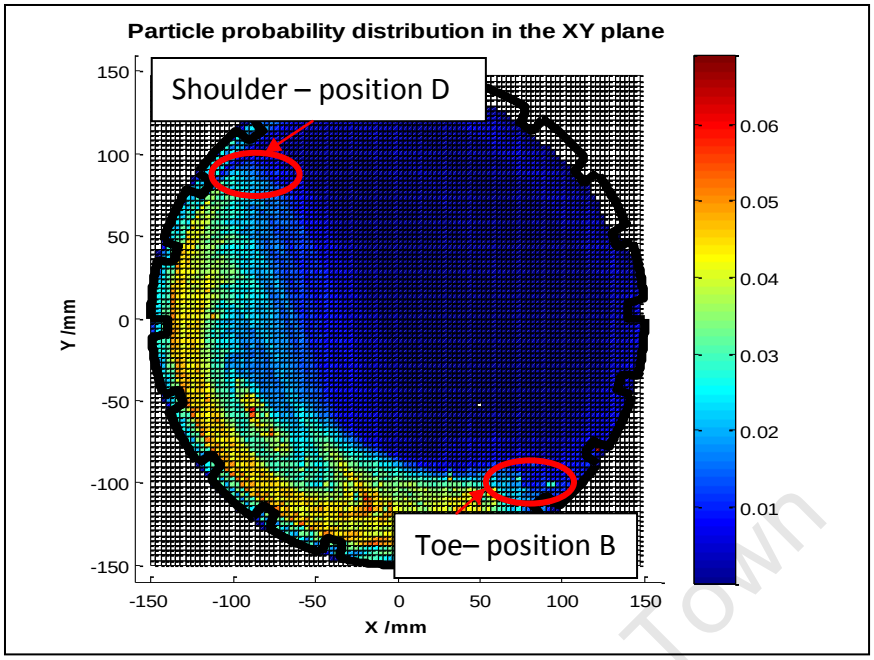

Figure 77: Probability Distribution at 30% mill fill, 85% mill speed and 10 mm lifter height

From Figure 76 and Figure 77 it can be seen that the toe and shoulder are not in the same position for the two conditions being evaluated. The approximate toe of the charge, at 30% mill fill, 55% mill speed and 10 mm lifter height, changes position when the mill speed is set to 85%. The toe and shoulder move clockwise from position A to B and C to D, respectively. The toe of the charge shifted to a lower position while the shoulder moved to a higher position. Although this method provides information on the relative positions of the toe and shoulder, it is too laborious. The method of extracting the charge features using a quantitative method was sought.

12.3.1.2 Toe and shoulder movement with surface extraction

The surface extraction method allows for quantitative analysis of the charge movement. The charge movement is observed by tracking the toe and shoulder angle of the charge. The toe and shoulder angle are determined from the charge free surface. The charge free surface was mapped out using the probability distribution and following the bulk charge, as shown in Figure 78 where the charge free surface is represented by the white dotted surface. The toe region is traditionally very difficult to define (Powell and Nurick (1996)). However, the toe region is defined as the lower part of the bulk charge, which is the last point of the surface.

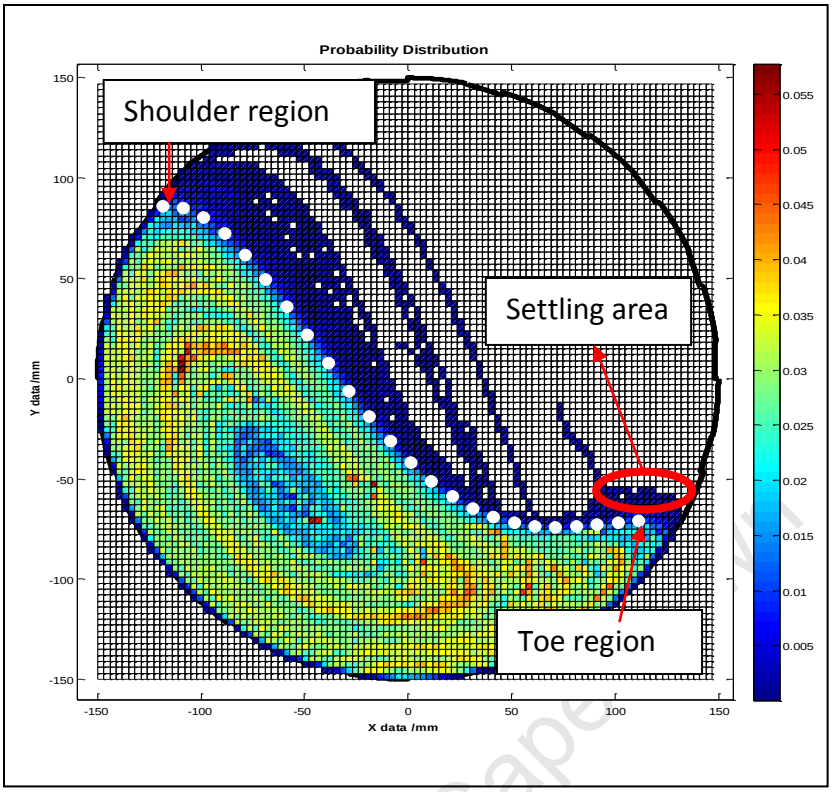

Figure 78: Probability Distribution at 40% mill fill, 55% mill speed and 1.5 mm lifter height

In Powell and Nurick (1996) the shoulder of the charge has been defined as the point at which the charge leaves the mill shell. The shoulder of the charge is defined as the first point on the charge free surface, as indicated in Figure 78. The current definition is in line with literature, because the dark (blue) area above the bulk charge indicates all the cataracting particles. Therefore the first point of the charge free surface is seen as the point at which the particles begin to separate from the mill shell.

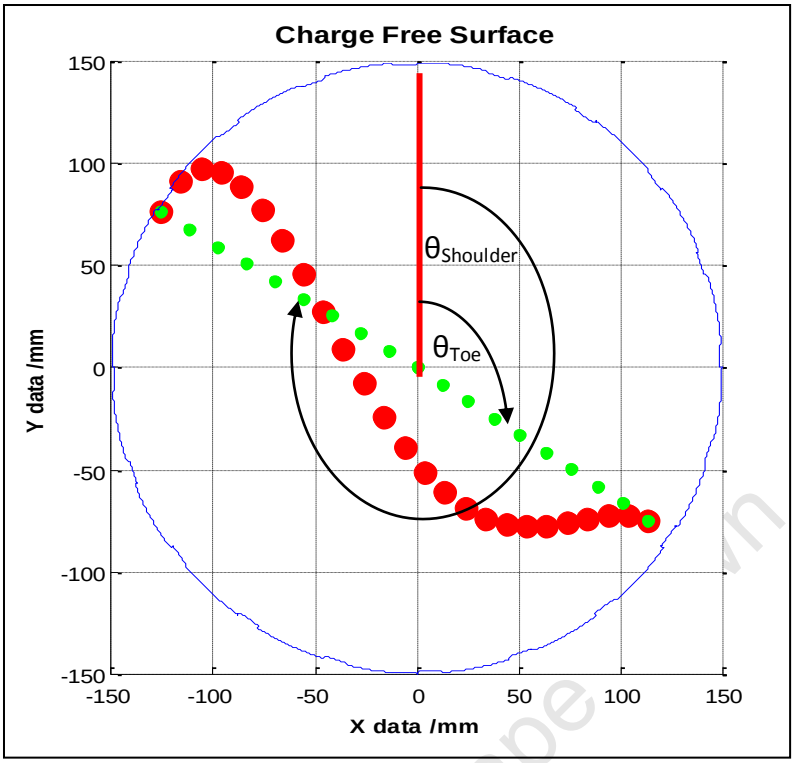

Figure 79: Charge free surface at 40% mill fill, 70% mill speed and 1.5 mm lifter height

Only using the extracted surface the toe and shoulder angle can be determined. de Haas et al (2010) used a similar method.

The angles of the toe (θ_{Toe}) and shoulder ($\theta_{Shoulder}$) are measured from a vertical line going through the center of the mill, which is shown as the solid (red) line in Figure 79. The direction of measurement is dependent on the direction of the charge's movement and hence the mill's rotation. All the experiments were run clockwise. Therefore the manner in which the angles are measured is consistent throughout. The measurement direction in de Haas et al (2010) is opposite to what is shown in Figure 79, because the mill rotated in the anti-clockwise direction in their work. Toe and shoulder angles from all experiments performed in this work are given in Table 19 in section 16.10 in the appendix. The analysis performed focused on the effect of lifter height on the toe and shoulder angle at different mill speeds and mill fill respectively. When the effect of lifter height is being analyzed, then the mill speed and mill fill will be held constant.

12.3.1.3 Lifter height effect on the toe and shoulder

This chapter shows the results of the toe and shoulder analysis by varying the lifter height.

Figure 80 to Figure 82 show the effect of lifter height on the shoulder angles for various volumetric filling degrees at speeds of 85%, 70% and 55% critical speed, respectively. The lifter height appears to have an influence on the shoulder angle. The effect is more pronounced at higher mill speeds. The trend indicates an increase in shoulder angle with an increase in lifter height.

Figure 83 to Figure 85 shows the effect of lifter height on the toe angle for various filling degrees at speeds 85%, 70% and 55% critical speed. It was observed that variations in the toe angle with the lifter height were more pronounced at the speed of 70% critical. The toe angle increases with an increase in lifter height from the 3mm to the 10 mm lifter at 20%, 30% and 40% mill filling. At 55% and 85% critical the lifter height has an insignificant effect on the toe angle.

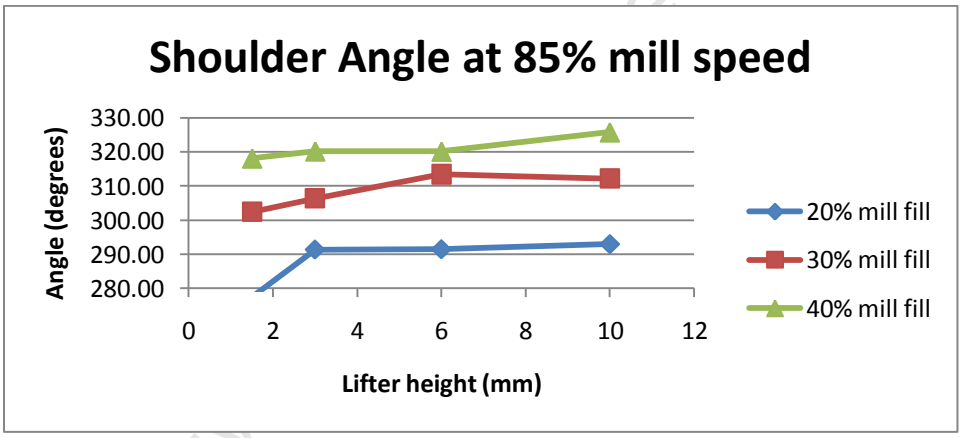

Figure 80: Shoulder angle at different lifter heights at 85% mill speed

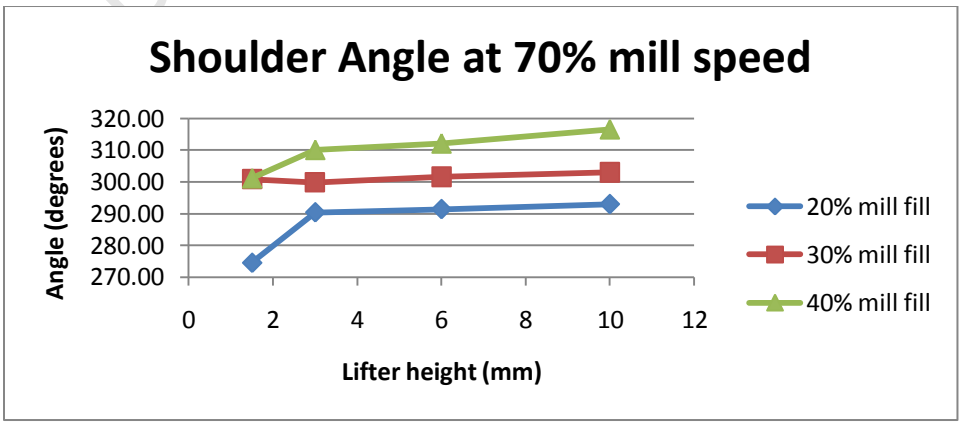

Figure 81: Shoulder angle at different lifter heights at 70% mill speed

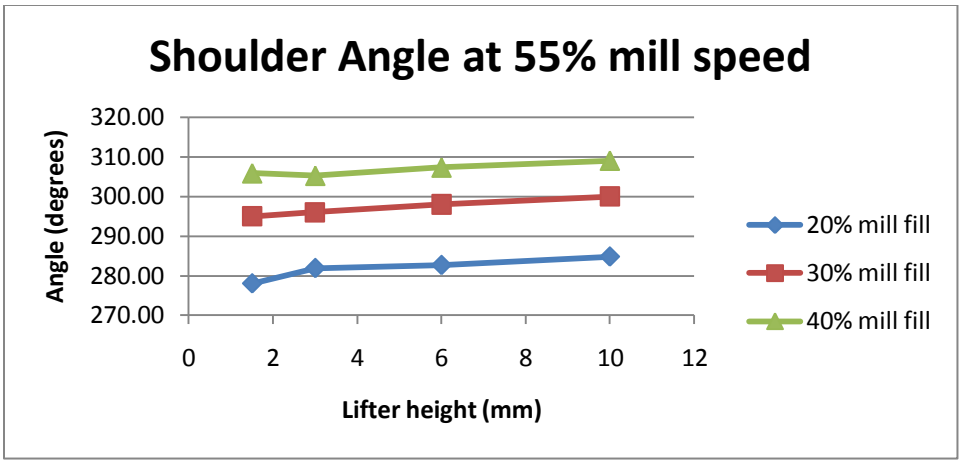

Figure 82: Shoulder angle at different lifter heights at 55% mill speed

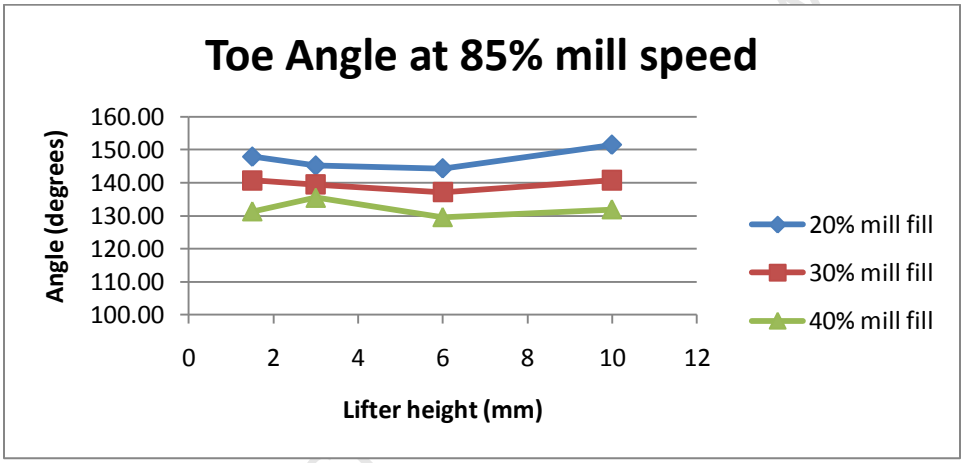

Figure 83: Toe angle at different lifter heights at 85% mill speed

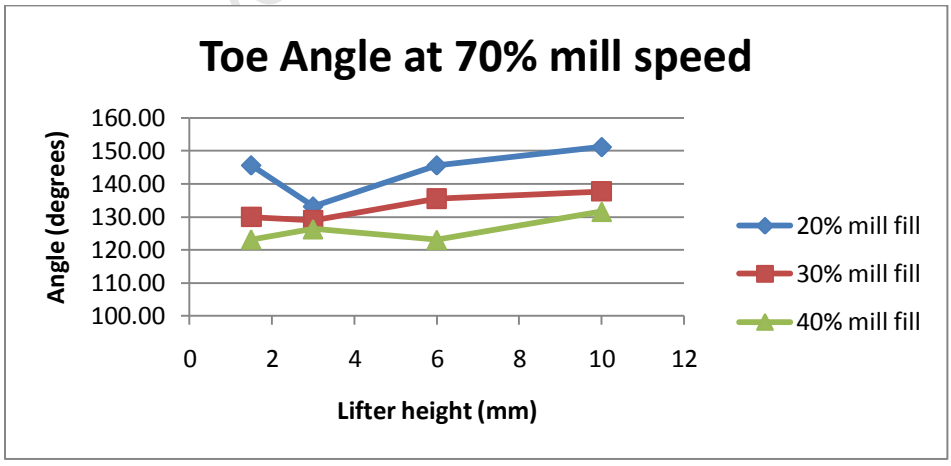

Figure 84: Toe angle at different lifter heights at 70% mill speed

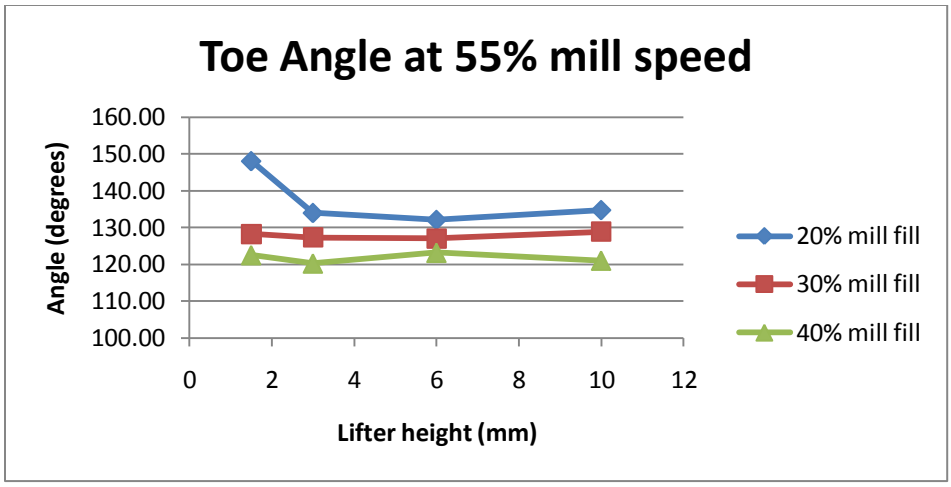

Figure 85: Toe angle at different lifter heights at 55% mill speed

12.3.2 Lifter height effect on the charge size

The charge size is a value that is a natural progression from the toe and shoulder angle data. The charge size is determined by the angle (θ_{Charge}) between the toe and the shoulder of the charge. Once the toe and shoulder angle are known, then the charge size angle can be determined by simply subtracting the shoulder angle from the toe angle. This is the same as the method used in de Haas et al (2010).

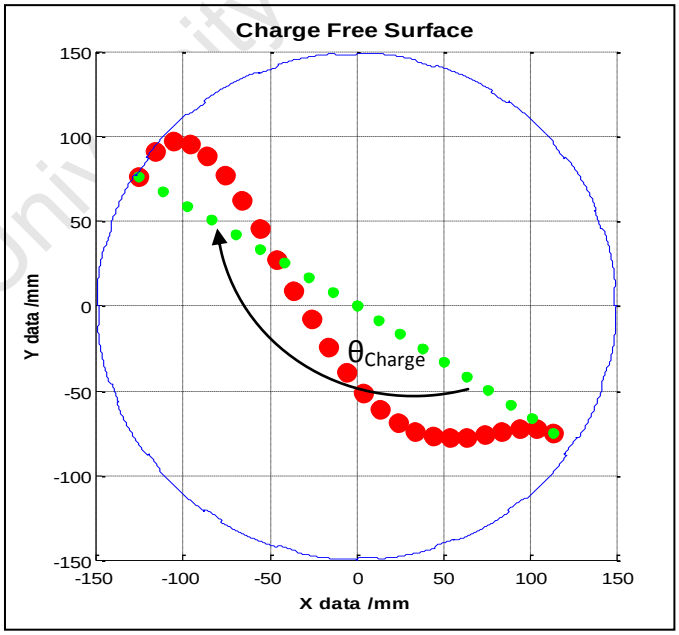

Figure 86: Charge free surface at 40% mill fill, 70% mill speed and 1.5 mm lifter height

The charge size analysis can be guided by the results of the toe and shoulder angle analysis. The charge size is dependent on the behavior of the toe and shoulder angle.

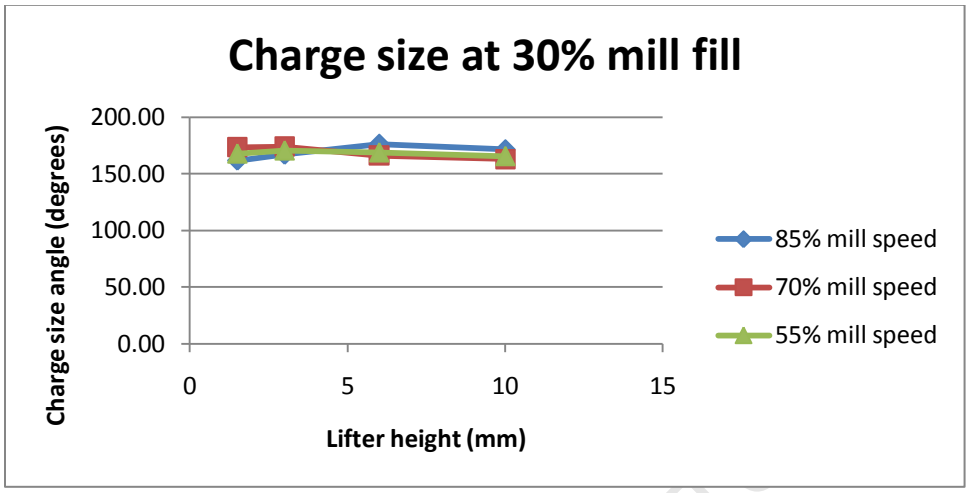

Figure 87: Charge size at different lifter heights at 30% mill fill

Figure 87 shows the charge size at 30% volumetric filling for the mill operated at 85%, 70% and 55% critical speed. It can be seen that the charge size did not vary with lifter height at these operating conditions.

12.3.3 Lifter height effect on the toe height

The toe height of the charge is another characteristic that has been extracted from the data. The toe height is the distance from the top of the charge toe to the line perpendicular to the mill shell as can be seen in Figure 88.

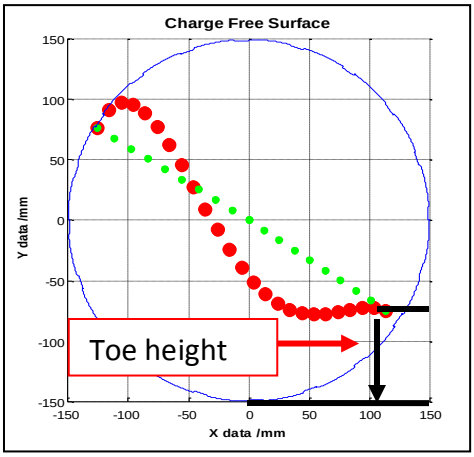

Figure 88: Definition of the toe height

Figure 89 shows the variation of the toe height with lifter height for the mill operated at 20% filling at speeds of 85%, 70% and 55% critical speed. At 55% and 70% critical speed the toe height initially increases from approximately 36 mm to 56 mm after which it decreases, as shown in Figure 89. However, the toe height remains constant at 85% critical until 6 mm and then decreases from 38 mm to 20 mm.

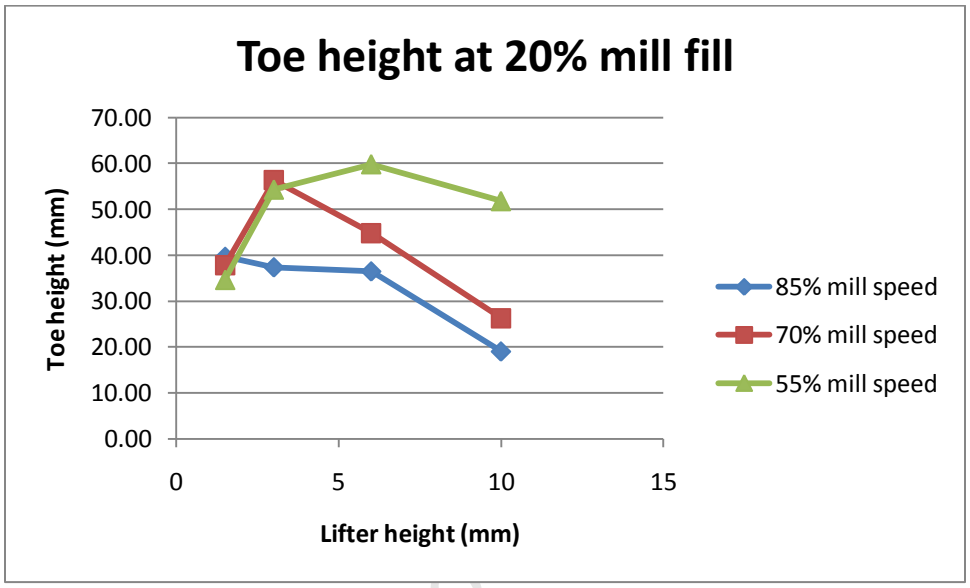

Figure 89: Toe height at different lifter heights at 20% mill fill

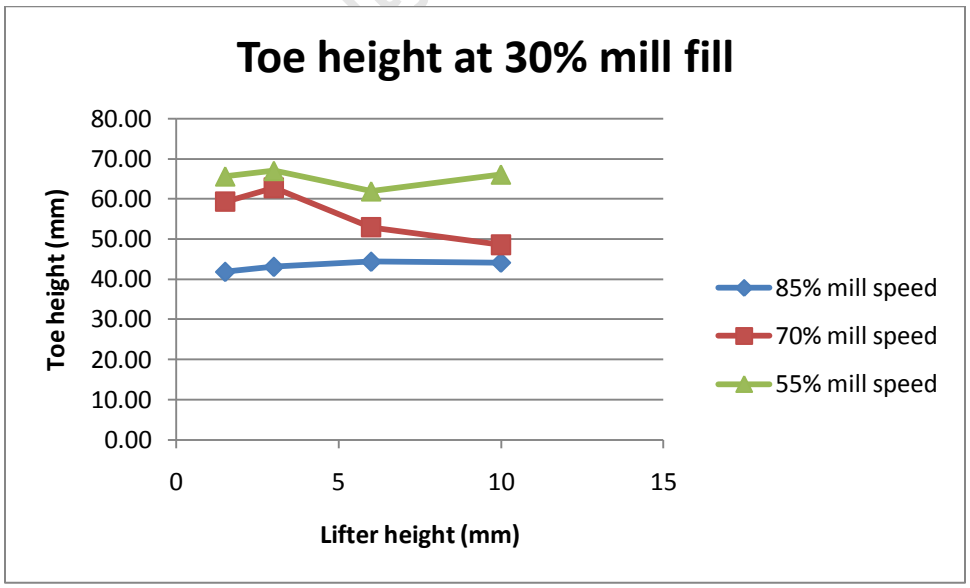

Figure 90: Toe height at different lifter heights at 30% mill fill

Figure 90 shows the variation of the toe height with lifter height for a mill operated at 30% filling at speeds of 85%, 70% and 55% critical. At 85% and 55% critical speed the toe height remains constant from 1.5 mm to 10 mm. However, at 70% critical the toe height decreases from 60 mm to 50 mm after the 3 mm lifter height.

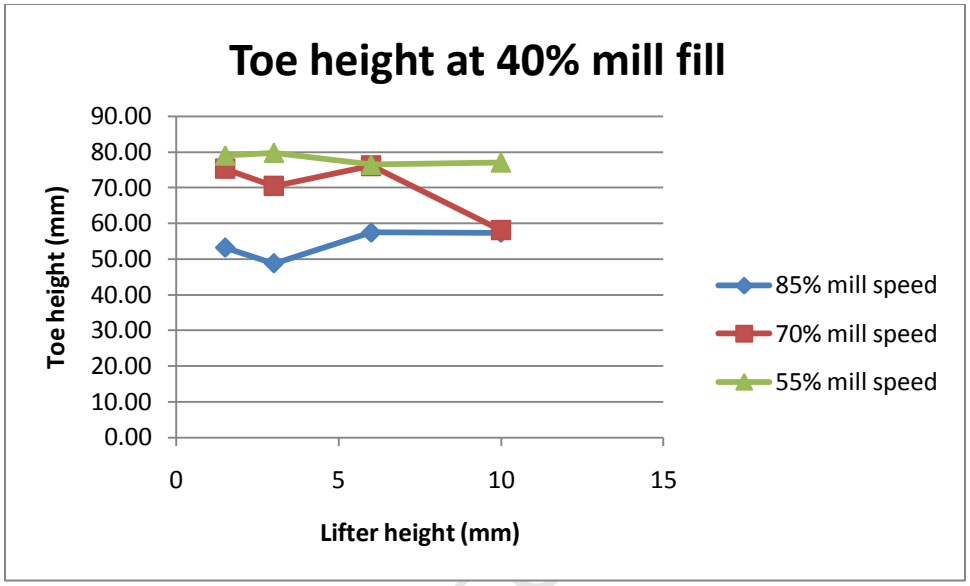

Figure 91: Toe height at different lifter heights at 40% mill fill

Figure 91 represents the toe height variation at 40% filling at 85%, 70% and 55% critical speed. At 55% critical speed the toe height is constant from 1.5 mm to 10 mm lifter height. The toe height decreases from 75 mm to 60 mm at 70% critical speed. Conversely, the toe height at 85% critical speed increases from 50 mm to 58 mm from the 3 mm lifter height.

12.4 Velocity profile analysis

The velocity profile analysis is a comparison between the theoretical velocity profile and experimental data obtained from PEPT time-average velocity data.

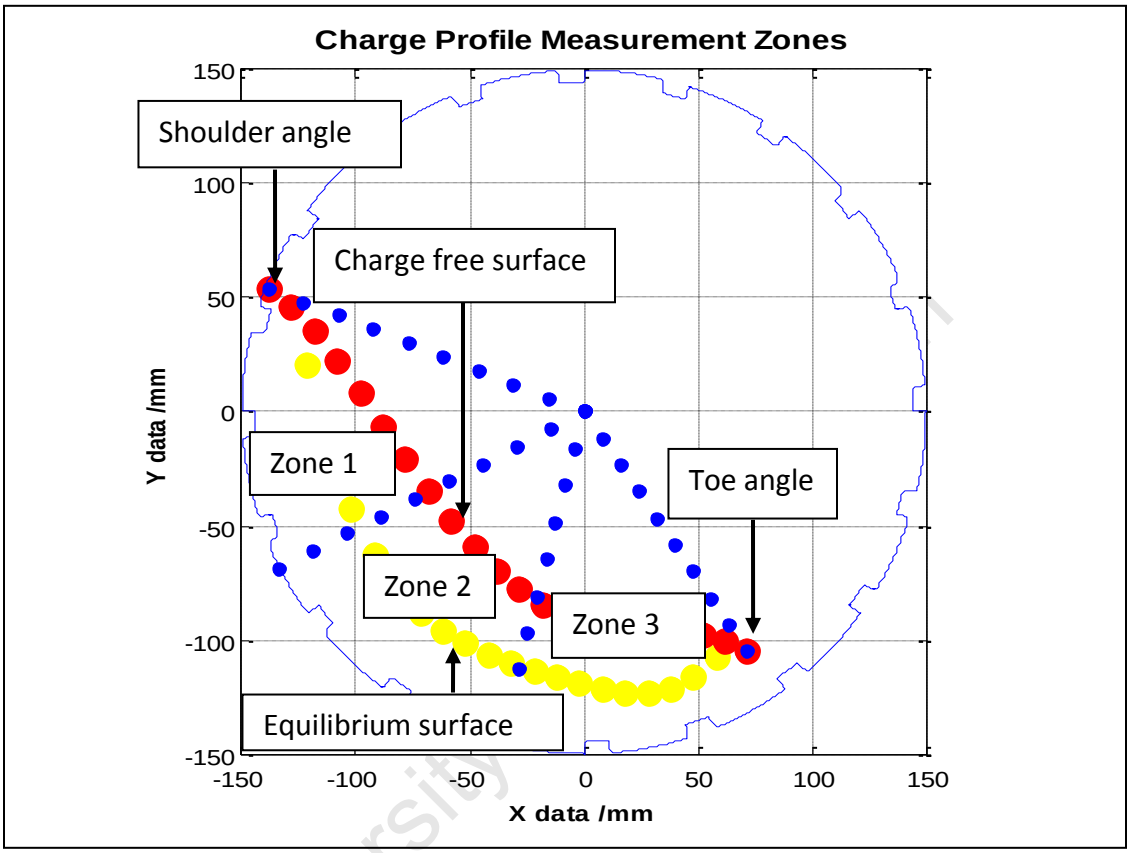

Figure 92: Dividing charge into sections at 20% mill fill, 70% mill speed and 6mm lifter

Before the zones can be determined the shoulder and toe region of the charge need to be defined. In this case the first and last data point of the charge free surface is the shoulder and toe of the charge, respectively. Then the toe and shoulder angle of the charge is determined by measuring the angle from the y-axis at x = 0 in a clockwise direction, which is the direction of the mill's rotation. Once the toe and shoulder angle are determined they can be used to calculate the charge's body. The charge body is then divided into 3 equal pieces, which then creates the measurement zones. The toe angle, shoulder angle and charge body change with different operating conditions, hence the measurement zones change. Zone 1 represents the approximate behaviour in the shoulder region. The en masse region is represented by zone 2 and zone 3 would approximate the behaviour in the toe region.

12.4.1 Theoretical velocity profile sensitivity analysis

The theoretical velocity profile is developed using granular flow theory. The resultant equation for the velocity profile is as follows:

$$v_x = \left(\rho g \sin\theta + \frac{dP}{dx} + F_f(y)\right)\frac{(y^2 - L_2 y)}{2\mu} + \frac{v_{mill}\, y}{L_2} \qquad where \qquad F_f(y) = \mu_e F_N(y)$$

Of the variables that form part of the velocity profile equation a handful are extracted from the PEPT data, a few are well known constants or given data and the others are estimated. Table 9 is a summary of all the variables and which categories they fall into.

Table 9: Constants for theoretical velocity profile equation

Variables	Units	Constant	PEPT Data	Estimated	Description
ρ	kg/m3	X			Density
g	m/s^2	X			Gravitational acceleration
dP/dx	Pa	X			Applied pressure in x-direction
μ	Pa*s			X	Viscosity
v_{mill}	m/s		X		Tangential velocity at the mill shell
L_2	m		X		Distance from the equilibrium surface to the mill shell
F_N	N		X		Normal force
μ_e	dimensionless			X	Friction coefficient
θ	degrees		X		Angle line perpendicular to the mill shell bottom

The only two variables that are estimated are viscosity (μ) and the friction coefficient (μ_e), as can be seen in Table 9. The viscosity is defined as a free variable, because viscosity of granular material is ill-defined. The friction coefficient does not have a significant effect on the velocity profile, even with large increases. The friction coefficient sensitivity analysis can be seen in Figure 93. The behaviour is explained by the magnitude of the normal force. The normal force in this system is insignificant, because of the small masses in the system. Through scale up and considering industrial systems the normal force will become more important. The free variable and friction coefficient values are chosen for the greatest agreement between the experimental and theoretical velocities. The friction coefficient is 0.9, which is the approximate value of friction between two glass surfaces. The free variable chosen for the velocity model is 85 Pa*s.

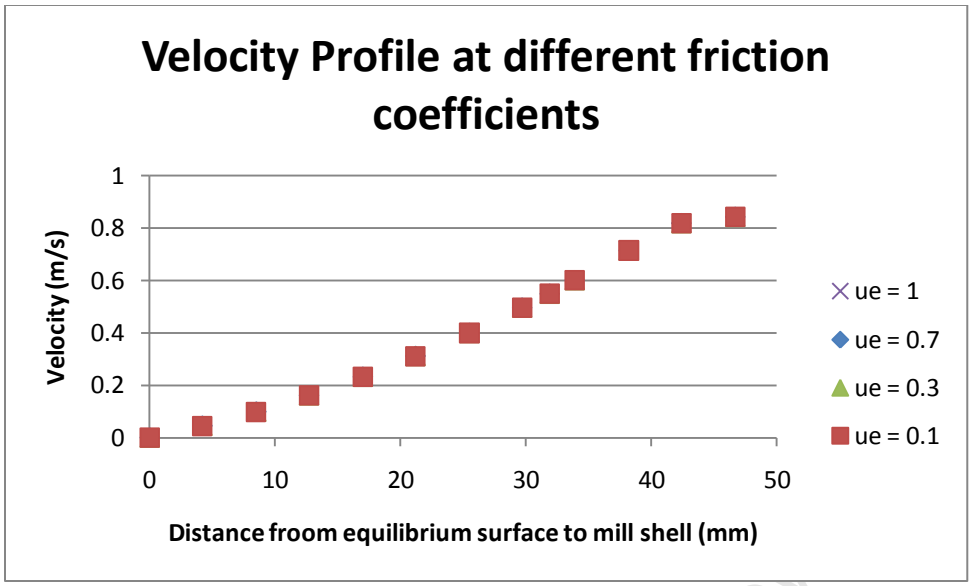

Figure 93: Sensitivity analysis of the velocity profile varying friction coefficient at a viscosity of 15 at 30% mill fill, 70% mill speed and 6 mm lifter

12.4.2 Methods of comparison

The comparison between the theoretical and experimental data sets aims to determine how close the experimental data matches the theoretical data. The three different methods used to compare the velocity profile data are visual, statistical agreement and error quantification.

A purely visual method with any supporting data is limited. Only comments based on estimating the fit can be made. In this case the visual method is supplemented with supporting data in the form of error bars for the experimental data. Despite the addition of the data the analysis is qualitative.

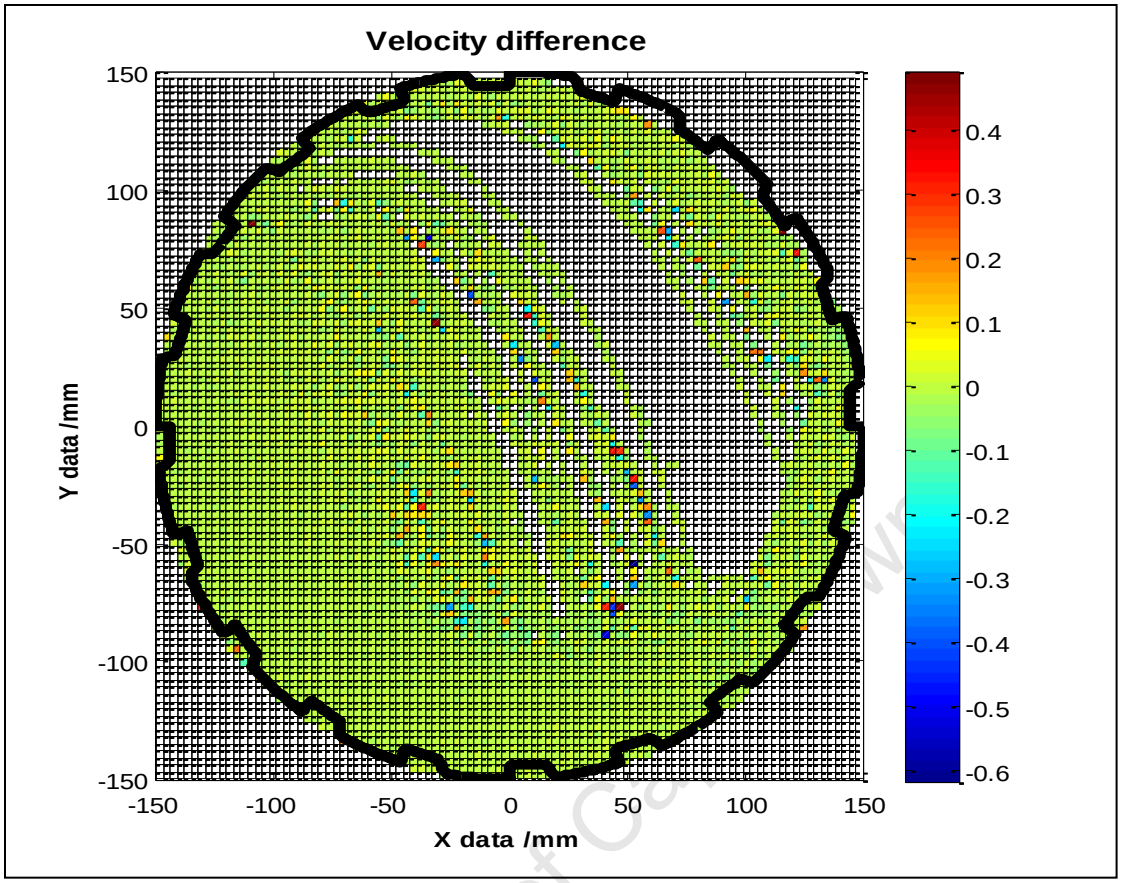

Figure 94: Velocity standard deviation at 20% mill fill, 85% mill speed and 6 mm lifter

Numeric schemes are used to produce velocity and position/standard plots from the raw PEPT data. Velocities along the path of the particle are determined and consequently the differences between consecutive velocities are calculated. The velocity differences are averaged across the bins to obtain a measure of the standard deviation of the velocities in the respective bins. The plot of averaged velocity differences for 20% mill fill, 85% mill speed and 6 mm lifter is shown in Figure 94. The standard deviation values are then extracted along the same line as the velocity values, as can be seen in Figure 95.

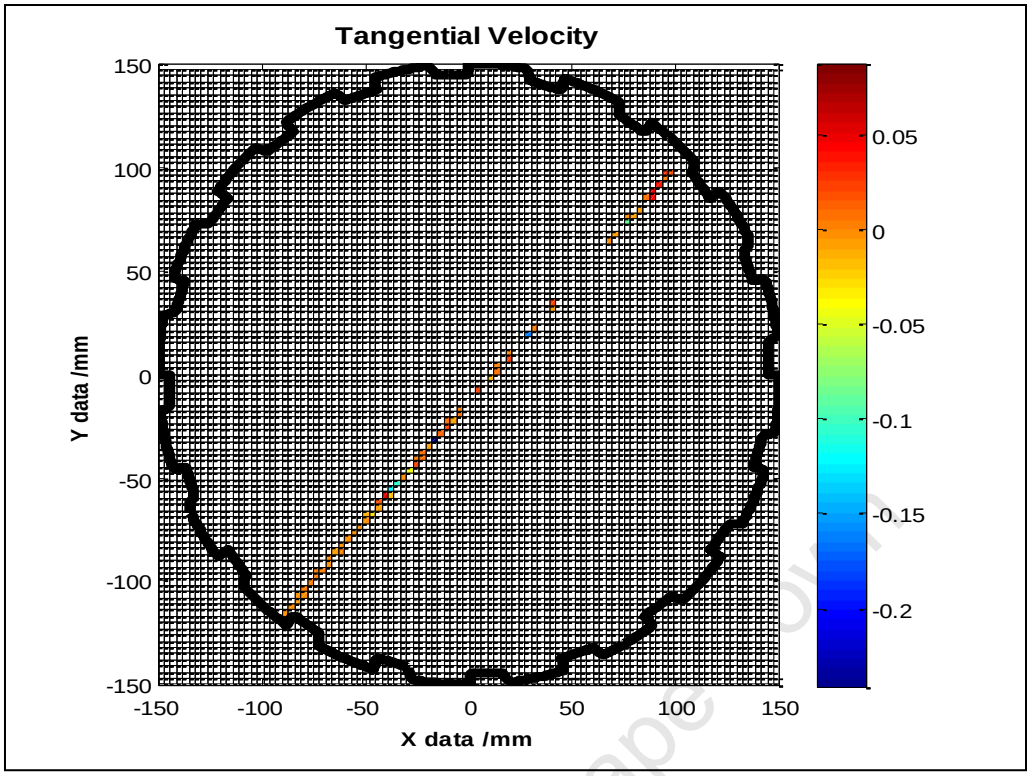

Figure 95: Standard deviation extracted along the velocity extraction line

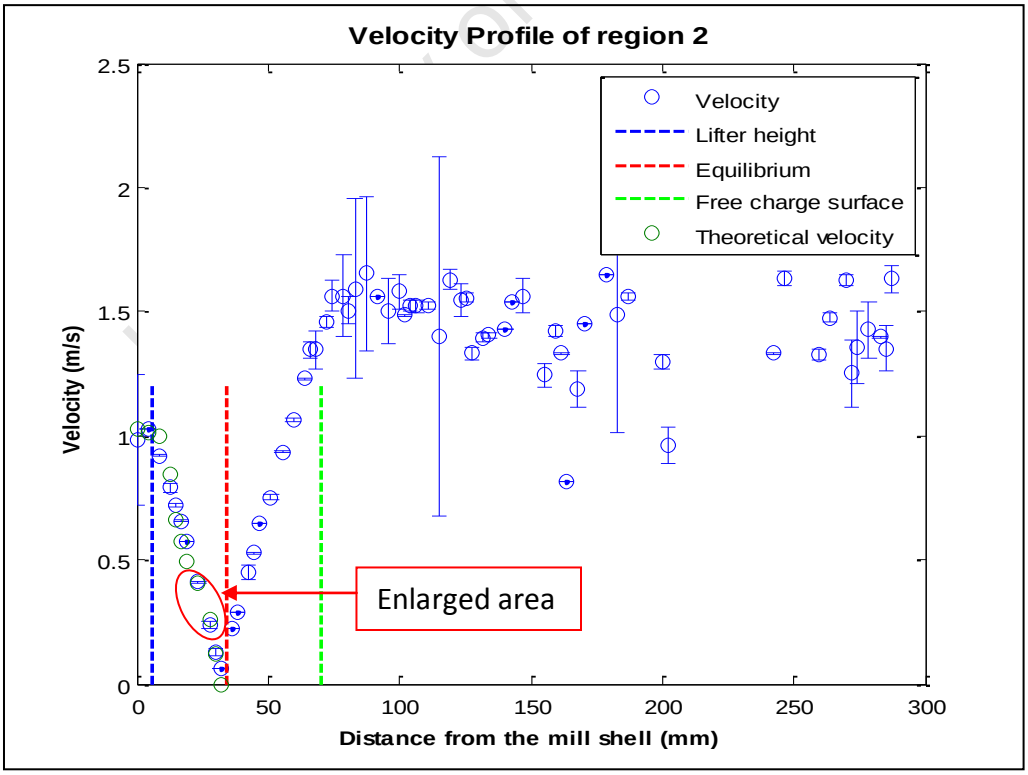

Figure 96: Velocity profile comparison with error bars at 20% mill fill, 85% mill speed and 6 mm lifter in zone 2

Once the data is extracted it is added to the experimental data, as can be seen in Figure 96. The error is three times the standard deviation, so that the data falls into the 99% confidence interval. To evaluate how the experimental data compares with the theoretical data an area of Figure 96 was enlarged. In Figure 97 error bars were added to make it easy to make visual comparisons. The first case labeled 'A' represents the theoretical data falling within the limits of the experimental data, which is the 99% confidence interval. The second case 'B' shows an instance where the theoretical data does not fall within the experimental data limits.

For every experimental run and zone the frequency of theoretical and experimental data agreement was counted. In order for the theoretical data to be in agreement with the experimental data the theoretical data needed to fall within the upper or lower limit of the experimental data. The upper limit is three times the standard deviation (99% confidence) added to the average value. The lower limit is three times the standard deviation (99% confidence) subtracted from the average value. A comparison was made by taking the percentage of the number of agreements from the total amount of data within the boundary of the mill shell and equilibrium surface, which is the first method of comparison.

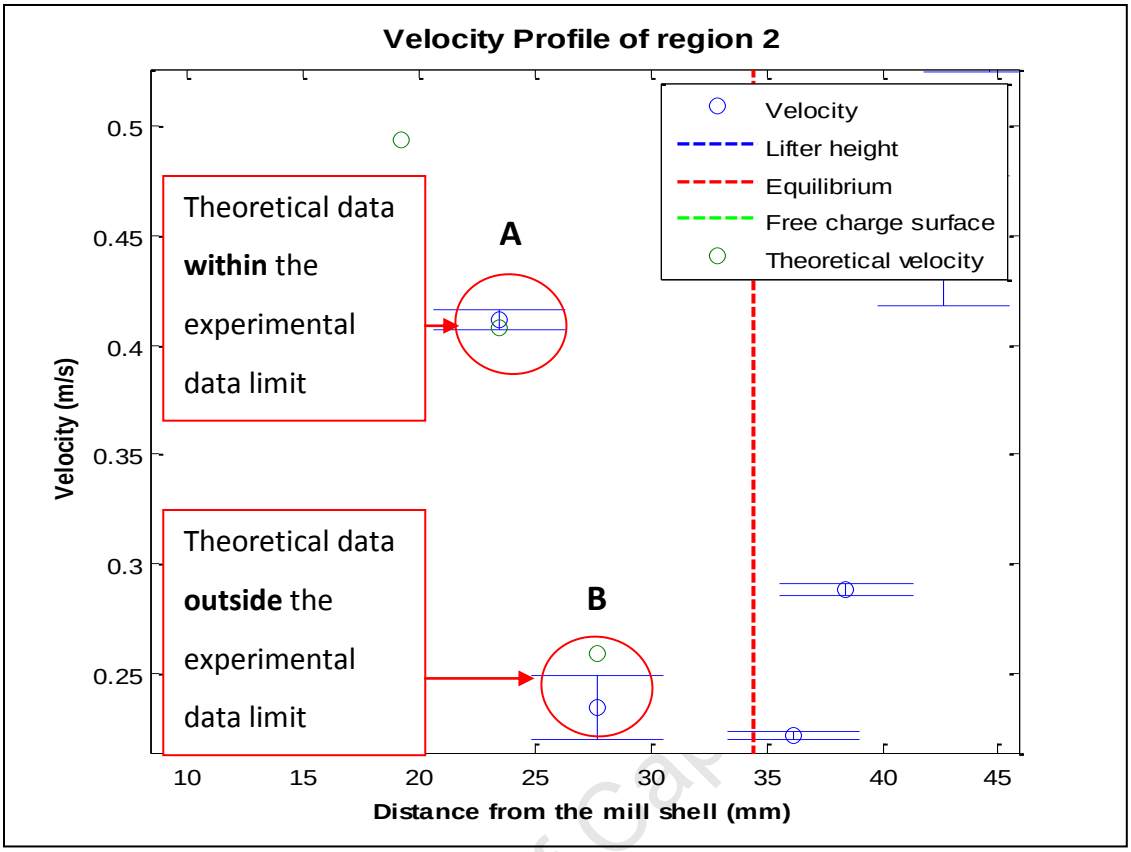

Figure 97: Enlarge area of the velocity profile analysis

The second method takes the absolute difference between all the experimental and theoretical data sets. The difference is taken from the limits of the experimental data and not from the average experimental velocity value. Therefore the difference is calculated from the boundary of the 99% confidence interval. The absolute error is scaled with respect to the experimental velocity. Hence the error is represented as a percentage of experimental velocity, because the experiment is the basis of comparison. Errors in the x-axis values of the experimental and theoretical data are ignored, because they have the same x-axis values. Therefore only the velocity values need to be considered during the analysis.

12.4.3 Comparing experimental and theoretical velocity profile data

The velocity profile comparison between experimental and theoretical data was done for 3 different mill fills, 3 different mill speed, 4 different lifter heights and 3 different zones. Instead of comparing individual zones at different conditions, the 'best' and 'worst' data sets were analyzed. A good data set is defined as a data set where the theoretical and experimental data

are in statistical agreement (99% confidence interval). A bad data set is seen as a data set without agreement between the experimental and theoretical data. Hence the best data sets are those with the largest amount of data in agreement and the worst are the data sets with the largest differences between the theoretical and experimental data. A summary of 10 mm and 6 mm lifter velocity analysis data is presented in Table 10 and the full data set available in section 16.6 in the appendix. The velocity analysis summaries only take the agreement, disagreement and error quantification in account. This is because the quantification of agreement is numerical and is more reliable than the visual method.

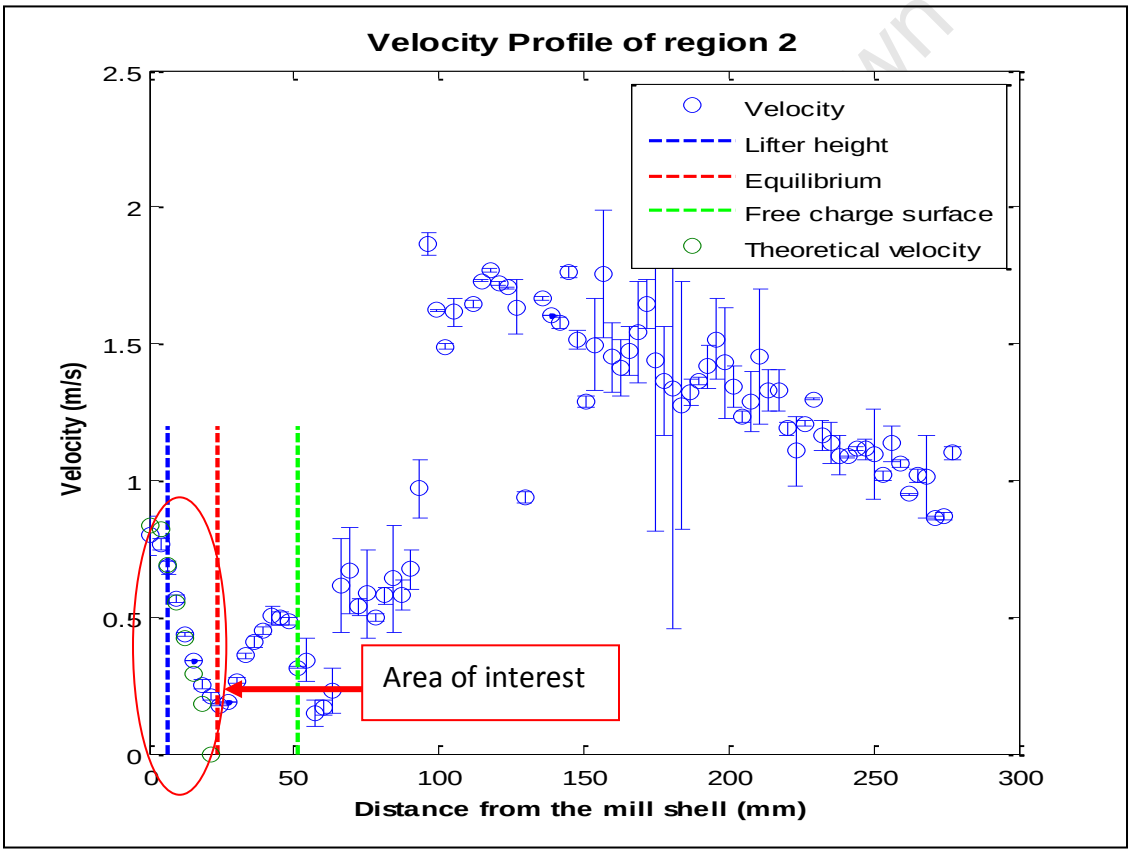

Figure 98: Velocity profile at 20% mill fill, 70% mill speed and 6 mm lifter in zone 3

The first set of data analyzed was retrieved from an experiment with the mill operating at 20% mill fill, 70% mill speed and 6 mm lifter height in zone 3. This data set was chosen as it is deemed to be one of the best data sets. Figure 98 shows the velocity profile across the diameter of the mill shown in Figure 95. It should be noted that Figure 98 does not allow for detailed comaprisons to be made. Although visually the experimental and theoretical data

seem to match well with each other. To view the details a section of the figure is enlarged and is represented in Figure 99. It can be seen that some of the data falls within and others outside the experimental limits. Of the 8 pairs of data in Figure 99 three sets fall within the limits (shown by circle), while the rest of the data falls outside of the limits. The agreement between the experimental and theoretical data seems to be 38%. The aforementioned agreement counting alogrithm has been setup to count the amount of times the data sets are in agreement. The data set with a black arrow does not agree but is close. The visual method cannot discriminate to this level of detail. Therefore, when summarizing the data for all the runs only the counting alogrithm results are used.

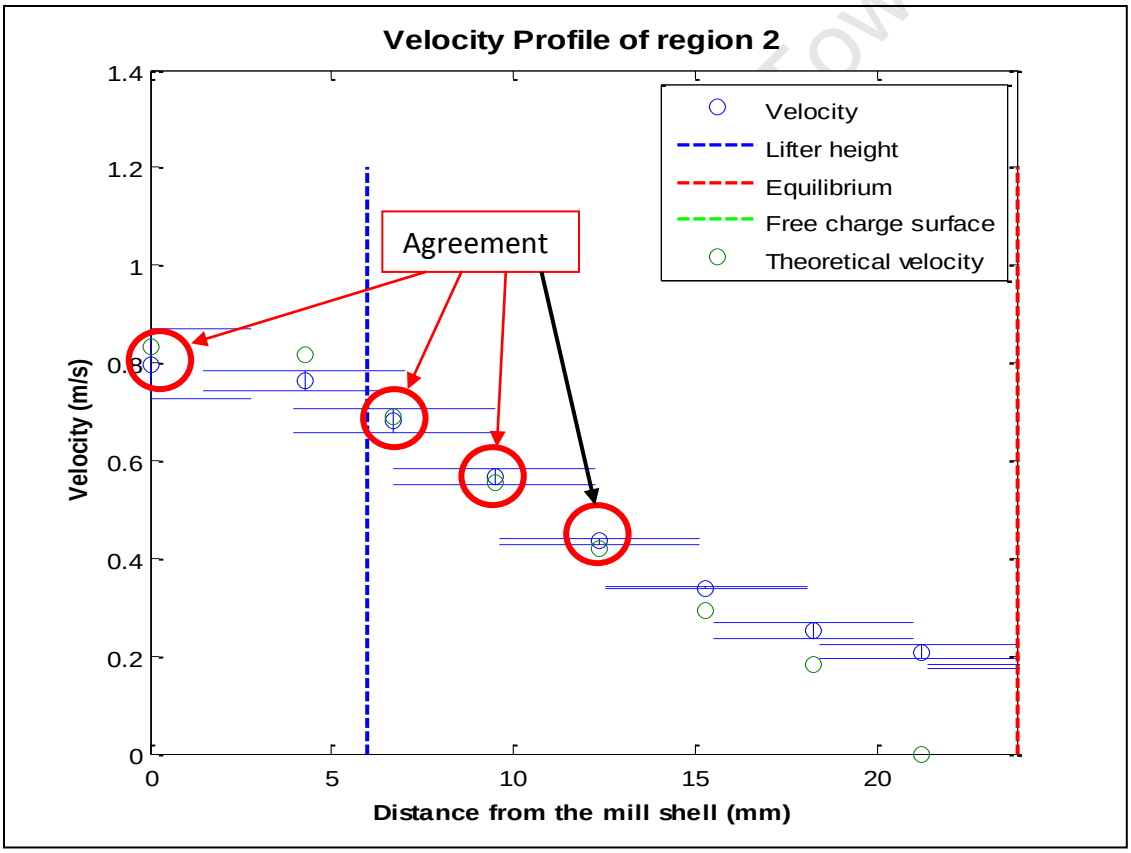

Figure 99: Enlarged area for the velocity profile at 20% mill fill, 70% mill speed and 6 mm lifter in zone 3

Another important indicator of fit is the absolute and relative error. The absolute and relative errors are represented by Figure 100 and Figure 101, respectively. The absolute error can also be seen as a residual plot (Figure 100), which usually gives an indication of the goodness of a trend line fit.

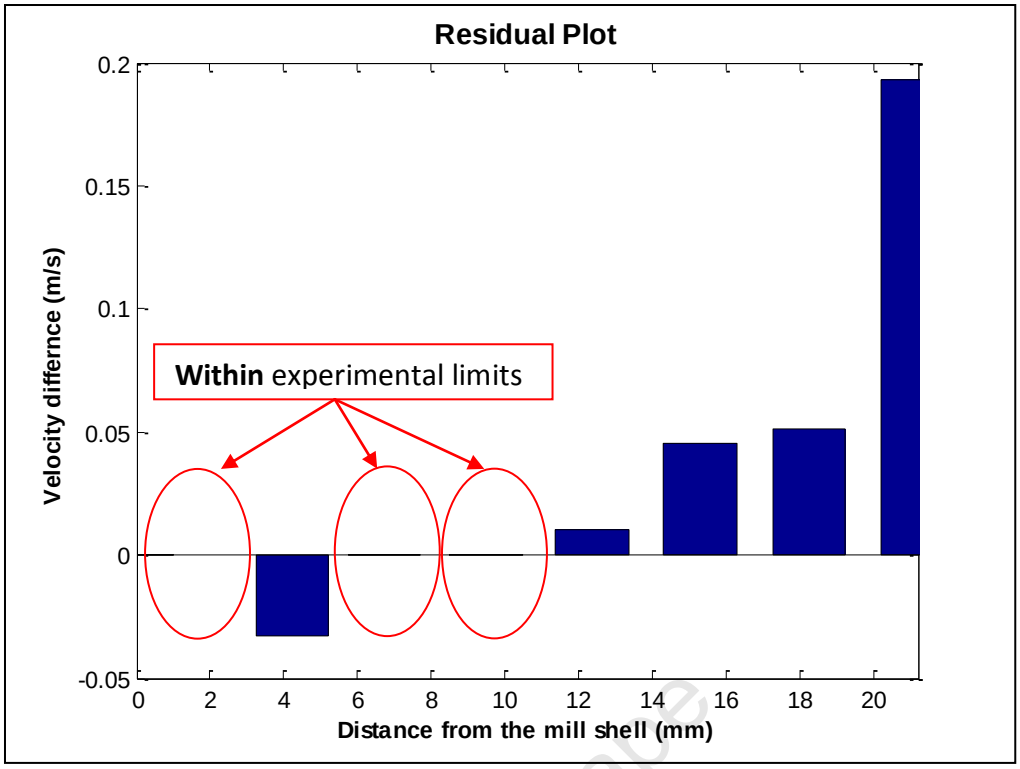

Figure 100: Absolute difference between the theoretical and experimental data for 20% mill fill, 70% mill speed and 6 mm lifter in zone 3

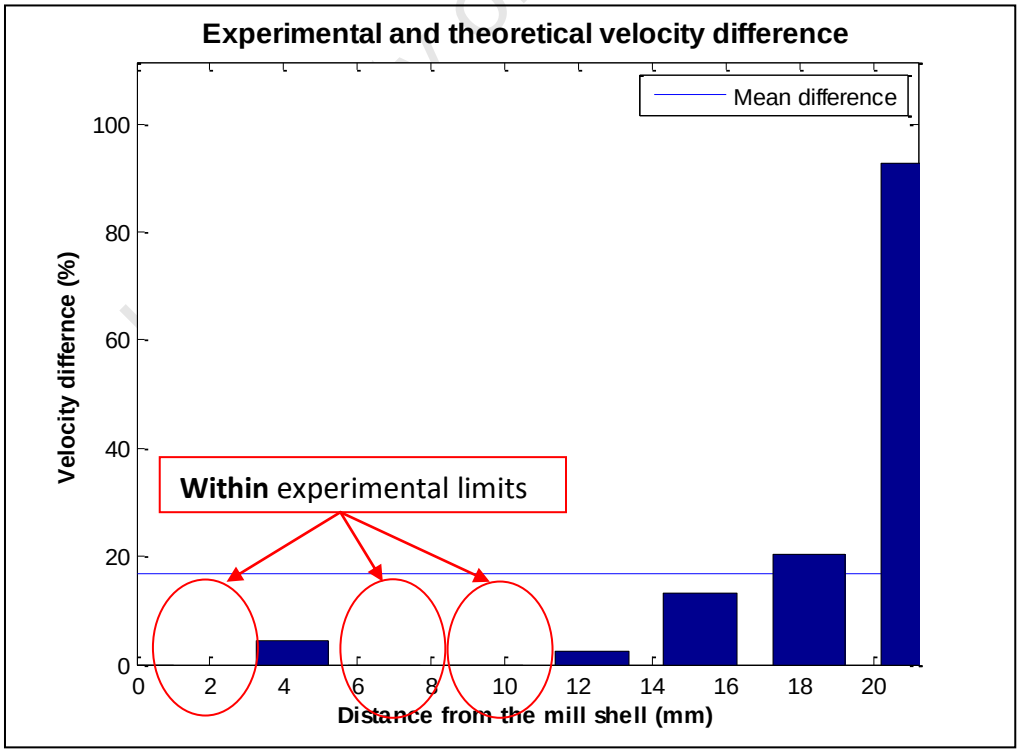

Figure 101: Percentage velocity difference for 20% mill fill, 70% mill speed and 6 mm lifter in zone 3

The calculated difference, also defined as the absolute difference, gives an indication of the magnitude and more importantly the direction. The positive errors represent a situation where the experimental data is larger than the theoretical data and the negative errors show the opposite. If the error is positive the theory under-predicts the velocity and if the error is negative the theory over-predicts the velocities. The absolute difference could give an indication of error trends. Error trends assist in highlighting if the errors are systematic or caused by certain variables chosen for the equations. The relative velocity difference only gives an indication of the magnitude of the difference and not the direction. The mean of the relative difference is taken as an indicator of the accuracy of the theoretical data to the experimental data. This allows for simpler comparison between experimental runs and theory. Taking the mean of the relative difference allows for data sets with different amounts of data points to be compared.

The differences in the residual plot need to be equally distributed for a good fit. In Figure 100 it is not well distributed, but the differences are small and there is a small amount of data. Therefore the uneven distribution of the error is not significant. The three areas with zero difference are indicators of agreement between the experimental limits and theory (Figure 100).

The relative error in Figure 101 puts the absolute error in Figure 100 into perspective. The relative error scales the absolute error to a relatable quantity, which is the mean experimental velocity. The absolute and relative error can also be used to identify the data sets in agreement with each other. The data sets in agreement are characterized by a value of 0% difference. The data sets that are in agreement are shown in Figure 101.

There is good agreement between the theoretical predictions and the experiments for the data set obtained at 20% mill fill, 70% mill speed and 6 mm lifter height in zone 3. A summary of the analysis for 20% mill fill, 70% mill speed and 6 mm lifter height in zone 3 is highlighted with green cirlces in Table 10. Data sets with good a match between the theoretical model and the experimental data are those with relatively low error values. The data sets with an error below

25% is c onsidered to be low. Table 10 shows the data sets that have these characteristics . The data from the entire experimental matrix is provided in section 16.6 in the appendix.

Table 10: Summary of the average difference, Total data, Agreement data and % Agreement data

			Average difference			Total Amount of data			Agreement			% Agreement			
Mill fill	**Mill speed**	**Lifter height**	***Zone 1***	***Zone 2***	***Zone 3***	***Zone 1***	***Zone 2***	***Zone 3***	***Zone 1***	***Zone 2***	***Zone 3***	***Zone 1***	***Zone 2***	***Zone 3***	***Mean***
20%	85%	10 mm	15.0%	31.6%	19.3%	13	9	10	3	0	0	23%	0%	0%	8%
20%	70%	10 mm	18.3%	45.0%	25.1%	13	9	6	0	1	0	0%	11%	0%	4%
20%	55%	10 mm	19.4%	33.3%	25.7%	12	13	7	3	1	1	25%	8%	14%	16%
30%	85%	10 mm	29.4%	40.3%	19.6%	17	14	8	1	1	1	6%	7%	13%	9%
30%	70%	10 mm	36.6%	41.1%	26.5%	16	16	9	1	1	1	6%	6%	11%	8%
30%	55%	10 mm	37.3%	43.2%	29.2%	16	17	10	1	2	1	6%	12%	10%	9%
40%	85%	10 mm	38.0%	34.4%	19.6%	23	17	9	0	1	1	0%	6%	11%	6%
40%	70%	10 mm	37.1%	47.6%	28.6%	22	15	9	1	1	1	5%	7%	11%	7%
40%	55%	10 mm	38.0%	55.0%	35.3%	20	21	12	2	0	1	10%	0%	8%	6%
20%	85%	6 mm	16.6%	16.3%	21.2%	12	11	8	1	3	1	8%	27%	13%	16%
20%	70%	6 mm	18.5%	16.1%	17.5%	13	12	8	4	2	3	31%	17%	38%	28%
20%	55%	6 mm	28.7%	30.4%	33.3%	10	12	8	1	1	1	10%	8%	13%	10%
30%	85%	6 mm	35.6%	40.8%	26.2%	17	13	8	0	0	1	0%	0%	13%	4%
30%	70%	6 mm	36.8%	37.6%	30.3%	16	13	9	1	0	0	6%	0%	0%	2%
30%	55%	6 mm	32.8%	45.6%	35.7%	14	16	11	0	1	0	0%	6%	0%	2%
40%	85%	6 mm	32.9%	38.0%	21.7%	23	17	8	1	1	3	4%	6%	38%	16%
40%	70%	6 mm	34.4%	47.8%	38.3%	19	20	12	0	0	1	0%	0%	8%	3%
40%	55%	6 mm	40.2%	59.6%	40.9%	20	22	13	0	1	1	0%	5%	8%	4%

The other side of the analysis is the bad data. The bad data is characterized by low agreement values and high average error values. From Table 10 an example of a data set where the velocity profile model predictions do not match the experimental data (shown by red circles). The experiment was performed when the mill was operated at 40% mill fill, 55% mill speed and 10 mm. Under these conditions the theoretical velocity deviated from the experimental values especially in zone 2. Figure 102 represents the data extraction across the entire length of the mill. The significant differences between the experimental data and the theory results are evident particularly in zone 2.

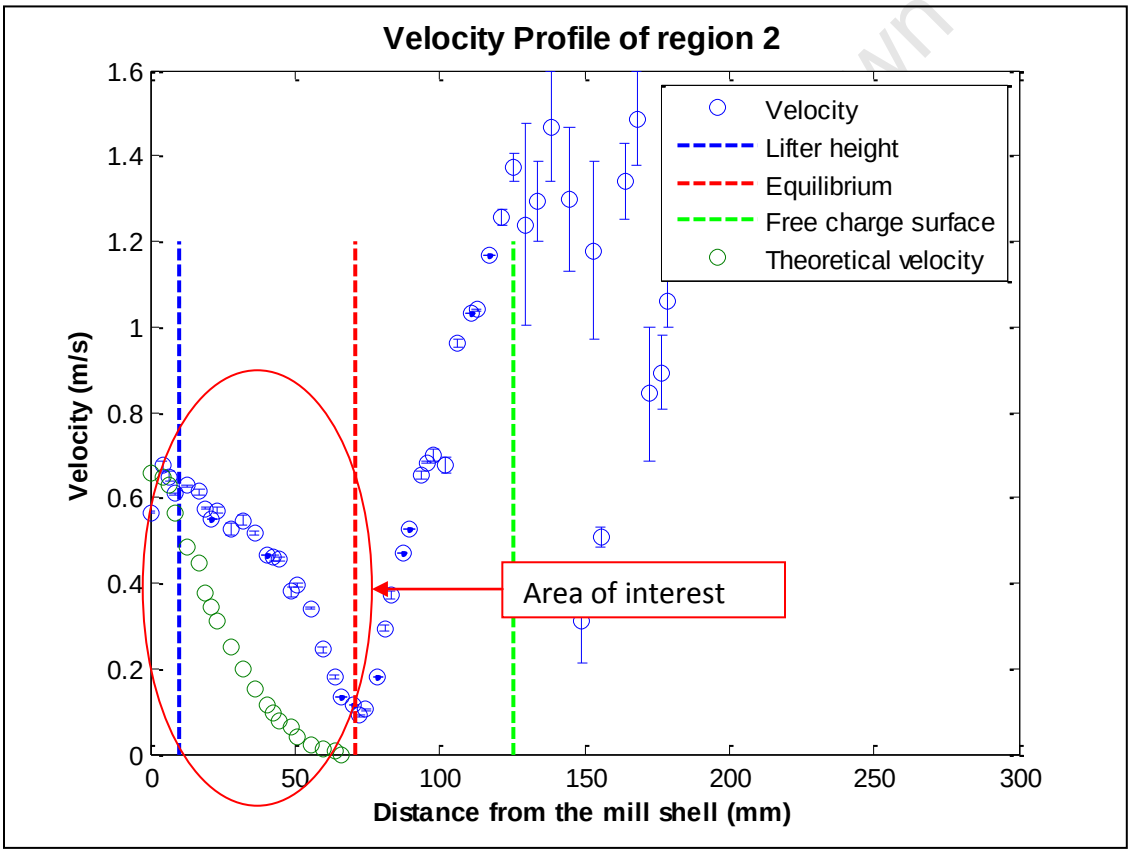

Figure 102: Velocity profile at 40% mill fill, 55% mill speed and 10 mm lifter in zone 2

The residual plot in Figure 103 shows that there is no agreement between the predicted and experimental velocities for the section of the mill analyzed. The absolute differences are significant and are not well distributed.

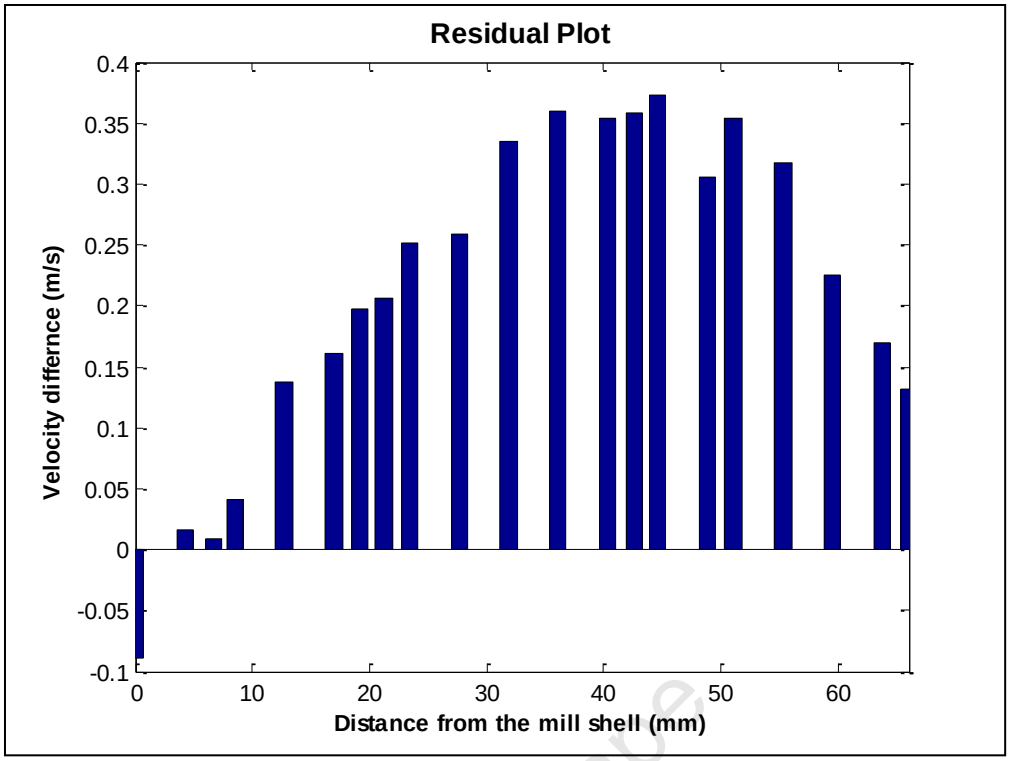

Figure 103: Absolute difference between the theoretical and experimental data for 40% mill fill, 55% mill speed and 10 mm lifter in zone 2

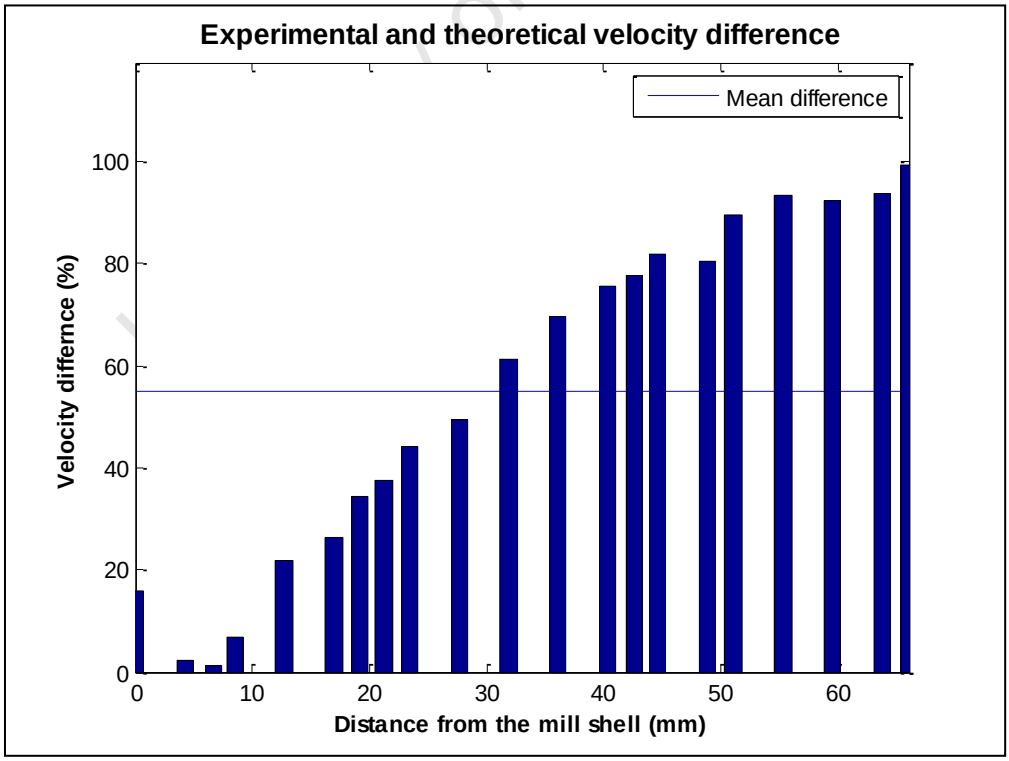

Figure 104: Percentage velocity difference for 40% mill fill, 55% mill speed and 10 mm lifter in zone 2

Figure 104 shows the plot of the relative error for data from the experiments performed at 40% mill fill, 55% mill speed and 10 mm lifter height. The plot shows that there are significant differences between the experimental and predicted velocity values. The data also indicate that the difference increases from the shell towards the centre of the mill.

12.4.4 Statistics of good statistical data sets

Data sets with good match between the predicted and experimental velocity profile have been defined by average difference below 25% and high agreement values greater than 15%. Data sets with a good match between the predicted and experimental data are summarized in Table 11.

Table 11: Summary of all good data sets

Mill filling	Mill speed	Lifter height	Zone	Mean Difference	% Agreement
20%	85%	10 mm	1	15.0%	23%
20%	55%	10 mm	1	19.4%	25%
20%	85%	6 mm	2	16.3%	27%
20%	70%	6 mm	1	18.5%	31%
20%	70%	6 mm	2	16.1%	17%
20%	70%	6 mm	3	17.5%	38%
40%	85%	6 mm	3	21.7%	38%
20%	85%	3 mm	1	15.0%	25%
20%	70%	3 mm	2	23.3%	18%
20%	70%	3 mm	3	19.5%	22%
30%	70%	3 mm	3	22.3%	20%
20%	85%	1.5 mm	3	26.3%	33%
30%	85%	1.5 mm	3	19.3%	33%

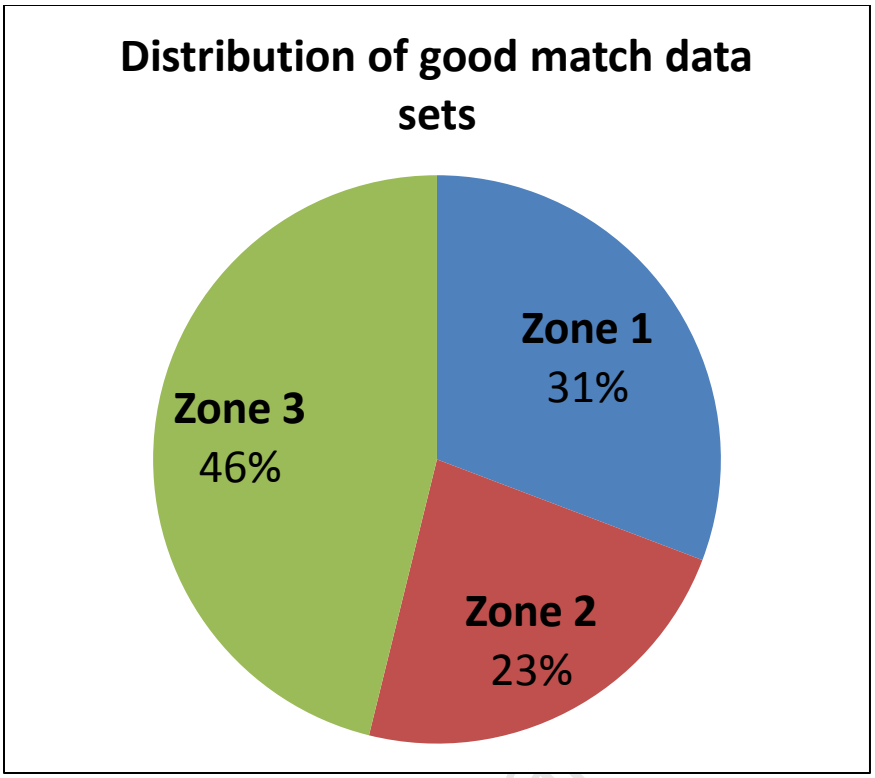

Figure 105: Distribution of good match data sets between predicted and experiments in the three different zones

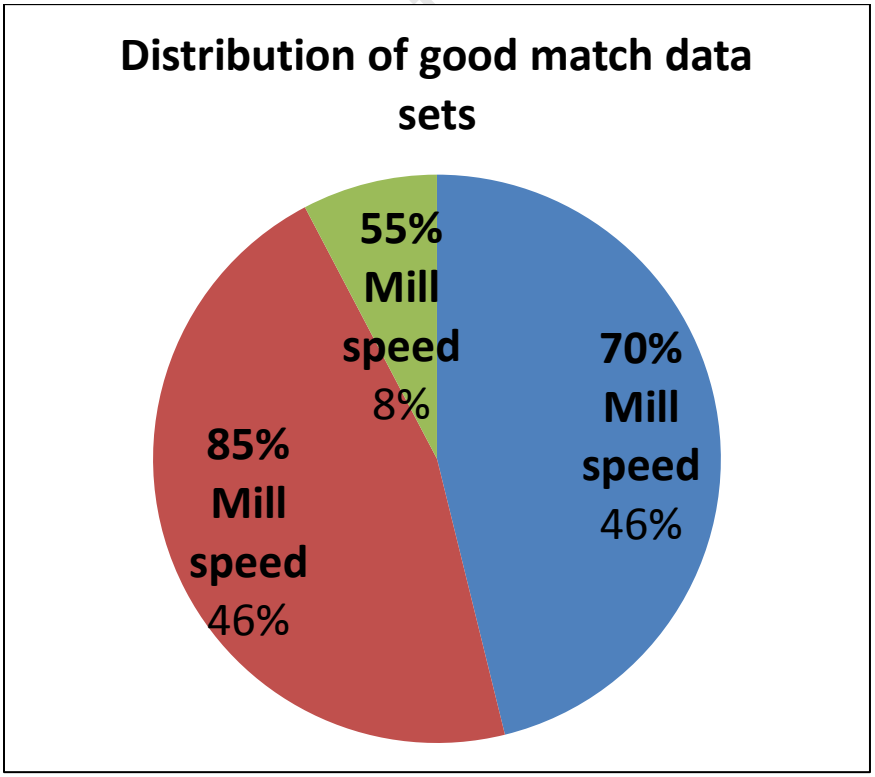

Figure 106: Distribution of good match data sets between predicted and experiments for the three different mill speeds

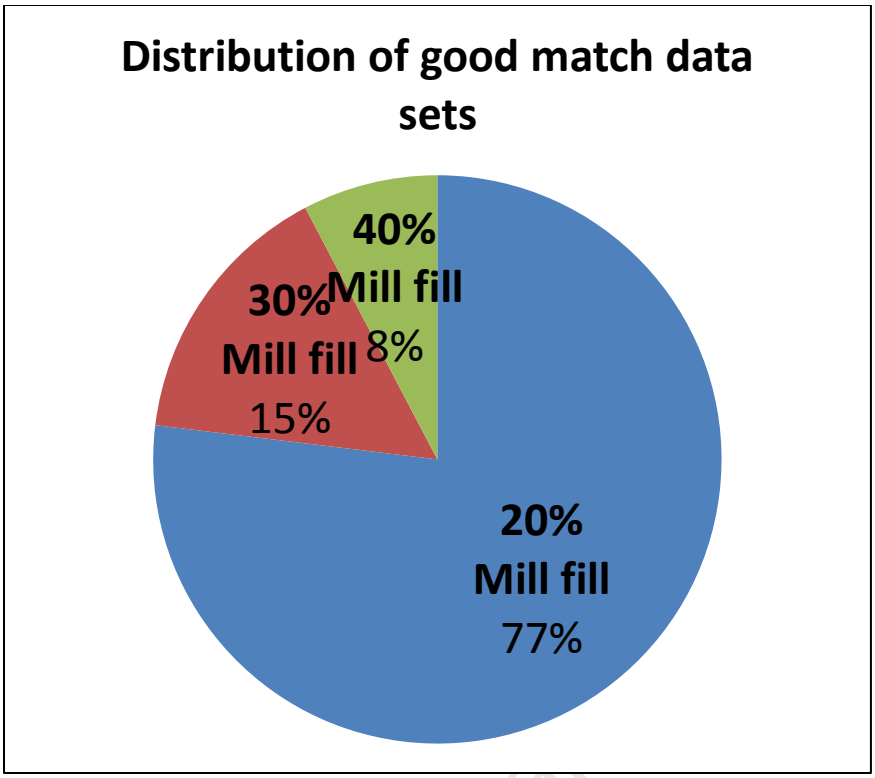

Figure 107: Distribution of good match data sets between predicted and experiments for the three different mill fills

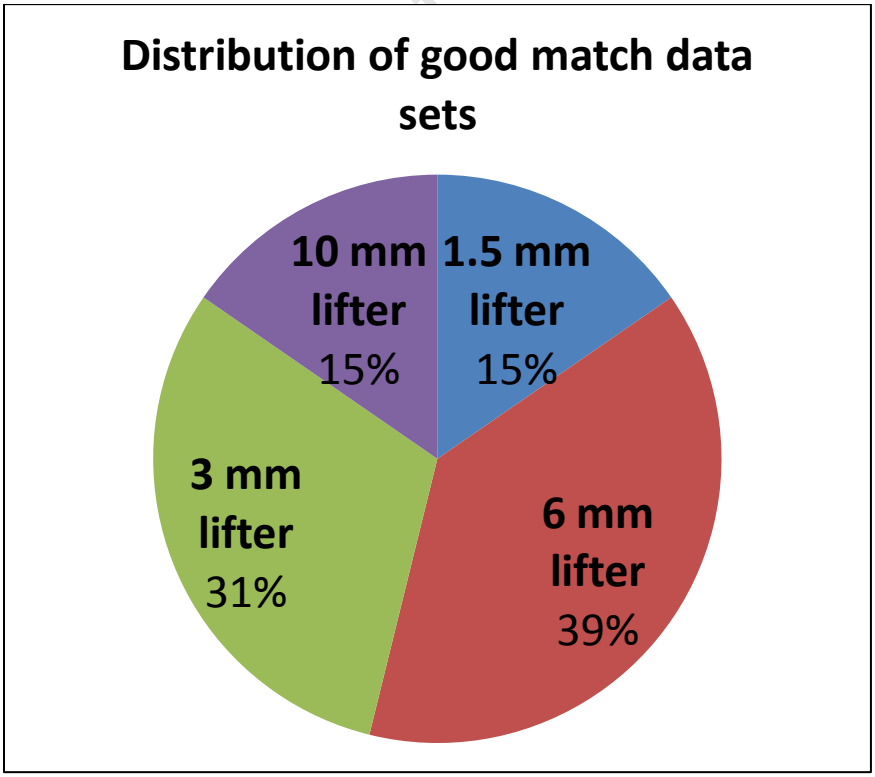

Figure 108: Distribution of good match data sets between predicted and experiments the three different lifter heights

The first analysis is done to assess the location in the charge where good matches were dominant. Figure 105 shows that most of the good matches were found in zone 3. 46% of the data sets had good matches in zone 3. Zone 2 on the other hand has 23% and Zone 1 31% of the good data sets.

The second analysis compares the matches between theoretical and experiments data at different mill speeds. The results of this analysis are found in Figure 106. From Figure 106 it can be seen that the least amount of good matches between the theoretical and experimental data was at a mill speed of 55%. Only 8% of the data sets showed good agreement between the theoretical and experimental data. The experiments performed at higher mill speeds have higher percentages of data with good matches.

The third analysis is completed by considering different mill fills. Figure 107 shows results for different mill fills distribution of data with good matches between theoretical and experimental data. From Figure 107 the 20% mill fill is the dominant mill fill value. The 20% mill fill value has 77% of the data sets had good matches, which is significantly more than 30% and 40% mill fill which have 15% and 8% respectively.

Further analysis was done on the match between theory and experimental data sets with different lifter heights. The results of the analysis are presented in Figure 108. From Figure 108 it can be seen that the 6 mm lifter height has the highest amount of data sets with a good match between theoretical and experimental data. The 3 mm lifter height is close with 31% of the good matches. The 10 mm and 1.5 mm have the lowest amount of data with good agreement.

13 Discussion

13.1 Introduction

This chapter provides a discussion of the key findings from the work. The interpretation of the data to provide insight on the influence of lifter height on some performance parameters of a tumbling mill is given.

The discussion chapter is divided up into two broad topics, namely charge profile and velocity profile analysis. The charge profile topic is further broken up into charge profile movement, charge size and toe height analysis.

13.2 Effect of lifter height on the velocity profile

The effect of lifter height on the velocity profile was considered in this work. This was done because the velocity is one of the key variables in the power models used in tumbling mills. Morrell used the velocity profile in the development of the Power Model (Morrell, 1993). In his model he shows how the power model is dependent on the velocity profile by using kinetic and potential energy to describe the power model. In addition to this most of the literature on lifters looks at power draw and energy consumption (Cleary (2001), Hlungwani et al (2003), Moys (1993), Djordjevic (2003), Djordjevic et al (2004), Mishra and Rajamani (1993)), therefore the relationship between the velocity profile and power draw or energy consumption is important in comminution. The velocity profile is related to the kinetic energy in the tumbling mill. An increase in the velocity profile will increase the kinetic energy (Morrell, 1993) which will lead to an increase in the power draw of the system. The research conducted using or measuring the velocity profiles (Govender et al (2011) and Perez-Alonso and Delgadillo (2012)) does no relate to the analysis in this chapter. Perez-Alonso and Delgadillo (2012) investigated the effect of lifter face angles and used the velocity profile to validate the 2D DEM simulation. Govender et al (2011) used the velocity profile to analyze the shear rates within a tumbling mill without varying the lifter configurations.

Comparison of velocity profile data at a specific mill fill and mill speed for all the lifter heights from specific zones were made. The aim is to isolate the effect of the lifter height by keeping the other variables constant.

13.2.1 Mill filling at 20%

At 20% mill fill and 85% mill speed the trends in Figure 67 to Figure 69 show an increase in the velocities magnitude with an increase in lifter height. The increases between 3 mm, 6 mm and 10 mm lifter are approximately uniform. However, the increase between 1.5 mm lifter and 3 mm lifter is significant and is greater than any increase seen between the other lifters.

The uniform increase in velocities with an increase in lifter height occurs because more material is keyed in and therefore more material near the mill shell has the angular speed of the mill. The term 'keyed in' describes material that is wedged between two lifters and is unable to move freely. An increase in velocity translates into a higher power draw, hence the data indicates there could be an increase in power draw with an increase in lifter height. This interpretation of the data agrees with the findings in Cleary (2001) and Hlungwani et al (2003). In both Cleary (2001) and Hlungwani et al (2003) it was found that there was an increase in power draw with an increase in lifter height. The opposite was observed in Mishra and Rajamani (1993), Djordjevic (2003) and Djordjevic et al (2004), where the power draw of the mills decreased with an increase in lifter height.

The velocity decrease from high to low lifters is similar, which means the slip between the layers from the mill shell to the equilibrium surface is consistent and behaves in the same way regardless of lifter height. The slip is similar because the friction coefficient between the layers is the same, as the charge is made entirely out of glass. The term slip in this context refers to a motion across a surface once the static frictional force has been overcome.

The significant difference between the 1.5 mm lifter and the other lifters is due to the lack of traction of the 1.5 mm lifters. The charge is not keyed in properly and it could be caused by a combination of a lack of force above the outer most material at 20% mill filling and the small lifter height. The lack of force above the outer most particles is caused by the reduced amount of material and hence mass at 20% mill filling. This creates slip and possibly a rolling action

which will result in smaller velocities as seen with the velocities of the 1.5 mm lifter. The same results would be seen in Powell (1991) if a system of a 5 mm ball and a 1.5 mm lifter were to be simulated. The angle of departure would be so low that the particle would only be partially lifted or not lifted at all.

The results so far show three possible variables that could affect the motion of a particle within a tumbling mill. The variables are friction coefficient, force due to mass/mill filling and lifter height.

13.2.2 Mill filling at 30%

This section discusses the results from the tests performed at 30% mill filling. It is expected that the velocities at the 30% mill filling are closer to each other. The increased mill filling should provide a greater force to increase traction and reduce the amount of slip between the particle layers.

Increases in velocities with an increase in lifter height are observed while operating at 30% mill filling for the speeds of 55%, 70% and 85%. These findings are similar to those found in section 13.3.1, Cleary (2001) and Hlungwani et al (2003). The opposite was found to occur in Mishra and Rajamani (1993), Djordjevic (2003) and Djordjevic et al (2004). Although, as initially stipulated the differences between the velocities is smaller than seen at 20% mill fill. The most significant change is the difference between the velocities at 1.5 mm and 3 mm which has considerably decreased. The possible reason for the decreased difference in velocities is with an increased loading there is more force on the charge near the mill shell and therefore the charge undergoes more friction, is keyed in more and as a result less slip is experienced.

The behaviour in Zone 3 (approximation of the toe region) at 85% mill speed is different when compared to Zones 1 (approximated area of the shoulder region of the charge) and 2 (approximated area of the body or en masse region of the charge), because the 1.5 mm and 3 mm lifter velocities in Zone 3 are similar as well as the velocities at 10mm and 6 mm lifter. The data indicates the degree of traction is the same for 1.5 mm and 3 mm lifters and 6 mm and 10 mm lifters. A possible reason for this behaviour could be the chaotic flow patterns in zone 3 (approximated toe region). At 85% mill speed the toe region will be an area where the particles

get mixed and are not well packed. Due to this behaviour the 3 mm and 10 mm lifter create the same traction as the 1.5 mm and 6 mm lifter, respectively. Another possible reason for the loss of traction is the reduced amount of settled material present in the toe region exerting force a downward force. Other than mixing at high mill speed (85%) the material will shift the charge up leaving less material in the toe region.

13.2.3 Mill filling at 40%

The main velocity profile trends from the mill operated at 40% mill filling and critical speeds of 55%, 70% and 85% are fairly close for different lifter. In some cases the velocities from different lifter heights cross each other. In other words, the lifter height does not show any influence on the velocity profile at 40% filling. This does not agree with the findings in Cleary (2001) and Hlungwani et al (2003) and the behaviour explained by Mishra and Rajamani (1993), Djordjevic (2003) and Djordjevic et al (2004). The charge could be behaving in such a manner due to the increased mass in the system. An increased mass translates into a greater downwards force. Therefore less slip is experienced between the particles. Less slip means there will be a much smaller difference between the velocity profiles of the different lifter heights. In this case there is not much difference between all lifter heights.

The exception to the previously mentioned trend is the behavior in zone 3 at 85% and 70% mill speed. It is observed that there is a significant difference between the velocity profiles of the different lifters. The data does not show the same closeness as seen in zone 1 and zone 2. The behavior could be different due to the nature of the toe region at higher mill speeds. In the toe region there could be less load on the particles at the mill shell when compared zone 1 or 2. The toe region becomes smaller as the mill speed increases, because the material to spread more to the shoulder region of the charge. Additionally the particles in the toe region are unsettled and bouncing, hence there is less weight (pressure/force) on the particles near the mill shell. The result is less frictions and traction between the mill shell and the charge. Thus the charge is less keyed in and for that reason there are significant differences between the velocities in zone 3 at 85% and 70% mill speeds. This phenomenon is not experienced at 55% mill speed, because the toe region is not significantly affected at low speeds.

13.2.4 General

Across all the experimental data it was found that the gradients of the velocity profiles at different lifter heights are similar, which has been highlighted in the initial plots. This could be a result of the charge having the same friction coefficient and therefore the same amount of slip. The gradient of the velocity profile gives an indication of the amount of shear experienced according to Newton's definition of shear. The magnitude of shear rate gives an indication of the amount of abrasion in various sections of the mill. Since the velocity profiles are fairly similar one can conclude that the shear rate is not influenced by lifter height. Therefore abrasion breakage cannot be tweaked by changing the lifter height which contradicts the findings of Djordjevic (2003) and Djordjevic et al (2004). In Djordjevic (2003) and Djordjevic et al (2004) it is argued that the abrasion breakage increases with an increase with lifter height. Additionally the amount of abrasion does affect the amount of fines that is produced in a mill. And increased abrasion would produce more fines. In Powell and Vermeulen (1993) and Makokha and Moys (2006) it was found that operating the mill with certain lifters the fine production can be increased. These findings are contradicted by the idea of the velocity gradients being constant and therefore resulting in the shear and abrasion being constant for the different lifter heights. The velocity gradient behavior could be explained by the constant friction coefficient (friction coefficient of glass on glass) throughout all the levels in the charge.

13.3 Toe and shoulder analysis

13.3.1 Lifter height effect on the toe and shoulder angle

The toe and shoulder angle for different lifter heights were extracted for the different mill operating conditions. The reference system for this part of the analysis was the study performed by de Haas et al (2010). Detailed research was conducted by Perez-Alonso and Delgadillo (2012) on the shoulder and toe angle. However, the lifter face angles were varied and not the lifter heights. Hence the data and analysis will not be used in this analysis.

The lifter height does seem to have an effect on the shoulder angle of the charge for different lifter heights. The trend shows subtle increases in shoulder angle with an increase in lifter height. The significant increases in shoulder angle occur between 1.5 mm and 3 mm lifters. It is

suspected that the general trend is a result of the charge being 'keyed in' and gaining more traction as the lifter heights increase. The behaviour of the charge can be explained with the fundamental understanding of work done by Powell (1991) and Powell (1990). A possible explanation for the charge behaviour is that the charge stays in longer contact with the lifter as the lifter height increases. Once the particles are outside of the bulk charge the particles will either flow down the bulk charge (cascading) or be flung across the mill into the toe region (cataracting). Before either movement commences the particle needs to travel along the lifter until it reaches the end of the lifter to enter into its motion. The greater the lifter height the further the distance the particle needs to travel to leave the lifter's surface and the more time the lifter has to elevate the particle to a greater height. In this case the height of the particle's departure is not measured, but rather the angular position it depart from. As mentioned before the data and theory in Powell (1991), Powell (1990) and Mishra and Rajamani (1993) support the increase in shoulder angle with an increase in lifter height. The research in Powell (1991) and Powell (1990) was about developing a fundamental model to predict the trajectories of the outer most grinding particle. In this study, it was argued that the particle would have to move along a longer lifter surface to reach free flight with higher lifters. Therefore the longer the particle spent on the lifter the higher its point of departure and therefore the greater the shoulder angle. Similar observations were made in Mishra and Rajamani (1993) using DEM simulations to predict the trajectories of the outermost particles. An increase in lifter height increased the shoulder height and therefore the point of departure against the mill shell.

The significant difference between the 1.5 mm and 3 mm lifter can be explained by the lack of traction created by the 1.5 mm lifter. The particles (5mm) in the charge would not require half a revolution to disembark from the 1.5 mm lifter. Therefore the moment the particle leaves the bulk charge it would start cascading down the bulk charge and it would not travel along the lifter (Powell (1991) and Powell (1990)). This would result in a much lower shoulder angle when compared to the 3 mm lifter. An additional reason for the lack of traction is the potential of the particles in the charge having a rolling motion. If the lifter height is not high enough to push the particles forward the particles will roll over the lifter and the charge will not be influenced by the 1.5 mm lifter.

The lifter height does not have a significant effect on the toe angle at a speed of 55% and 85% of critical. However, at a speed of 70% critical the lifter height appears to have a significant effect on the toe angle. The toe angle increases with an increase in lifter height at 70% mill speed. There is no direct comparison in McBride et al (2004) and Powell (1991), but from the description of the charge shifting to a higher position against the mill shell the toe angle effect can be inferred. A higher position against the mill shell will result in an increase in the toe angle. Therefore the inferred behaviour of the toe angle in McBride et al (2004) and Powell (1991) agree with the findings at 70% mill speed.

The results for the toe and shoulder angle do not match the expectations of the charge moving to a higher position against the mill shell as described in Powell (1991), Powell (1990) and McBride et al (2004). If this were the case, the toe and shoulder angle would have been significantly affected by the lifter height. It was expected that a greater portion of the charge is 'keyed in' as the lifter height increases and therefore the bulk charge would shift to a new position. It was assumed that the particle would need to travel a longer distance along the lifter surface in order to detach and therefore the particle would detach at a greater height as suggested in Powell (1991) and Powell (1990). Consequently the outer most particles should have been had an increased shoulder angle with an increase in lifter height, but this was not seen in the data presented for the shoulder angle.

13.4 Lifter height effect on the charge size

The charge size has a significant link to the toe and shoulder angles of the charge. The charge size is determined by subtracting the toe angle from the shoulder angle, so that the angle between both characteristic points is determined.

The charge size was analyzed with respect to lifter height. The results show that there is no effect on the charge size when changing the lifter height. The inconsistent behaviour of the charge size can be attributed to the inconsistent behaviour of the toe region with lifter height. The shoulder angle does have a consistent relationship with the lifter height, but it is not significant enough to translate into a consistent charge size relationship with lifter height. The findings disagree with the data found in McBride et al (2004). The data, in McBride et al (2004),

shows that the charge size increases with an increase in lifter height. The difference between the data sets could lie in the processing of the data. The data in McBride et al (2004) is taken from DEM simulations and was not used to process the probability distribution plots. These plots would give an indication of the time spent in any area within the mill, which was used for the PEPT data. Hence the point defined as the toe and shoulder region might have been less accurate, because it could have been based on a particle path only used a few times.

13.5 Lifter height effect on the toe height

The toe height is of interest, as it affects the area and the magnitude of impact. The toe height affects the velocity of the particles landing in the impact area and hence their momentum. Increasing the time in flight increases the velocity of the particle due to the gravitational acceleration. A higher momentum translates into a greater impact magnitude; hence the toe height affects the magnitude of impact.

The lifter height does have an effect on the toe height. Although, varying the lifter height does not produce a consistent trend between the different mill fillings. At 30% and 40% mill filling the effect of the lifter height is not as pronounced as at 20% mill filling. The average shifts in toe height at 30% and 40% mil filling are between 5 and 10 mm. The maximum toe height shift is 30 mm at 20% mill filling. Therefore lifter height has the most significant effect on the toe height at 20% mill filling.

At 20% mill filling, the toe height increases between the 1.5 mm and 3 mm lifter from approximately 36 mm to 56 mm at 70% and 55% mill speed. The increase in toe height could be explained by the possible change in movement of the particles from a rolling action to a motion with more traction in the toe region when changing from a 1.5 mm to a 3 mm lifter. The rolling action would allow the charge to form a thinner and longer 'tail' in the toe region. Once enough traction is created through an increase in lifter height the rolling action ceases which shortens the 'tail' of the toe region and compresses the particles into the toe region increasing the height of the toe region. The findings at 55% and 70% mill speed coincide with the data in McBride et al (2004), where an increase in lifter heights translates into an increase in toe height.

The toe height at 20% mill filling decreases at 70% and 85% mill speed and it occurs after the 3 mm and 6 mm lifters, respectively. It would indicate a significant change in charge shape. A decrease in toe height would occur if the toe region is allowed to develop a 'tail' where the material in the toe region is more thinly spread out in the toe region. Or if material is displaced from the toe region into the shoulder and en masse region due to increased friction and traction. In this case the latter is suspected to be the reason for the decrease in toe height. A combination of increased lifter height and centrifugal forces due to increased mill speeds increased the traction within the mill to decrease the toe height. In McBride et al (2004) the data shows that the toe height increases with an increase in lifter height. Therefore the findings in McBride et al (2004) contradict the findings made at 20% mill filling. It has to be noted that the percentage filling used for the McBride et al (2004) experiments was significantly more than 20% mill filling. An increased mill filling could influence the friction and traction the particles experience closer to the mill shell. An increase in mill filling could does increase the milling and could increase the force exerted on the particles close to the mill shell. Additionally DEM data was used which does not take into account the number of times a particle has taken a particular path. This means a particle could have gone through the path once to create an impression of an increase in toe height.

The toe height could be related to the toe angle and could give an indication of the magnitude of the impact in the toe region. This could give an additional online measurement by measuring the toe angle. The toe height could be related to the toe angle by the movement of the toe region. It is stipulated that the toe height increases with a decrease in toe angle.

13.6 Charge profile relationships

Through the behavior of the different charge profile characteristics it can be seen that there is a relationship between charge movement (toe and shoulder angle), charge size and toe height. The relationship between the charge size and toe and shoulder angles is imbedded in the definition of the charge size. The charge size is determined by measuring the toe and shoulder angle and then subtracting the toe angle from the shoulder angle. Therefore when the shoulder angle increases and the toe angle decreases the charge size will increase. If the shoulder angle

decreases and the toe angle increase the charge size decreases. If both the toe and shoulder angle increase or decrease then the magnitude of these changes are needed to determine the effect on the charge size. An example is the case where the shoulder angle increases more than the toe angle and then the charge size increases.

The effect the charge movement has on the toe height is one dimensional. The toe height is solely affected by the toe angle. The relationship is simple, where an increase in toe angle results in a decreased toe height and vice versa. The toe height also has a relationship with the charge size. When the charge size increases the toe angle decreases, which results in an increase in toe height. Therefore the charge characteristics are all interconnected. Once the relationships are defined all the charge profile characteristics can be inferred by one set of data, which will most likely be toe and shoulder angle.

13.7 Velocity Profile

13.7.1 Comparison between experimental and theory

Two methods are used to conduct the comparison between the experimental and theoretical data, namely the percentage agreement and mean error from the 99% confidence interval. The percentage agreement counts how many times the theoretical velocity data falls within the 99% confidence interval of the experimental data. The mean error is the average difference between the theoretical data and the 99% confidence interval's border. Data with a good fit will have a high percentage agreement (≥15%) and a low mean error (≤25%). Data with a bad fit will have a low percentage agreement (≤15%) and a high mean error (≥25%). The mean error is used to verify the closeness of the theoretical data to the experimental data. However, a greater emphasis is put onto the percentage agreement during the comparison.

The best fit between the theoretical and experimental data has an agreement of 38% (3 out of 8) and a mean error of 17.5%. The mill was operating at 20% mill fill with a 6 mm lifter height at a mill speed of 70% of critical in zone 3. The mean error is relatively high considering that it has 38% agreement and most errors have a value of below 20%. The largest contributor to the mean error is the last data point. The difference between the theoretical and experimental data for the last data point is 90%. The worst fits was found while operating the mill at 40% mill fill

with a 10 mm lifter at a mill speed of 55% of critical in zone 2. The percentage agreement was 0% and the mean error was 55%.

The data and analysis show that the experimental data is not satisfactorily predicted by the theoretical velocity profile model. These findings contradict the results in Govender et al (2011), where the difference between the experimental and theoretical data was not significant. The equation derived from the data could be used to predict the experimental data. However, it has to be noted that the equation developed in Govender et al (2011) is an empirical model. The model requires six constants and will only be accurate for the data set used to develop the model.

Despite the inaccuracies of the theoretical model, the underlining trend of the theoretical data when compared to the experimental data might give further insight into potential methods of improving the theoretical velocity profile model. The comparison between the theoretical and experimental data shows, with the help of the residual plots, that the theoretical data consistently under-predicts the experimental data. The component in the theoretical velocity profile model that influences the velocity the most is the shear and the friction coefficient. The friction coefficient is a constant and is related to the material inside the mill, hence the friction coefficient cannot be changed. The theory used to describe shear can be changed. The shear equation used in the current velocity model is defined by the Newtonian fluid assumption, where the shear is dependent on viscosity and the velocity gradient. An alternative would be the Bagnold equation (Bagnold (1954)), which includes physical properties (e.g. particle size and voidage) of the material. Using the Bagnold definition might assist in increasing the accuracy between the experimental and theoretical data.

13.7.2 Statistics of the good data sets

This analysis takes all the data sets with good fits and puts them into categories in terms of location and conditions. The analysis helps to understand situations where the velocity profile model was able to successfully predict the experimental outcomes.

The mill speed analysis shows that the least amount of good fits occurred when the mill was operated at 55% mill speed. At 55% mill speed only 8% of the data had good fits. The reason for

this could be that at 55% mill speed there is no shearing effect, which is a dominant effect in the velocity model. This is in stark contrast to both the 85% and 70% mill speed. The highest amount of good fits was found at 70% and 85% mill speed, where both had 46% of the data fitting well.

From the mill fill analysis the 20% mill fill had 77% of the data with good fits while 30% and 40% mill fill had only 15% and 8% of the good fits, respectively. This indicates that the velocity profile model matches experimental data well at low mill fills.

During the lifter height analysis it was found that both the 10 mm and 1.5 mm lifter has the lowest amount of good fits. The highest amount of good fits, which is 39%, was found when using the 6 mm lifters while the lifter height of 3 mm had 31%. Therefore the velocity profile model is best for the new and intermediate lifters and not the worn and extremely high lifters.

The velocity profile model predicts best at 20% mill fill at either 85% or 70% mill speed with a lifter height of 6 mm or 3 mm in zone 3 of the charge.

13.8 Value of velocity profile

The velocity profile is a base from which a new power model can be built, which has already been shown in Morrell (1993) where a velocity profile was the underpinning development to the resultant power model. The velocity profile can be used for an alternative analysis, where it is used to determine the power dissipation within the charge. The value in this analysis is the potential predictive ability of areas with high grinding and abrasion. Assuming the velocity profile is accurate and representative it can be used to determine the shear stress within the charge. Taking the difference between the shear stresses will result in force dissipation along the velocity profile reference plane. Then by multiplying the velocity with the dissipated force the dissipated power of the charge can be determined. Mapping the entire charge with these calculations, the high grinding and abrasion areas can be identified. The findings of this analysis will open research up into areas of particle segregation and manipulation of operating conditions to allow the desired particles to congregate at high grinding zones.

14 Conclusion

14.1 Introduction

This chapter presents the major findings of the work undertaken in this thesis. The effect of the lifter height on the velocity profile, toe and shoulder movement, charge size and toe height are presented. Then after a summary of the comparison of the theoretical and experimental velocity profile is given. A section on potential future work and suggestions on how to make the experiments and future work more comparable to real systems are given.

14.2 Effect of lifter height on the velocity profile

The effect of lifter height on the velocity profile was assessed for different volumetric fillings and mill speeds.

The lifter height has the most significant effect at a mill filling of 20%, where the velocity increased with an increase in lifter height. At 30% and 40% mill filling the lifter height does not have a significant effect. This is most apparent when the velocity profile for a 1.5 mm and 3 mm lifter are compared.

In addition the data showed that the velocity profile gradients at different lifter heights are similar. Hence according to Newton's definition of shear the shear is independent of lifter height and from this is could also be deduced that the amount of abrasion and fine production is independent of lifter height.

14.3 Lifter height effect on the toe and shoulder

Lifter height does not seem have an influence on the toe region, because no clear trend was found in any of the experimental data sets to suggest a relationship between lifter height and toe angle. A consistent trend was not found, because the toe region is a chaotic region and any subtle deviations will not be identified.

The shoulder angle is affected by the lifter height. The experiments and data have shown that an increase in lifter height increases the shoulder angle. The suspected reason is that the

charge particles take a longer time to discontinue contact with larger lifters and hence are carried to a higher position within the mill resulting in a larger shoulder angle.

14.4 Lifter height effect on the charge size

The lifter height does not have a significant effect on the charge size, because of the inconsistent relationship between the toe angle and the lifter height. The charge size is dependent on the toe and shoulder angle. The relationship between the shoulder angle and lifter height is not significant enough to influence the relationship of the charge size and lifter height.

14.5 Lifter height effect on the toe height

The toe height is affected by lifter height. The effect of the lifter height on the toe height is not well pronounced for the 30% and 40% mill filling, because the toe region for both mill fillings is not well defined as a result of the chaotic behaviour in the region. However, the lifter height effect on the toe height at a 20% mill filling highlights the trend well. Between 1.5 mm and 3 mm lifter the toe height increase and after the 3 mm lifter the toe height decreases.

14.6 Velocity Profile

14.6.1 Comparison between experimental and theory

An attempt to develop a model for the prediction of the velocity profile for the mill operated with different lifter profiles was made. The velocity profile from the model was then compared to the PEPT experimental data. It was found that the model matched the experiments in certain regions, but gave incorrect predictions in others. This is due to the influence of the shear component of the model. The friction coefficient is another variable, but it is a constant value because the charge is made up entirely of glass beads. The shear is currently defined by the Newtonian fluid assumption and it is dependent on viscosity and velocity gradients. The charge is not a fluid; hence an estimation of a viscosity for a solid carries a significant deviation from reality. The model predictions might improve if an alternate method of estimating the charge's shear would be used. A recommendation would be to use the Bagnold equation (Bagnold (1954)), which includes physical properties (e.g. particle size and voidage) of the material.

The objectives of the research have been met. The lifter height effect on the velocity profiles and the charge toe and shoulder have been evaluated. An attempt was made to develop a velocity profile model using granular flow theory and the PEPT data was used to validate the velocity profile model. The hypothesis was answered through the experiments and analysis and theses answers are presented in the conclusions. The key questions have been answered throughout the thesis.

The ultimate aim of the studies using the PEPT system to evaluate the influence of lifter bars on mill performance is to improve energy efficiency in tumbling mills.

14.7 Recommendations for future work

14.7.1 Potential adjustments to the velocity profile model

After all the analysis certain aspects of the velocity profile model have been identified for improvements. The following assumptions have been identified for change:

- Newtonian fluid
- Constant viscosity

The Newtonian fluid assumption is a simplification of the fluid behavior of the granular flow system. Instead of using the Newtonian assumption, the Bagnold equation (Bagnold (1954)) can be used to define shear. The Bagnold equation is unique, as it takes particle size and concentration into account. The viscosity term, as a whole, needs to be adjusted. Either the viscosity of the granular material needs to be estimated or it needs to be replaced by an equation that takes friction and drag into account. The other aspect of the equation that would need attention is the separately integrated friction. It might be more useful to integrate the friction component into the velocity equation, so that it is less dependent on experimental measurements.

15 References

Andersson, S. (2010). *Wear Simulation.* Royal Institute of Technology (KTH) Stockholm. Stockholm: Royal Institute of Technology (KTH) Stockholm.

Arbeiter, N., & Harris, C. (1982). Scale up and Dynamics of Large Grinding Mills - a Case Study. In A. Mular, & G. Jergensen II, *Design and Installation of Comminution Circuits* (pp. 491 - 505). New York: AIME.

Archard, J. (1953). Contact and rubbing of flat surfaces. *Journal of Applied Physics , 24* (1), 18-28.

Barbara, C. C. (2010). *COURS 2 : IMAGERIE MÉDICALE*. Retrieved 2 8, 2011, from http://www.ccsb.org/upload/Image/Machines/ECAM1.JPG

Bbosa, L., Govender, I., Mainza, A., & Powell, M. (2011). Power draw estimations in experimental tumbling mills using PEPT. *Minerals Engineering , 24*, 319-324.

Bird, R., Stewart, W., & Lightfoot, E. (2007). *Transport Phenomena* (Revised 2nd Edition ed.). New York: Wiley & Sons, Inc.

Böhm, T., Ancey, C., Frey, P., Jodeau, M., & Reboud, J. (2005). Experiments on gravity-driven particle flows in a turbulent stream. *Powders and Grains* .

Bond, F. (1962). Additions and revisions to 'Crushing and grinding calculations'. *Allison Chalmers Publication* .

Bond, F. (1961). Crushing and grinding calculations. *Allison Chalmers Publication* .

Bonnecaze, R., & Lister, J. (1999). Particle driven gravity currents down planar slopes. *Journal of Fluid Mechanics , 390*, p.75-91.

Box, T. E. (2011). *The Engineering Tool Box*. Retrieved December 7, 2011, from http://www.engineeringtoolbox.com/friction-coefficients-d_778.html

Choi, J., Kudrolli, A., Rosales, R., & Bazant, M. (2004). Diffusion and mixing in gravity-driven dense granualr flows. *Physical Reviw Letters , 92* (No. 17), 174301.

Cleary, P. (2001). Charge behaviour and power consumption in ball mills: sensitivity to mill operating conditions, liner geometry and charge composition. *International Journal of Mineral Processing* (59), 79-114.

Cleary, P., & Hoyer, D. (2000). Centrifugal mill charge motion and power draw:comparison of DEM predictions with experiment. *International Journal of Mineral Processing , 59* (2), 131-148.

Cundall, P., & Strack, O. (1979). A discrete numerical model for granular assemblies. *Geotechnique , 29*, 47-65.

Davis, E. (1919). Fine crushing in ball mills. *AIME Transactions , 61*, 250-296.

Djordjevic, N. (2003). Discrete element modelling of the influence of lifters on power draw of tumbling mills. *Minerals Engineering , 16* (4), 331-336.

Djordjevic, N., Shi, F., & Morrison, R. (2004). Determination of lifter design, speed and filling effects in AG mills by 3D DEM. *Minerals Engineering* , 1135 -1142.

Fuerstenau, D., & Abouzeid, A. (2002). The energy efficiency of ball milling in comminution. *International Journal of Mineral Processing , 67*, 161-195.

Fuerstenau, M., & Han, K. (2003). *Principles of Mineral Processing.* Littelton: SME.

Giovannoni, A. (2009). *Triangulation and smoothing of PEPT data.* University of Cape Town. Cape Town: University of Cape Town.

Govender, I. (2008). *Applied Physics Group, Physics Department, University of Cape Town*. Retrieved 2 8, 2011, from www.phy.uct.ac.za/.../xray/xray.htm

Govender, I., & Powell, M. (2006). An empiricial power model derived from 3D particle tracking experiments. *Minerals Engineering* , 1005-1012.

Govender, I., Mangesana, N., Mainza, A., & Franzidis, J.-P. (2011). Measurement of shear rates in a laboratory tumbling mill. *Minerals Engineering , 24* (3-4), p.225-229.

Govender, I., Powell, M., & Nurick, G. (2001). 3D particle tracking in a mill: A rigorous technique for verifying the DEM predictions. *Mineral Engineering , 14* (10), 1329-1340.

Handbook, E. (2004). *Engineer's Handbook*. Retrieved December 7, 2011, from http://www.engineershandbook.com/Tables/frictioncoefficients.htm

Hlungwani, O., Rikhotso, J., Dong, H., & Moys, M. (2003). Further validation of DEM modeling of milling-effects of liner profile and mill speed. *Minerals Engineering , 16* (10), 993-998.

Hogg, R., & Fuerstenau, D. (1972). Power relationships for tumbling mills. *Trans. SME/AIME* , 418-423.

Kalala, J., Bwalya, M., & Moys, M. (2005). Discrete element method (DEM) modeling of evolving mill liner profiles due to wear. Part III. Industrial case study. *Minerals Engineering , 18* (15), 1392-1397.

Kallon, D., Govender, I., & Mainza, A. (2011). Circulation rate modelling of mill charge using positron emisson particle tracking. *Minerals Engineering , 24*, 282-289.

Liddell, K. (1986). The effect of mill speed, filling and pulp rheology on the dynamic behaviour of the load in a rotary grinding mill. *MSc Thesis* , University of Witwatersrand.

Makokha, A. B., & Moys, M. H. (2006). Towards optimising ball-milling capacity: Effect of lifter design. *Minerals Engineering , 19*, 1439-1445.

Mc Bride, A., Govender, I., Powell, M., & Cloete, T. (2004). Contribution to experimental validation of the discrete element method applied to tumbling mills. *Engineering Computations - International Journal for Computer-Aided Engineering and Software , 21* (No. 2/3/4), p119-136.

Meaders, R., & MacPherson, A. (1964). Technical Design of Autogenous Mills. *Mining Engineering* , 81-83.

Mellmann. (2001). The transverse motion of solids in rotating cylinders - forms of motion and transition behavior. *Powder Technology* (118), 251-270.

Miner, W. (2005). *A tool wear comparative study in turning versus computer simulation in 1018 steel.* Brigham Young University. Utah: Brigham Young University.

Mishra, B., & Rajamani, R. (1993). Numerical simulation of charge motion in a ball mills: lifter bar effect. *Society for Mining, Metallurgy and Exploration* , 86-90.

Molinari, J., Ortiz, M., Radovitzky, R., & Repetto, E. (2000). *Finite-element modeling of dry sliding wear in metals.* California Institute of Technology. California: CALTECH.

Morrell, S. (1993). *The prediction of power draw in wet tumbling mills.* University of Queensland. Queensland: University of Queensland.

Morrison, A. (2011). *In conversation.* Cape Town: Universiaty of Cape Town.

Morrison, A., Bbosa, L., Newling, J., Fowkes, N., & Govender, I. (2010). *Positron Emission Particle Tracking.* University of Cape Town. Cape Town: Universiy of Cape Town.

Moys, M. (1990). A model for mill power as affected by mill speed, load volume and liner design. *Preprints of the 7th European Symposium of Comminution* , 395-607.

Moys, M. (1993). A model of mill power as affected by mill speed, load volume and liner design. *Journal of South African Institute of Minerals and Metallurgy* , 135-141.

Napier-Munn, T., Morrell, S., Morrison, R., & Kojovic, T. (2005). *Mineral Comminution Circuits Their Operation and Optimisation* (3rd Edition ed.). Queensland: Julius Kruttschnitt Mineral Research Centre.

Othmer, K. (2007). *Kirk-Othmer Encyclopedia of Chemical Technology* (5th Edition ed.). New York: John Wiley & Sons, Inc.

Parker, D. J., Dijkstra, A. E., Martin, T. W., & Seville, J. P. (1997). Positron emission particle tracking studies of spherical particle motion in rotating drums. *Chemical Engineering Science , 52* (13), 2011-2022.

Parker, D., & Fan, X. (2008). Positron emission particle tracking—Application and labelling techniques. *Particuology , 6* (1), 16-23.

Parker, D., Allen, D., Benton, D., Fowles, P., & McNeil, P. (1997). Developments in particle tracking using the Birmingham Positron Camera. *Nuclear Instruments and Methods in Physics Research , 392* (1-3), 421-426.

Parker, D., Broadbent, C., Fowles, P., Hawkesworth, M., & McNeil, P. (1993). Positron emission particle tracking: A technique for studying flow within engineering equipment. *Nuclear Instruments and Methods Physics Research Section A , 326*, 592-607.

Parker, D., Forster, R., Fowles, P., & Takhar, P. (2002). Positron emission particle tracking using the new Birmingham positron camera. *Nuclear Instruments and Methods in Physics Research Section A , 477* (1-3), 540-545.

Perez-Alonso, C., & Delgadillo, J. (2012). Experimental validation of 2D DEM code by digital image analysis in tumbling mills. *Minerals Engineering* , 20-27.

Powell, M. (1993). *A study of charge motion in rotary mills.* University of Cape Town. Cape Town: University of Cape Town.

Powell, M. (1990). Improving the Design of the Liners of Rotary Mills. *International Deep Mining Conference: Innovations in Metallurgical Plant.* Johannesburg: SAIMM.

Powell, M. (1991). The effect of liner design on the motion of the outer grinding elements in a rotary mill. *International Journal of Mineral Processing* , 163-193.

Powell, M., & Nurick, G. (1996). A study of charge motion in rotary mills-Part 1: Extension of the Theory. *Minerals Engineering , 9* (2), 259-269.

Powell, M., & Nurick, G. (1996). A study of charge motion in rotary mills-Part 2: Experimental work. *Minerals Engineering , 9* (3), 343-350.

Powell, M., & Nurick, G. (1996). A study of charge motion in rotary mills-Part 3: Analysis of Results. *Minerals Engineering , 9* (4), 399-418.

Powell, M., & Vermeulen, L. (1993). The influence of liner design on the rate of production of fines in a rotary mill. *Minerals Engineering* , 169-183.

Powell, M., Smit, I., Radziszewski, P., Cleary, P., Rattray, B., Eriksson, K., et al. (2005). *The Selection and Design of Mill Liners.* Cape Town: University of Cape Town.

Rastello, M., Ancey, C., Ousset, F., Magnard, R., & Hopfinger, E. (2002). An experimental study of particle-driven gravity currents on steep slopes with entrainment of particles. *Natural Haxards and Earth System Sciences* , p.181-185.

Rezaeizadeh, M., Fooladi, M., Powell, M., & Mansouri, S. (2010). Experimental observations of lifter parameters and mill operation on power. *Minerals Engineering , 23*, 1182-1191.

Van Heerden, M. (2011). *In conversation.* Cape Town: IThemba Labs.

Venugopal, R., & Rajamani, R. (2001). 3D simulation of charge motion in tumbling mills by discrete element method. *Powder Technology , 115* (2), 157-166.

Vermeulen, L. (1985). The lifting action of lifter bars in rotary mills. *Journal of South African Institute of Mining and Metallurgy* , 15-63.

Welty, J., Wicks, C., Wilson, R., & Rorrer, G. (2001). *Fundamentals of Momentum, Heat and Mass Transfer* (4th Edition ed.). New York: John Wiley & Sons, Inc.

16 Appendices

16.1 Velocity Profile Development Theory

16.1.1 Introduction to granular flow theory

Granular flow theory characterizes the flow and mechanics of granular material. The types of granular material can vary widely from coffee beans to coal. The granular flow concept is not size limited, which means the particle's size can vary from a bolder to small steel bearings. The applicability of granular flow theory stretches across different industries and environmental situations. The industries that are most affected by granular flow theory are those that deal with materials handling such as the chemical, metallurgical and pharmaceutical industries to name a few. In the field of science granular flow theory has been used to model and describe the movement of a few natural occurrences such as avalanches and volcanic eruptions to name a few.

Usually granular flow theory is treated as a two phase system. Water or gas is modeled with the granular material. An example of such systems is the fluidized bed, which can be driven by air or water. Frequently granular flow modeling is conducted on systems with a mixture of water and granular material flowing down an incline plate. Research done by Bonnecaze and Lister (1999) dealt with the gravity driven flow of a fluid and granular material. Böhm et al (2005) and Rastello et al (2002) also published papers on the same subject, except the granular material that Böhm et al (2005) used were glass beads compared to the sawdust that was used by Rastello et al (2002). This again highlights the wide applicability of granular flow theory and its size independence.

Granular flow theory is frequently used for single phase systems as well. The research on single phase systems, where the focus is solely on the granular material, has more practical descriptions and experimental setups. The single phase systems can range from grain silos to pharmaceutical drying units. An example of the balance between a practical system and the underlying fundamentals can be seen in the research conducted by Choi et al (2004) on the

particles drained from a silo. The focus of the research was on the transport properties of the particles being drained.

The same balance between fundamentals and a practical system needs to be struck in this research, which is based on a tumbling mill. The granular flow theory will be used for a single phase system in this research. The granular flow theory will be used to model the behaviour of the particles in a tumbling mill by using a continuum approximation. The novel approach for the tumbling mill modeling will be guided by experimental observations

16.1.2 Observations

The granular flow theory is a fundamental development of the flow regions in a charge. Despite the fundamental nature, a real and practical picture of the system needs to be built up. Experimental tracking data using the Positron Emission Particle Tracking (PEPT) is used to build up an understanding of the charge of the mill. The PEPT data that is presented in this chapter does not represent research specific data. The data is shown to highlight certain characteristics of the charge and assist in the development of the granular flow theory.

16.1.2.1 Positron Emission Particle Tracking (PEPT)

The PEPT method is a 3D particle tracking method that uses a powerful camera to track nuclear irradiated particles. For further information on the camera and its performance, please refer back to the literature review. The way the PEPT system works and operates has been discussed on the literature review, but the data processing has not been mentioned yet.

The PEPT method is used to analyze the velocity function, because PEPT measures the average velocity of a particle in experimental tumbling mill accurately. An example of this can be seen in Figure 109. In addition to the velocity readings the PEPT method is able to represent the probability distribution of the particles in the experimental mill, which can be seen in Figure 111.

The PEPT data used in this project are based on tracking glass beads in an experimental tumbling mill. This is not a reflection of the limitations of the PEPT system, but rather a result of the simplified experimental setup. The PEPT system is able to track particles in real systems,

where the charge is made of slurry. In Govender et al (2010) irradiated glass beads were tracked while in a slurry, which was made of approximately 1 mm bluestone particles. The difference between the experiments is the clarity and accuracy of the experiments. The β^+ gamma-rays of the irradiated particle in the glass bead experiments have to travel through less material and less dense material. Therefore the data has a greater accuracy.

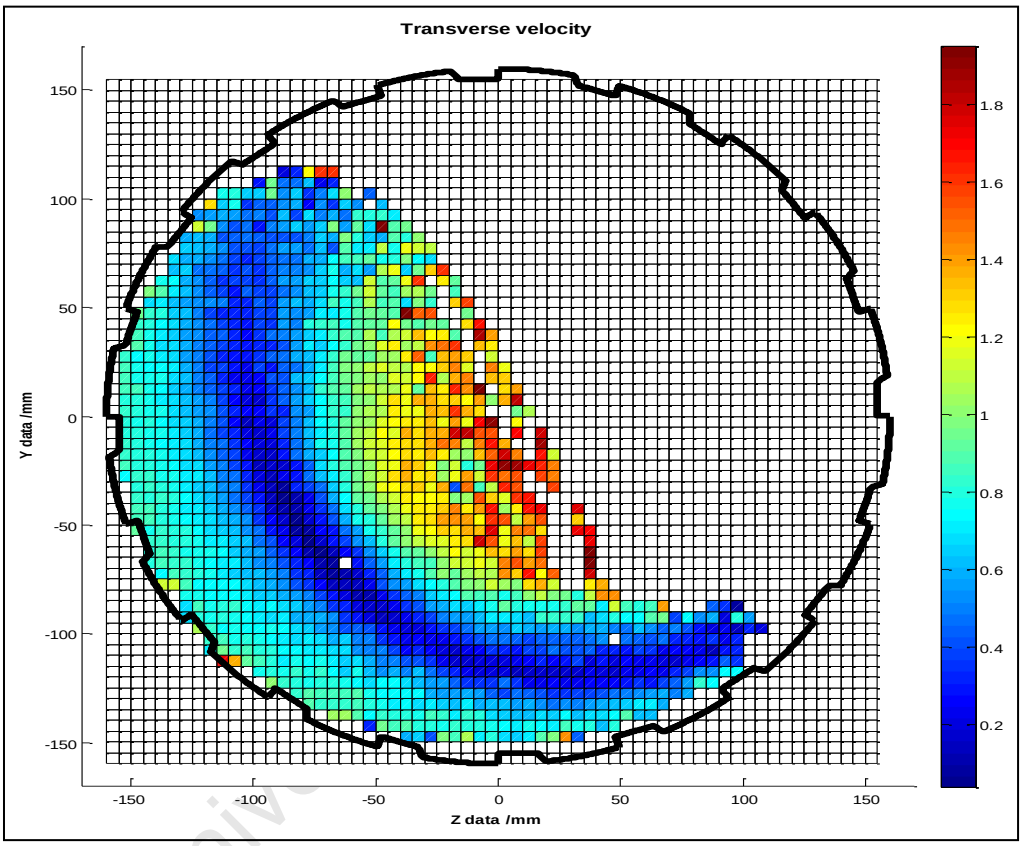

Figure 109: Transverse velocity

16.1.2.2 Different flow regions

The PEPT data can be presented in different ways. Figure 109 and Figure 110 are examples of the same variable being presented in two different ways. Both methods will assist in describing the characteristics of the charge. From Figure 110 it is clear to see that there are two different flow regions in the charge. These flow regions are separated by turning points, which are the moments the particles change the velocity direction and therefore direction of flow. Changing the direction of the velocity means that there is a point at which the particle has a zero velocity. Therefore every different layer of particles will have a different point at which it is zero, which

creates a line of zero velocities. However this is not isolated to the slice of data that we are exposed to and it is true for the entire charge. Therefore the zero velocity line actual is a zero velocity surface. The zero velocity surface is called the equilibrium surface (Powell and Nurick (1996)) and it presented by the solid (red) line in Figure 110. It can clearly be seen in Figure 109 that the equilibrium surface from Figure 110 follows a similar form to the dark blue region in Figure 109, this confirms the observation. The definition of the equilibrium surface was first presented in Powell and Nurick (1996), where it was visually determined from experimental x-ray data. In Mc Bride et al (2004) a DEM model was validated using the comparison between the equilibrium surface of the DEM and experimental x-ray data. The flow regions below (region 2) and above (region 1) the equilibrium surface are significantly different. The flow pattern in region 2 is steady and consistent in terms of its velocity magnitudes when compared to that of region 1, which can also be seen in Figure 109. The velocities vary between about 0 m/s to 0.8 m/s. The same cannot be said for the flow pattern of region 1, as it is more volatile and has a larger range of velocity values. The velocities of the particles in region 1 increase outwards to the center of the mill. The velocities in region 1 vary between 0 m/s to above 1.8 m/s. The increase in velocity is because of the cataracting region of the charge. The cataracting region of the charge can be identified by the larger velocities, which means the cascading region of the charge can therefore also be identified. The cascading region of the charge is the layer of charge between the cataracting charge and the equilibrium surface. Region 1 has two different flow patterns, but this will be properly defined further on.

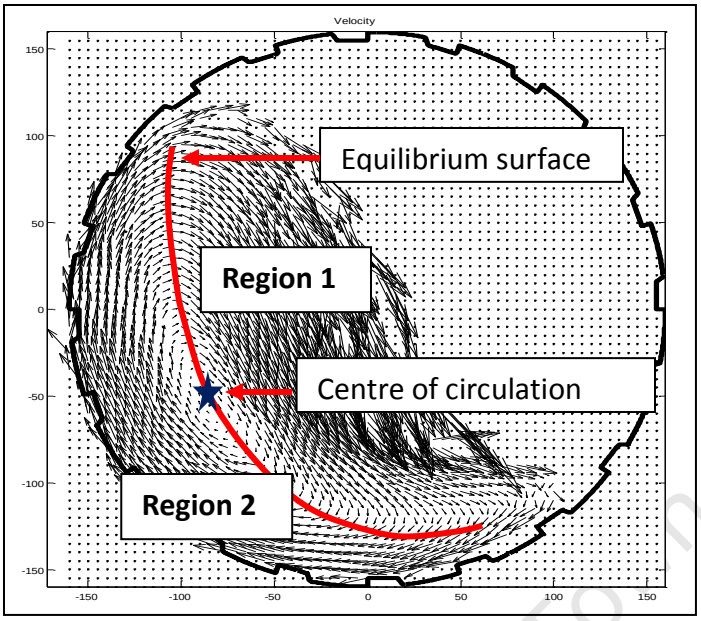

Figure 110: Velocity plot indicating the COC and equilibrium surface

16.1.2.3 Charge characteristics

The characteristics of the charge are the physical features of the charge in the experimental mill. The charge characteristics that can be identified by the PEPT data are the center of circulation (COC), equilibrium surface and the charge free surface. The equilibrium surface has already been defined and explained. It is represented by the red line in Figure 110.

The COC (Powell and Nurick (1996)) is a unique point in the charge and can be found on the equilibrium surface. According to Powell and Nurick (1996) the COC is the point around which the entire charge in the mill circulates. It is the point at which there is an absolute zero velocity in all directions, which is different to the equilibrium surface. The equilibrium surface is direction specific. This means that there is a different equilibrium surface for each direction (x,y and z). The equilibrium surface that is used for this flow description is specific to the x-direction. The COC is the point at which all these equilibrium surfaces intersect each other. The blue star in Figure 110 represents the COC of the data set.

Region 1 has two flow patterns, namely the cascading charge and the cataracting charge. The surface separating both regions is called the charge free surface. Using the velocity and particle probability distribution data it is possible to identify the charge free surface. The charge free

surface in Figure 109 can be identified as the surface below the cataracting material (yellow and red region). The cataracting material can also be clearly identified by the dark blue region in Figure 111. The probability distribution of the particles is determined by using the time spent in a specific bin (Small Square in grid); therefore the higher the velocity the less time spent in the bin and the lower the distribution. The cataracting region can therefore be clearly separated from the main charge body. The charge free surface is represented by the white line in Figure 111. The white line follows a similar trend line that tracks the charge material in Figure 109.

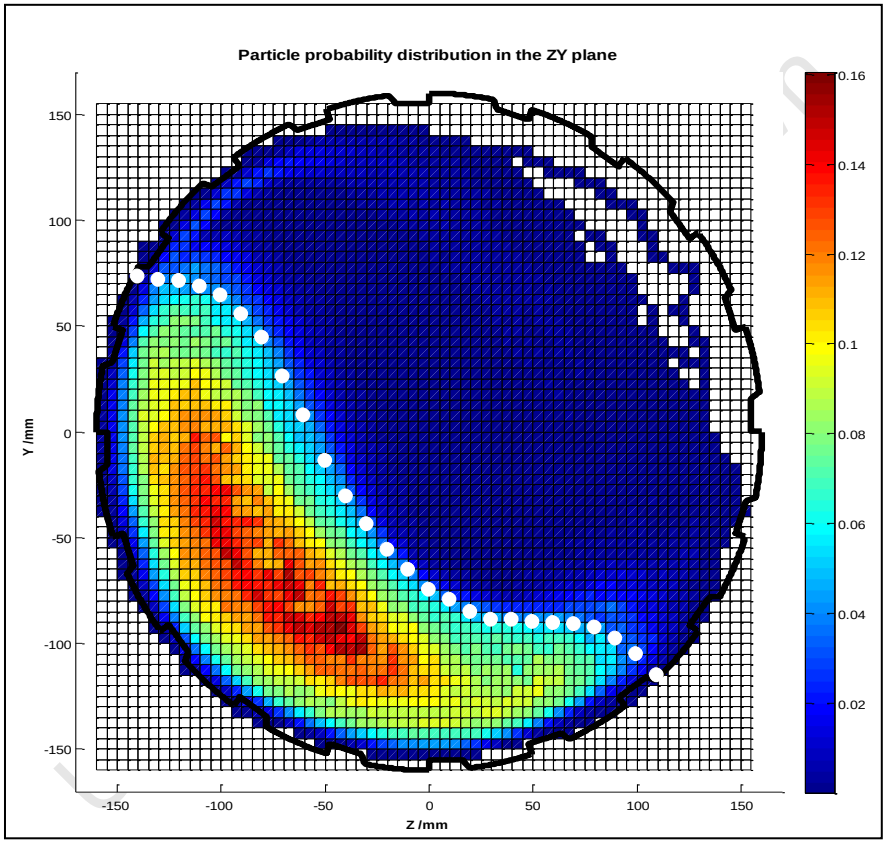

Figure 111: Particle probability distribution

All the charge features will be tracked and defined numerically in order to be accurate. The descriptions so far are meant to explain the concept of each characteristic, as they will be used in the granular flow theory development.

16.1.3 Approach

The approach taken for the fundamental modeling of the velocity profile is based on the charge and particle observations. The charge in the mill will be modeled as a fluid. The fluid behaviour approximation is made because of the nature of the particle movement. The particles movement can be divided up into three types. The first type is a force driven flow, where the particles are driven up the side of the mill to a certain turning point by the forces exerted on them by the mill and lifters. This type of flow is observed in region 2 and can be seen in Figure 109 and Figure 110. The second type of flow is a free flowing gravity driven flow. This type of flow can be seen in region 1 in Figure 109 and Figure 110 between the equilibrium surface and the in-flight material. The last type of flow occurring in the mill is the material that is in flight, which is in region 1. The in-flight material is called the cataracting charge and can be seen as the material with the high velocities (yellow and orange colours) in Figure 109 and Figure 110.

Interactions between individual particles are not taken into account in the velocity profile development, because a continuum approximation (fluid approximation) is made. Therefore the control volumes used are not bounded by the size of a particle and can be any size (multiple particles) as per requirements of the assumptions made. A force balance over a control volume is required to predict the flow and velocity at which the different particles travel. The Navier-Stokes will be used to describe the forces, pressures and shear stress acting on the control volume (particles).

16.1.4 Analysis of flow regions

16.1.4.1 Defining area of interest

The area of interest for the granular flow theory is the main body of the charge in the experimental mill. The main body of the charge will for now exclude the cataracting material. Therefore the material in flight will be ignored for this part of the development of the granular flow theory. The cataracting material is left out, because it cannot be adequately explained by the fluid mechanics used so far. An additional consideration is that the cataracting region does not contribute to the power draw of the system. The main body of the charge is separated by the charge free surface, which is the boundary between the cascading and cataracting material.

The charge free surface is represented by the blue dots in Figure 112. The charge free surface shown in Figure 112 is an accurate representation of the charge free surface and it is extracted by using Figure 111. In this case the charge free surface is used to illustrate the boundary of the main charge body.

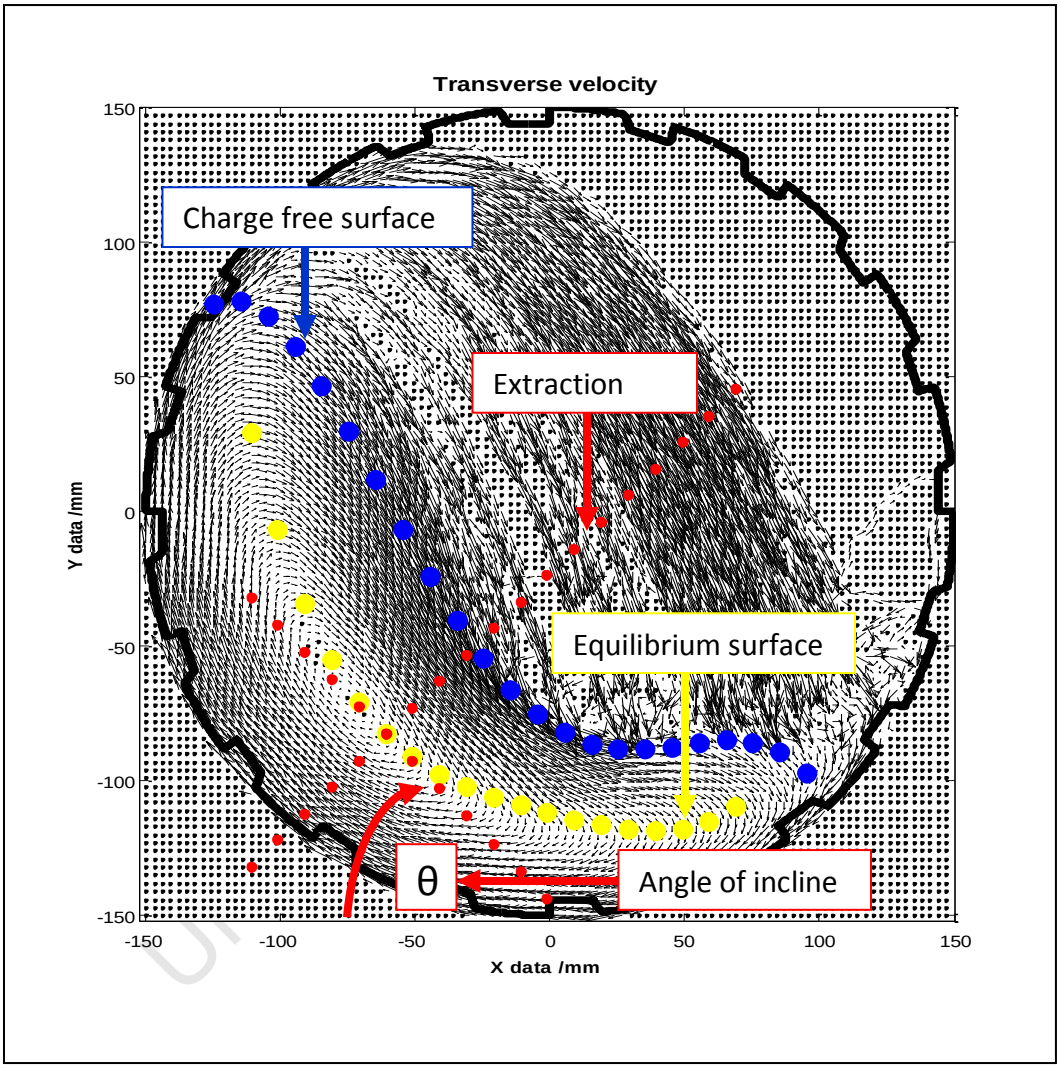

Figure 112: Velocity plot indicating the area of interest

The equilibrium surface is represented by the yellow line in Figure 112. The charge free surface and equilibrium surface are important to the development of the granular flow theory, as these charge characteristics represent the boundary layers of the fluid flow. The other important boundary is the mill shell. With correctly defined boundary layers the desired fluid flow region can be extracted and simplified. The flow region of interest is represented by a line that is

perpendicular to and passes through the equilibrium surface, which in this case is represented by the red line in Figure 112. The red line is called the extraction line, because it is the line along which the experimental data will be extracted. The extraction line is perpendicular to the equilibrium surface, so that the tangential velocities of the fluid are parallel with the boundary layer and so that any changes in slope of the equilibrium surface can be tracked and easily incorporated into the granular flow model. The angle by which the equilibrium surface changes, is represented by θ in Figure 112 and it is measured from the line perpendicular to the extraction line. This configuration will allow for the flow region in any part of the charge to be determined.

16.1.4.2 Simplification of flow regions

The flow regions chosen by the yellow line in Figure 112 can be simplified to Figure 113. Figure 113 clearly shows the different flow direction and boundary layers of the charge. The three different boundary layers of the flow region are the mill shell, COC (equilibrium surface) and the cascading region (charge free surface). The boundary layers allow for different fluid velocities to be set. The fluid at the mill shell will have the same velocity as the mill shell. The velocity of the mill shell is dependent on the mill rotation and radial distance from the center of the mill. The relationship is described by the following equation below. The rotational speed of the mill (ω) is in radians/s and the radial distance from the mill center (r_{exp}) is in m.

$$V_{mill} = \omega r_{\exp} \text{ (m/s)}$$

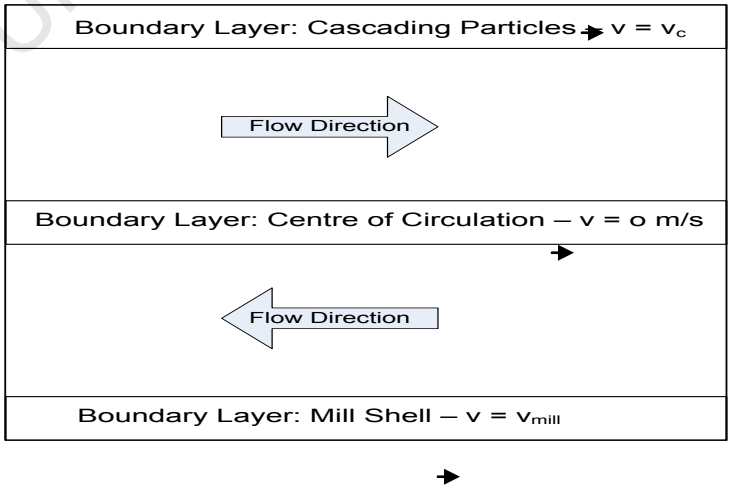

Figure 113: Simplified flow regions and boundary layers of the fluid

The velocity of the fluid at the COC (equilibrium surface) boundary is zero, as this is the point at which the particles in the charge change directions. Change in direction means that at some point there has to be a zero velocity, which in this case is the COC. The fluid velocity in the cascading region will be the same as the material cascading down the charge free surface, which in this case is described by v_c. Despite the simplification of the flow regions the direction of flow is at an angle to the surface on which the mill is standing. The angle is represented by θ and its angle and its orientation is described by the blue line in Figure 112.

16.1.4.3 Separating the different flow regions

The flow region above and below the equilibrium surface are quite different in nature, as mentioned before. The particles below the equilibrium surface (region 2) are densely packed and their velocities do not vary significantly at different flow layers. The same cannot be said for the particles above the equilibrium surface (region 1), as their velocities are different and they are loosely packed. The particles in region 1 have different velocities along a flow layer, because of the shape of the charge free surface. The charge free surface has a slight S-shape, which means the gradient of the surface across which the particles move changes. The steeper the gradient the greater the acceleration will be and the higher the particle velocity. The loose packing in region 1 is a result of low normal forces, because there is no significant amount of material above region 1. With these differences in mind the different flow regions of the main body of the charge will be dealt with separately. Figure 114 and Figure 115 show a simplified flow diagram of the lower and upper flow regions of the chosen flow region (chosen by the yellow line).

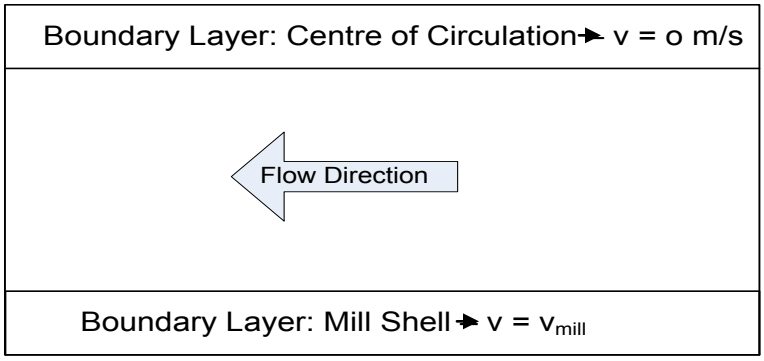

Figure 114: Lower flow region

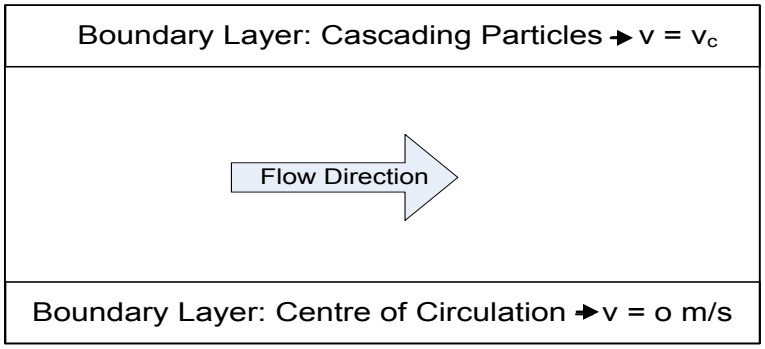

Figure 115: Upper flow region

The simplified flow regions will form the basis of the fundamental flow models for both flow regions. The boundary conditions and flow types will allow for the simplifications of the general flow relations.

16.1.5 Developing a velocity profile function for Region 2

The general Navier-Stokes equation has been reduced to the following equation:

$$\rho \frac{\mathrm{D}\mathbf{v}}{\mathrm{D}t} = \rho \boldsymbol{g} - \boldsymbol{\nabla} P + \mu \boldsymbol{\nabla}^2 \mathbf{v}$$

For a detailed derivation and explanation of the Navier-Stokes equation please refer to section 16.2 in the appendix.

16.1.5.1 Assumptions

In order to reduce the equation to its current state the following assumptions were made:

5. Laminar flow
6. Incompressible flow (constant density)
7. Constant viscosity
8. Newtonian fluid

Laminar flow is used in this model, as the velocities that have been observed in main body of the charge in the experimental mill have not been high (<1m/s), as can be seen in Figure 109.

Assuming an incompressible fluid is accurate for the fluid in region 2 and it is an approximation for the fluid in region 1. Assuming an incompressible fluid means the fluid will have a constant

density. The dense packing of the particles in region 2 allows for a constant density, which means per unit volume the number of particles present is approximately the same. The fluid in region 1 is loosely packed and its density decreases towards the charge free surface. The decrease in density is a result of a combination of a decreasing mass force on each particle tending towards the charge free surface and the variable gradient of the charge free surface.

The viscosity is temperature and pressure dependent. Therefore as there is no significant temperature change and pressure does not have a significant effect on the fluid, the viscosity can be assumed to be constant.

A Newtonian fluid is assumed, because the particles in the charge are mono-size. Mono-size particles have consistent flow behaviour and therefore constant rheological behaviour. This would not necessarily be the case for a particle size distribution with a large amount of particles that are smaller than the larger particles.

16.1.5.2 Velocity profile for Region 2

The velocity profile derivation will be based on the flow simplification seen in Figure 116. The region of interest is the flow region between the COC and the mill shell (region 2).

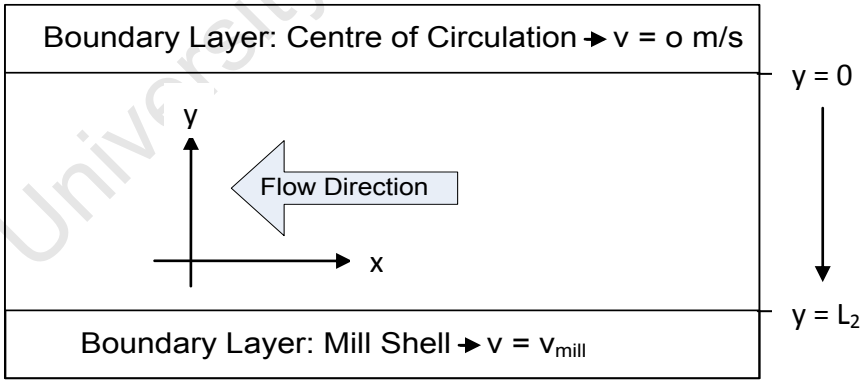

Figure 116: Simplification of Region 2

The direction of the coordinate system can be seen in Figure 116. The direction of flow of the fluid and therefore the velocity of the fluid is perpendicular to the y-axis of the coordinate system, because the coordinate system for the velocity profile is perpendicular to the charge free surface. The force balance appropriate to region 2 is the modified Navier-Stokes equation:

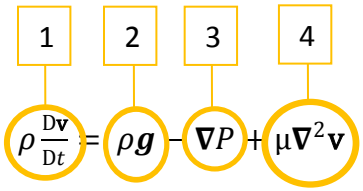

The vector components (highlighted variables) of the modified Navier-Stokes equation need to be defined for the particular system. The simplification of the flow region 2, Figure 116, clearly shows that there is only flow in the x-direction relative to the coordinate system. Therefore the system can be described as follows:

Defining variables in the modified Navier-Stokes equation

1. $\rho \frac{D\mathbf{v}}{Dt} = 0$
2. $\rho \boldsymbol{g} = -\rho g_x$
3. $\boldsymbol{\nabla} P = \frac{dP}{dx}$
4. $\mu \boldsymbol{\nabla}^2 \mathbf{v} = \mu \frac{d^2 v_x}{dy^2}$

The first variable describes the change in momentum in the system. In the region of interest there is no change in the cross sectional area of the flow, which means there is no change in fluid velocity. Therefore the system has steady flow and hence the momentum of the system is zero. The second variable describes the gravitational force that the control volume experiences in the x-direction. The gravitational acceleration is in terms of the x-component, so that gravity's effect in the x-direction can be taken into account in case of an incline. The third variable is the pressure the control volume experiences in the system. Therefore any applied pressure to the system would be taken into account with this variable. The final variable is the shear stress acting on the control volume and it is defined by the Newtonian fluid assumption.

Defining equation for region 2's flow

$$0 = -\rho g_x - \frac{dP}{dx} + \mu \frac{d^2 v_x}{dy^2}$$

$$\frac{d^2 v_x}{dy^2} = \left(\rho g_x + \frac{dP}{dx}\right) 1/\mu$$

Once the variables have been defined they can be compiled and rearranged as can be seen above.

Integration

$$\frac{dv_x}{dy} = \left(\rho g_x + \frac{dP}{dx}\right) y/\mu + C_1$$

$$v_x = \left(\rho g_x + \frac{dP}{dx}\right) y^2/2\mu + C_1 y + C_2$$

Once the equation has been rearranged, the equation is integrated. The integration results in constants C_1 and C_2, because the integrals are indefinite integrals as they do not have limits at the time of integration. The constants in the v_x expression are eliminated by the boundary conditions of the system. The first set of boundary conditions for the system is:

1st Boundary Conditions

$$y = 0$$

$$v_x = 0$$

The first boundary condition describes the conditions at the COC (equilibrium surface) of the charge. The second boundary condition of the system is the condition at the mill shell and it is described as follows:

2nd Boundary Conditions

$$y = L_2$$

$$v_x = v_{mill}$$

Using the boundary conditions to solve for the constants in the v_x expression results in the following equations:

Solving with boundary conditions

$$C_2 = 0$$

$$C_1 = \frac{v_{mill}}{L_2} - \left(\rho g_x + \frac{dP}{dx}\right) L_2 / 2\mu$$

Using the expressions of C_1 and C_2 in the v_x expression allows for the basic velocity function to be derived, as can be seen below.

Velocity profile

$$v_x = \left(\rho g_x + \frac{dP}{dx}\right) \frac{(y^2 - L_2 y)}{2\mu} + \frac{v_{mill}\, y}{L_2}$$

The velocity profile for region 2 does need to be adjusted in order to mimic the conditions of a CV (particle) in region 2. The flow region 2 is at an angle to the surface on which the mill is standing. The angle is describes in Figure 112 and this angle is translated into the velocity profile by defining ρg_x.

$$\rho g_x = \rho g \sin\theta$$

The newly defined ρg_x is replaced and the velocity profile extends to the following expression:

$$v_x = \left(\rho g \sin\theta + \frac{dP}{dx}\right) \frac{(y^2 - L_2 y)}{2\mu} + \frac{v_{mill}\, y}{L_2}$$

Frictional forces

The velocity profile above is the profile of a fluid between two plates with specific conditions. The reality is that we are actually dealing with particles that are flowing down a bed of particles. Any object that moves past another object while in contact will be subject to friction. There are two types of friction. The first is a static friction which applies to objects that are stationary. Once a force is applied to the object and the object starts to move, the static friction is replaced by a kinetic friction. The kinetic friction is a movement retarding force, because it acts in the opposite direction of the object's movement and as it increases it will decrease the object's velocity. The glass particles in the charge experience kinetic friction and it will therefore be taken into account in the velocity function. The kinetic friction expression is as follows:

$$F_f = \mu_e F_N$$

F_N (N) is the normal force of the CV (glass particle) and μ_e (dimensionless) is the estimated coefficient of kinetic friction. The frictional coefficient of glass particles needs to be estimated or measured (experimentally estimated), because its value is not known and has not been measured in literature.

In order to define the normal force (F_N) of the particle, a force balance on the particle is needed. Two different situations will occur in this system. The first situation is a force balance on a particle on top of the charge and the other is a force balance of a particle in the charge. A force balance of both situations can be seen in Figure 117 and Figure 118. The force balances represent two different flow situations, but the aspect that is being highlighted is the difference that the position of the particle makes to the approach of friction. The force balances however assume that the particles are directly above and below each other, as can be seen in Figure 119 option 2. This approximation eliminates one particle wedged between four particles, as can be seen in Figure 119 option 1.

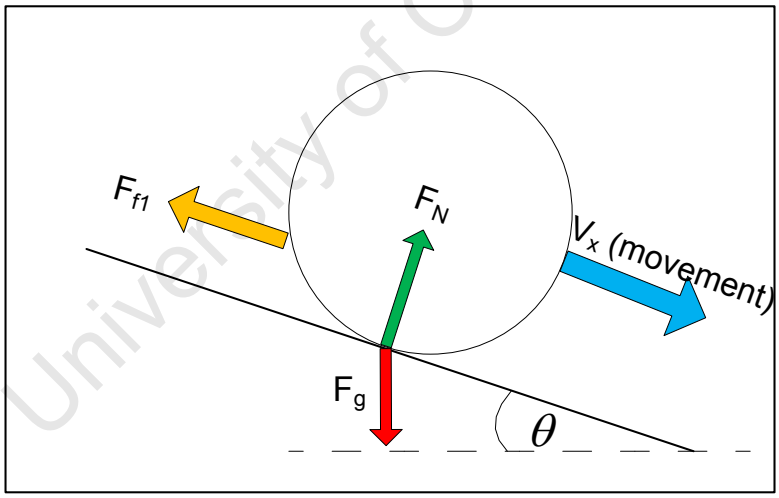

Figure 117: Forces acting on a particle on the top of the charge

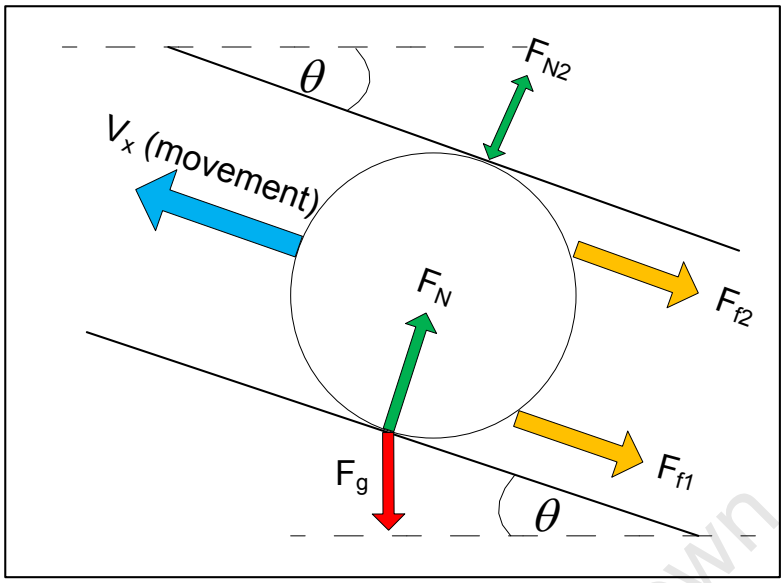

Figure 118: Forces acting on a particle in the charge

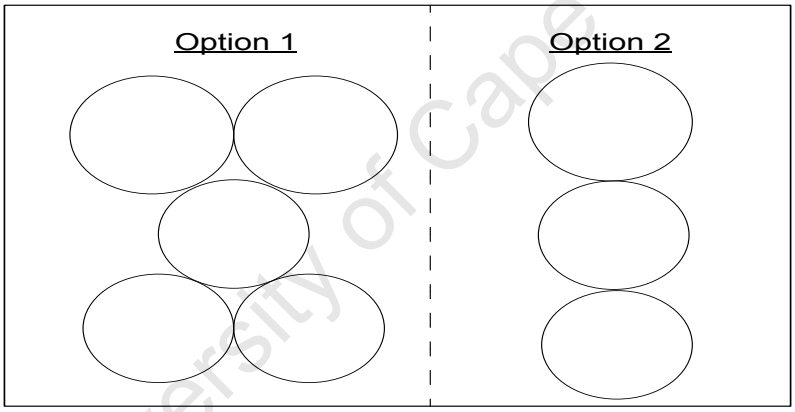

Figure 119: Particle packing

Force Balance of top particle

The force balance for a particle on the top of the charge is a special case in the system. The only particles that find themselves in this situation are found in a thin layer of cascading particles on the charge. These particles act as the charge free surface boundary. Therefore this special case will only be applicable to a specific set of particles in region 1.

The magnitude of the frictional force on the top particle is dependent on F_N. F_N is however dependent on F_g. An adjustment (cos θ) is made to F_g, so that the incline angle of the particle is taken into account. The result of the adjustment is seen below.

$$F_N = F_g \cos\theta$$

F_g (N) on the other hand is dependent on mass (m in kg) and the gravitational acceleration (g in m/s^2), as can be seen below. F_N (N) is therefore dependent on mass.

$$F_g = mg$$

F_N in this case represents the normal force that the particles on the top of the charge experience. These particles do not have any other particles above them to add more force to the normal force. This however is not the case with the particles in the body of the charge.

Force Balance of a particle in the charge

From Figure 118 it can be seen that there are two frictional forces that affect the particle in the charge. There are two ways of including both frictional forces. The first is to independently determine of the frictional force (F_{f1}) of a single particle ignoring the particles above it. The affect of the particles above are separately determined by F_{f2}. F_{f2} is dependent on F_{N2}, which takes the mass above the particle into account. Then by adding F_{f2} and F_{f1} the total frictional force is determined.

The other method uses the summation of the normal forces (F_N). The normal force of the particle of interest is added to the normal force of the particles above. This then determines the total normal force on the particle of interest. The total normal force is then used to determine the total frictional force on the particle of interest. This is the method that is used for this derivation of the frictional force on particle within the charge.

F_N for the particles in the charge body increases from the charge free surface to the mill shell. The force balance on a particle in the charge will experience the same forces the particle on the top of the charge experiences with the addition of F_{N2}. In Figure 118 it is clear to see where and how the additional force (F_{N2}) is applied to the particles. F_N for the particle in the charge is as follows:

$$F_N = F_g \cos\theta + F_{N2}$$

In order to describe a normal force on any particle in the charge, an indefinite summation is defined:

$$F_{N,k} = \sum_{i=k}^{i=1} F_{N,i} = \sum_{i=k}^{i=1} F_{g,i} \cos\theta = \sum_{i=k}^{i=1} m_i g \cos\theta$$

Determining the mass at any point in the area of concern is not a simple task, as the particles are spherical. Accurately determining the change in mass along a single sphere would require a characteristic equation describing the shape of the particle and then determining the volume with the equation as a function of particle length. This will then need to be repeated for the rest of the particles that are stacked below the top particle. Instead of the aforementioned complexity, the mass change along the a set of particles, which are stacked on top of each other, will be estimated by a rectangular volume with the length of the stack of particles and width and depth of the diameter of a particle. The estimated volume can be seen in Figure 120. The mass of the particles will then be determined by the density of the glass particles. Using this method will over-estimate the volume of the particles and therefore will over estimate the mass of the particles. Although a degree of over-estimation will occur, the mass as a function of the volume's length will be much simpler to solve.

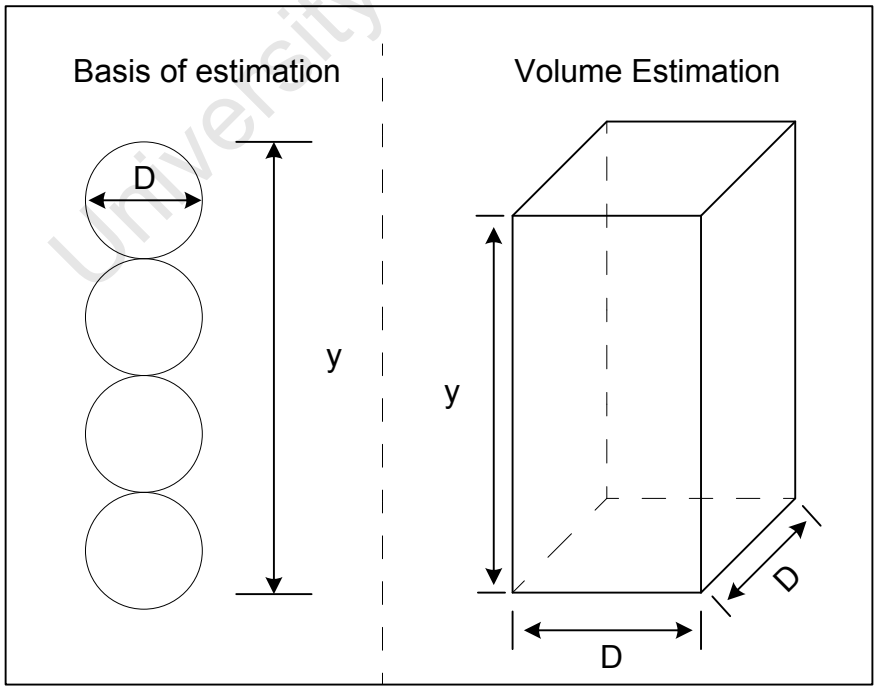

Figure 120: Volume estimation for stacked particles

The change in mass from the charge free surface to the mill shell is defined by the volume of particles as a function of y and the density of the glass particle:

$$m(y) = D^2 y\rho$$

M (kg) is the mass of the particles, D^2 (m^2) is the cross sectional area of the rectangular body, y (m) is the length of the rectangular body (length of the stacked particles) and ρ (kg/m^3) is the density of the glass particles.

The normal force of the particles in the charge therefore becomes a function of y, as can be seen below.

$$F_N(y) = m(y)g\cos\theta$$

In a similar manner the frictional force of the particle in the charge becomes a function of y.

$$F_f(y) = \mu_e F_N(y)$$

The expression for F_f describes the total force acting on a particle anywhere in the charge. This expression is added to the velocity profile in the following manner:

$$v_x = \left(\rho g \sin\theta + \frac{dP}{dx} + F_f(y)\right)\frac{(y^2 - L_2 y)}{2\mu} + \frac{v_{mill}\, y}{L_2}$$

The frictional force is added to the pressure drop and mass force, because it acts in the same direction as the aforementioned variables. The direction in which the frictional force is acting is illustrated in Figure 117 and Figure 118.

16.2 Derivation of Navier-Stokes equations

The approach taken for the modeling of the particle flow requires all the forces, pressures and shear acting on a control volume (CV) to be defined. A general equation that takes all these aspects into account is Newton's 2nd law for any CV, which is seen below. This derivation has been adapted from Welty et al (2001) with contributions from Bird et al (2007). The vectors in the equation below are the bold variables (F,v and n).

$$\sum \boldsymbol{F} = \iint_{C.S.} \mathbf{v}\rho(\mathbf{v}\cdot\mathbf{n})\,\mathrm{dA} + {}^{\delta}/_{\delta t}\iiint_{C.V.}\rho\mathbf{v}\,\mathrm{dV}$$ (Newton's 2nd Law)

The equation states that:

$$\left\{\begin{matrix}\text{Sum of all the external forces}\\ \text{acting on a control volume}\end{matrix}\right\} = \{\text{Net linear momentum efflux}\} + \left\{\begin{matrix}\text{Time rate of change of linear momentu}\\ \text{with in the control volume}\end{matrix}\right.$$

A more common way of stating Newton's 2nd law is 'The *net force on a body is equal to the product of the body's mass and its acceleration*'. Both statements are alluding to the same relationship under different conditions. In this case the condition is a force balance across a CV. The CV has been reduced to three distinct surfaces, which will be used for the development of the force balance around the control volume. The reduced CV is represented by Figure 121, Figure 122 and Figure 123.

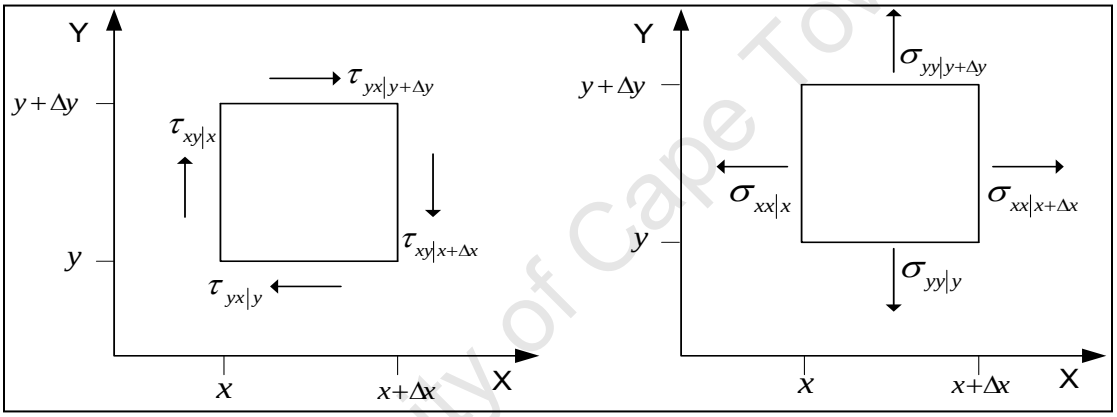

Figure 121: XY-plane of control volume

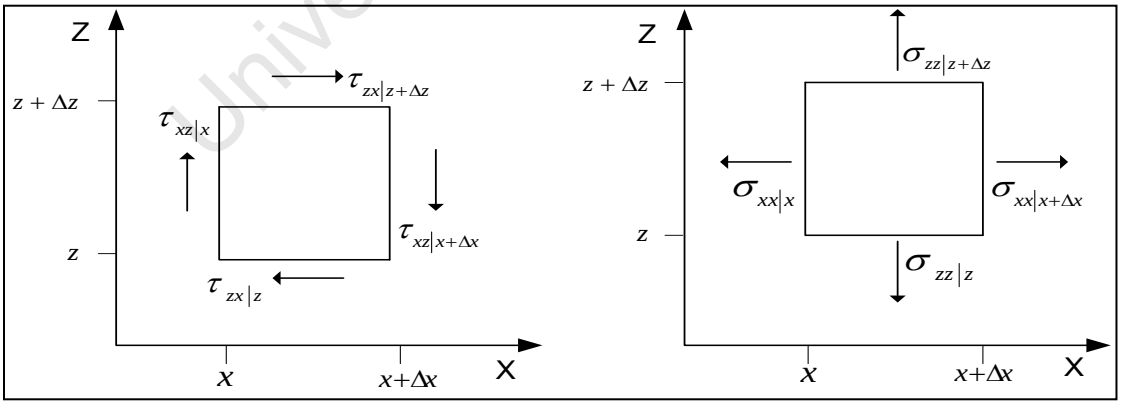

Figure 122: XZ-plane of the control volume

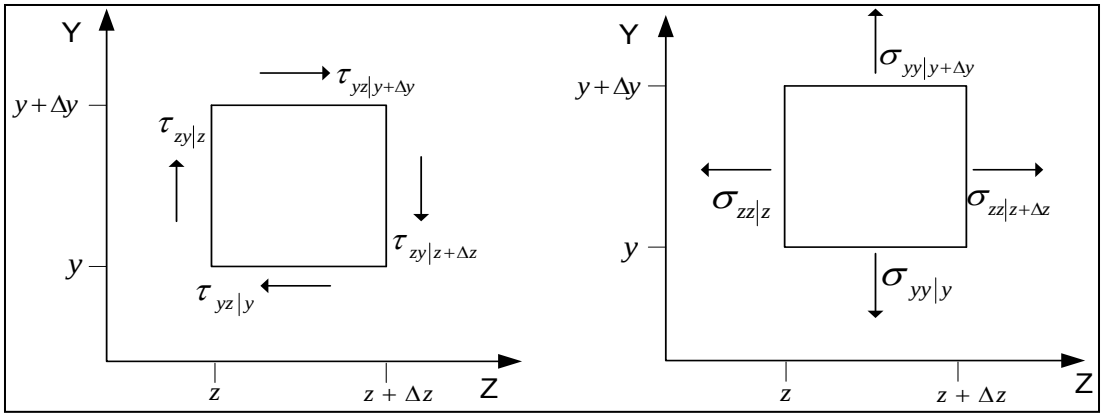

Figure 123: ZY-plane of the control volume

To make the derivation of the force balance easier to follow and more transparent, Newton's 2nd law for any CV will be split up into smaller sections. The equation will be divided up into three sections:

$$\underbrace{\sum \boldsymbol{F}}_{\text{Section 1}} = \underbrace{\iint_{C.S.} \mathbf{v}\rho(\mathbf{v}\cdot\mathbf{n})\,\mathrm{dA}}_{\text{Section 2}} + \underbrace{{}^{\delta}/_{\delta t} \iiint_{C.V.} \rho\mathbf{v}\,\mathrm{dV}}_{\text{Section 3}}$$

Section 1, section 2 and then lastly section 3 will be analyzed for the desired CV, which can be seen in Figure 121, Figure 122 and Figure 123.

16.2.1 Section 1

Section 1 of Newton's 2nd law takes all the external forces acting on the CV into account. The forces that contribute to section 1 are the shear stresses and normal stresses acting on the CV, as well as the mass force of the CV. An example of such a force balance is shown below. The force balance in this case is for a fluid flowing in the x-direction.

$$\sum \mathrm{F_x} = (\sigma_{xx}|_{x+\Delta x} - \sigma_{xx}|_x)\Delta y\Delta z + \left(\tau_{yx}\big|_{y+\Delta y} - \tau_{yx}\big|_y\right)\Delta x\Delta z + \left(\tau_{zx}|_{z+\Delta z} - \tau_{yx}\big|_z\right)\Delta x\Delta y + \rho g_x \Delta x\Delta y\Delta z$$

Normal Stress (σ_{xx})

The normal stress, which is represented by σ_{xx}, allows for the divergence of the CV to be taken into account. This means that any expansion/contraction of the fluid due to temperature or

pressure changes will be taken into account by the normal stress. The normal stress acts in all directions (x, y and z-direction), but it is flow direction specific. If the flow was in the x-direction, then x-component shear stress would act on the CV and not the y or z-component normal stresses. The surface area over which the normal stress acts is perpendicular to the x-direction, which means that the normal stress acts over the area ΔyΔz.

Shear Stress (τ_{yx})

The shear stress for a flowing fluid is a flow and movement retarding force and it is represented by τ_{yx} and τ_{zx} for flow in the x-direction. The shear stress in a fluid is the equivalent to the frictional force on an object when moving. At the boundary layer of a flowing fluid a maximum shear stress will translate into a zero velocity zone. Although at a minimum shear stress a maximum velocity zone will be found. The shear stress for a flowing fluid is parallel to the flow and it will act against the direction of flow. Then the areas over which the shear stresses will act are ΔxΔz for τ_{yx} and ΔxΔy for τ_{zx}.

Mass force

The mass force in section 1 is last term in the equation above. The mass force is the gravitational force on the CV due to its mass. The mass in the CV is a function of the volume of the CV and density of the fluid. Hence the mass of the CV is represented by ρ·ΔxΔyΔz. The gravitational force acting on the CV appears as a component vector, because the affect of the gravitational force will differ according to the coordinate system and its potential incline/decline.

After dividing by Δx·Δy·Δz and taking the limits of Δx, Δy and Δz, the following equation is produced:

$$\lim_{\Delta x,\Delta y,\Delta z\to 0} \frac{\sum F_x}{\Delta x \Delta y \Delta z} = \frac{\delta \sigma_{xx}}{\delta x} + \frac{\delta \tau_{yx}}{\delta y} + \frac{\delta \tau_{zx}}{\delta z} + \rho g_x$$

The y-component and z-component balances are developed in a similar manner and the results are the following equations:

$$\lim_{\Delta x,\Delta y,\Delta z\to 0}\frac{\sum F_y}{\Delta x\Delta y\Delta z}=\frac{\delta\sigma_{yy}}{\delta y}+\frac{\delta\tau_{xy}}{\delta x}+\frac{\delta\tau_{zy}}{\delta z}+\rho g_y$$

$$\lim_{\Delta x,\Delta y,\Delta z\to 0}\frac{\sum F_z}{\Delta x\Delta y\Delta z}=\frac{\delta\sigma_{zz}}{\delta z}+\frac{\delta\tau_{xz}}{\delta x}+\frac{\delta\tau_{yz}}{\delta y}+\rho g_z$$

16.2.2 Section 2

Section 2 of Newton's 2nd law is a momentum balance around the entire CV and takes all the possible directions of momentum flow into account (x, y and z-direction). The momentum in Newton's 2nd law for an arbitrary CV is described as a momentum efflux (flux). Hence the momentum across the CV is determined with a surface of the CV. In this case the momentum in the x-direction is a product of the x-component momentum efflux and the surface perpendicular to the x-direction, which is ΔyΔz. The same approach is used for the other momentum flows, namely the y and z-direction momentum flow. The momentum efflux balances with their respective areas are represented in the equation below.

$$\lim_{\Delta x,\Delta y,\Delta z\to 0}\frac{\iint_{C.S.}\mathbf{v}\rho(\mathbf{v}\cdot\mathbf{n})\,dA}{\Delta x\Delta y\Delta z}=\lim_{\Delta x,\Delta y,\Delta z\to 0}\left[\frac{(\rho\mathbf{v}v_x|_{x+\Delta x}-\rho\mathbf{v}v_x|_x)\Delta y\Delta z}{\Delta x\Delta y\Delta z}+\frac{\left(\rho\mathbf{v}v_y\big|_{y+\Delta y}-\rho\mathbf{v}v_y\big|_y\right)\Delta x\Delta z}{\Delta x\Delta y\Delta z}+\frac{(\rho\mathbf{v}v_z|_{z+\Delta z}-\rho\mathbf{v}v_z|_z)\Delta x\Delta y}{\Delta x\Delta y\Delta z}\right]$$

Once the momentum balance is setup it is divided by Δx·Δy·Δz, where the limits of Δx, Δy and Δz are taken and the following equation is produced:

$$\lim_{\Delta x,\Delta y,\Delta z\to 0}\frac{\iint_{C.S.}\mathbf{v}\rho(\mathbf{v}\cdot\mathbf{n})\,dA}{\Delta x\Delta y\Delta z}=\frac{\delta(\rho\mathbf{v}v_x)}{\delta x}+\frac{\delta\left(\rho\mathbf{v}v_y\right)}{\delta y}+\frac{\delta(\rho\mathbf{v}v_z)}{\delta z}$$

The partial derivative of each direction dependent variable is taken. In this case ρv_i, where i can be x, y or z, and **v** are direction dependent.

$$\lim_{\Delta x,\Delta y,\Delta z\to 0}\frac{\iint_{C.S.}\mathbf{v}\rho(\mathbf{v}\cdot\mathbf{n})\,dA}{\Delta x\Delta y\Delta z}=\mathbf{v}\underbrace{\left[\frac{\delta(\rho v_x)}{\delta x}+\frac{\delta\left(\rho v_y\right)}{\delta y}+\frac{\delta(\rho v_z)}{\delta z}\right]}_{\text{Section A}}+\rho\left[v_x\frac{\delta\mathbf{v}}{\delta x}+v_y\frac{\delta\mathbf{v}}{\delta y}+v_z\frac{\delta\mathbf{v}}{\delta z}\right]$$

Section A in the equation above is replaced by the continuity equation, which can be seen below.

$$d\rho/_{dt} + \frac{\delta}{\delta x}(\rho v_x) + \frac{\delta}{\delta y}\left((\rho v_y)\right) + \frac{\delta}{\delta z}((\rho v_z)) = 0 \text{ (Continuity equation)}$$

Once the continuity equation has been inserted, the following equation is formed:

$$\lim_{\Delta x,\Delta y,\Delta z\to 0} \frac{\iint_{C.S.} \mathbf{v}\rho(\mathbf{v}\cdot\mathbf{n})\,dA}{\Delta x\Delta y\Delta z} = -\mathbf{v}\frac{d\rho}{dt} + \rho\left[v_x\frac{\delta \mathbf{v}}{\delta x} + v_y\frac{\delta \mathbf{v}}{\delta y} + v_z\frac{\delta \mathbf{v}}{\delta z}\right]$$

16.2.3 Section 3

The last section of Newton's 2nd law for an arbitrary CV is section 3. Section 3 takes the time rate of change of the momentum in a CV into account. The volume over which this occurs is defined by ΔxΔyΔz, which is the CV volume.

$$\lim_{\Delta x,\Delta y,\Delta z\to 0} \frac{{}^{\delta}/_{\delta t}\iiint_{C.V.}\rho\mathbf{v}\,dV}{\Delta x\Delta y\Delta z} = \frac{\left({}^{\delta}/_{\delta t}\right)\rho\mathbf{v}\,\Delta x\Delta y\Delta z}{\Delta x\Delta y\Delta z}$$

The rate term in Newton's 2nd law is divided by ΔxΔyΔz and the limits of Δx, Δy and Δz are taken.

$$\lim_{\Delta x,\Delta y,\Delta z\to 0} \frac{{}^{\delta}/_{\delta t}\iiint_{C.V.}\rho\mathbf{v}\,dV}{\Delta x\Delta y\Delta z} = \frac{\delta}{\delta t}\rho\mathbf{v}$$

The partial derivative of the time dependent variables are taken, which are ρ and **v**.

$$\lim_{\Delta x,\Delta y,\Delta z\to 0} \frac{{}^{\delta}/_{\delta t}\iiint_{C.V.}\rho\mathbf{v}\,dV}{\Delta x\Delta y\Delta z} = \rho\frac{\delta \mathbf{v}}{\delta t} + \mathbf{v}\frac{\delta \rho}{\delta t}$$

16.2.4 Compiling all the sections

All the sections of Newton's 2nd law for an arbitrary CV have been explicitly developed for the desired CV. Combining all sections (sections 1,2 and 3) results in the following expressions for the different components:

Component x

$$\underbrace{\rho\left[\frac{\delta v_x}{\delta t} + v_x\frac{\delta v_x}{\delta x} + v_y\frac{\delta v_x}{\delta y} + v_z\frac{\delta v_x}{\delta z}\right]}_{\text{Section}} = \underbrace{\frac{\delta \sigma_{xx}}{\delta x} + \frac{\delta \tau_{yx}}{\delta y} + \frac{\delta \tau_{zx}}{\delta z} + \rho g_x}_{\text{Section 1}}$$

Component y

$$\rho\left[\frac{\delta v_y}{\delta t} + v_x\frac{\delta v_y}{\delta x} + v_y\frac{\delta v_y}{\delta y} + v_z\frac{\delta v_y}{\delta z}\right] = \frac{\delta \sigma_{yy}}{\delta y} + \frac{\delta \tau_{xy}}{\delta x} + \frac{\delta \tau_{zy}}{\delta z} + \rho g_y$$

Component z

$$\rho\left[\frac{\delta v_z}{\delta t} + v_x\frac{\delta v_z}{\delta x} + v_y\frac{\delta v_z}{\delta y} + v_z\frac{\delta v_z}{\delta z}\right] = \frac{\delta \sigma_{zz}}{\delta z} + \frac{\delta \tau_{xz}}{\delta x} + \frac{\delta \tau_{yz}}{\delta y} + \rho g_z$$

In order to shorten the notation of the equations a substantial time derivative is used and the following is obtained:

Component x

$$\rho\frac{Dv_x}{Dt} = \frac{\delta \sigma_{xx}}{\delta x} + \frac{\delta \tau_{yx}}{\delta y} + \frac{\delta \tau_{zx}}{\delta z} + \rho g_x$$

Component y

$$\rho\frac{Dv_y}{Dt} = \frac{\delta \sigma_{yy}}{\delta y} + \frac{\delta \tau_{xy}}{\delta x} + \frac{\delta \tau_{zy}}{\delta z} + \rho g_y$$

Component z

$$\rho\frac{Dv_z}{Dt} = \frac{\delta \sigma_{zz}}{\delta z} + \frac{\delta \tau_{xz}}{\delta x} + \frac{\delta \tau_{yz}}{\delta y} + \rho g_z$$

The equations above are fully developed force balance equations for a CV using Netwon's 2nd law for arbitrary CV under any conditions.

Stokes viscosity relation

To further develop Newton's 2nd law into an expression that describes the forces on the CV, a definition for shear stress and normal stress needs to be found. The form of the shear and normal stress are dependent on the type of fluid and flow. The assumptions are laminar flow and a Newtonian fluid. The flow of the fluid is laminar, because once steady state is reached in

an experimental mill there is little mixing movement of the particles between each other. A turbulent flow would be characterized by a continuous mixing of particles with different sizes and densities. Whereas it has been shown by Powell and Nurick (1996) that once steady state is reached the particles stay put in their segregated layers. The combination of laminar flow and a Newtonian fluid allow for the normal and shear stress to be defined as:

Shear Stress

$$\tau_{xy} = \tau_{yx} = \mu\left(\frac{\delta v_x}{\delta y} + \frac{\delta v_y}{\delta x}\right)$$

$$\tau_{yz} = \tau_{zy} = \mu\left(\frac{\delta v_y}{\delta z} + \frac{\delta v_z}{\delta y}\right)$$

$$\tau_{zx} = \tau_{xz} = \mu\left(\frac{\delta v_z}{\delta x} + \frac{\delta v_x}{\delta z}\right)$$

Normal Stress

$$\sigma_{xx} = \mu\left(2\frac{\delta v_x}{\delta x} - \frac{2}{3}\boldsymbol{\nabla}\cdot\mathbf{v}\right) - P$$

$$\sigma_{yy} = \mu\left(2\frac{\delta v_y}{\delta y} - \frac{2}{3}\boldsymbol{\nabla}\cdot\mathbf{v}\right) - P$$

$$\sigma_{zz} = \mu\left(2\frac{\delta v_z}{\delta z} - \frac{2}{3}\boldsymbol{\nabla}\cdot\mathbf{v}\right) - P$$

The normal and shear stress are both influenced by the viscosity and velocity of the fluid. The difference between both stresses is the pressure (P) that is present in the normal stress expression. The pressure in the normal stress expression is the pressure resulting from external forces outside of the control volume's reference frame. These forces are direction dependent and have an effect on the divergence of the control volume, hence it forms part of the normal stress' expression. An example of this would be the pressure of an upstream pump that affects a downstream fluid flow.

The normal and shear stress relations shown above are also known as Stokes viscosity relations. These relations are directly dependent on the type of fluid flow and fluid that is being observed. A Newtonian fluid is assumed, because of the flow characteristics of the glass beads. Non-

Newtonian fluids have a step change in flow characteristics once a certain amount of agitation has been added to the system. The fluid's viscosity increases or decreases making it flow less or more easily respectively. These characteristics are not seen in the agitation of the glass bead system; hence the Newtonian assumption can be made.

16.2.5 General Navier-Stokes Equations

The general Navier-Stokes relationship is developed through the addition of the Stokes viscosity relations. Adding the Stokes viscosity relations of each component to its Newton's 2nd law equation results in the following equations:

Component x

$$\rho \frac{\mathrm{D}v_x}{\mathrm{D}t} = \rho g_x - \frac{\delta \mathrm{P}}{\delta x} - \frac{\delta}{\delta x}\left(\frac{2}{3}\mu \boldsymbol{\nabla} \cdot \mathbf{v}\right) + \boldsymbol{\nabla} \cdot \left(\mu \frac{\delta \mathbf{v}}{\delta x}\right) + \boldsymbol{\nabla} \cdot (\mu \boldsymbol{\nabla} v_{\mathrm{x}})$$

Component y

$$\rho \frac{\mathrm{D}v_y}{\mathrm{D}t} = \rho g_y - \frac{\delta \mathrm{P}}{\delta y} - \frac{\delta}{\delta y}\left(\frac{2}{3}\mu \boldsymbol{\nabla} \cdot \mathbf{v}\right) + \boldsymbol{\nabla} \cdot \left(\mu \frac{\delta \mathbf{v}}{\delta y}\right) + \boldsymbol{\nabla} \cdot \left(\mu \boldsymbol{\nabla} v_{\mathrm{y}}\right)$$

Component z

$$\rho \frac{\mathrm{D}v_z}{\mathrm{D}t} = \rho g_z - \frac{\delta \mathrm{P}}{\delta z} - \frac{\delta}{\delta z}\left(\frac{2}{3}\mu \boldsymbol{\nabla} \cdot \mathbf{v}\right) + \boldsymbol{\nabla} \cdot \left(\mu \frac{\delta \mathbf{v}}{\delta z}\right) + \boldsymbol{\nabla} \cdot (\mu \boldsymbol{\nabla} v_{\mathrm{z}})$$

16.2.6 Modified Navier-Stokes Equation

An assumption on the density of the charge is made, that allows for the general Navier-Stokes equations to be further modified and made simpler. It is assumed that the density of the fluid (charge) is constant. This assumption is not accurate, but this aspect will be further discussed in the later parts of the theory section. Assuming a constant density for the fluid means that the divergence function in the Navier-Stokes equation is zero.

$\boldsymbol{\nabla} \cdot \mathbf{v} = 0$ (Incompressible flow)

A constant density means that the fluid is incompressible; therefore any pressure on the CV will deform the CV instead of decreasing/increasing its volume. Then by reducing the equation to a vector based equation allows for one equation to express the force balance around the CV.

$$\rho \frac{\mathrm{D}\mathbf{v}}{\mathrm{D}t} = \rho \boldsymbol{g} - \boldsymbol{\nabla} P + \mu \boldsymbol{\nabla}^2 \mathbf{v}$$

16.3 Data preprocessing

Table 12: Preprocessing variables used to optimize the triangulation algorithm

		Conditions		
Experiments no.	Section	Events	Fopt	Error (mm)
1	1	450	10	5
	2	350	15	5
	3	150	10	5
2	1	200	20	5
	2	300	15	5
	3	200	20	5
3	1	250	20	5
	2	350	15	5
	3	300	20	5
4	1b	350	15	5
	2b	150	20	5
	2c	250	15	5
5	1a	350	20	5
	2b	150	20	5
	3c	350	15	5
6	1a	250	15	5
	2b	150	15	5
	3c	200	10	5
7	1	300	10	5
	2	350	10	5
	3	400	15	5
8	1	350	15	5
	2	250	20	5
	3	250	15	5
9	1	350	20	5
	2	350	25	5
	3	200	25	5
10	1	150	10	5
	2	250	20	5
	3	200	10	5
11	1z	200	10	5
	2z	250	15	5
	3z	150	15	5
12	1	300	20	5

	2	250	20	5
	3	400	25	5
13	1	400	15	5
	2	150	20	5
	3	300	15	5
14	1	200	15	5
	2	200	15	5
	3	300	20	5
15	1	250	15	5
	2	250	15	5
	3	250	15	5
16	1	200	25	5
	2	200	10	5
	3	300	15	5
17	1	200	15	5
	2	200	15	5
	3	300	25	5
18	1	300	20	5
	2	400	25	5
	3	250	25	5
19	1	300	10	5
	2	350	15	5
	3	350	15	5
20	1	200	20	5
	2	400	25	5
	3	250	30	5
21	1	350	10	5
	2	300	15	5
	3	300	15	5
22	1	200	10	5
	2	300	10	5
	3	250	15	5
23	1	250	15	5
	2	300	20	5
	3	200	15	5
24	1	250	15	5
	2	250	15	5
	3	350	25	5
25	1	350	10	5
	2	350	15	5
	3	350	20	5

28	1	350	20	10
	2	300	15	5
	3	350	30	5
29	1	300	10	5
	2	250	15	5
	3	150	15	5
34	1z	250	15	5
	2z	250	15	5
	3z	250	15	5
35	1z	300	30	5
	2z	250	15	5
	3z	300	15	5
36	1z	300	20	5
	2z	350	15	5
	3z	350	25	5
37	1	150	10	5
	2	350	15	5
	3	350	15	5
38	1	200	15	5
	2	130	10	5
	3	350	10	5
39	1	300	25	5
	2	200	10	5
	3	100	15	5
40	1	250	25	5
	2	250	25	5
	3	250	20	5
41	1	250	15	5
	2	250	25	5
	3	250	25	5
42	1	250	20	5
	2	250	15	5
	3	250	15	5

16.4 Data processing

Table 13: Correction vectors for the experimental data to center data to desired reference frame

	Correction (centre into mill)		
Experiment	x	y	z
1	11	-57	0

2	11	-57	0
3	11	-57	0
4	18	-54	0
5	20	-55	0
6	20	-54	0
7	16	-55	0
8	16	-54	0
9	16	-54	0
10	12	-62	0
11	18	-61	0
12	11	-61	0
13	16	-61	0
14	15	-61	0
15	14	-60	0
16	8	-60	0
17	8	-60	0
18	8	-60	0
19	25	-65	0
20	25	-65	0
21	25	-65	0
22	18	-66	0
23	19	-66	0
24	20	-65	0
25	15	-66	0
28	15	-66	0
29	15	-66	0
34	26	-64	0
35	26	-64	0
36	26	-64	0
37	19	-64	0
38	24	-63	0
38_3c	18	-63	0
39	19	-63	0
40	17	-64	0
41	18	-64	0
42	18	-64	0

16.5 Theoretical velocity profile sensitivity analysis

16.5.1 Sensitivity analysis of the friction coefficient

Table 14: Summary table of the friction coefficient sensitivity analysis

ue = 0.1		ue = 0.3		ue = 0.7		ue = 1	
Distance (m)	Velocity (m/s)	Distance (m)	Velocity (m/s)	Distance (m)	Velocity (m/s)	Distance (m)	Velocity (m/s)
0.000	0.000	0.000	0.000	0.000	0.000	0.000	0.000
0.004	0.045	0.004	0.045	0.004	0.045	0.004	0.045
0.009	0.099	0.009	0.099	0.009	0.099	0.009	0.099
0.013	0.162	0.013	0.162	0.013	0.162	0.013	0.162
0.017	0.232	0.017	0.232	0.017	0.232	0.017	0.232
0.021	0.312	0.021	0.312	0.021	0.312	0.021	0.312
0.026	0.400	0.026	0.400	0.026	0.400	0.026	0.400
0.030	0.496	0.030	0.496	0.030	0.496	0.030	0.496
0.032	0.550	0.032	0.550	0.032	0.550	0.032	0.550
0.034	0.601	0.034	0.601	0.034	0.601	0.034	0.601
0.038	0.715	0.038	0.715	0.038	0.715	0.038	0.715
0.042	0.819	0.042	0.819	0.042	0.819	0.042	0.819
0.047	0.843	0.047	0.843	0.047	0.843	0.047	0.843

16.6 Comparing experimental and theoretical velocity profile data

Table 15: Summary table for the statistical the velocity profile analysis

			Average difference			Total Amount of data			Agreement			% Agreement			
Mill filling	**Mill speed**	**Lifter height**	Zone 1	Zone 2	Zone 3	Zone 1	Zone 2	Zone 3	Zone 1	Zone 2	Zone 3	Zone 1	Zone 2	Zone 3	Average
20	85	10	15.0%	31.6%	19.3%	13	9	10	3	0	0	23%	0%	0%	8%
20	70	10	18.3%	45.0%	25.1%	13	9	6	0	1	0	0%	11%	0%	4%
20	55	10	19.4%	33.3%	25.7%	12	13	7	3	1	1	25%	8%	14%	16%
30	85	10	29.4%	40.3%	19.6%	17	14	8	1	1	1	6%	7%	13%	9%
30	70	10	36.6%	41.1%	26.5%	16	16	9	1	1	1	6%	6%	11%	8%
30	55	10	37.3%	43.2%	29.2%	16	17	10	1	2	1	6%	12%	10%	9%
40	85	10	38.0%	34.4%	19.6%	23	17	9	0	1	1	0%	6%	11%	6%
40	70	10	37.1%	47.6%	28.6%	22	15	9	1	1	1	5%	7%	11%	7%
40	55	10	38.0%	55.0%	35.3%	20	21	12	2	0	1	10%	0%	8%	6%
20	85	6	16.6%	16.3%	21.2%	12	11	8	1	3	1	8%	27%	13%	16%
20	70	6	18.5%	16.1%	17.5%	13	12	8	4	2	3	31%	17%	38%	28%
20	55	6	28.7%	30.4%	33.3%	10	12	8	1	1	1	10%	8%	13%	10%
30	85	6	35.6%	40.8%	26.2%	17	13	8	0	0	1	0%	0%	13%	4%
30	70	6	36.8%	37.6%	30.3%	16	13	9	1	0	0	6%	0%	0%	2%
30	55	6	32.8%	45.6%	35.7%	14	16	11	0	1	0	0%	6%	0%	2%
40	85	6	32.9%	38.0%	21.7%	23	17	8	1	1	3	4%	6%	38%	16%
40	70	6	34.4%	47.8%	38.3%	19	20	12	0	0	1	0%	0%	8%	3%
40	55	6	40.2%	59.6%	40.9%	20	22	13	0	1	1	0%	5%	8%	4%
20	85	3	15.0%	47.8%	21.5%	12	10	8	3	0	1	25%	0%	13%	13%
20	70	3	23.5%	23.3%	19.5%	12	11	9	0	2	2	0%	18%	22%	13%
20	55	3	21.9%	25.7%	37.1%	10	13	10	0	0	0	0%	0%	0%	0%
30	85	3	22.9%	46.7%	18.1%	18	12	9	0	0	1	0%	0%	11%	4%
30	70	3	27.1%	45.3%	22.3%	15	13	10	1	0	2	7%	0%	20%	9%
30	55	3	32.3%	49.1%	36.2%	16	17	11	0	1	0	0%	6%	0%	2%
40	85	3	41.3%	49.7%	21.2%	21	14	7	1	0	1	5%	0%	14%	6%

40	70	3	47.3%	52.6%	27.7%	22	18	10	2	0	1	9%	0%	10%	6%
40	55	3	43.5%	60.3%	46.7%	19	19	13	0	0	1	0%	0%	8%	3%
20	85	1.5	41.3%	21.2%	26.3%	8	7	6	0	1	2	0%	14%	33%	16%
20	70	1.5	33.4%	21.4%	33.7%	7	8	6	0	0	0	0%	0%	0%	0%
20	55	1.5	51.3%	26.5%	43.0%	6	7	7	0	0	0	0%	0%	0%	0%
30	85	1.5	28.1%	40.6%	19.3%	16	13	9	2	0	3	13%	0%	33%	15%
30	70	1.5	33.3%	50.4%	23.2%	15	15	10	1	1	0	7%	7%	0%	4%
30	55	1.5	30.4%	54.0%	46.4%	14	17	12	2	1	1	14%	6%	8%	10%
40	85	1.5	45.4%	49.5%	24.5%	22	18	8	1	0	1	5%	0%	13%	6%
40	70	1.5	48.9%	55.3%	23.8%	22	20	11	0	0	1	0%	0%	9%	3%
40	55	1.5	45.1%	57.9%	47.9%	18	22	14	1	0	0	6%	0%	0%	2%

16.7 Statistics of good data

Table 16: Summary of all good data sets

Mill filling	Mill speed	Lifter height	Zone	Mean Difference	% Agreement
20%	85%	10 mm	1	15.0%	23%
20%	55%	10 mm	1	19.4%	25%
20%	85%	6 mm	2	16.3%	27%
20%	70%	6 mm	1	18.5%	31%
20%	70%	6 mm	2	16.1%	17%
20%	70%	6 mm	3	17.5%	38%
40%	85%	6 mm	3	21.7%	38%
20%	85%	3 mm	1	15.0%	25%
20%	70%	3 mm	2	23.3%	18%
20%	70%	3 mm	3	19.5%	22%
30%	70%	3 mm	3	22.3%	20%
20%	85%	1.5 mm	3	26.3%	33%
30%	85%	1.5 mm	3	19.3%	33%

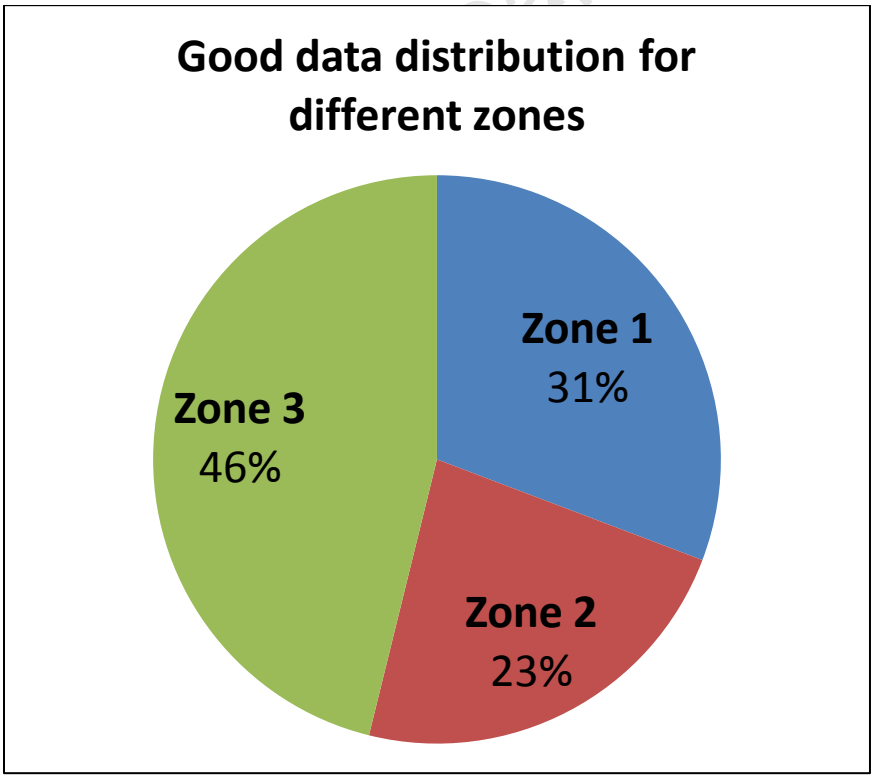

Figure 124: Good data sets in different zones

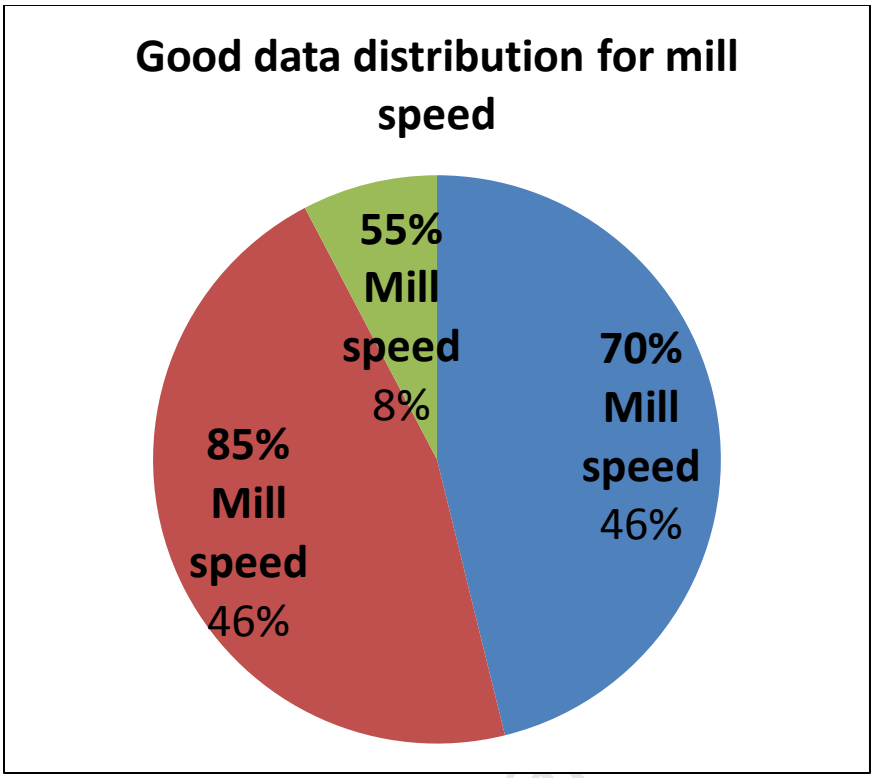

Figure 125: Good data for different mill speeds

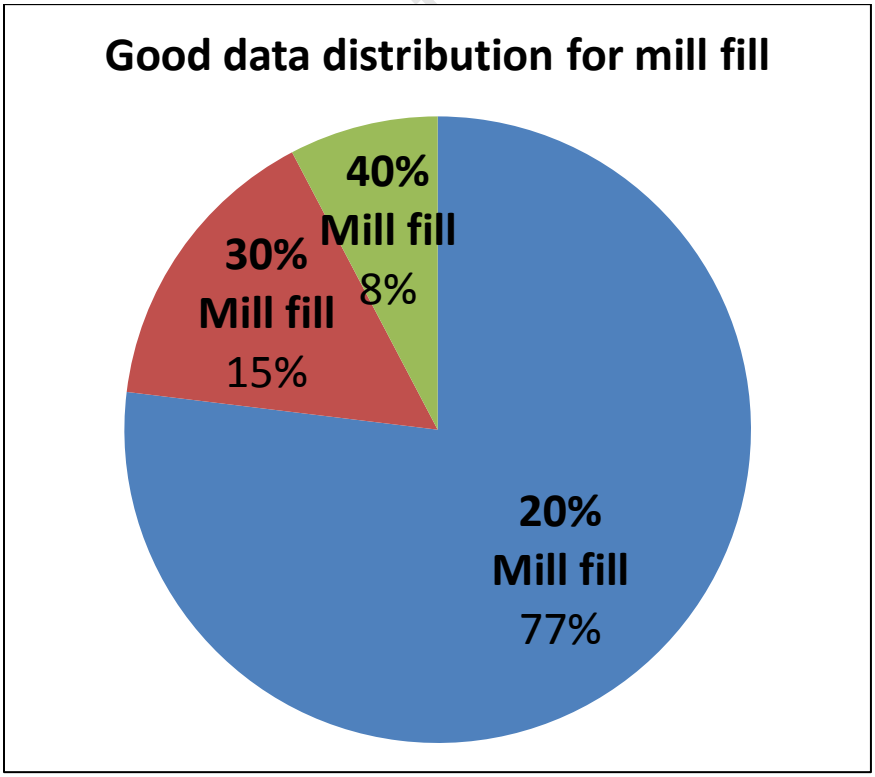

Figure 126: Good data sets for different mill fills

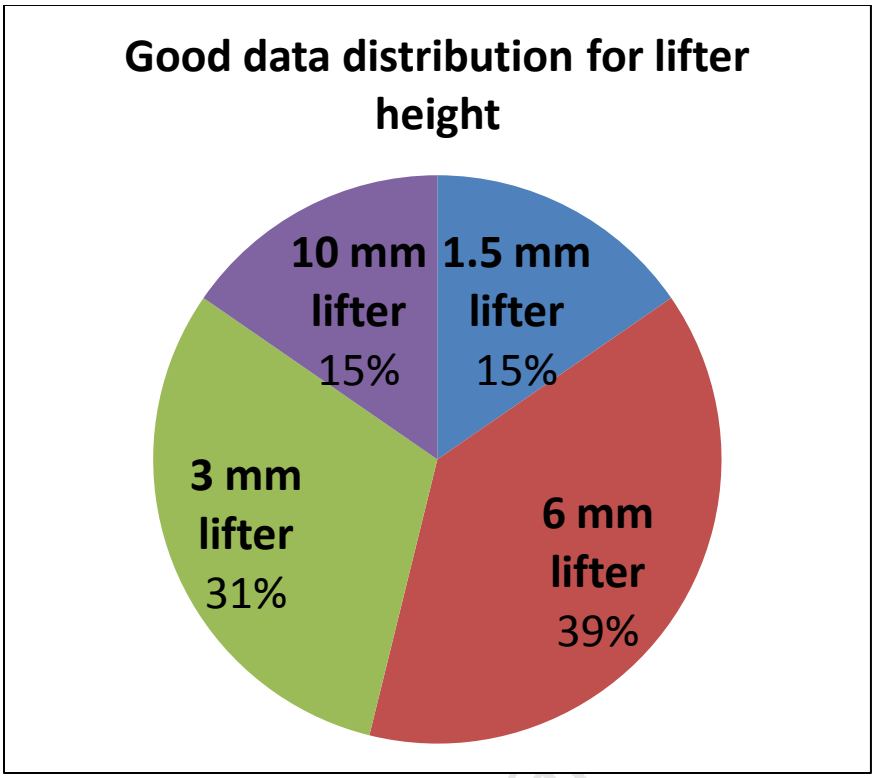

Figure 127: Good data sets for different lifter heights

16.8 Statistics of good visual data

Table 17: Summary table for the visual the velocity profile analysis

			Average difference		
Mill filling	**Mill speed**	**Lifter height**	Zone 1	Zone 2	Zone 3
20	85	10	15.0%	31.6%	19.3%
20	70	10	18.3%	45.0%	25.1%
20	55	10	19.4%	33.3%	25.7%
30	85	10	29.4%	40.3%	19.6%
30	70	10	36.6%	41.1%	26.5%
30	55	10	37.3%	43.2%	29.2%
40	85	10	38.0%	34.4%	19.6%
40	70	10	37.1%	47.6%	28.6%
40	55	10	38.0%	55.0%	35.3%
20	85	6	16.6%	16.3%	21.2%
20	70	6	18.5%	16.1%	17.5%
20	55	6	28.7%	30.4%	33.3%
30	85	6	35.6%	40.8%	26.2%
30	70	6	36.8%	37.6%	30.3%
30	55	6	32.8%	45.6%	35.7%

40	85	6	32.9%	38.0%	21.7%
40	70	6	34.4%	47.8%	38.3%
40	55	6	40.2%	59.6%	40.9%
20	85	3	15.0%	47.8%	21.5%
20	70	3	23.5%	23.3%	19.5%
20	55	3	21.9%	25.7%	37.1%
30	85	3	22.9%	46.7%	18.1%
30	70	3	27.1%	45.3%	22.3%
30	55	3	32.3%	49.1%	36.2%
40	85	3	41.3%	49.7%	21.2%
40	70	3	47.3%	52.6%	27.7%
40	55	3	43.5%	60.3%	46.7%
20	85	1.5	41.3%	21.2%	26.3%
20	70	1.5	33.4%	21.4%	33.7%
20	55	1.5	51.3%	26.5%	43.0%
30	85	1.5	28.1%	40.6%	19.3%
30	70	1.5	33.3%	50.4%	23.2%
30	55	1.5	30.4%	54.0%	46.4%
40	85	1.5	45.4%	49.5%	24.5%
40	70	1.5	48.9%	55.3%	23.8%
40	55	1.5	45.1%	57.9%	47.9%

Table 18: Summary table for the best visual the velocity profile analysis

Mill filling	Mill speed	Lifter height	Zone	Mean Difference
20%	85%	10 mm	1	15.0%
20%	70%	10 mm	1	18.3%
20%	55%	10 mm	1	19.4%
30%	85%	10 mm	1	29.4%
20%	85%	10 mm	3	19.3%
20%	70%	10 mm	3	25.1%
20%	55%	10 mm	3	25.7%
30%	85%	10 mm	3	19.6%
30%	70%	10 mm	3	26.5%
30%	55%	10 mm	3	29.2%
40%	85%	10 mm	3	19.6%
40%	70%	10 mm	3	28.6%
20%	85%	6 mm	1	16.6%
20%	70%	6 mm	1	18.5%
20%	55%	6 mm	1	28.7%
20%	85%	6 mm	2	16.3%

20%	70%	6 mm	2	16.1%
20%	85%	6 mm	3	21.2%
20%	70%	6 mm	3	17.5%
30%	85%	6 mm	3	26.2%
40%	85%	6 mm	3	21.7%
20%	85%	3 mm	1	15.0%
20%	70%	3 mm	1	23.5%
20%	55%	3 mm	1	21.9%
30%	85%	3 mm	1	22.9%
30%	70%	3 mm	1	27.1%
20%	70%	3 mm	2	23.3%
20%	55%	3 mm	2	25.7%
20%	85%	3 mm	3	21.5%
20%	70%	3 mm	3	19.5%
30%	85%	3 mm	3	18.1%
30%	70%	3 mm	3	22.3%
40%	85%	3 mm	3	21.2%
40%	70%	3 mm	3	27.7%
20%	85%	1.5 mm	2	21.2%
20%	70%	1.5 mm	2	21.4%
20%	55%	1.5 mm	2	26.5%
20%	85%	1.5 mm	3	26.3%
30%	85%	1.5 mm	1	28.1%
30%	85%	1.5 mm	3	19.3%
30%	70%	1.5 mm	3	23.2%
40%	85%	1.5 mm	3	24.5%
40%	70%	1.5 mm	3	23.8%

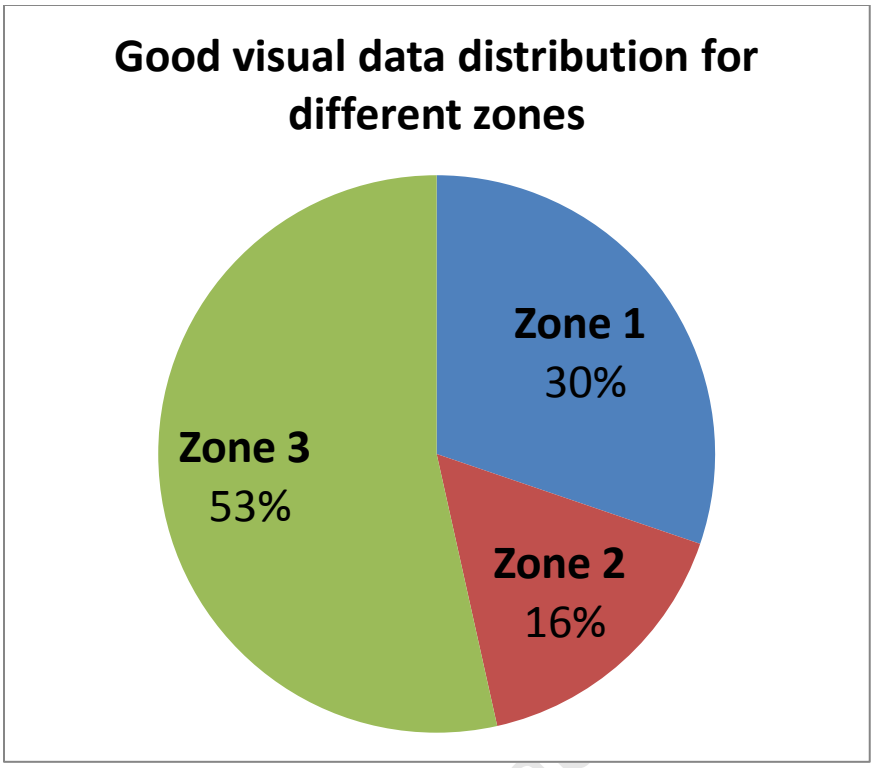

Figure 128: Good visual data sets in different zones

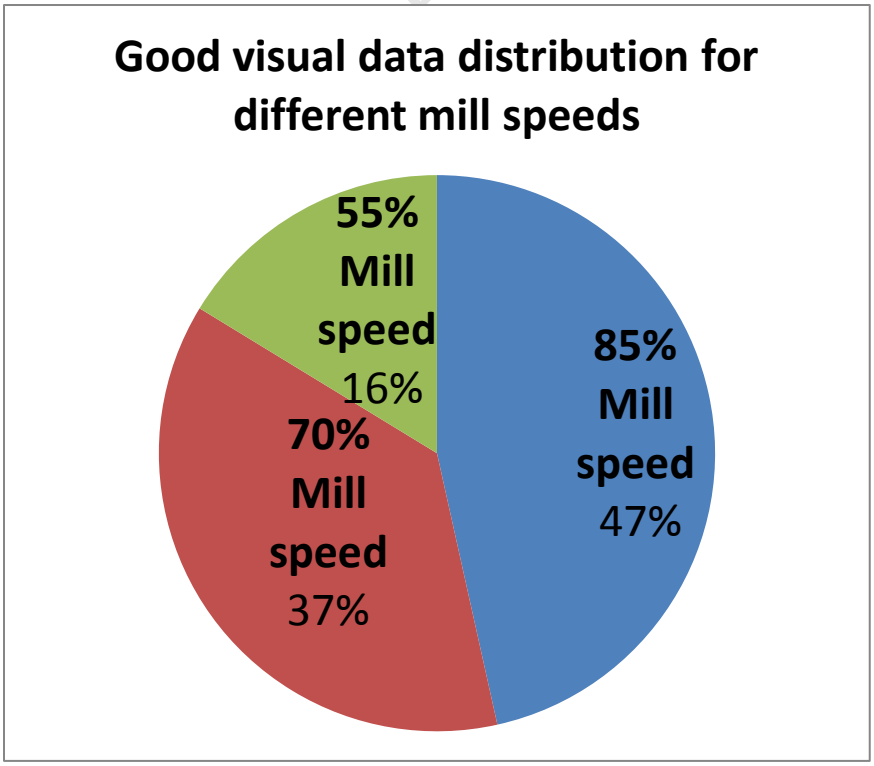

Figure 129: Good visual data sets in different mill speeds

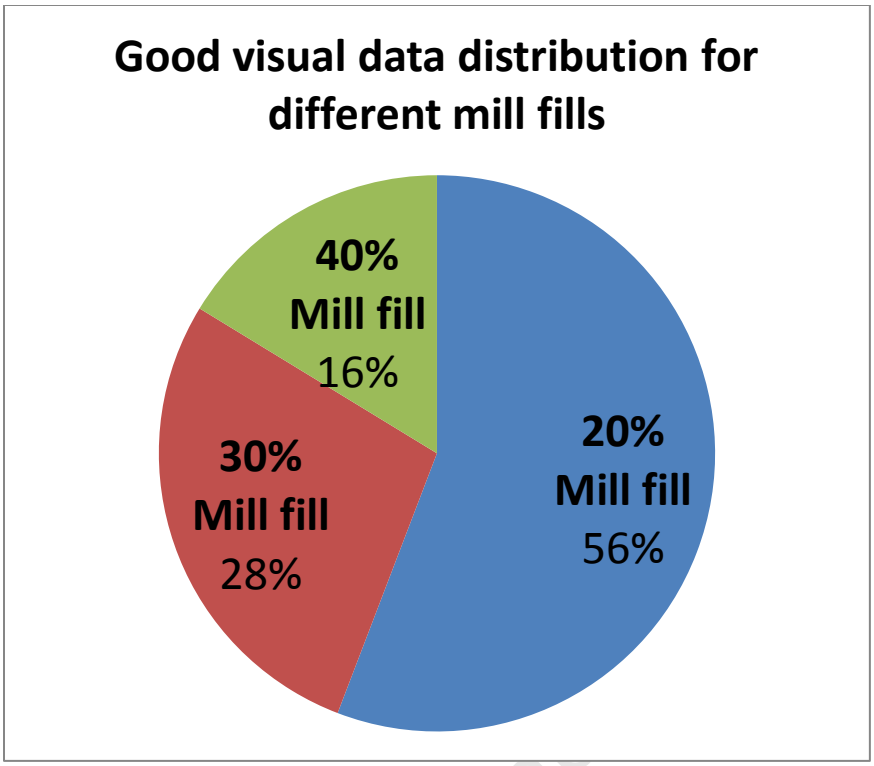

Figure 130: Good visual data sets in different mill fills

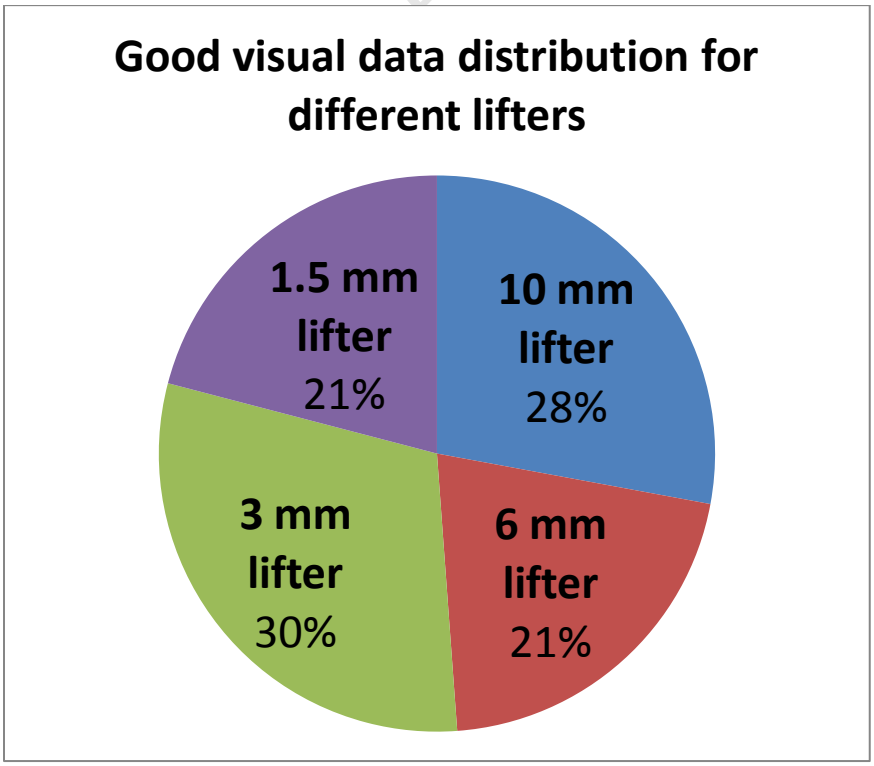

Figure 131: Good visual data sets in different lifter heights

16.9 Effect of lifter height on velocity profile

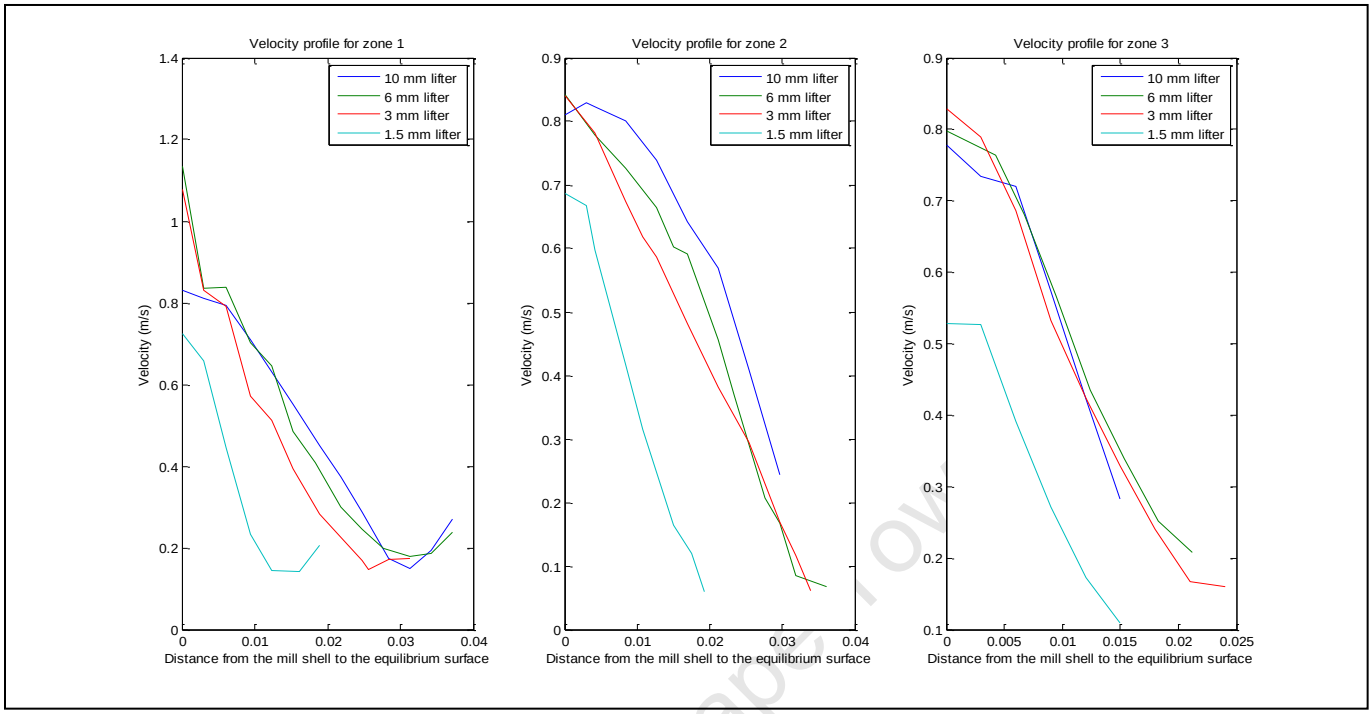

Figure 132: Velocity profile analysis for 20% mill fill and 70% mill speed with varying lifter heights

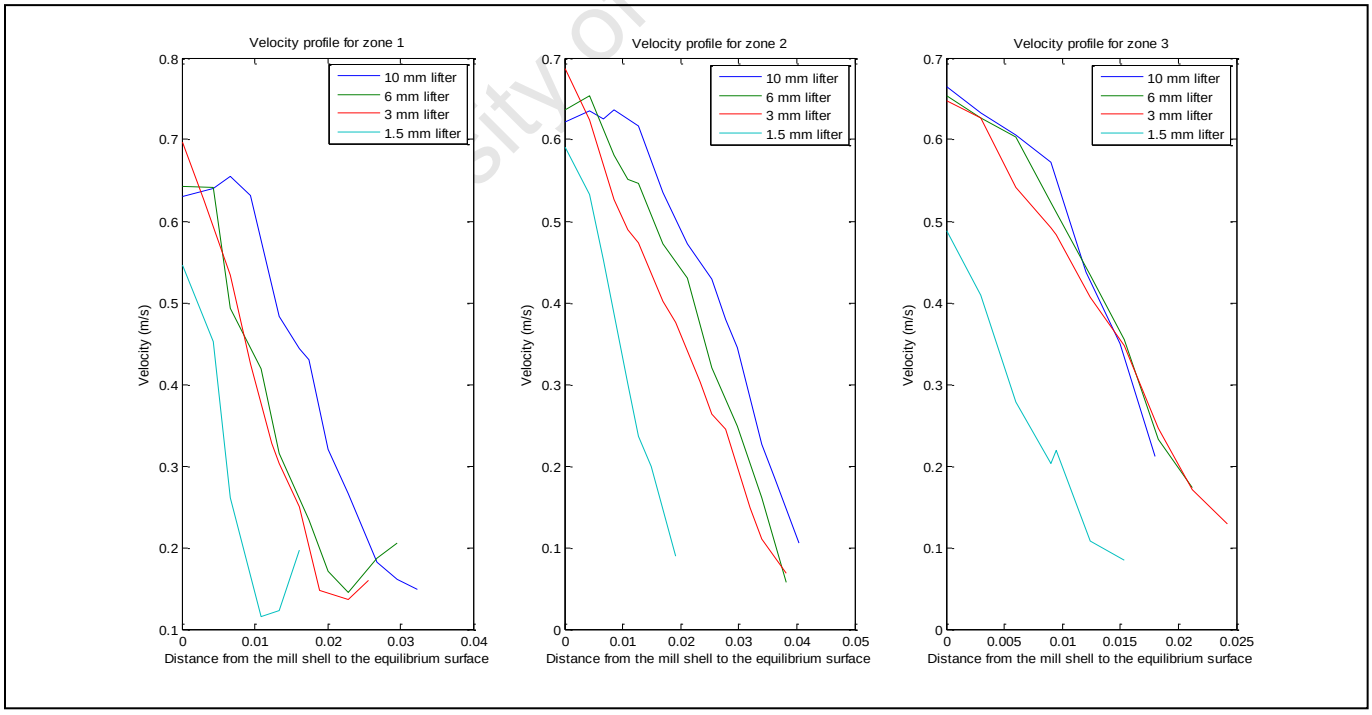

Figure 133: Velocity profile analysis for 20% mill fill and 55% mill speed with varying lifter heights

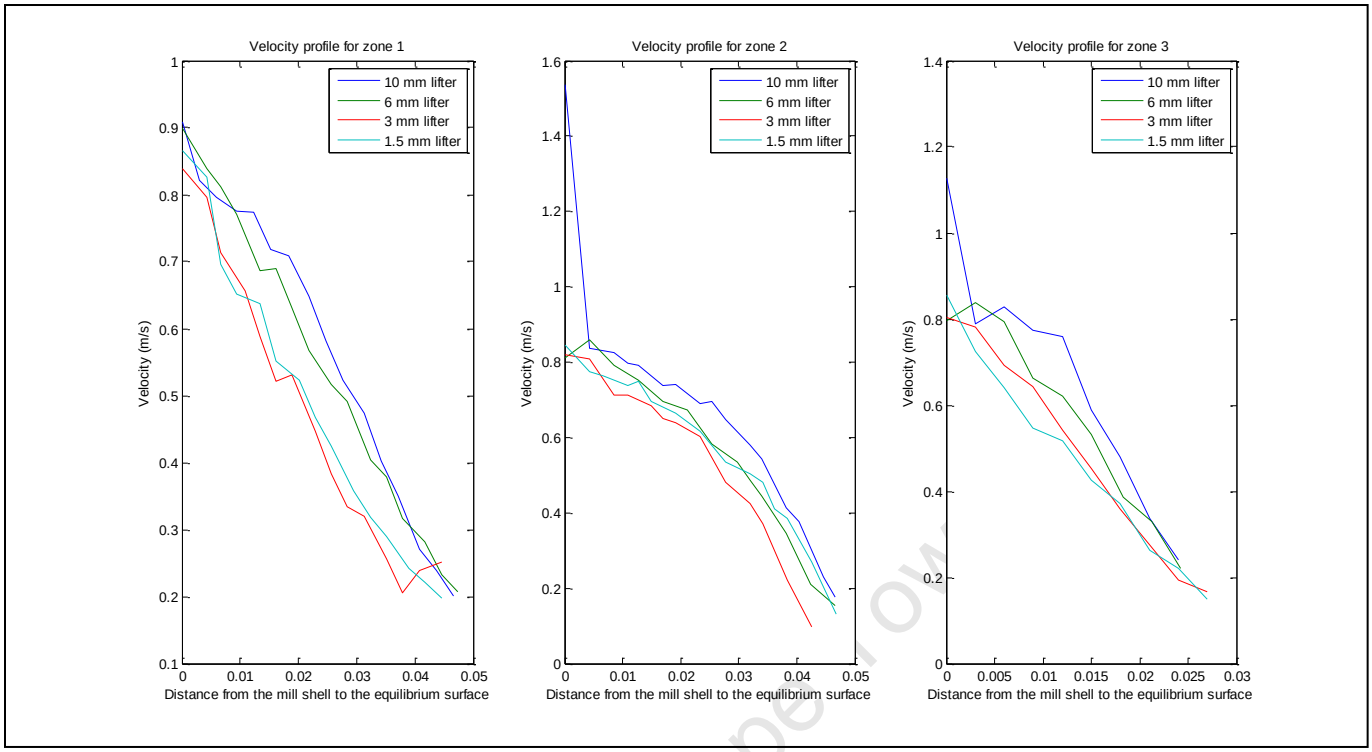

Figure 134: Velocity profile analysis for 30% mill fill and 70% mill speed with varying lifter heights

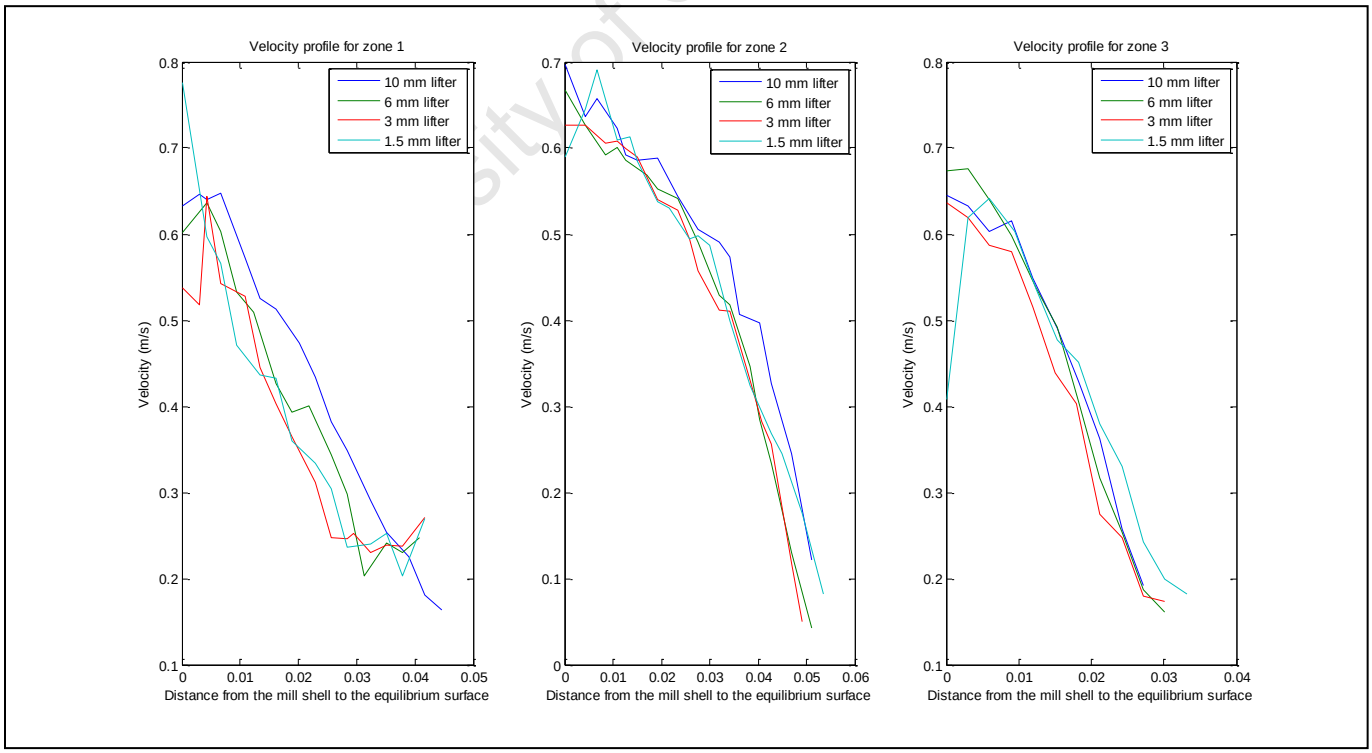

Figure 135: Velocity profile analysis for 30% mill fill and 55% mill speed with varying lifter heights

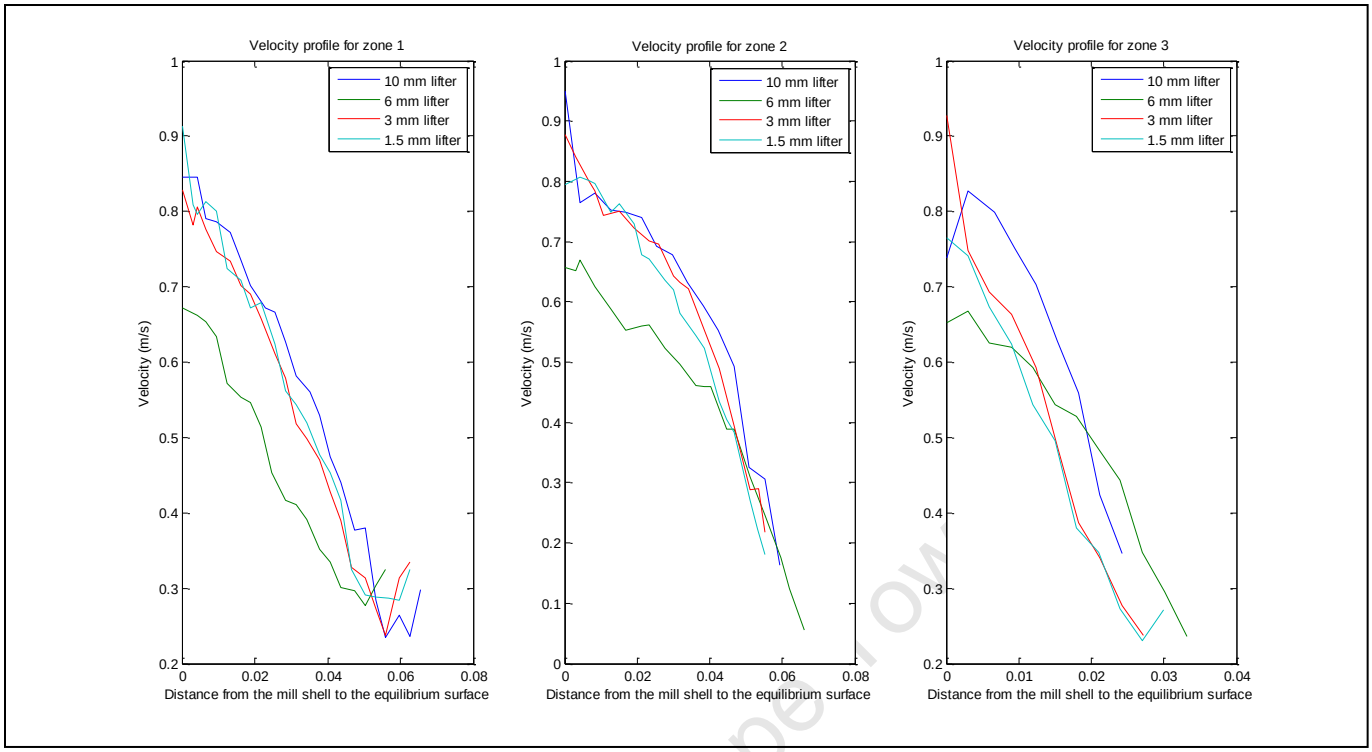

Figure 136: Velocity profile analysis for 40% mill fill and 70% mill speed with varying lifter heights

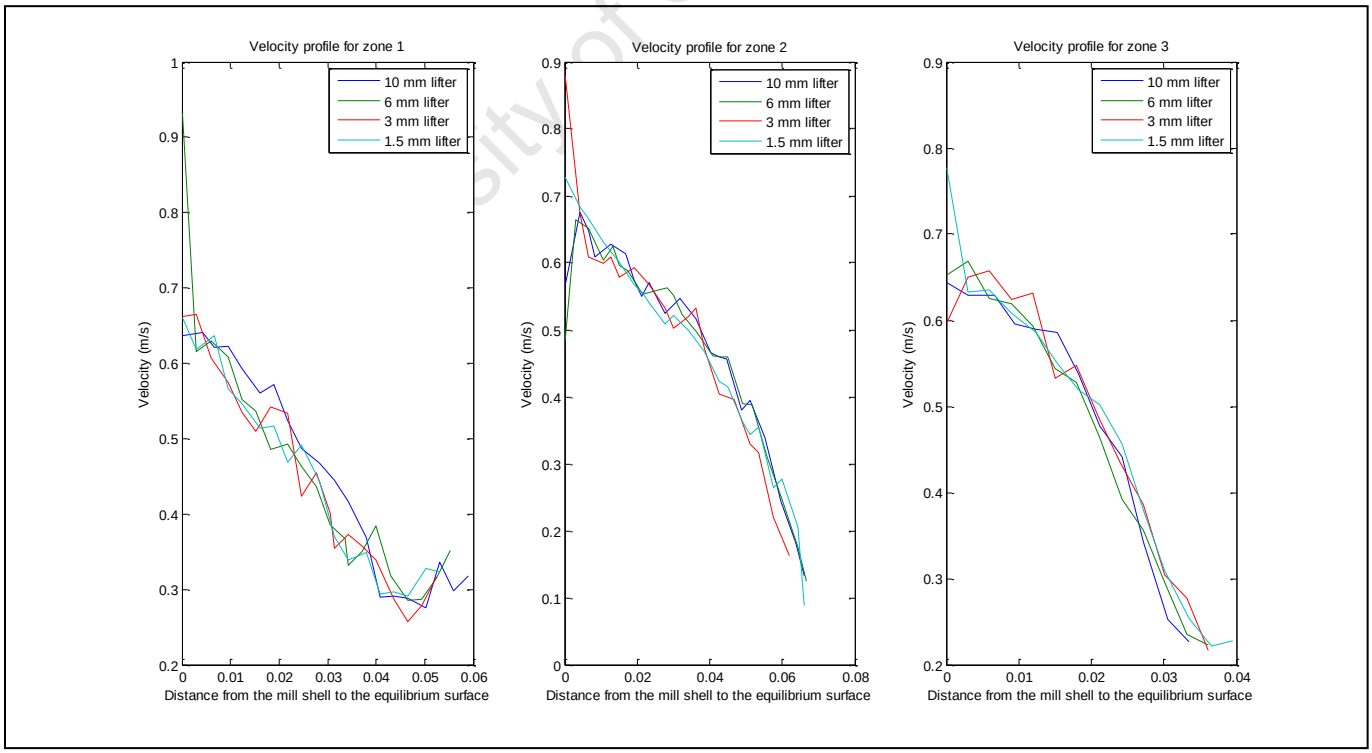

Figure 137: Velocity profile analysis for 40% mill fill and 55% mill speed with varying lifter heights

16.10 Charge profile movement

Table 19: Toe and shoulder angles, charge size and toe height with varying mill conditions

Mill filling	Mill speed	Lifter height	Toe Angle (°)	Shoulder Angle (°)	Charge size (°)	Toe height (mm)
20	85	10	151.51	286.54	135.04	19.00
20	70	10	151.21	283.70	132.49	26.25
20	55	10	134.81	284.81	150.00	51.78
30	85	10	140.78	312.18	171.40	44.12
30	70	10	137.77	303.02	163.04	48.57
30	55	10	128.89	296.15	165.67	66.11
40	85	10	131.96	325.81	178.85	57.37
40	70	10	131.63	316.54	175.30	58.05
40	55	10	121.05	309.04	183.80	77.12
20	85	6	144.34	291.47	147.13	36.49
20	70	6	145.66	291.41	145.75	44.83
20	55	6	132.14	282.68	152.26	59.81
30	85	6	137.18	313.46	176.28	44.34
30	70	6	135.54	301.60	166.06	52.93
30	55	6	127.03	297.41	168.95	61.92
40	85	6	129.56	320.16	190.60	57.42
40	70	6	123.13	312.11	185.35	76.16
40	55	6	123.18	307.32	184.14	76.48
20	85	3	145.18	291.39	153.76	37.38
20	70	3	133.18	290.41	157.23	56.35
20	55	3	134.04	281.90	150.34	54.29
30	85	3	139.51	306.40	166.89	43.06
30	70	3	129.04	299.89	174.00	62.75
30	55	3	127.33	297.99	170.66	67.02
40	85	3	135.48	320.23	188.69	48.80
40	70	3	126.35	310.11	183.75	70.43
40	55	3	120.26	305.26	184.99	79.80
20	85	1.5	147.88	277.54	138.08	39.67
20	70	1.5	145.67	274.51	136.20	37.77
20	55	1.5	148.12	278.03	129.91	34.62
30	85	1.5	140.75	302.48	161.73	41.82
30	70	1.5	130.00	300.88	173.43	59.27
30	55	1.5	128.25	296.19	167.94	65.65
40	85	1.5	131.34	318.15	186.81	53.20
40	70	1.5	123.25	301.22	177.97	75.31
40	55	1.5	122.52	305.87	183.35	79.05

16.11 Charge Size

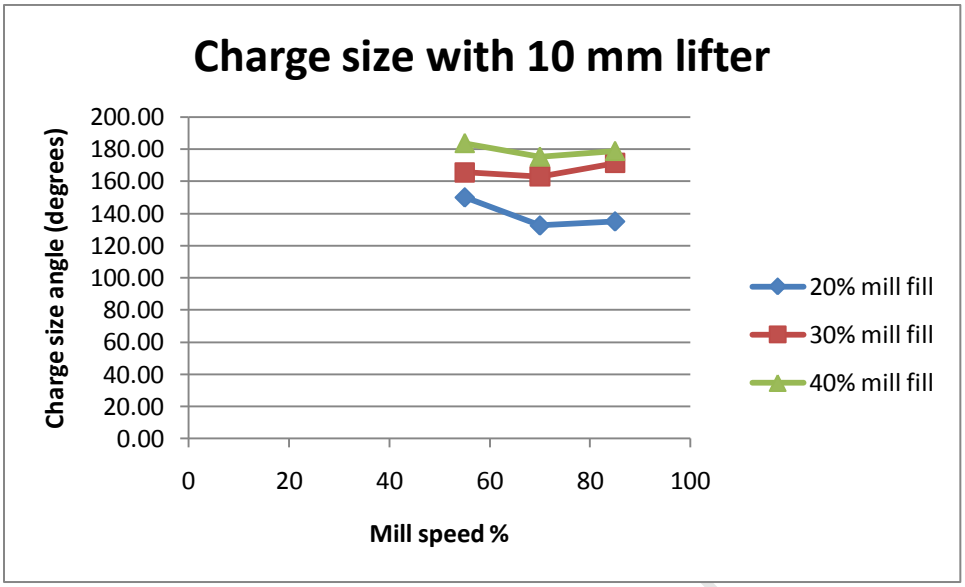

Figure 138: Charge size at different mill speeds at 10 mm lifter height

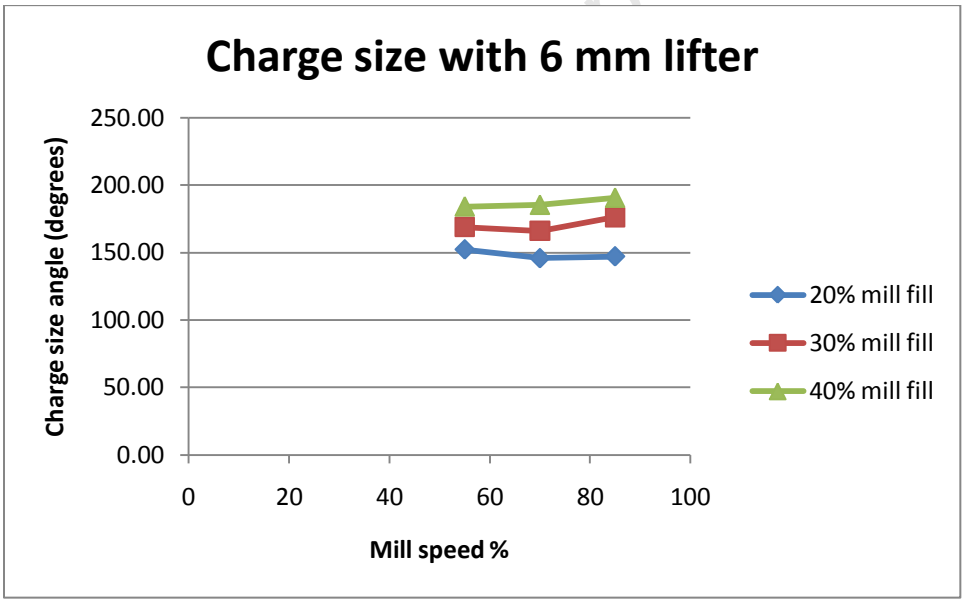

Figure 139: Charge size at different mill speeds at 6 mm lifter height

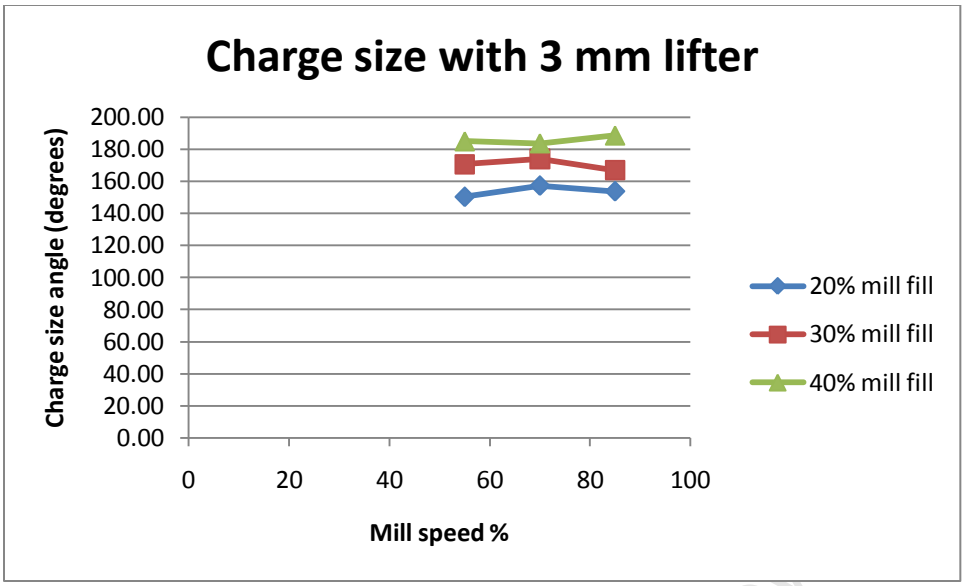

Figure 140: Charge size at different mill speeds at 3 mm lifter height

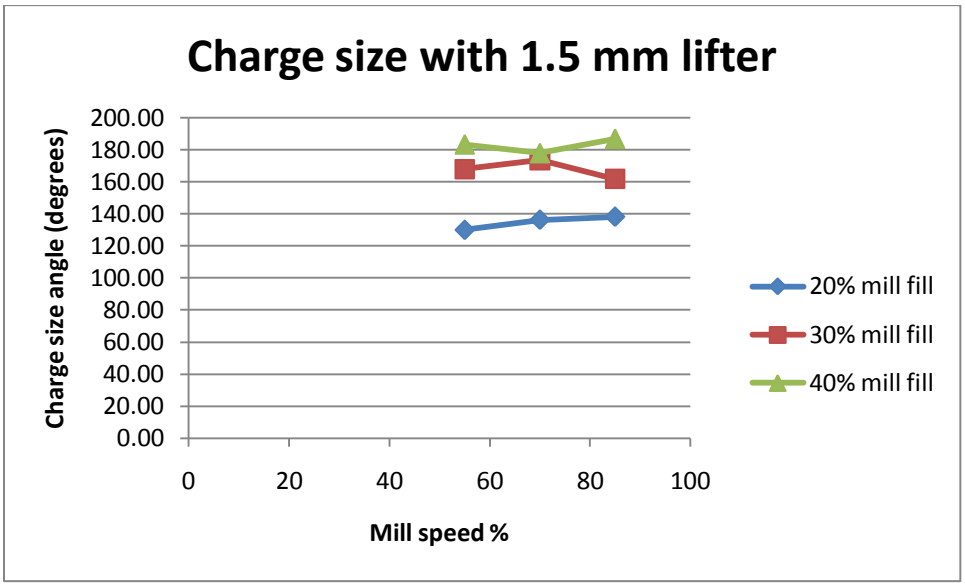

Figure 141: Charge size at different mill speeds at 1.5 mm lifter height

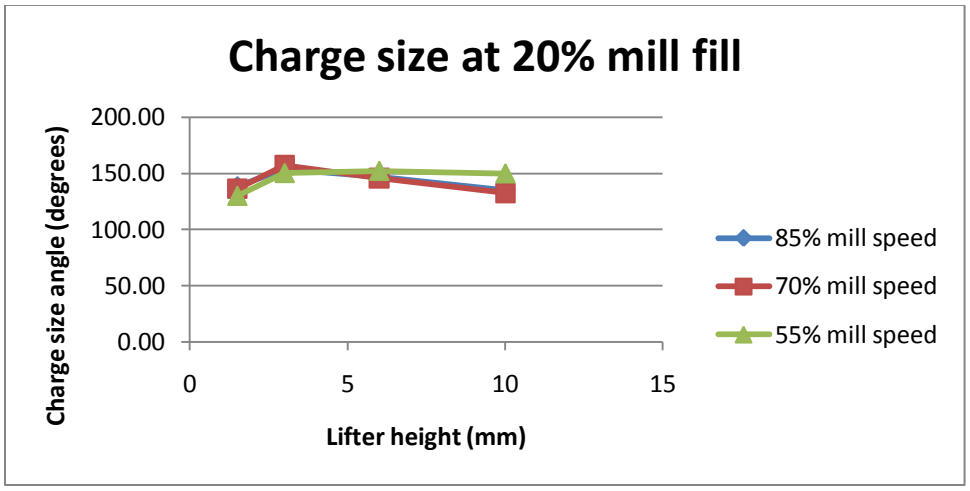

Figure 142: Charge size at different lifter heights at 20% mill fill

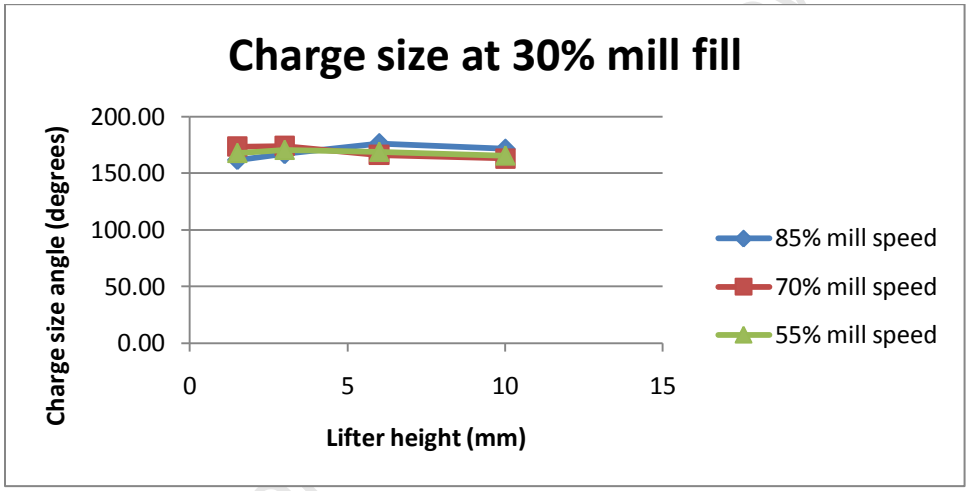

Figure 143: Charge size at different lifter heights at 30% mill fill

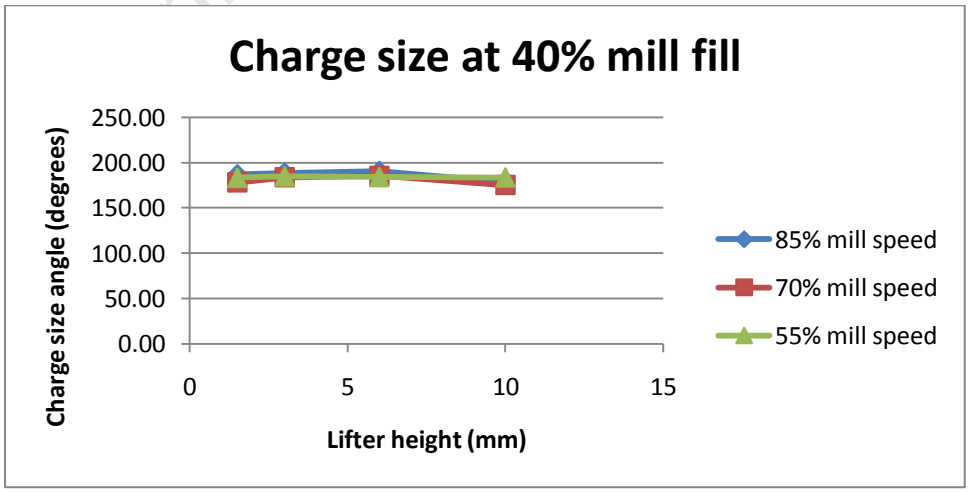

Figure 144: Charge size at different lifter heights at 40% mill fill

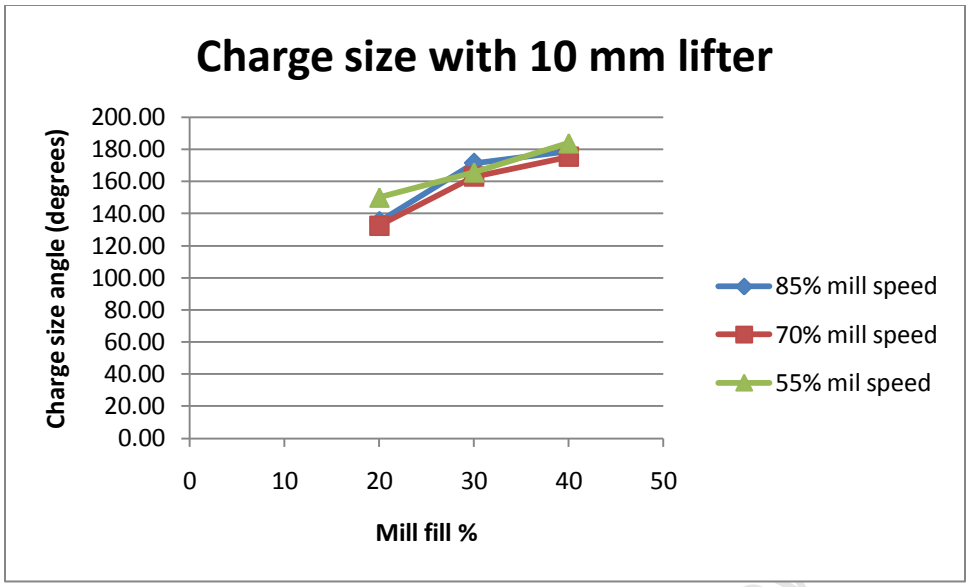

Figure 145: Charge size at different mill fills at 10 mm lifter height

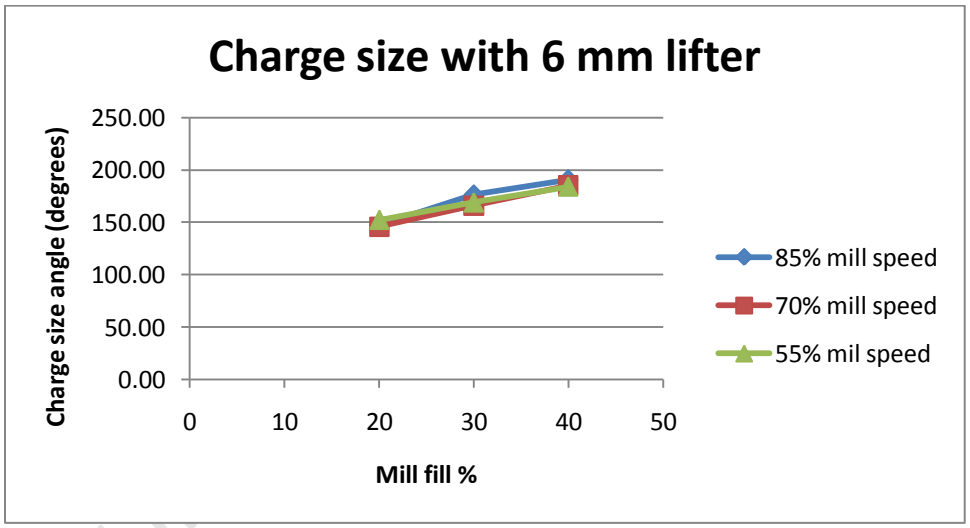

Figure 146: Charge size at different mill fills at 6 mm lifter height

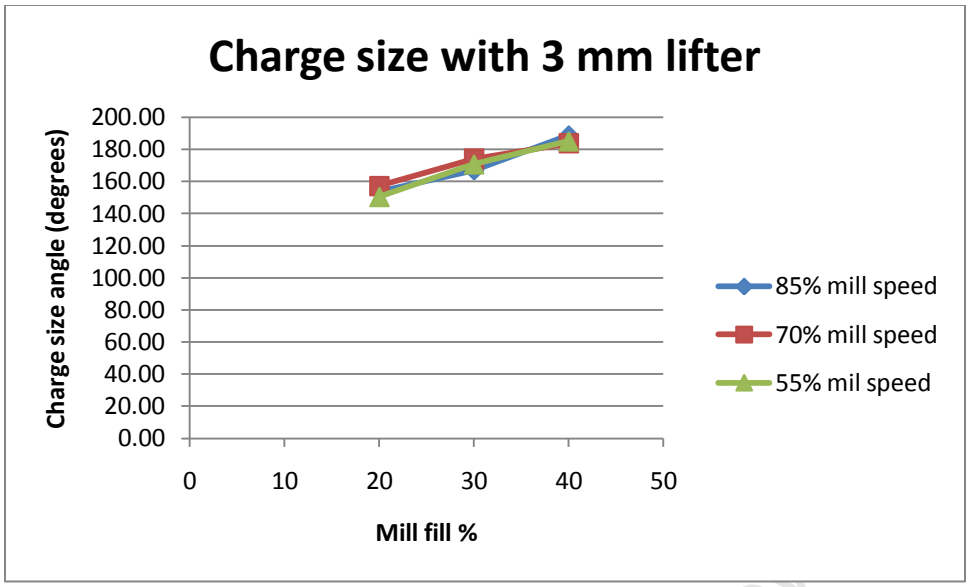

Figure 147: Charge size at different mill fills at 3 mm lifter height

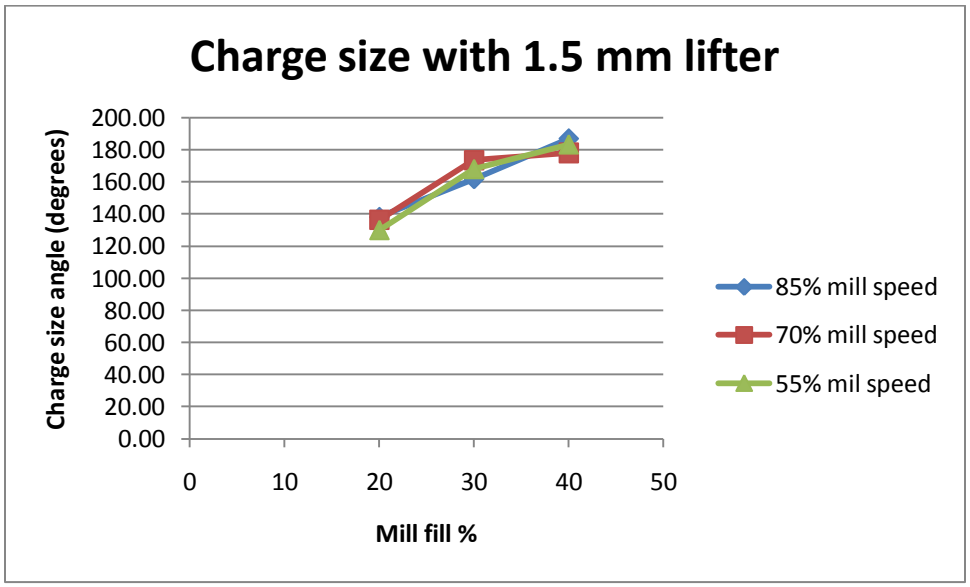

Figure 148: Charge size at different mill fills at 1.5 mm lifter height

16.12 Toe height

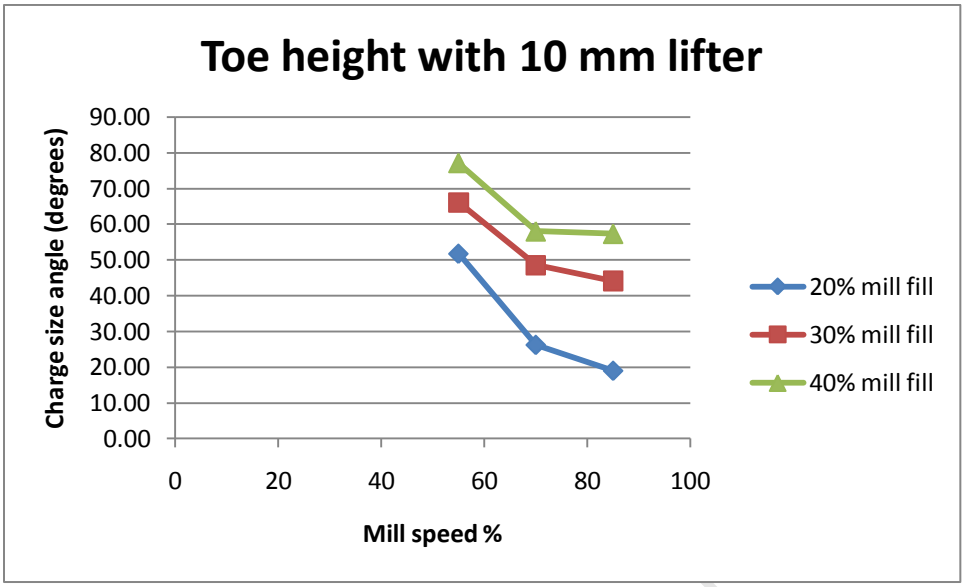

Figure 149: Toe height at different mill speeds at 10 mm lifter height

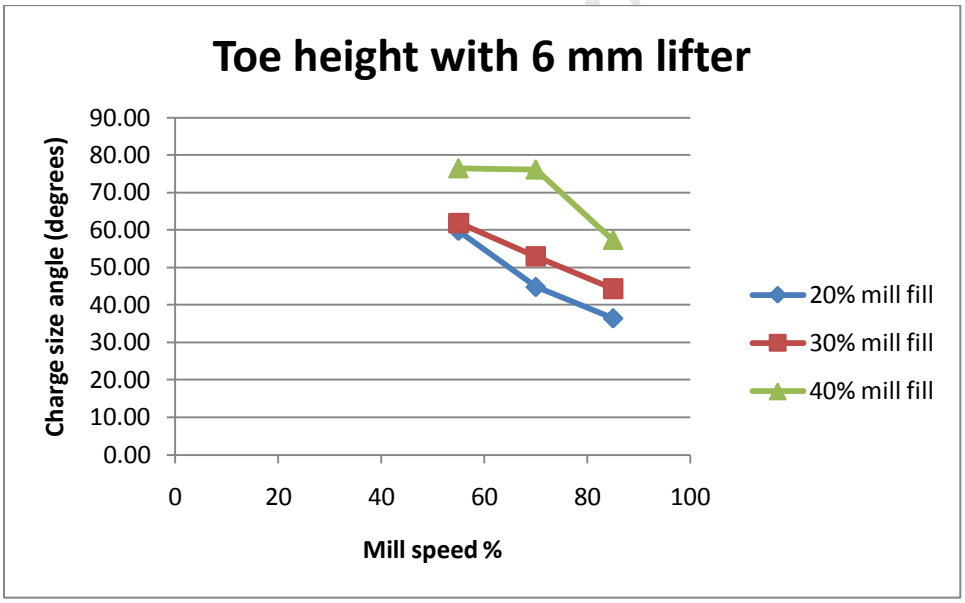

Figure 150: Toe height at different mill speeds at 6 mm lifter height

Figure 151: Toe height at different mill speeds at 3 mm lifter height

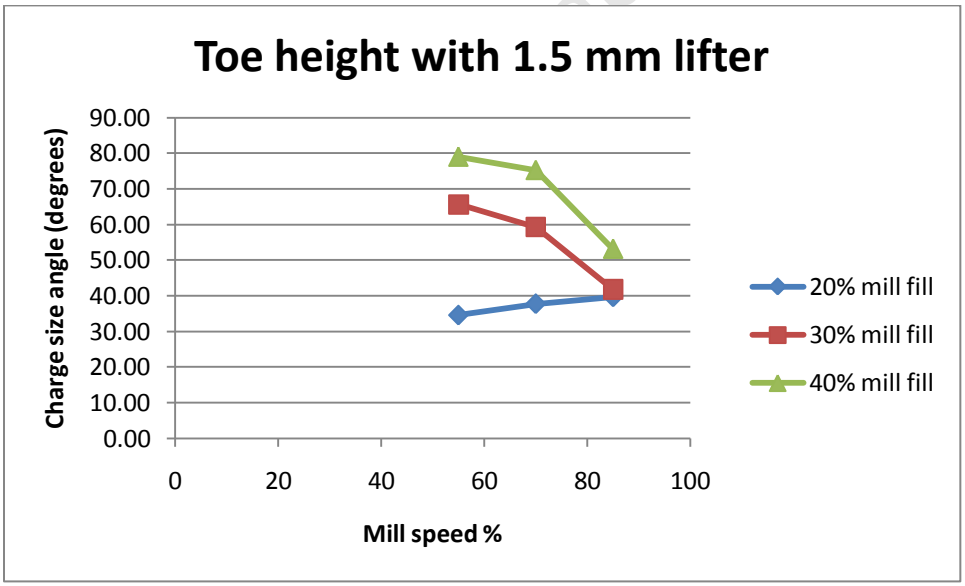

Figure 152: Toe height at different mill speeds at 1.5 mm lifter height

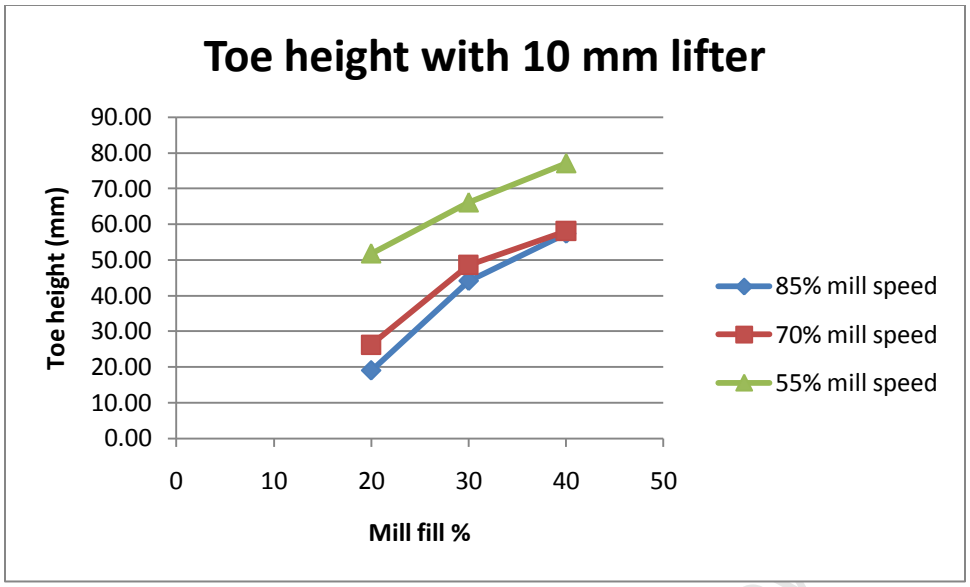

Figure 153: Toe height at different mill fills at 10 mm lifter height

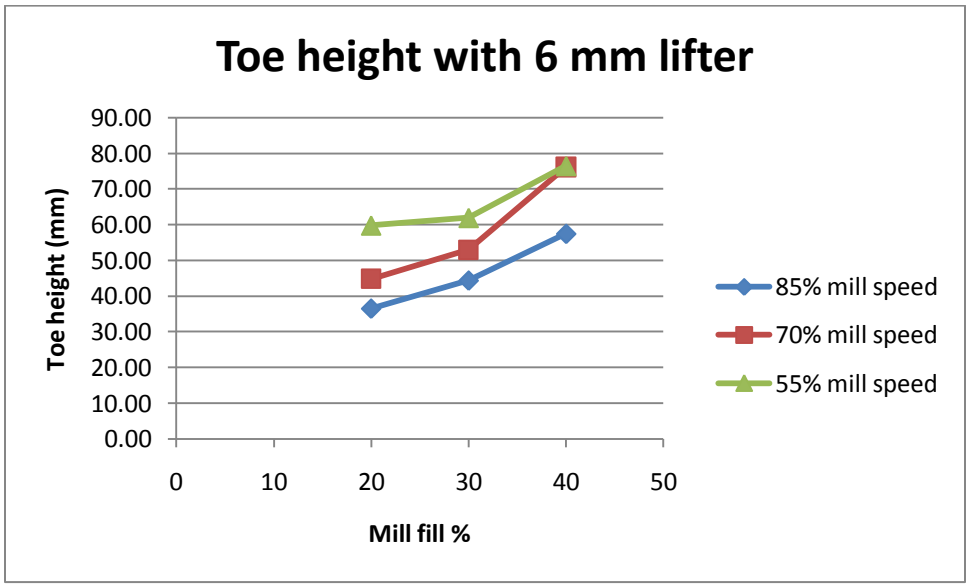

Figure 154: Toe height at different mill fills at 6 mm lifter height

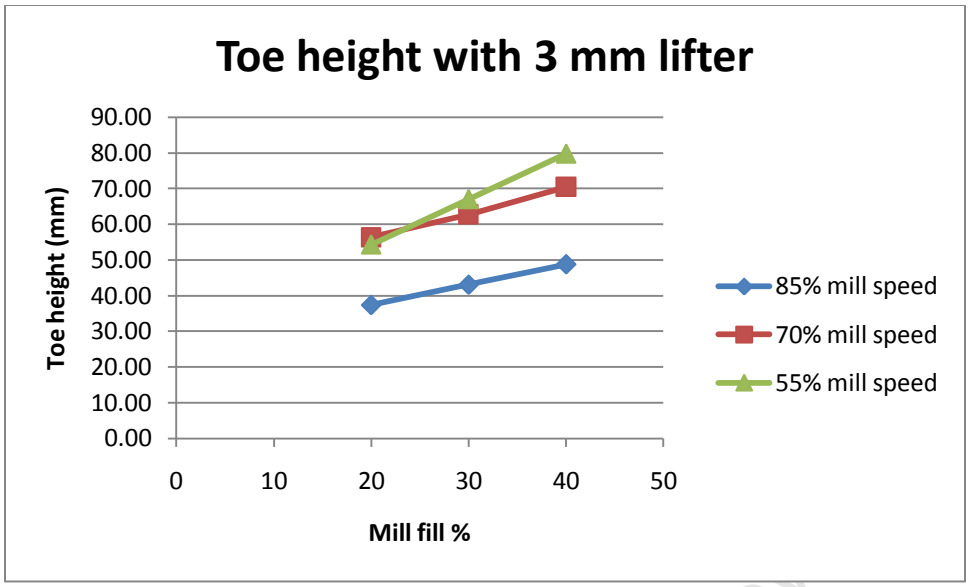

Figure 155: Toe height at different mill fills at 3 mm lifter height

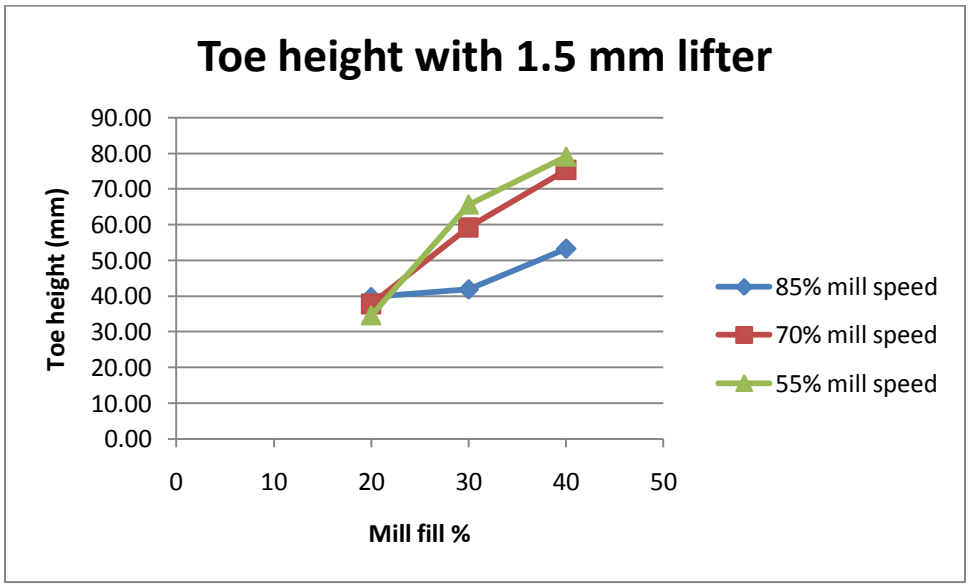

Figure 156: Toe height at different mill fills at 1.5 mm lifter height

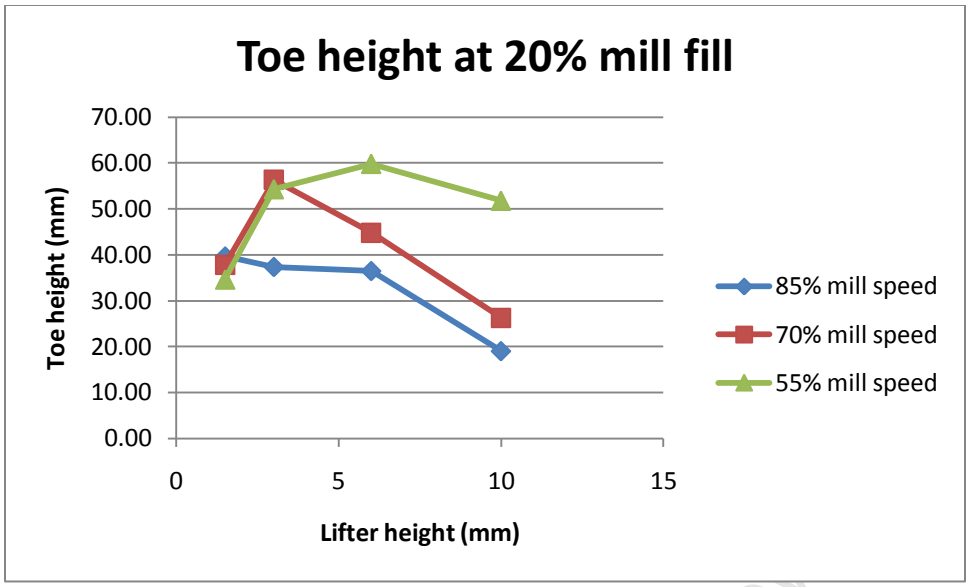

Figure 157: Toe height at different lifter heights at 20% mill fill

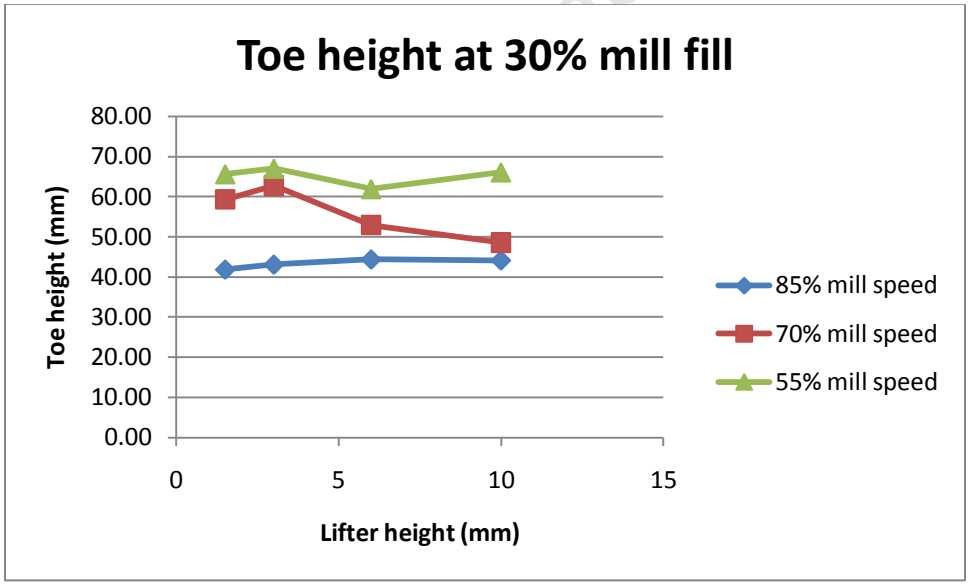

Figure 158: Toe height at different lifter heights at 30% mill fill

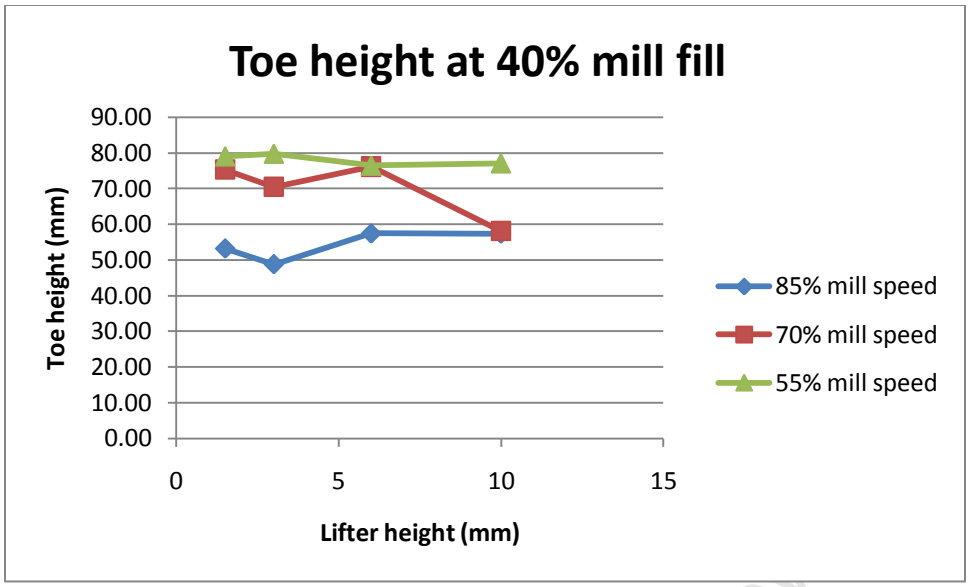

Figure 159: Toe height at different lifter heights at 40% mill fill

16.13 Experimental instructions

Emptying and filling the experimental mill

1. Move mill and steel base out of PEPT camera
2. Secure mill and steel base on adjustable trolley
3. Unscrew all the screws holding the hatch to the mill
4. Remove black grips from base structure of the mill
5. Attach grips to the hatch of the mill
6. Used grips to open hatch
7. Tilt mill and empty into a tray

➢ Use hands to assist and make sure most of the glass beads are out of the mill

8. If necessary, find the tracer and remove it from the tray by using a Geiger Counter
9. Weigh the glass bead to make up charge require
10. Transfer glass beads into the mill

11. Use mill opening from the hatch to refill the mill with glass beads
12. Close and tighten hatch
13. Unscrew grips and reattach to steel base

Step by step instructions

Pre-experimental checks

1. Make sure mill is aligned
2. Make sure location markers have been used if necessary
3. Make sure the tachometer has been attached to the steel base and is in the correct position
4. Make sure all the experimental mill's parts are available (screws, bolts,…..etc)
5. Prepare glass beads to make up the desired charge level

Experimental Procedure

1. Attach desired lifter to the mill (take note of lifter height)

- Start with 10mm lifters and then descending height

2. Add glass beads to the experimental mill
3. Align the mill
4. Take location marker measurements
5. Add radioactive glass bead to charge
6. Set the mill speed with speed controller
7. Start data recording
8. Allow the experimental mill to run for 45 minutes in total

- Data is recorded in 15 minute intervals because of the size of the resultant data files

Changing variables of the experimental mill:

9. Vary mill speed from 85% to 55% keeping mill filling and the lifter configuration constant

- Run experiment for 45 minutes

10. Take readings for every mill speed

- One tracer is used for all the mill speeds

11. Stop data recording when all the mill speeds have been recorded
12. Stop mill rotation
13. Take radioactive glass bead out
14. Change mill filling value by adding in 10% mill filling (which has been prepared) keeping the lifter configuration constant
15. Repeat steps 4 to 14 until all desired mill fillings have been recorded
16. Take out all the glass beads
17. Take radioactive glass bead out
18. Change lifter configuration

- Take note of the lifter characteristics (lifter height)

19. Repeat steps 2-17 for the new lifter

Once all data has been collected for the different mill speeds, mill fillings and lifter configurations, the data is then stored and initial data processing commences.

16.14 Surface extraction instructions

The detailed instructions for the surface extraction are as follows:

- Use the ‘hold on’ function in the ‘command window’

  - This allows the probability plot to stay plotted even when other codes are running

- In ‘Command Window’ use the ‘ginput’ function

  - ginput allows the data points to be gathered and then displayed

- Use the ginput function to track the charge free surface from the plot

  - Therefore the charge free surface data is logged with the ginput function

- Charge free surface data is displayed in the ‘command window’

  - Press enter for the last data point

- Take the charge free surface data and put it through a spline smoothing function